

DISSERTATION

NANOFIBER REINFORCEMENT OF A GEOPOLYMER MATRIX FOR IMPROVED  
COMPOSITE MATERIALS MECHANICAL PERFORMANCE

Submitted by

AKM Samsur Rahman

Department of Mechanical Engineering

In partial fulfillment of the requirements

For the Degree of Doctor of Philosophy

Colorado State University

Fort Collins, Colorado

Summer 2015

Doctoral Committee:

Advisor: Donald W Radford

Walajabad S Sampath

Troy B Holland

Paul Heyliger

Copyright by AKM Samsur Rahman 2015

All Rights Reserved

## ABSTRACT

### NANOFIBER REINFORCEMENT OF A GEOPOLYMER MATRIX FOR IMPROVED COMPOSITE MATERIALS MECHANICAL PERFORMANCE

Geopolymers have the potential to cross the process performance gap between polymer matrix and ceramic matrix composites (CMC), enabling high temperature capable composites that are manufactured at relatively low temperatures. Unfortunately, the inherently low toughness of these geopolymers limits the performance of the resulting fiber reinforced geopolymer matrix composites. Toughness improvements in composites can be addressed through the adjustments in the fiber/matrix interfacial strength and through the improvements in the inherent toughness of the constituent materials. This study investigates the potential to improve the inherent toughness of the geopolymer matrix material through the addition of nanofillers, by considering physical dimensions, mechanical properties, reinforcing capability and interfacial bond strength effects.

A process optimization study was first undertaken to develop the ability to produce consistent, neat geopolymer samples, a critical precursor to producing nano-filled geopolymer for toughness evaluation. After that, single edge notched bend beam fracture toughness and un-notched beam flexural strength were evaluated for silicon carbide, alumina and carbon nanofillers reinforced geopolymer samples treated at various temperatures in reactive and inert environments. Toughness results of silicon carbide and carbon nanofillers reinforced geopolymers suggested that with the improved baseline properties, high aspect ratio nanofillers with high interfacial bond strength are the most capable in further improving the toughness of geopolymers. Among the high aspect ratio nanofillers i.e. nanofibers, 2vol% silicon carbide whisker (SCW) showed the highest improvement in fracture toughness and flexural strength of ~164% & ~185%,

respectively. After heat treatment at 650 °C, SCW reinforcement was found to be effective, with little reduction in the performance, while the performance of alumina nanofiber (ANF) reinforced geopolymer significantly reduced. By means of SEM, EDS and X-ray diffraction techniques, it was found that the longer and stronger SCW is more capable of reinforcing the microstructurally inhomogeneous geopolymer than the smaller diameter, shorter ANF. After heat treatment at 760 °C, the effectiveness of SCW as reinforcement in both fracture toughness and flexural strength was reduced by ~89% and ~43%, respectively, while, the ANF filled materials performed worse than the neat geopolymer. A strong interaction was suggested between ANF and geopolymer at high temperature by means of chemical reactions and diffusion. SEM & X-ray diffraction results suggested the formation of  $Al_4C_3$  on the SCW surface, which could reduce the interface strength between SCW and geopolymer. Therefore it is suggested that the interface strength should be as high as required for load transfer and crack bridging.

Finally, to investigate the potential synergy of a nano-filled matrix material and the fiber/matrix interface toughening mechanism of a continuous fiber composite, composite specimens were produced and tested. Flexural and shear strengths of Nextel 610 continuous fiber reinforced 2vol% SCW filled geopolymer matrix composites were investigated. Specimens were produced with cleaned Nextel fiber and with carbon-coated fibers to investigate the combinations of nano-filled matrix with continuous reinforcement that is well bonded (cleaned fiber) versus poorly bonded (carbon-coated fiber) to the matrix. The results showed that flexural strength of cleaned and coated fiber composites improved by ~35% and ~21% respectively, while shear strength of the similar composite systems improved by ~39.5% and ~24%. The results verified the effectiveness of SCW in toughening not only the neat geopolymer, but also continuous fiber reinforced geopolymer matrix composites.

## ACKNOWLEDGEMENTS

I would like to sincerely thank Dr. Donald Radford for his constant guidance, enthusiasm and insight through the project.

I would also like to thank, Pyromeral Inc for their research grade geopolymers which was the primary material to conduct this project. My thanks go to ANF technologies (Estonia) and superior graphite for supporting my project with their Alumina nanofiber and Silicon Carbide nanoparticles, respectively. I am thankful to Franklin A. Graybill Statistical Laboratory for assisting me to conduct the statistical data analysis of my project. Thank you to Dr. Troy B Holland for guiding me in analyzing the properties of brittle materials and brittle matrix composites. Thank you to Dr. Waltraud M. Kriven, Professor of University of Illinois for her help in gaining insight about the chemistry of geopolymers. Thank you to Dr. Patrick Mccurdy for assisting me in performing SEM and EDS analysis. Thank you to Patrick Jackson for helping me in preparing geopolymers composite samples for the verification of my research hypothesis.

Most of all I am grateful to my parents for their boundless support with their patience & prayer for accomplishing this project. Obviously, I would like to thank my wife Shammy and daughter Saamiya for their patience and understanding and their support on the weekends and holidays when I was conducting research experiments in the lab.

## TABLE OF CONTENTS

ABSTRACT.....	ii
ACKNOWLEDGEMENTS.....	iv
LIST OF TABLES.....	xiii
LIST OF FIGURES.....	xv
1 INTRODUCTION.....	1
1.1 Aim.....	1
1.2 Problem Background.....	1
1.2.1 Problem Statement.....	8
1.3 Thesis Structure.....	8
2 BACKGROUND & LITERATURE REVIEW.....	10
2.1 Current CMC Fabrication Technique.....	10
2.2 Structure of Geo-polymer.....	11
2.3 Phase Transformation of Geopolymer.....	15
2.4 Choice of Nanomaterials.....	18
2.5 Nanofiller and Geopolymer Interface.....	19
2.6 Thermal Analysis and the Interfacial Condition.....	20
2.7 Fracture Surface Evaluation.....	21
2.8 Types of Fracture Toughness.....	22
2.9 Toughness Measurement Techniques.....	24

2.10	Experimental Design .....	28
2.10.1	Main Effects.....	28
2.10.2	Interaction Effects.....	28
2.10.3	Factorial Design.....	29
2.11	Nanomaterial Mixing Techniques .....	31
2.12	Nano-filler in Fiber Reinforced Composites .....	32
2.13	Conclusion .....	32
3	MATERIALS OF THE EXPERIMENTATION .....	34
3.1	Inorganic Polymer .....	34
3.2	Nano-materials of the Experimentation .....	35
3.3	Trade Name & Collection of Nanomaterials.....	39
3.4	Conclusion.....	42
4	GEOPOLYMER PROCESSING OPTIMIZATION .....	44
4.1	Processing of MEYEB for Evaluation of Cure Schedule .....	44
4.1.1	Specimen Preparation .....	46
4.1.2	Evaluation of Effects of Process Variations .....	48
4.2	Characterization Techniques .....	48
4.2.1	Process-Induced Linear Shrinkage .....	48
4.2.2	Thermo-gravimetric Analysis .....	49
4.2.3	Mechanical Properties.....	50

4.2.4	Evaluation of Porosities and Voids.....	52
4.2.5	Microstructural Analysis.....	53
4.3	Preliminary Results-Processing Evaluation .....	53
4.3.1	Effect of Cure Time on Shrinkage and Compression Strength.....	54
4.3.2	Effects of Drying and Postcure on the Shrinkage.....	56
4.3.3	Mechanical Properties.....	60
4.3.4	Compression Strength Related to Process Schedule.....	60
4.3.5	Elastic Modulus Evaluation .....	61
4.4	Conclusion.....	62
5	EVALUATION OF PROCESSED GEOPOLYMER .....	64
5.1	Specimen Preparation.....	65
5.2	Mold Design for Non-Cylindrical Specimens.....	65
5.3	Sample Degasification.....	68
5.4	Preparation of the Specimen .....	70
5.5	Characterization Technique.....	74
5.5.1	Un-notched Bend Beam Test .....	75
5.5.2	Notched Bend Beam Test .....	75
5.5.3	Variations in the Sample Geometry .....	78
5.5.4	Flexural Modulus Measurement .....	79
5.5.5	Analysis of Thermal Stability .....	81



5.5.6	Microstructure Analysis.....	82
5.6	Results .....	82
5.6.1	Effect of Extended Heat Treatment on Compressive Strength.....	82
5.6.2	Effect of Extended Heat Treatment on Flexural Strength .....	83
5.6.3	Effect of Extended Heat Treatment on Fracture Toughness.....	84
5.6.4	Effect of Extended Heat Treatment on Flexural Modulus.....	86
5.6.5	Thermal Stability of Cured and Post Processed MEYEB.....	88
5.6.6	Evaluation of Density through the Processing.....	94
5.6.7	Evaluation of Thermal Expansion with Processing Schedules.....	96
5.6.8	Understanding the Curing Process through Microstructure Evaluations.....	100
5.7	Conclusion.....	104
6	EFFECTIVENESS OF NANOFILLERS ON TOUGHENING.....	106
6.1	Evaluation of Interfacial Strength .....	107
6.2	Preliminary Study on the Nano-reinforcement .....	107
6.2.1	Full Factorial Design.....	108
6.2.2	Fractional Design .....	109
6.2.3	Test Matrix.....	110
6.2.4	Alias and Confounding .....	111
6.3	Comprehensive Approach with Nano-reinforcement .....	113
6.3.1	Nanomaterials for comprehensive test Plan.....	114

6.3.2	Matrix for Comprehensive Test Plan.....	114
6.4	Sample Preparation Technique.....	116
6.4.1	Mixing of Nanomaterials .....	116
6.4.2	Processing and Curing of Nano-Reinforced Sample .....	117
6.4.3	Sample Preparation for XRD .....	117
6.5	Characterization Technique.....	118
6.5.1	Un-notched Bend Beam Test .....	118
6.5.2	Notched Bend Beam Test .....	118
6.5.3	Verification of the Notch Effect in the Notched Bend Beam Test .....	118
6.5.4	Flexural Modulus Measurement .....	119
6.5.5	Thermogravimetry Analysis .....	119
6.5.6	Fractography .....	120
6.5.7	EDS.....	120
6.5.8	XRD .....	121
6.6	Results of the Nano-reinforcement Study .....	121
6.6.1	Evaluation of the Nanofiller Dispersion .....	121
6.6.2	Evaluation of Interfacial Strength.....	123
6.6.3	Thermal Analysis of the Nanomaterials .....	125
6.6.4	Results-Preliminary Studies.....	128
6.6.5	Results- Comprehensive Studies.....	144

6.7	Conclusion.....	160
7	OVERALL DISCUSSION .....	162
7.1	Evaluation of Neat Geopolymer.....	163
7.2	Effect of Nano-reinforcement .....	168
7.3	Effectiveness of Aspect Ratio of Nano-filler .....	171
7.4	Effectiveness of Interfacial Strength.....	172
7.5	Thermal Effects on the Nanofiller’s Stability and Interfacial Strength .....	176
7.6	Effectiveness of Nanofillers at High Temperature.....	184
7.7	Future Works.....	192
8	FIBER REINFORCED COMPOSITES .....	194
8.1	Experimental Technique .....	194
8.1.1	Carbon Coated and Clean Fiber Processing.....	194
8.2	Preparation of the Mold for Composite Processing .....	196
8.3	Calculation of the Required Fiber Amount .....	197
8.4	Composite Preparation Technique .....	197
8.5	Volume Fraction Calculation .....	199
8.6	Characterization .....	199
8.7	Results .....	201
8.7.1	Effect of Nano-reinforcement on the Flexural Strength .....	202
8.7.2	Effect of Nano-reinforcement on the Shear Strength .....	203

8.8	Discussion .....	205
8.9	Conclusion.....	210
9	OVERALL SUMMARY .....	211
	REFERENCES .....	214
	APPENDIX.....	223
	APPENDIX A: PROPERTIES OF THE MATERIALS .....	223
	A1. Properties of PR-XT19 CNFs .....	223
	A2. Properties of Silar SC 9M Silicon carbide whisker .....	224
	A3. Properties of HSC Silicon Carbide Nanoparticles .....	224
	A4. Size distribution of Silicon Carbide particles .....	225
	A5. Properties of Acetal Co-Polymer .....	226
	A6. Typical properties of 3M™ Nextel™ 610 Ceramic Fiber .....	227
	A7. Specifications of AMTEK EDAX Octane Series Silicon Drift Detectors.....	228
	APPENDIX B: CALCULATIONS .....	229
	B1. Calculation of the Failure strength of ANF .....	229
	B2. Failure strain calculation of the nanofibers .....	230
	B3. Estimation of Particle Diameter and Inter-particle Porosities.....	231
	B4. Calculation of Minimum length of Nano-fillers .....	236
	B5. Calculation of the Theoretical Fiber Mass in the Composite.....	237
	APPENDIX C: IMAGES & MICROSTRUCTURES .....	238

C1: Images of Samples .....	238
C2: Poly-condensed and Coalesced Materials Area with Temperature.....	240
C3: Estimation of Pull out Length of Nanofillers .....	243
C4: Data of EDS Analysis .....	249
LIST OF ABBREVIATIONS.....	255

## LIST OF TABLES

Table 2.1. Physical properties of conventional ceramic and geopolymer <sup>29</sup> .....	15
Table 2.2: Several fracture toughness measurement techniques. ....	27
Table 2.3 Responses from different runs using main and interaction effects.....	30
Table 3.1. Properties of nano-materials of the investigations.....	37
Table 3.2 Properties of the fiber used in the composite fabrication .....	42
Table 4.1. Cure schedule, Series 2.....	45
Table 5.1 Mechanical tests performed on the neat MEYEB samples.....	71
Table 5.2. Coefficients for the Polynomial $g(a/w)$ for Three-point Flexure.....	77
Table 5.3. Typical dimensions of the specimen prepared for the SEVNB test .....	78
Table 5.4. Dimensions of the compression and flexure test specimens.....	79
Table 6.1. Variables and their levels for investigations of fracture toughness .....	108
Table 6.2. Variables with 2 levels for investigations of fractional factorial design .....	109
Table 6.3. Test matrix for nanomaterials reinforced MEYEB to perform ( $1/2$ ) fractional factorial .....	111
Table 6.4. Alias structure with confounding in the $1/2$ replicate fractional factorial designs .....	112
Table 6.5. Comprehensive test plan.....	113
Table 6.6. Combined & extended test plan including full factorial plan.....	115

Table 6.7. Weight loss of Alumina nanofiber (ANF) at different temperature and environment .....	126
Table 6.8. Weight loss of SCW at different temperature and environment.....	128
Table 6.9. Summary of toughness results from preliminary studies.....	135
Table 6.10. ANNOVA chart showing the results from the design of experiments .....	138
Table 6.11. Breaking loads of the notched and un-notched beam of equivalent thickness .....	157
Table 8.1. Dimensions of the cavities in the mold assembled with the T-bars.....	197
Table 8.2. Test matrix of the fiber reinforced composite samples.....	199
Table 8.3. Compositions of Nextel 610 fiber reinforced MEYEB composites with and without nano-reinforcement. ....	201

## LIST OF FIGURES

Figure 2.1 Descriptive model of alkali activation of fly ash based geopolymer. ....	12
Figure 2.2 (b) Formation of Poly-sialate framework. ....	13
Figure 2.3. (a) Metakaolin based geopolymer with $\text{SiO}_2:\text{Al}_2\text{O}_3 = 3$ (b) Flyash based geopolymer showing unreacted fly ash particles in geopolymer matrix. ....	14
Figure 2.4. A $\text{Na}_2\text{O}-\text{Al}_2\text{O}_3-\text{SiO}_2$ ternary phase diagram with some well-known compounds .....	17
Figure 2.5. Fracture surface of alumina specimen from fracture toughness test .....	22
Figure 2.6: Various modes of fracture toughness .....	24
Figure 3.1. Alumina nanofiber block with the demonstration of fire retardancy .....	39
Figure 3.2. PR-19-XT De-bulked CNFs .....	40
Figure 3.3. De-agglomerated bulk Silicon Carbide Whiskers .....	41
Figure 4.1. Mold preparation and curing of MEYEB in a sealed environment. ....	47
Figure 4.2. Schematic presentation of MEYEB curing inside the sealed molds. ....	47
Figure 4.3. Experimental set up of load-displacement measurement with extensometer. ....	51
Figure 4.4. Method for weighing sample submerged in water .....	53
Figure 4.5. Samples cured in a sealed environment at $80^\circ\text{C}$ for (a) 1 hr (b) 24 hr .....	54
Figure 4.6. Average linear shrinkage after initial cure at various times .....	55
Figure 4.7. Compressive strength after cure in a sealed environment .....	55



Figure 4.8. 2hr and 10hr cures followed by drying and postcure, (a) Temperature profile, and (b) Linear cure shrinkage .....	57
Figure 4.9. 24hr initial cures, drying & postcure, (a) Temperature profile (b) Linear cure shrinkage .....	58
Figure 4.10. Cure shrinkage summary (a) Drying and post-cure component, (b) Total shrinkage .....	59
Figure 4.11. Compression strength comparison for the various process schedules.....	61
Figure 4.12. Clip gage displacement vs. load cell response during compression test. ....	62
Figure 5.1. Molds for SEVNB specimens prepared using Acetal plastic.....	66
Figure 5.2. Mold assembly for initial curing of MEYEB in vertical orientation.....	67
Figure 5.3. Slots for the samples in the mold and their dimensions (In millimeter). ....	67
Figure 5.4. Assembly of a mold with rectangular slots for curing MEYEB in vertical orientation. ....	68
Figure 5.5. Sample degassing in a cold environment. ....	69
Figure 5.6 Assembly of the Mold with MEYEB in a sealed PE bagging.....	71
Figure 5.7. Notch preparations on the sample surface using a notch preparation station.....	72
Figure 5.8. Fixture for the sharpening of the notch tip. ....	73
Figure 5.9. (a) Notch formation with diamond wafer blade and (b and c) notch tip sharpened using razor blade (250 $\mu\text{m}$ thick) sprinkled with diamond paste (7 $\mu\text{m}$ ).....	74

Figure 5.10. Notch geometry on a 30 mm span bend beam specimen (a) Overall view and (b) Expanded view of the notch in (a). .....	76
Figure 5.11. Neat MEYEB samples for (a) compression strength and (b) flexural strength measurement .....	78
Figure 5.12. Comparison of theoretical and average load displacement profile for Al-6061 .....	80
Figure 5.13 Effect of temperature on compressive strength of MEYEB in oxygen.....	83
Figure 5.14 Effect of temperature and environment on flexural strength of MEYEB .....	84
Figure 5.15. Effect of temperature and environment on fracture toughness of neat MEYEB .....	85
Figure 5.16. Fracture toughness of neat MEYEB at various temperatures in reactive and non-reactive environment.....	86
Figure 5.17. Flexural modulus of neat MEYEB processes at various temperatures and environments.....	87
Figure 5.18. TGA and DTA of neat MEYEB treated through schedule B2 after initial cure at 80 °C .....	89
Figure 5.19. TGA of neat MEYEB treated through schedule B2 after initial cure at 80 °C ( in time domain).....	90
Figure 5.20 TGA and DTA of neat MEYEB at 80-600 C (after initial cure at 80 °C) followed schedule A1 (ramp of 5 °C/min ) .....	91

Figure 5.21 DTA of freshly cured samples while postcured (a) following schedule B-2 and (b) at 5 °C/min .....	92
Figure 5.22 TGA and DTA of neat MEYEB while reheated at 5° C/min after post heat treatment at 650 °C .....	93
Figure 5.23 Density change of MEYEB during post cure as a function of temperature .....	95
Figure 5.24 Dilatometer profile of sample B2 after post cure with (a) heating and cooling (b) cyclic heating & cooling with intermediate hold (c) no hold and (d) second heating .....	98
Figure 5.25 Thermal expansions of fully processed specimens followed by various schedule ...	99
Figure 5.26 SEM images of MEYEB followed by schedule B2 (a) cured at 80 °C,post processed at (b) 250 °C, (c) 650 °C and (d) treated at 870 °C.....	101
Figure 5.27 Diameter of particles and porosities of neat MEYEB with temperature.....	102
Figure 5.28 SEM images of sample followed by schedule (a) A1 and (b) B2 after processed at 650 °C (O <sub>2</sub> ). .....	103
Figure 6.1. Nanoparticle mixing in MEYEB using a Rolling mill .....	117
Figure 6.2 (a) Neat MEYEB & (b-d) MEYEB mixed with 2 vol% (b) ANF & (c) SCW (d) CNF in a suspension .....	122
Figure 6.3 Fracture surfaces of (a) neat (b) 2vol% ANF (C) 2vol% SCW and (d) 2vol% CNF added MEYEB ( At x16 magnification) .....	123

Figure 6.4. Fracture surface of (a) Carbon Nanofiber (CNF) (x2000 magnification) (b) Silicon Carbide Whiskers (SCW) (x10,000 magnification) and (c) Alumina nanofiber (ANF) (x10,000 magnification) reinforced MEYEB.....	124
Figure 6.5. Thermal degradation (TG%) of alumina nanofibers (ANF) at 650 °C and 760 °C in oxygen and nitrogen, respectively. ....	126
Figure 6.6. Thermal degradation (Tg%) of Silicon Carbide Whisker (SCW) at 650 °C and 760 °C in oxygen and nitrogen, respectively. ....	127
Figure 6.7. Fracture surfaces of ANF reinforced and treated at 760 °C in (a) oxygen and (b) nitrogen. ....	129
Figure 6.8. Fracture surface of ANF reinforced and treated at 650 °C in (a) oxygen and (b) nitrogen. ....	130
Figure 6.9. Fracture surface of CNF reinforced and treated at 650 °C in (a) oxygen and (b) nitrogen. ....	130
Figure 6.10. Fracture surface of Carbon nanofiber reinforced and treated at 760 °C in (a) oxygen and (b) nitrogen.....	130
Figure 6.11. Fracture toughness of neat and ANF and ANP reinforced MEYEB with various volume fractions of nanomaterials.....	132
Figure 6.12. Fracture toughness of neat and CNF and CNP reinforced MEYEB with various volume fractions.....	133

Figure 6.13. Load-cross head displacement profiles of neat and Alumina nanofiber reinforced MEYEB specimens in notched beam flexural strength (SEVNB) test.....	134
Figure 6.14 PARETO chart showing the main and interaction effects of the variables.....	137
Figure 6.15. Experimental results of the main effect of A- Volume Fraction, B-Aspect Ratio, D-Temperature and E-Environment.....	139
Figure 6.16. Experimental results of the combined effect of A- Volume Fraction, B-Aspect Ratio, C-Interfacial Strength, D-Temperature and E-Environment.....	140
Figure 6.17. Variations in toughness of MEYEB with the addition of SCW nano-fillers in different volume fractions and treated at 350 °C.....	142
Figure 6.18. Variations in toughness of MEYEB with addition of SCW nanofillers.....	143
Figure 6.19 Toughness of neat and various nano-fillers (low and high aspect ratio) reinforced MEYEB treated at 250 °C.....	145
Figure 6.20. Toughness of neat and various high aspect ratio nano-fillers reinforced MEYEB at various temperatures and environments.....	146
Figure 6.21. Toughness of neat and various high aspect ratio nano-fillers reinforced MEYEB at 650 °C in oxygen and nitrogen.....	148
Figure 6.22. Flexural strength of neat MEYEB and MEYEB reinforced with low and high aspect ratio nanofillers treated at 250 °C. ....	149
Figure 6.23. Flexural strength of neat and various high aspect ratio nanofillers reinforced MEYEB at various temperatures in nitrogen and oxygen environment. ....	150

Figure 6.24. Flexural strength of neat and various low aspect ratio nano-fillers reinforced MEYEB at various temperatures nitrogen and oxygen environment. ....	152
Figure 6.25. Flexural strength of neat and various high aspect ratio nanofillers reinforced MEYEB at 650° C in reactive and non-reactive environment.....	153
Figure 6.26. Variations in the flexural modulus of MEYEB with the addition of 2vol % nanofillers. ....	155
Figure 6.27. Variations in the fracture toughness with the variations in the ratio of notch length to depth (a/w) of the samples treated at 650 °C (O <sub>2</sub> ). ....	156
Figure 7.1. Solidification process of neat MEYEB in (a) liquid form with particles and (b) solid form after cured for 24 hr at 80 °C .....	163
Figure 7.2. Various phases present in neat geopolymer cured (a) 24 hr at 80 °C (b) post processed at 250 °C and (c) response to corresponding compression strength cured 24 hr at 80 °C and post processed at 250 °C.....	164
Figure 7.3 Area of Poly-condensed structure of neat MEYEB heat treated at various temperatures. (Detailed analysis with subsequent SEM images can be found in Appendix C2) .....	165
Figure 7.4. Variations in the (a) compression strength and (b) phase transformation of geopolymer with the variations in treatment temperature. ....	167
Figure 7.5 Toughness and compression strength variations with temperature.....	168

Figure 7.6. Pareto effect chart showing the effects of the variables on fracture toughness of MEYEB.....	169
Figure 7.7. (a) Main effect of volume fractions of alumina & carbon nanomaterials and (b) Effect of volume fractions of SCW at constant thermodynamic conditions on $K_{IC}$ .....	171
Figure 7.8. Effect of aspect ratio at low and high temperature in nitrogen. ....	172
Figure 7.9. Dispersion of 2 vol% (a) CNF (b) SCW (c) ANF and (d) Simulated model representing 2 vol% nanofillers at 650 °C. ....	173
Figure 7.10. Evaluation of interfacial strength of (a) CNF/geopolymer and (b) SCW/ geopolymer interface.....	174
Figure 7.11. Toughness contributions of low and high interfacial strength nanomaterials at low and high temperature in nitrogen. ....	175
Figure 7.12. Bridging of SCW and ANF with the structure of geopolymer.....	176
Figure 7.13. Toughness contribution, $dK_{IC}$ of (a) SCW and (b) ANF at low and high temperature in nitrogen and % $dK_{IC}$ of SCW and ANF in (c) nitrogen and in (d) oxygen. ....	178
Figure 7.14. Morphology of (a) ANF and (b) SCW reinforced geo-polymer at low temperature (250 °C). (c) Enlarged view of ANF reinforced poly-condensed structure. ....	180
Figure 7.15. Atomic wt % of elements on the (a) poly-condensed and particle structures & (b) on the nano-fillers and poly-condensed structure of ANF and SCW reinforced geo-polymer, respectively (The atomic wt% represents the respective EDS spectrums shown in Figure 7.14.) .....	181

Figure 7.16. Descriptive model showing the dispersion of (b) SCW and (c) ANF in the geopolymer matrix.....	183
Figure 7.17. Net increase in toughness using 2%SCW and expected net increase in toughness using 4% SCW in various treatment temperatures. ....	185
Figure 7.18. Pull out of SCW at (a) 250 °C & (b) 650 °C in N <sub>2</sub> (x2000 magnification).....	186
Figure 7.19. EDS of (a) bulk SCW & 2 vol% SCW in MEYEB at (b) 250 °C and (c) 650 °C..	187
Figure 7.20. Elements of SCW on (a) bulk SCW, (b) 250 °C and (c) 650 °C.....	188
Figure 7.21. XRD of neat MEYEB at (a) 650 °C (O <sub>2</sub> ) and (b) 870 °C (O <sub>2</sub> ) & 2 % and 4% SCW reinforced MEYEB at (a) 650 °C (O <sub>2</sub> ) (All treated for 5 hours). ....	189
Figure 7.22. A model presenting the interface layer formation at high temperature (Not drawn in scale; weak interface is shown as a black solid layer). ....	190
Figure 7.23. Morphological transformation showing diffusion of ANF with thermal treatment from (a) 80 °C to (b) 650 °C (O <sub>2</sub> ). ....	191
Figure 7.24. Various elements of 2vol %ANF reinforced geopolymer at 80 °C and 650 °C (in O <sub>2</sub> ). ....	192
Figure 8.1. CVD furnace used to modify the sizing of the surface of fiber tow into a carbon deposited layer. ....	195
Figure 8.2. Nextel 610 fiber with (left) clean and (right) carbon deposited surface.....	196
Figure 8.3. Steel mold & T-bar for the fabrication of fiber reinforced composites.....	196



Figure 8.4. Clean Nextel 610 reinforced (a) Neat and (b) 2 vol% SCW nanofilled MEYEB composites treated at 250 °C. ....	202
Figure 8.5. Flexural strength of 0% and 2% SCW nanofilled MEYEB reinforced with clean Nextel 610 fiber treated at 250 °C.....	203
Figure 8.6. Short beam test specimen prepared from clean Nextel 610 reinforced (a) 0 vol% and (b) 2 vol% SCW nanofilled MEYEB composites treated at 250 °C. ....	204
Figure 8.7. Short beam shear strength of neat and 2% SCW nanofilled MEYEB reinforced with clean Nextel 610 fiber treated at 250 °C. ....	205
Figure 8.8. (a) Flexural and (b) Shear strengths of neat matrix & clean fiber, 2%SCW reinforced matrix & clean fiber, neat matrix & coated fiber and 2%SCW reinforced matrix & coated fiber composite. ....	206
Figure 8.9. Net improvement in flexural strength of geopolymer matrix, continuous clean and coated fiber reinforced geopolymer matrix composites with the additions of 2% SCW nano-fillers. ....	207
Figure 8.10. Crack propagation of (b) neat (c) 2% SCW reinforced composite through the length of short beam specimen (c) viewing perpendicular to the thickness (at 16x magnification). (The direction of the crack is shown using the arrow). ....	208
Figure 8.11. The representation of the crack that propagated through the length to the end of (a) clean neat (N-CL610-M250) (b) clean fiber and 2% SCW reinforced specimen (N-CL610-SCW-M250) (at 16x magnification).....	209

Figure 8.12. Crack Propagation of coated fiber reinforced neat ( N-CC610-M250) and coated fiber& 2&SCW reinforced (N-CC610-SCW-M250) MEYEB matrix composite. (The direction of the crack is shown using the arrow)..... 210

# 1 INTRODUCTION

## 1.1 Aim

This study aims at investigating the effectiveness of nano-fillers in toughening of geopolymer for potential application as the matrix materials for continuous fiber reinforced composites. More specifically the objective of this study is to investigate this optimum effectiveness of various nanofillers in fracture toughness of the geopolymer based on their physical dimensions, mechanical properties, reinforcing capability and interfacial bond strength. To perform this investigation the supporting study aims at sufficiently understanding the processing of inorganic polymer and evaluating mechanical performance of the geopolymer to be able evaluate the effect of nano-reinforcement.

The aims of the study will be accomplished by using some characterization approaches including flexural testing, notched beam testing, microstructure and x-ray diffractions for evaluating geopolymer materials after the processing conditions. Based on the outcomes of such evaluations a set of optimal processing conditions will be determined. Then suitable nanofillers will be explored and investigated for their effectiveness in toughening of the geopolymer and continuous fiber reinforced geopolymer composites.

## 1.2 Problem Background

Ceramic materials are attractive candidates for high temperature applications. However, conventional ceramic materials are considered difficult to process and the conventional processing requires a great deal of energy. Sintering, one of the ceramic processing techniques involves very high pressure and temperature for the densification of the powder materials<sup>1</sup> which

results in a significant amount of shrinkage in the material. The problem with high temperature processing in commonly available ceramic matrix composite (CMC) is the lack of wetting , interfacial reactions between the constituent materials<sup>2</sup>, and high void content in the resulting composite. In addition, due to the differential CTE of the ceramic matrix and reinforcing fibers, residual stress develops during the cool down process, which often leads to the biggest structural problems in CMC's. One approach for CMCs to address these problems would be to develop a low temperature processing technique. Organic polymers are relatively easily processed at lower temperature but only be operated to 400 °C at the maximum<sup>3</sup>, while conventional ceramics are often appropriate at temperatures as high as 1000 °C or so. Inorganic polymer, geopolymer has the potential to fill this gap between processing and performance, having reasonably easy processing near room temperature, yet offering performance potential in the 400 °C – 800+ °C range. Also the liquid processing of geopolymer at low temperature increases the wetting of fiber which reduces the void content and allows interfacial reactions which increase interfacial strength between the fiber and matrix. Therefore geopolymer can be a suitable material for medium to high temperature composites by avoiding the difficulties associated with conventional CMC processing. However, only few studies<sup>4,5,6,7,16</sup> have demonstrated geopolymer as a suitable matrix material for continuous fiber reinforced composites. The focus of the current study is to establish a broader baseline to offer geopolymer as the matrix materials for high temperature continuous fiber reinforced composites and address its critical mechanical properties especially fracture toughness using nanofillers.

Geopolymer is a low temperature curable inorganic polymer with relatively high porosity and low mechanical properties. Low toughness is a primary concern for geopolymer material that limits the performance of fiber reinforced geopolymer matrix composites. Toughness of this

composite is sensitive to process induced cure shrinkage and residual stress development. These two factors increase the crack density<sup>8</sup> and lead to the failure of the composites. Crack control approach is therefore necessary to reduce the detrimental effect of the brittleness of the materials and control the processing flaws<sup>9</sup>. This approach is therefore the subject of this study which focuses on the origin and development of flaws in the geopolymer and ways to minimize it through process modifications.

Initial trials of preparing the neat, baseline geopolymer material as a standalone matrix were unsuccessful; even though fiber reinforced inorganic geopolymer matrix composites had been successfully produced<sup>10, 5</sup>. There was insufficient processing data for neat geopolymer. In addition, the neat matrix processed earlier resulted in lower strength and higher micro crack densities. These observations indicated the necessity for an investigation into optimized processing conditions. The goal of this process optimization is primarily to process geopolymer with reduced shrinkage and improved compressive strength, which would indirectly suggest lower crack density and a higher degree of cross linking. Previous study suggests that process-induced shrinkage of an inorganic polymer can be sub-divided into three forms, which are (i) curing, or polycondensation, (ii) drying, and (iii) densification by diffusion<sup>11</sup>. Shrinkage of inorganic polymer during the polycondensation occurs at a relatively low temperature (80 °C) in the presence of moisture. Drying induced shrinkage can be seen at temperatures up to 250 °C, while the high temperature postcure is expected to only result in diffusion driven shrinkage. Adequate humidity during the cure stage is suggested to reduce the shrinkage of the inorganic polymer by ensuring the completion of cross-linking during the poly-condensation reaction<sup>12</sup>. Heating rates and the duration of intermediate temperature dwells during drying, at least up to 250 °C, would seem critical in controlling the evaporation of physically attached liquids, and

help reduce process-induced shrinkage and possible cracking. An earlier investigation on the curing of inorganic polymer, based on thermal degradation, suggested that post processing at 250°C and then at 650 °C, described as 2<sup>nd</sup> and 3<sup>rd</sup> processing stages, respectively, had only a minor effect on the shrinkage related phenomena<sup>13,11</sup>. The current study focuses on the investigation of the effect of the variations in the heating rates and dwell times at various stages of processing.

Although processing reduces shrinkage and improves compressive strength of inorganic geopolymer, it results into limited improvement in the fracture toughness. In order to improve this property there is a need for developing the crack resistance in the material which is possible through the modification of the microstructure and/or usage of various reinforcements. There are many toughening mechanisms that have been suggested for both organic polymers and monolithic sintered ceramics including continuous fibers<sup>14</sup> , Short fibers<sup>15, 16</sup> , whiskers<sup>17, 18, 19</sup> , nano-particles<sup>20,21</sup> , nano-fibers<sup>22, 23</sup> and nano-plateletes<sup>24</sup>.

The presence of nano-reinforcements increases toughness of brittle materials by at least one of the three mechanisms<sup>25</sup>. The first mechanism is associated with the deflection of the propagated cracks, which is originated due to the presence of the reinforcements at the crack front. The second one is associated with the absorption of the crack propagation energy resulting from the pull out and de-bonding of reinforcements<sup>26</sup>. The third one is the crack bridging mechanism, which is related to hold the two cracked faces together in order to prevent the brittle material from failure<sup>27</sup>.

Due to very high strength, modulus and increased surface area, nanofillers are highly effective in toughening brittle materials. It has been suggested that nanofillers intercept the crack tip and

increase toughness by the crack deflection mechanism. They also resist process induced cracking and reduce the number of defects in the brittle materials. High aspect ratio nano-materials including, nanotubes, nano-fibers and whiskers are preferable in reducing the defects and increasing toughness by crack bridging mechanism.

Pull out and de-bonding of the reinforcements which often plays important roles in toughening of fiber reinforced conventional ceramic matrix, is not effective in toughening of geopolymer, because due to low toughness of geopolymer nanofillers are required to carry sufficient loads and deflect in-plane micro-cracks to out of the plane. In order for the load transfer and bridging the micro-cracks, there should be sufficient interfacial strength between nanofillers and geopolymer. The strength of nanofillers also play important role in toughening. Evans<sup>28</sup> suggested a governing equation of the toughness improvement ( $\Delta k_{IC}$ ) of brittle materials using randomly oriented nanofillers in which case nanofillers pull out does not contribute to toughness. The equation is as follows-

$$\Delta k_{IC} \approx \frac{v_f * d * S^2}{E} + 4 * F_i * v_f * \frac{\left(\frac{d}{R}\right)}{(1-v_f)} \quad (1)$$

Where  $F_i$  is the interfacial energy,  $v_f$  the volume fraction;  $d$ ,  $R$ ,  $S$  &  $E$  the de bond length, diameter, & strength of nanofillers, respectively and  $E$  the modulus of the composite. According to equation (1), toughness improvement using nanofillers is proportional to the strength of nanofillers and interfacial strength between nanofillers and geopolymer.

Toughening mechanism of geopolymer also differ from that of conventional ceramic matrix composites due to its inherently low elastic modulus<sup>29</sup> and relatively high porosity 12. In the conventional ceramics matrix composites where fiber and matrix have comparable modulus (SiC

fiber reinforced SiC matrix composites for example), stress transfer through the fiber-matrix bond is not as important, since in this case fibers act in the matrix as crack stoppers. Weak interface allow the crack to be blunted as the fiber is approached and energy is absorbed by failing the interface, generating single long de-bonds at the surface of the fibers<sup>30</sup>.

Unlike conventional ceramic matrix composites, a strong interface allows a good stress transfer between low modulus geopolymer and high performance nanofiller, which has the potential to increase strength and toughness. High interfacial strength increases the overall modulus of the nano-reinforced geopolymer and reduces the potential to interface failure in the continuous and high modulus fiber reinforced inorganic matrix composites. Thus high interfacial strength is expected to increase the toughness of nano-reinforced inorganic geopolymer and composite. Nano-materials with high modulus also induce annular micro-cracks at the crack tip<sup>31, 32</sup>, which is a mechanism of increasing toughness by dissipating crack energy. Therefore, stiffness/modulus of the nanofiller and interfacial strength plays a very important role in toughening of geopolymer.

It is known that the cured inorganic polymers are inherently porous<sup>33</sup>. Depending on the base materials<sup>33</sup> of the geopolymer and the processing conditions<sup>11</sup> the pore sizes of the geopolymer can vary from few micrometers to nanometers. It is suggested that <sup>34</sup> the porosities act as annular micro-cracks and performs crack blunting at the crack tip, assuming the radius of the pore is greater than the crack tip. In addition, inter-particle fracture energies may be minimized by the crack deflection due to ordered array of porosity. Crack propagation from pore to pore is therefore considered as an added advantage and possible toughening mechanism to the inorganic geopolymer. Therefore, both high-strength nanofillers and inherent porosity of inorganic geopolymer can create a coupling effect as a combination of micro-structural modification<sup>35</sup> and



micro-crack toughening. The current study focuses on investigating the effect of the strength and modulus of the nanofillers as well as the strength of the nanofiller/geopolymer interface on the potential to toughening of porous geopolymer matrix.

Temperature and environments have reasonable effects on the toughening of geopolymer matrix composites (GMC). Previous studies conducted at Center for Materials Manufacture and Structures (CMMS) lab at Colorado State University<sup>10,13,14</sup> suggest that processing temperature and environment have effects on the microstructure of inorganic geopolymer matrix and nano fillers/ geopolymer interface, which also influence the fracture toughness of the same. From the previous studies on mechanical testing it has been found that the interfacial strength of the continuous fiber reinforced inorganic geopolymer matrix composite has a significant impact on the overall mechanical performance, including fracture toughness. Also some variations were observed in the modulus and toughness results in response to the thermal treatment in the reactive environment, which suggests thermal and environmental effects on the continuous fiber/matrix interface. However, no direct study has been performed to investigate thermal and environmental effects on the interfacial strength between geopolymer matrix and nanofiller interface. Previous studies also lacks in investigating the effects of diffusion of the nano-fillers on toughening of inorganic geopolymer with the variations in temperature and environment. Thermal diffusion plays an important role in structural stability and integrity of nanofillers embedded into the matrix which affects to their performance in toughening. Also high temperature oxidation reduces the effectiveness of several nanofillers. Therefore it is important to understand the effect of both temperature and environment on the toughening of geopolymer matrix through the usage of nanomaterials. The current study is aimed at investigating the effects of the several variables, mainly the aspect ratio and interfacial strength of nanofillers and

temperature and various environments on the performance of nanofillers in toughening geopolymer matrix.

### ***1.2.1 Problem Statement***

A hypothesis is therefore proposed, which is that the nano-reinforcement in the geopolymer can result in improved toughness, which can translate into improved toughness of continuous fiber reinforced/geopolymer matrix composites. High aspect ratio nano-fillers including nanofibers and whiskers are predicted to be more effective in toughening geopolymer than nanoparticles. Given the low Young's modulus of geopolymer relative to conventional ceramic matrix materials and nanomaterials a high interfacial strength at the nanofiller/geopolymer interface is believed to result in improved toughness of nanofiller/geopolymer system. High interfacial strength at the nano-filler/geopolymer interface is therefore predicted to result in improved effectiveness of high aspect ratio nano-fillers in toughening geopolymer. So, the aim of the research is to assess the effectiveness of nanoparticles as a method of toughening geopolymer and to determine the relative effectiveness as it relates to aspect ratio and bond strength.

### **1.3 Thesis Structure**

The detail of this thesis is described in eight chapters which include the literature reviews, materials, preliminary investigations, toughening of neat and continuous fiber reinforced geopolymer (GMC) inorganic polymer and future recommendations.

Chapter 2 discusses backgrounds on various processing and toughening mechanisms that play important roles in processing and toughening of geopolymer and continuous fiber reinforced geopolymer matrix composites. This chapter also explores the scopes and limitations of various reported fracture toughness measurement techniques and the widely accepted ones.

Chapter 3 explores the materials of this investigation. This includes the exploration of the properties of geopolymer and various nanomaterials suitable for toughening of inorganic geopolymer matrix composites

Chapter 4 describes the preliminary studies related to the optimum processing of geopolymer based on the evaluation of process related shrinkage and development of mechanical properties including compressive strength and modulus.

Chapter 5 evaluates the properties of geopolymer. This chapter focuses the effect of extended treatment temperature and environments on various mechanical and thermal properties of optimally processed geopolymer matrix.

Chapter 6 investigates the effectiveness of various aspect ratios and interfacial strength of nanomaterials in toughening of inorganic geopolymer. These results were verified with the evaluation of microstructure, analysis of the elements and phase transformations.

Chapter 7 combines the discussion on the interpretation that supports the hypothesis of the dissertation. It includes the baseline properties of the geopolymer that leads to the toughening of nano-reinforced geopolymer at various thermodynamic conditions. Toughness and associated mechanical properties were verified with the evaluation of microstructure, phase transformations and elements of both inorganic geopolymer and nanofillers and the interface.

Chapter 8 verifies the effectiveness of nano-reinforcement in the continuous fiber reinforced inorganic geopolymer matrix composites.

Chapter 9 summarizes the results and discussions.

## 2 BACKGROUND & LITERATURE REVIEW

This review includes various aspects of nanomaterials related to the toughening of geo-polymer. Part of this review includes comparison between the processing of ceramic matrix and geo-polymer matrix composites, physical and chemical structure of geo-polymer, development of the processing experiments and various characterization techniques related to the evaluation of mechanical properties including flexure strength and fracture toughness.

### 2.1 Current CMC Fabrication Technique

Several fabrication routes are currently available<sup>2</sup> for the fabrication of ceramic matrix composites (CMC). SiC fiber and SiC matrix composite is commonly known CMC. For the fabrication of SiC/SiC composites two routes were developed so far. In one route as developed by NASA, at first, chemical vapor infiltration (CVI) coated fiber tows with approximately 40 vol% was cast into component with SiC particulates. Then the cast component was heated to 1400 °C to complete the non-reactive melt matrix infiltration. In another route as developed by General Electric, at first Chemical vapor deposition (CVD) coated SiC fiber was pre-impregnated with polymer based matrix. Then the component was fabricated using any suitable technique for example, filament winding. The component fabrication was completed with the simultaneous SiC matrix formation and melt infiltration process at temperature near 1400 °C which is termed as reactive melt infiltration.

High processing temperature often causes the loss of fiber strength by the diffusion of Si across the coating. Both CMC processing routes create excess Si in the matrix which cause creep at temperatures near 1100 °C, lower than the processing temperatures. Additionally, during the

high temperature processing and matrix formation exothermic reactions that occur develop residual stress in the fiber and matrix interface. Therefore, conventional CMCs are not recommended to use at higher than processing temperatures. On the other hand, geo-polymer is generally processed at much lower temperature which is in close approximation to thermoset polymer resin processing, but it can survive easily in the 400 °C - 800 °C range without much loss in weight<sup>12</sup>, density and mechanical performance<sup>13</sup>.

## **2.2 Structure of Geo-polymer**

Geo-polymer is formed by mixing alumino-silicate materials with Alkali or alkali –silicate solutions. Geo-polymerization process has three steps-

1. Dissolution
2. Poly-condensation
3. Precipitation

Geo-polymerization starts with the dissolution of Si and Al from Si and Al rich starting materials, fly ash for example. Geo-polymerization is described in a model similar to alkali activated binder as developed by Fernando et al<sup>36</sup>. This model shows that an alkali attack on the spherical fly ash particles, the precursor materials, which results in the dissolution of Si and Al ions and the reduction of the original large particles. The model as presented in Figure 2.1 shows the dissolution of large fly ash particles into small precipitation into the geo-polymer network.

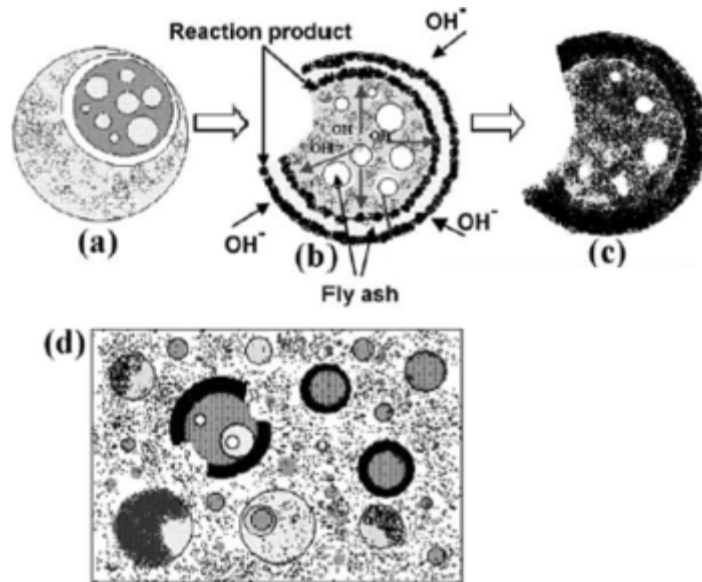


Figure 2.1 Descriptive model of alkali activation of fly ash based geopolymer<sup>36</sup>.

The dissolved Si and Al ions are suggested to take part in the formation of the complex geopolymer network through the process called polycondensation<sup>12</sup>. Preliminary unit in the polycondensation is the ortho-sialate molecule which is formed in an alkali environment, as shown in Figure 2.2 (a). Three ortho-sialate units form hexagonal cycle Tri-sialate structure which results in the release of alkali. Liberated alkali reacts again to form a poly-sialate framework, which is shown Figure 2.2(b).

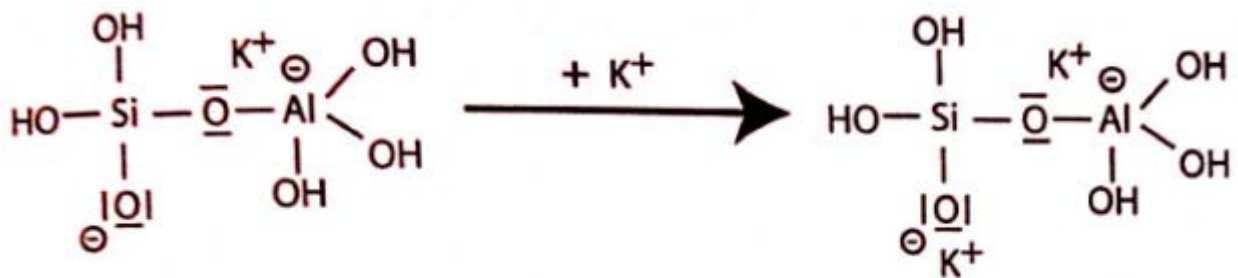


Figure 2.2 (a) Initial step of geo-polymerization with the formation ortho-sialate molecule<sup>12</sup>

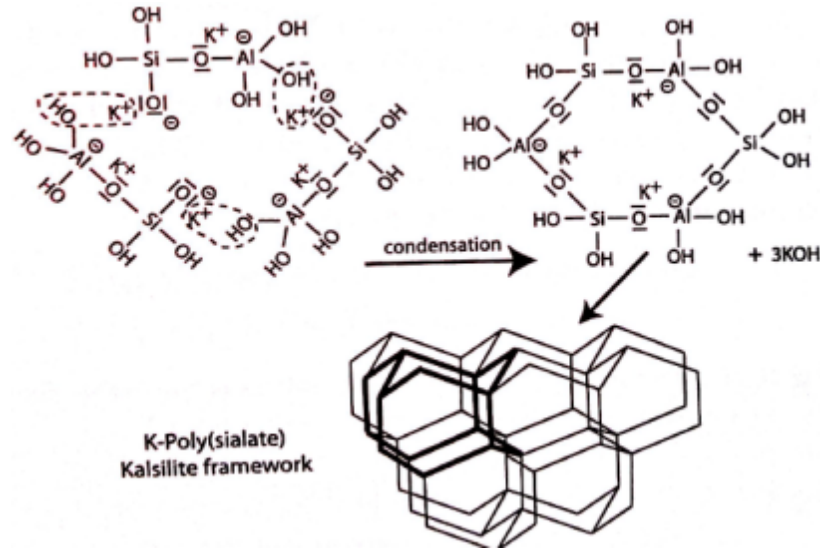
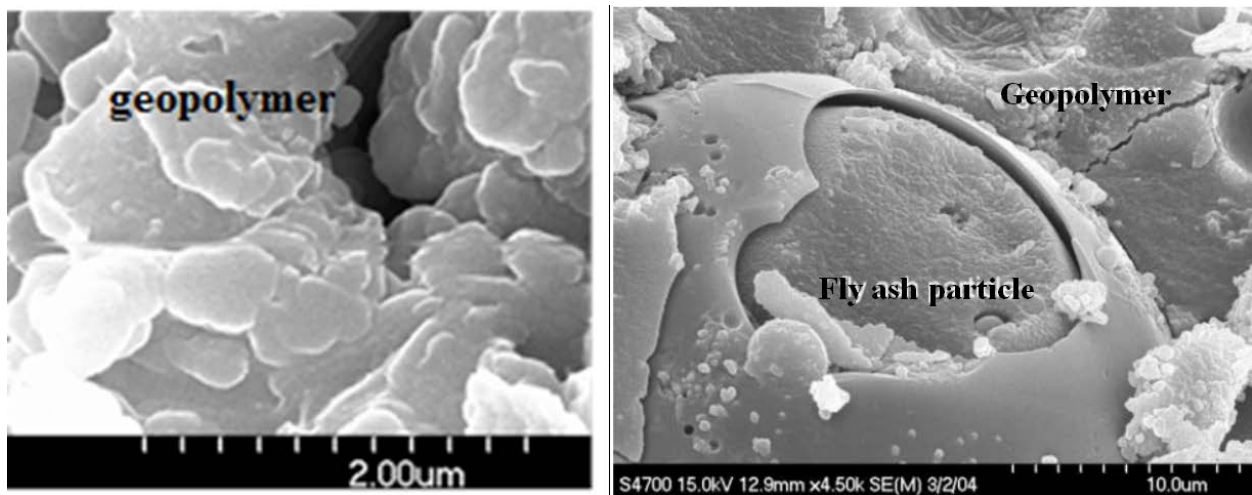


Figure 2.2 (b) Formation of Poly-sialate framework<sup>12</sup>.

As soon as the poly-condensation process completes the undissolved remnant of the starting materials precipitate in the form of dispersed particles. The size and homogeneity of the dispersed particles depend on the initial cure time. With the prolonged initial cure, more molecules of the starting materials dissolve in the poly-condensed network which results in the smaller and evenly distributed precipitates. This extended dissolution results in the smaller inter-particle porosity. On the other hand, if the initial cure time is insufficient, larger particles heterogeneously precipitate which result into higher inter-particle porosity. Therefore, cure time plays an important role in the processing of geopolymer as a way of controlling the density and porosity.

Starting materials also has the ability to control the geo-polymerization process and the structure of geopolymer. The starting materials of geopolymer are alumino-silicate which is normally derived from metakaolin and fly ash<sup>12</sup>. Metakaolin based geopolymer is sourced from Kaolinite which is a clay mineral,  $\text{Al}_2\text{Si}_2\text{O}_5(\text{OH})_4$ . Fly ash based geopolymer contains alumino-silicate

rich fly ash, which is sourced from blast furnace slag<sup>37,38,39,40</sup>. It has been demonstrated that, since metakaolin has a very high surface area compared to fly ash, the reactivity of metakaolin based geopolymer is very high compared to fly ash based geopolymer<sup>33,41</sup>. Therefore it is more likely that fly ash based geopolymer contains more un-reacted materials. The comparison between the microstructures of metakaolin and fly ash based geopolymer is shown in Figure 2.3. It is seen that the precipitates of geopolymer flakes are smaller in metakaolin based geopolymer than the unreacted fly ash particles embedded into fly ash based geopolymer. This observation leads to the understanding the aspects of various types of precursors and their relations to the microstructures of the geopolymers derived from those precursors.



(a)

(b)

Figure 2.3. (a) Metakaolin based geopolymer with  $\text{SiO}_2:\text{Al}_2\text{O}_3 = 3^3$  (b) Flyash based geopolymer showing unreacted fly ash particles in geopolymer matrix<sup>42</sup>.

Typical properties of polysialate geopolymer and some conventional ceramic matrix were highlighted by Joseph Brown<sup>29</sup>. Those are summarized in Table 2.1. It is seen in Table 2.1 that the modulus and fracture toughness of polysialate geopolymer is much lower than that of all the



conventional ceramic materials, which are disadvantageous for typical structural applications. But the density and the curing temperature of this geopolymer are much lower than those ceramic materials, which makes it much appealing as the matrix for fiber reinforced composites. Due to these low mechanical properties, it is often combined with nanofiller and continuous fiber for high temperature structural applications.

Table 2.1. Physical properties of conventional ceramic and geopolymer<sup>29</sup>

	SiC	Si <sub>3</sub> N <sub>4</sub>	Al <sub>2</sub> O <sub>3</sub>	Polysialate
Tensile Modulus (GPa)	400	193	380	10
Density (kg/m <sup>3</sup> )	3000	3000	3800	1600
Curing Temperature (°C)	1200	1500	1400	80
Fracture Toughness (MPa√m)	3-5	6-8	3-5	<1

### 2.3 Phase Transformation of Geopolymer

It is important to understand the phase transformation of geopolymer with the variations in the composition, nano-reinforcement and heat treatment. Geopolymers are generally formed in a various ratios of SiO<sub>2</sub>/Al<sub>2</sub>O<sub>3</sub>, Al<sub>2</sub>O<sub>3</sub>/Na<sub>2</sub>O and SiO<sub>2</sub>/Na<sub>2</sub>O. Potassium based geopolymer is formed with the ratios of SiO<sub>2</sub>/Al<sub>2</sub>O<sub>3</sub>, Al<sub>2</sub>O<sub>3</sub>/K<sub>2</sub>O and SiO<sub>2</sub>/K<sub>2</sub>O. The chemical structures of geopolymer and Zeolite are similar to each other.

Zeolite has a stable hierarchical structure containing microporous alumino-silicate materials. This ordered structure results into well-developed crystalline phase which is easily observed by

x-ray diffraction technique. Zeolite and geopolymer are chemically similar to each other, however geopolymer is considered as metastable materials with less ordered structure<sup>43</sup> which tends to reach the stability with the sacrifice in mechanical strength<sup>44</sup>. With the start of the geopolymer gel formation zeolite precursor have been suggested to form as the nucleation sites for the growth of geopolymer gel and formation of geopolymer. It is suggested that this nano-crystalline zeolite structure is embedded into amorphous formation of geopolymer<sup>45,46</sup>.The formation of amorphous or semi-crystalline or fully crystalline geopolymer phase depends on several factors including the variations of the reactions due to the variations in the type and concentration of alkaline activator<sup>47</sup>, water concentration, SiO<sub>2</sub>/Al<sub>2</sub>O<sub>3</sub> ratio<sup>48, 49</sup>and hydrothermal conditions<sup>50</sup>.

Figure 2.4 presents Na<sub>2</sub>O-Al<sub>2</sub>O<sub>3</sub>-SiO<sub>2</sub> ternary phase diagram with some well-known aluminosilicate compounds including metakaolin, zeolite and geopolymer with various compositions of Na<sub>2</sub>O, Al<sub>2</sub>O<sub>3</sub> and SiO<sub>2</sub><sup>44</sup>. The purpose of this diagram is to present the variations in phases with the variations in the composition. In the ternary diagram the configurations labeled as 1 through 7 represent the geopolymer materials with various ratios of Na<sub>2</sub>O, Al<sub>2</sub>O<sub>3</sub> & SiO<sub>2</sub>. When various thermal treatment takes place the original composition of geopolymer also changes, which results into the transformation from amorphous to crystalline phase<sup>51</sup>.

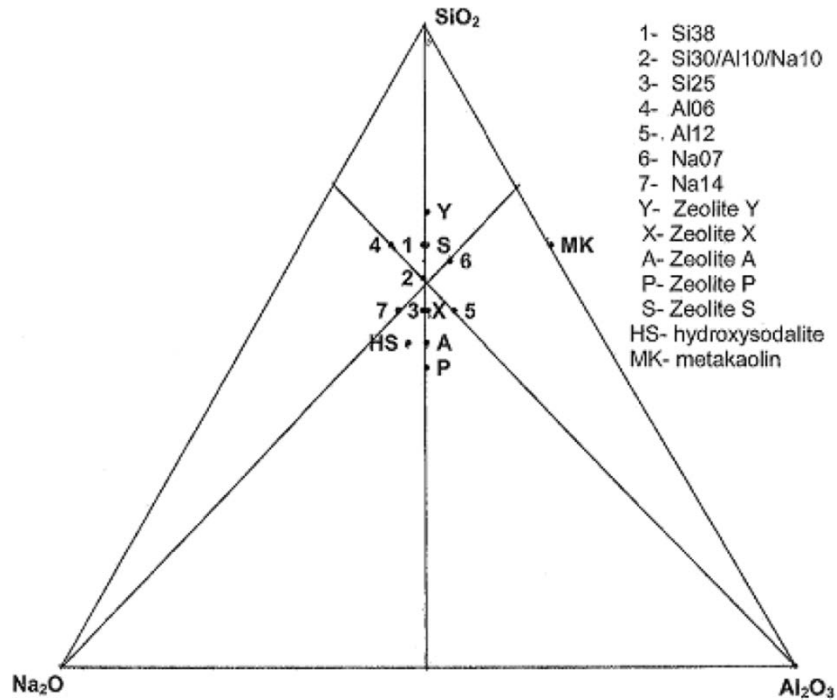


Figure 2.4. A  $\text{Na}_2\text{O}-\text{Al}_2\text{O}_3-\text{SiO}_2$  ternary phase diagram with some well-known compounds<sup>44</sup>

Phase transformations also have been suggested by the nucleation of geopolymer gel through the application of crystalline seeds<sup>52</sup>. Nano-reinforcements can act as this seed in geopolymer. Chemical kinetics between the reinforced nanomaterials and geopolymer gel is the key factor in the phase transformation of geopolymer. However this transformation simultaneously affects the mechanical strength of geopolymer<sup>44</sup>. The current study is extended to investigate the simultaneous effects of nanomaterials on mechanical strengths and onset of crystalline phases for possible transformation of geopolymer toward highly ordered zeolite.

## 2.4 Choice of Nanomaterials

A wide variety of nanomaterials (both organic and inorganic types) have been reported as the fillers for toughening of organic/inorganic polymer<sup>53,54</sup> matrix. Chemical configurations of the nanofillers are essential to understand in selecting the appropriate nanofillers for a particular type of matrix. It is stated that due to the similarities in chemical configurations, inorganic nano-fillers are expected to disperse more effectively than organic nanofillers in inorganic polymer matrix and therefore are more effective in toughening. Silicon carbide particle<sup>55</sup> and whiskers<sup>17, 18</sup> have been reported as the fillers for improved mechanical performance of brittle materials including monolithic ceramic and inorganic polymer (geopolymer) matrix. It has been reported that Silicon Carbide can be applied as a nano-filler in inorganic polymer materials in order to improve the fracture toughness and damage tolerance<sup>55, 56</sup>.

Alumina nanomaterial is a reasonably new choice for reinforcing composite matrix. A study performed by Bugaeva<sup>57</sup> has shown that surface modified Alumina nanofibers increased strength and toughness of alumina matrix. This crystalline (beta type) high modulus and high strength inorganic nanomaterial has the potential to improve damage tolerance, strength and toughness of geopolymer matrix, which has similar brittleness nature as alumina ceramics.

Carbon nanofibers (CNFs) and other carbon nanomaterials have been extensively reported as filler for organic/inorganic polymer matrix. CNFs offer several advantages to the matrix which includes the improvement in fracture toughness, flexure strength and thermal properties. CNFs are known for their high surface area, high aspect ratio and very high tensile strength. However, CNFs are difficult to disperse into many resin systems due to the hierarchical structure, strong Vander Waal force<sup>58</sup> and hydrophobic nature<sup>59</sup>. CNFs produced in Chemical vapor deposition

(CVD) process are grown from the vapor phase, which generally makes CNFs entangled during growth, producing a mesh-like configuration<sup>60</sup>. Dispersion of CNFs in the geopolymer slurry is even more difficult as compared to the organic polymeric matrices<sup>61</sup>, since the particles in the slurry hinder the free movement of CNFs. Many processes including functionalization<sup>62</sup>, debulking<sup>63, 64</sup> and in-situ growth<sup>65</sup> facilitate uniform dispersion and alignment of CNFs. However, findings from researchers suggest that, maximum dispersible fraction of CNFs in the polymeric resin without agglomeration is approximately 2 vol. %<sup>66</sup>.

## **2.5 Nanofiller and Geopolymer Interface**

Interfacial bond strength between nanomaterials and geopolymer has a significant effect on the nano-based toughening. This section explores some of the aspects of the surface associated with the interfacial strength between two materials. Many researchers suggested that similarities in chemical structure and atomic configuration between the solids are favorable for high solid-solid interfacial strength<sup>67</sup>. Also solid to solid interfacial strength depends on the elastic stretching, de-cohesion and jump to separation<sup>68</sup>. Nanomaterials with high surface energies tend to have more wettability with inorganic polymer compared to one with low surface energies, because the difference in the surface energy between the polymer and nanomaterials favors lowering the contact angle between them. Nanomaterial with high surface energy has the potential to create chemical bonding with inorganic polymer at the liquid state. Surface chemistry of nano-fillers controls the nature of interface bond strength between the nanomaterial and inorganic geopolymer<sup>18</sup>. Free elements on the surface of nanomaterials<sup>55</sup> can also contribute to the chemical bonding by contributing to chemical species into the matrix phase during high temperature processing. Therefore high temperature treatment has the potential to modify this chemical bonding and therefore alter the interfacial strength between the nanomaterial and

geopolymer. Similarly it is important to understand the presence of any free element on the surface that may contribute to the bonding strength. Free elements can be estimated from the evaluation of the x-ray energy spectroscopy associated with the elements of the nanomaterials. EDS is the tool to perform this analysis.

## **2.6 Thermal Analysis and the Interfacial Condition**

Thermal analysis leads to the understanding of the curing and the stages of processing of neat and nano-reinforced inorganic polymer. It helps to understand the phase stability at high temperature. Commonly available thermal analyses techniques are Thermo Gravimetric Analysis (TGA), Differential Thermal Analysis (DTA) and Thermal Mechanical Analysis (TMA). The purposes of these analyses are to understand the phase stability, changes in morphology, dehydration and thermodynamic behavior in various stages of cure and processing. Through the thermal analysis it is also possible to interpret the changes in the interfacial bond strength between inorganic geopolymer and nanomaterials during the cure, post process and further treatment at high temperature.

Owing to their inorganic framework, inorganic polymer, geopolymer exhibits excellent thermal stability, far in excess of that of organic polymers<sup>65</sup> and traditional cements<sup>69</sup>. These characteristics allow inorganic geopolymer as a potential candidate for high temperature fiber reinforced composites. However, thermal mismatch between the fiber and inorganic matrix leads to develop residual stress. Minimal expansion and shrinkage is desirable characteristics of geopolymer for being a successful matrix material. Study of TMA helps understand the thermal expansion characteristics of geopolymer at various stages of processing and treatment temperature. Rickard et al<sup>70</sup> showed a regional breakdown of thermal expansion/shrinkage to

relate this to various thermodynamic transformations at a typical range of processing and use temperatures. Their study suggested that with gradual changes in temperature, inorganic geopolymer experience both shrinkage and expansions at various rates depending on dehydration, dehydroxy-lation, diffusion and densification processes. Further, performing TGA and DTA on their material<sup>70</sup> helped understand the subsequent weight losses, thermal stability and possible reaction kinetics related to similar phenomena observed in thermal expansion analysis.

Nanofillers have the potential to nucleate new phases in the geopolymer. It has been suggested that this sort of nucleation is driven by physical and chemical interactions between the nanofillers and geopolymer which require kinetic energy input<sup>50</sup>. Thermal analysis ( TGA, DTA and TMA) therefore seems to be helpful in understanding the solid-liquid and solid-solid interface condition between the nanomaterial inorganic geopolymer interface at various stages of processing and treatment temperatures.

## **2.7 Fracture Surface Evaluation**

Fracture surface evaluation is an essential technique for investigating the interfacial strength between geopolymer and nanofillers. Investigation of the fracture surface helps in finding some important information related to interfacial strength which includes the interface separation and dispersion of nanomaterials. Another important evaluation technique is fractography.

Fractography is a technique for understanding the nurture of fracture and the type of energy absorption due to crack propagation. The determination of the fracture origin gives an understanding on the nature of fracture, brittle or ductile for example. Figure 2.5 is a typical presentation of fracture surface of a brittle material failed under tension while the crack

originated from the notch<sup>71</sup>. This figure shows that, when the crack originates the crack accelerates from zero to the terminal velocity upto a certain region, which is called fracture mirror. In many cases this mirror may not be found, since the visibility of mirror depends on the strength of the material. However, the hackle marks are normally found in the region of the fracture surface where the material releases maximum energy. More hackle marks are the indicators to the release of higher fracture energy. More features can be observed in the fracture surface due to the porous nature of the material. Hackle marks can propagate from the pore. Also in the case of porous materials the coarse hackle lines are found. Porosities may introduce new feature which is called wake hackle. To get such information more accurately it is always important to investigate the fracture halves than only viewing the half.

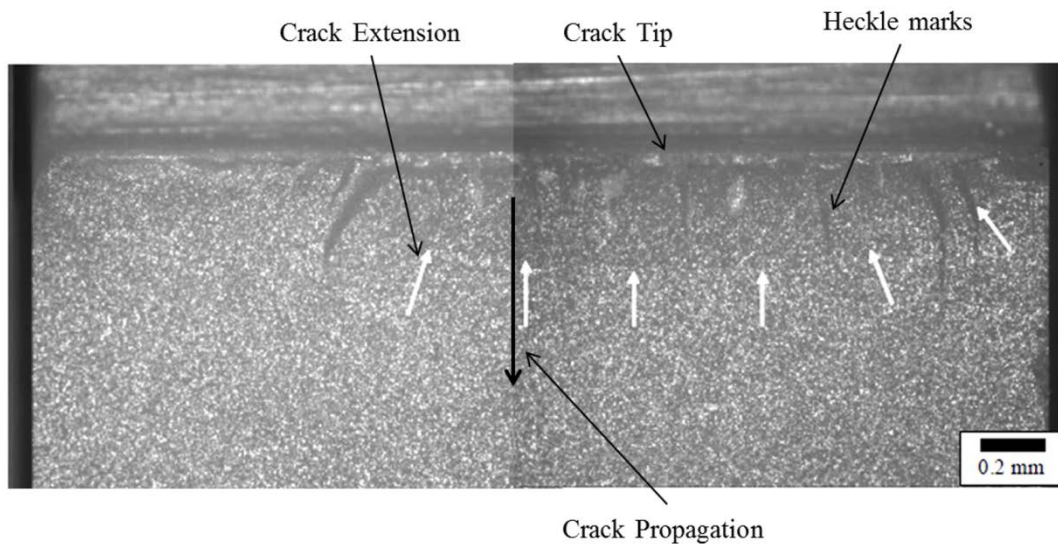


Figure 2.5. Fracture surface of alumina specimen from fracture toughness test<sup>71</sup>

## 2.8 Types of Fracture Toughness

Fracture toughness is the resistance of the material to the preexisting crack propagation. It is measured from the energy that is released while the crack propagates in a direction followed by a



startup or pre-existing crack. It is an important mechanical property especially for brittle materials, because once the crack starts, brittle materials lack sufficient plastic deformation to stop the crack.

Fracture toughness is measured into three basic modes of crack propagation. Mode I fracture toughness is measured from a condition where tensile loading is applied in a perpendicular direction to the crack plane and crack front. This is analogous to edge dislocation. Mode I fracture toughness is the primary mode of fracture toughness that reveals the materials resistance to crack propagation under pure tensile loading. Therefore it is a usual practice to measure the mode-I fracture toughness. This is presented in an abbreviated term  $K_{IC}$ , which means fracture toughness in crack opening mode-I. Fracture toughness in mode-II arises while the applied loading is in parallel direction to the crack plane and perpendicular to the crack front. Mode- III fracture toughness condition or tearing mode can arise while the tensile loading is in parallel to the crack plane and crack front. Figure 2.6 is the presentation of various modes of fracture toughness excerpted from David Roylance<sup>72</sup>. In order for understanding the changes in the geopolymer materials toughness behavior with processing and nano-reinforcement, only mode-I fracture toughness will be explored through this current investigation.

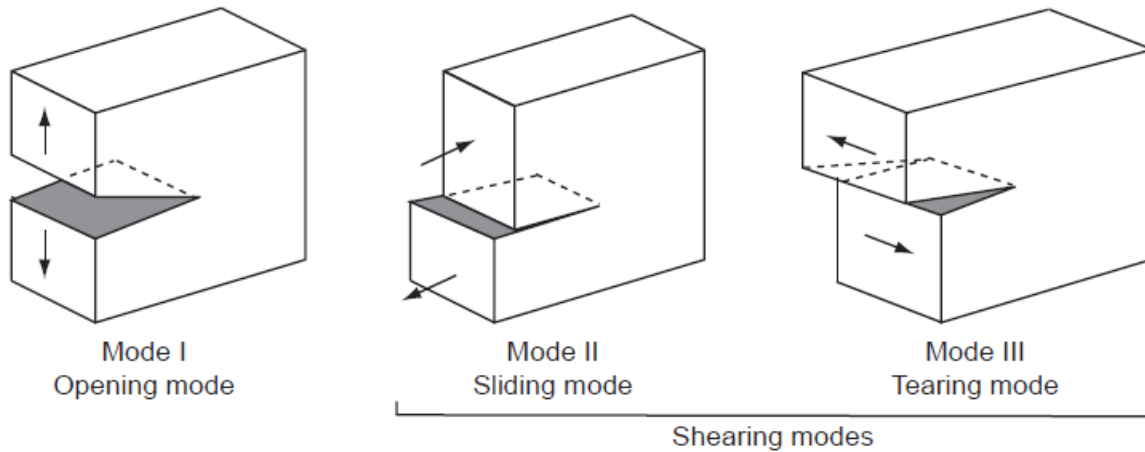


Figure 2.6: Various modes of fracture toughness<sup>72</sup>

## 2.9 Toughness Measurement Techniques

Measurement of mode I fracture toughness ( $K_{Ic}$ ) is one of the key interests of this project. Measurement techniques of fracture toughness vary with material types. For brittle materials, where apparently no appreciable plastic deformation is observed, Linear Elastic fracture mechanics (LEFM) approach is generally applicable. In the LEFM approach it is assumed that the material is isotropic and linearly elastic. Based on this assumption, the stress field near the crack tip is calculated using the theory of elasticity. When the stresses near the crack tip exceed the material fracture toughness, the crack starts to flow (see Figure 2.5). LEFM approach is valid only when inelastic deformation is small compared to the size of the crack. Brittle materials don't experience any plastic deformation and therefore LEFM is used in the fracture toughness measurement. Based on this theory, the stress field near a crack tip is a function of location, the loading conditions and the geometry of the specimen.

An appropriate toughness measurement technique depends on many factors including materials type, geometry, loading conditions and the easiness of sample preparation. A wide variety of

fracture toughness measurement techniques have been demonstrated<sup>8,73-81</sup>, majority of which are dependent on the physical properties of the materials of interest. With these variations in testing techniques, the ultimate goal is to accurately measure fracture toughness in a way that the results can be compared to the techniques developed by the reported research groups<sup>100</sup>. The objective of this verification is to accurately measure fracture toughness of the inorganic geopolymer which is necessary to prove the proposed hypothesis.

Fracture toughness measurement techniques can be divided into two main categories. In one technique, fracture toughness is calculated from the direct measurement of crack length emanating from an indentation on a material with no pre crack, which is termed as indentation fracture test. To perform this test, a Vicker's indentation technique is normally applied to emanate the crack, which can be correlated to toughness,  $K_{IC}$  using the following relationship<sup>73</sup>

$$K_{IC} = \alpha \left( \frac{E}{H} \right)^{1/2} \frac{P}{a^{3/2}} \quad (2)$$

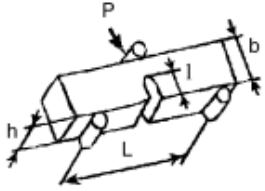
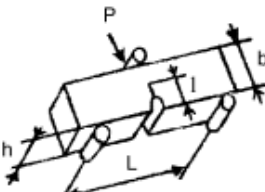
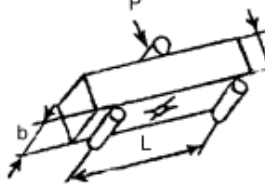
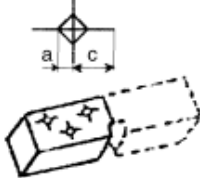
Where, P is the applied load for indentation, E is the modulus, H is the Vicker's hardness, a is the radial crack length measured from the center of the indent and  $\alpha$  is the empirical constant which depends on the materials.

Unfortunately, due to the uncontrolled crack growth, indentation technique arises some uncertainties in the case of many brittle materials. Cracking mechanism in the most brittle materials allow only the linear elastic deformation and no apparent plastic deformation. Conversely, indentation technique depends on the shear deformation and hardness which are strong functions of indentation load and materials<sup>74</sup>. Due to these functional dependencies, researchers have developed different co-relations by curve fitting using a wide range of brittle

materials with commonly known properties<sup>75,76</sup>. However, none of those relations are validated by conducting experiments using materials with unknown toughness<sup>77</sup>. In addition, indentation creates a three dimensional deformation which induces residual stress around the crack. A group of researchers<sup>78,79</sup> has demonstrated that indentation technique in the reinforced ceramics reveals an artificial reduction of crack length due shear deformation, which results in higher than actual fracture toughness values. This means that, indentation technique is not ideal for measuring fracture toughness of nano-reinforced materials. However, this technique can be useful in investigating damage tolerance or resistance to forming cracks, which may be important for materials to some applications where contact resistance is necessary.

A direct approach of fracture toughness measurement involves the application of the load to measure the load bearing capacity of a pre cracked sample. Due to the ability to measure the actual load bearing capacity, this approach moderately counts the effect of reinforcement in the materials<sup>8</sup>. The direct approach of toughness measurement is a two-step process - (1) Creation of starter crack and (2) Propagation of the crack until it reaches the critical length, which results in the critical stress intensity. A number of direct measurement techniques have been reported in this respect, which includes Single edge notch beam (SENB) and single edge V-notch beam (SEVNB), single edge pre-crack beam (SEPB), indentation Strength (IS) and Chevron notch beam (CNB). Several of those test methods can be presented with the sample and loading geometry as in Table 2.2 excerpted from Gogotsi et al<sup>80</sup>. Since all of these techniques require a complete failure of the material, these are considered as direct toughness measurement techniques.

Table 2.2: Several fracture toughness measurement techniques<sup>80</sup>.

Method	Specimen
Single edge notched beam SENB	
Single edge precracked beam SEPB	
Indentation strength IS	
Indentation fracture IF	

In SEVNB technique, toughness is directly measured by creating a simple notch on the surface subjected to tensile loading. Toughness measured in this technique is a strong function of notch depth, however, this technique does not account for the effect of notch root radius, which is very important in measuring the actual toughness<sup>81</sup>. SEVNB technique depends on creating a sharp notch, such that the size of the notch tip is as close as atomic radius, where only a small fraction of applied load would be required to start the crack. Once the crack starts, the fracture toughness is resulted from the resistance to propagate the crack until the critical crack length is attained.

Therefore, toughness measurement in SEVNB technique generates reproducible fracture toughness data. This technique is adopted in the current research.

## **2.10 Experimental Design**

Design of experiments is a systematic method to determine the effect of the factors in the possible output of the process. In other words, this is an approach to find the cause and affect relationships between the factors and the process outputs. The Design of experiments is a statistical approach to find the significance of the factors affecting the process output. Design of experiment is a sophisticated statistical tool that effectively separates the main and interaction effects of the variables and allows the designer to evaluate importance of one variable over other. It is usually referred as the preliminary study to understand the limits of the variables. The upper and lower limits of each variable are usually set as +1 and -1. It is required to choose a suitable range where the effects of the variable on the output are the most significant.

### ***2.10.1 Main Effects***

This is the effect of one independent variable on the process output or response while the effect of other independent variables is ignored. When a number of variables contribute simultaneously on a response, main effects help understand the significance of one variable over another one. An example of the main effect can be presented as the effect of the volume fraction of nanomaterials on the fracture toughness of geopolymer.

### ***2.10.2 Interaction Effects***

This is the simultaneous effect of two or more variables on the process output or response. This interaction occurs when the effect of one independent variable on the response changes

depending on the level of another independent variable. An interaction means that the effect of one independent variable on a dependent variable is not the same for all levels of the other independent variable. Interaction is a complex multivariable effect which provides more precise information than simplified main effect. For example, the effect of changing interfacial strength with the changes in the aspect ratio of nanofillers on the process output, fracture toughness can be classified as an interaction effect. Interaction effect can be more complicated when the effects of more than two variables are required to investigate simultaneously.

### ***2.10.3 Factorial Design***

Factorial design is an acceptable technique to investigate main and interaction effects of the variables chosen in any design of experiment. Factorial design is helpful in investigating the interaction effects of various independent variables on the dependent variables or process outputs. An example related to the current investigation is to find the effects of three variables on the response to fracture toughness,  $K_{IC}$ . The variables and their levels are as follows, Aspect ratio, AR (+1 & -1), Interfacial strength, IS (+1 & -1) and volume fraction, VF (+1 & -1). According to factorial design total runs to perform for these two level variables are  $2^3=8$ . The responses from the runs using main and interaction effects are shown in Table 2.3.

Table 2.3 Responses from different runs using main and interaction effects

Runs	Main Effects			Interaction Effects				Response
	Aspect Ratio, AR	Interfacial strength, IS	Volume fraction, Vf	AR*IS	AR*Vf	IS*VF	AR*IS*VF	
1	-	-	-	+	+	+	-	Y1
2	+	-	-	-	-	+	+	Y2
3	-	+	-	-	+	-	+	Y3
4	+	+	-	+	-	-	-	Y4
5	-	-	+	+	-	-	+	Y5
6	+	-	+	-	+	-	-	Y6
7	-	+	+	-	-	+	-	Y7
8	+	+	+	+	+	+	+	Y8

From the 8 runs above, the main effect of aspect ratio (AR) is found from the average difference in fracture toughness when aspect ratio is set high (+1) and low (-1). In other words, it can be found using the following equation

$$(\Delta K_{IC})_{AR} = \frac{Y_2+Y_4+Y_6+Y_8}{4} - \frac{Y_1+Y_3+Y_5+Y_7}{4} \quad (3)$$

Similarly, main effect of interfacial strength (IS) can be found using the following equation

$$(\Delta K_{IC})_{IS} = \frac{Y_3+Y_4+Y_7+Y_8}{4} - \frac{Y_1+Y_2+Y_5+Y_6}{4} \quad (4)$$



Main effect of volume fraction (VF) can be found using the following equation

$$(\Delta K_{IC})_{VF} = \frac{Y5+Y6+Y7+Y8}{4} - \frac{Y1+Y2+Y3+Y4}{4} \quad (5)$$

Similarly, interaction effects of aspect ratio and interfacial strength (AR\*IS) can be found using the following equation

$$(\Delta K_{IC})_{AR*IS} = \frac{Y1+Y4+Y5+Y8}{4} - \frac{Y2+Y3+Y6+Y7}{4} \quad (6)$$

Interaction effects of other two combinations can be found using the following equations

$$(\Delta K_{IC})_{AR*VF} = \frac{Y1+Y3+Y6+Y8}{4} - \frac{Y2+Y4+Y5+Y7}{4} \quad (7)$$

$$(\Delta K_{IC})_{IS*VF} = \frac{Y1+Y2+Y7+Y8}{4} - \frac{Y3+Y4+Y5+Y6}{4} \quad (8)$$

There are many statistical tools available for analyzing and presenting the effects of the variables obtained from the design of experiments. Among them analysis of variations (ANNOVA) and PARETO charts can be named.

## 2.11 Nanomaterial Mixing Techniques

Nanomaterials have high surface area which favors the entrapment of air during the mixing of nanomaterials in a liquid polymer. This entrapped air essentially creates voids in the cured sample which results in the reduction in the structural integrity and mechanical strength. Therefore, during the nanomaterial mixing process it is highly recommended to eliminate air bubbles as much as possible. In order to avoid entrapment of air, nanomaterials are generally mixed at low speed or in vacuum.

Various techniques for mixing nanomaterials into liquid polymer include shear mixing, stirring, vibration and ultrasonic irradiation. Mechanical stirring can entrap a large volume of air into the polymer. Ultrasonic irradiation technique utilizes a high frequency sound pressure wave which

creates sufficient energy for homogeneous mixing of nanomaterials into polymer; however this technique generates heat during the mixing process, which initiates the curing of the premixed polymer. A low speed three roll shear mixture facilitates mixing of nanomaterials without a significant air entrapment into the polymer. Therefore this technique is ideal for mixing of nanomaterials, even at a large volume fraction.

## **2.12 Nano-filler in Fiber Reinforced Composites**

Ultimate goal of nano-reinforcement in the geopolymer matrix material is to improve the overall properties of fiber reinforced composites. As previously mentioned, several studies highlighted the effectiveness of this nano-reinforcement in toughening and strengthening of various continuous fiber- geopolymer matrix composites<sup>10,13,14</sup>. However most of those studies were unable to highlight the underlying mechanism of those toughening and strengthening of continuous fiber reinforced composites through the direct understanding of the mechanism that relates to the toughening and strengthening of neat matrix materials. Therefore it is necessary to focus into the evaluation of inorganic geopolymer as a viable matrix material for the continuous fiber reinforced composites.

## **2.13 Conclusion**

The reported experimental results and theoretical establishment suggests that the variations in the microstructure and phases of geopolymer depend on the starting materials and their ratios. Unreacted particles act as reinforcement in the geopolymer network which increases overall mechanical performance. Processing mechanism has a strong relationship with the microstructure and phase morphology which controls the mechanical and thermal properties of geopolymer. Improvements of these properties are dependent on the suitable processing

parameters including the time and temperature at various stages of cure and post processing. Nanofillers have significant potential in modifying micro-structure and improving mechanical strength. The extent of these improvements depends on the selection of suitable nanomaterials with optimum physical properties and the ability to interact with the respective geopolymer. The significance of these experimental investigations has been explored through the statistical design of experiments.

From the review of several literatures it has been explored that due to the brittleness nature of geopolymer fracture toughness is one of the important mechanical properties which is needed to understand for any viable application of this material into continuous fiber reinforced composite. Pre notched beam (SEVNB) flexural strength measurement can be considered as a suitable technique for the evaluation of fracture toughness.

The review included the effectiveness of nanofillers in toughening and strengthening of various materials. However, there is a limited investigation on the effect of various aspects of nanofillers on the key mechanical properties of geopolymer. The major outcome of the thesis will be derived from a systematic study to explore the effectiveness of those aspects of nanofillers on geopolymer performance towards the application as the matrix to the continuous fiber reinforced composite. The observed effects of those aspects on the underlying toughening mechanism of inorganic geopolymer at various thermodynamic conditions will be investigated through the choice of efficient testing and characterization techniques.

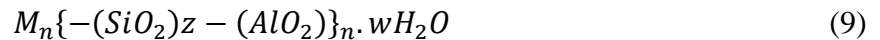
### 3 MATERIALS OF THE EXPERIMENTATION

This chapter explores the materials of the current investigation. This includes the exploration of the properties of inorganic geopolymer and various nanomaterials. Among various properties of nanofillers, aspect ratio, chemical structure, surface morphology, thermal and mechanical properties are of the primary interests.

#### 3.1 Inorganic Polymer

The trade name of the inorganic polymer of the current investigation is MEYEB™. MEYEB is a research grade inorganic polymer obtained from Pyromeral systems Inc. The inorganic polymer, MEYEB, was obtained as a suspension of inorganic polymer resin. It is a Potassium balanced, polysialate<sup>82</sup> with the ratio of Si:Al of 1:1 and proprietary proportions of K<sub>2</sub>O/SiO<sub>2</sub> and H<sub>2</sub>O/K<sub>2</sub>O. MEYEB is supplied in a suspension of various chemicals including potassium silicate, aluminum oxide, silicon dioxide, aluminum phosphate and water. MEYEB is similar to geopolymer. For simplicity and to be consistent this inorganic polymer is mentioned as geopolymer throughout the current investigation.

Polymerization of MEYEB is the result of a polycondensation reaction, which requires an ionic balance of the sialate network in the presence of positive alkali ions (Na<sup>+</sup>, K<sup>+</sup> and Cs<sup>+</sup>, etc.). The corresponding empirical formula for the inorganic polymer is;



Where, M is the alkali cation, z is the ratio of Si:Al, n is the degree of polymerization, and w is the number of water molecules<sup>12</sup>.

MEYEB is a potassium-balanced poly (-siloxo-) silate (PSS). Such materials consist of various proportions of Si and Al in a tetrahedral network of Alumino-silicate<sup>83</sup>. The tetrahedral network is the chemical backbone of the inorganic polymer, which is made of a SiO<sub>4</sub> and AlO<sub>4</sub> covalent structure, bonded by oxygen atoms, in an alternating fashion. A fully cured inorganic polymer consists of a network of amorphous fine particles separated by nano-pores<sup>84</sup>. This represents a significant difference from the conventional monolithic ceramic materials however, both exhibit the brittleness characteristics. MEYEB has a very limited shelf life and handling time. Polycondensation of MEYEB in an alkali environment is a highly reactive process which can start at low temperature<sup>82</sup>. In order to prevent MEYEB from uncontrolled poly-condensation during the handling, MEYEB is usually stored at freezing condition, below -25 °C. Also MEYEB is supplied as a liquid slurry mixture in a plastic bottle and shipped in a cryogenic box.

### **3.2 Nano-materials of the Experimentation**

Various nanomaterials were selected to enable the investigation of the effect of the variations in their aspect ratios and relative interfacial bond strength with MEYEB. To maintain the variations in interfacial strengths with MEYEB these nanomaterials were chosen based on the variations in the surface energies and chemical configurations of the surfaces. The intention of using various types of nanomaterials is to investigate their potential to toughen the MEYEB as a matrix material at various environments for a continuous fiber reinforced composite.

Three types of nanomaterials were chosen in a batch of low and high aspect ratios. The chemical compositions of the batches of these nanomaterials are – Alumina (Al<sub>2</sub>O<sub>3</sub>), Silicon Carbide (SiC) and Carbon, respectively. Chemical structure suggests that the former two nanomaterials are inorganic and the later one is organic. All the nanomaterials are crystalline in nature. In order to

maintain the variations in the geometry two types of nanomaterials were chosen for each batch with low and high aspect ratios respectively. This result in selecting a total of six types of nanomaterials which are mentioned below-

Alumina Nano Fiber (ANF)

Alumina Nano Particles (ANP)

Silicon Carbide Whisker (SCW)

Silicon Carbide Particles (SCP)

Carbon Nano Fiber (CNF)

Carbon Nano Particles (CNP)

Properties of these nanomaterials are presented in Table 3.1. Inorganic nanomaterials are expected to have better interfacial strength with MEYEB due the similarities in the chemical configuration. The aspect ratio (L/D) of the nanofibers and silicon carbide whiskers are comparable, which are approximately 40. It is notable that the tensile strength and modulus of SCW and CNF are higher compared to that of ANF; however failure strains of all the nanofillers are comparable, which is in the range of 1.0-1.5%, approximately. Failure strains of the nanofibers were calculated by dividing the tensile strength by the modulus, which are found in Table 3.1. Strength of ANF is calculated using the load deflection profile of single nanofiber measured using Atomic Force Microscopy (AFM) technique. The calculations on the strength of ANF and failure strains of all the nano-fibers can be found in Appendix B1& B2.

Table 3.1. Properties of nano-materials of the investigations

Nano materials	Batch A		Batch B		Batch C	
	Alumina		Silicon Carbide		Carbon	
Major constituent	Al <sub>2</sub> O <sub>3</sub>		SiC		C	
Type	Nanofiber	Nano-particles	Nanofiber	Nano particles	Nanofiber	Nano-particles
Designation	ANF	ANP	SCW	SCP	CNF	CNP
Diameter (nm)	40	40	400	400	150	150
Length (nm)	1500	40	16,000	400	4000-5000	150
Aspect Ratio	~40	1	~40	1	~40	1
Surface Area (BET) (m <sup>2</sup> /g)	155	155	120-190	20	25	
Surface Energy, (mJ/m <sup>2</sup> )	5900 <sup>85</sup>				120-140	
Density(g/cc)	0.4	0.4	3.2	3.2	0.032	0.032
Modulus (GPa)	220 to 257 <sup>86</sup> (Bulk)	220 to 257 <sup>86</sup> (Bulk)	580 <sup>87</sup>	580 <sup>87</sup>	600 <sup>88</sup>	600 <sup>88</sup>
Tensile Strength (GPa)	2.38 <sup>86</sup>		8.4 <sup>87</sup>		8.7 <sup>88</sup>	
Failure Strain (%)	1.08		1.44		1.45	
Oxidation Stability (°C)	1200-1400 <sup>89</sup>	1200-1400 <sup>89</sup>	1650 <sup>90</sup>	1650 <sup>90</sup>	500 <sup>91</sup>	500 <sup>91</sup>

Among the nanomaterials in Table 3.1, chemical network of Alumina and SiC are in close proximity with MEYEB, however this is not the case for carbon nanomaterials. It is known that the nanomaterials with high surface energies tend to have more wettability than the one with low surface energies, because in the case of the high surface energy difference between nanomaterials and MEYEB attract MEYEB toward the nanomaterial and create lower contact angle compared to low surface energy nanomaterial. Based on the chemical configurations and surface energies of three types of nanomaterials it is expected that that the wettability of MEYEB with carbon nanomaterials and alumina nanomaterials are low and high, respectively and with SiC nanomaterials are in between.

Both Alumina and Silicon carbide nanomaterials have similarities in the chemical network with MEYEB; however Alumina is expected to have more interfacial bond strength with this aluminosilicate based geopolymer. Previous studies<sup>14</sup> suggest that the strength of the continuous Alumina fiber/MEYEB interface is higher than continuous SiC fiber/MEYEB interface. Studies with micro fiber reinforced composites suggested some important correlations between the mechanical performance of the composites and interfacial strength. From this study it was found that continuous and clean SiC microfiber reinforced MEYEB had weaker fiber/matrix interface than that of continuous and clean Alumina fiber reinforced MEYEB. While the flexure strength of SiC fiber reinforced MEYEB was found lower compared to alumina fiber reinforced MEYEB, the toughness results showed the opposite trend. Higher flexural strength and lower toughness of micro fiber reinforced composites suggest higher interfacial strength between the fiber and matrix. Based on the finding from this study one can expect that, the interphase of SiC nanofilles/ MEYEB is weaker compared to that of alumina nanofiber/MEYEB. However in order to translate the results of micro fiber reinforced matrix to nanofillers reinforced matrix it is



important to ensure that the surface stoichiometry of both micro fibers and nanofillers are similar. Fracture surface analysis is performed later in this respect to compare the interfacial strength between various nanomaterials and MEYEB.

### 3.3 Trade Name & Collection of Nanomaterials

The trade name of the Alumina nanofiber of this investigation is Nafen™. Nafen™ was collected from ANF technologies<sup>89</sup> Estonia, through the material transfer agreement (MTA). According to the supplier, Nafen was produced co-aligned in a block upto 15 cm long. The diameter of individual nanofiber is approximately 40 nm. Nafen™ has hydrophilic nature and high surface energy, which allows them to mix easily with the polymer that has hydrophilic nature as well. Due to the hydrophilic nature Nafen can absorb as much as 10 wt% of moisture. As reported by the supplier, alumina nanofiber has superior fire retardancy. A block of alumina nanofiber is shown in Figure 3.1.



Figure 3.1. Alumina nanofiber block with the demonstration of fire retardancy <sup>89</sup>

CNFs were purchased from Applied Science Incorporated under the commercial name Pyrograph®-III, type, PR-19-XT, where XT defines the grade of the CNFs. PR-19-XT is the de-bulked CNFs form of the tight bundles of PR-19 CNFs. After debulking process the bundles of CNFs loose much of Vander Waal force which results into loose structures of CNFs bundle. The micrograph in Figure 3.2 represents magnified views of the de-bulked PR-19 CNFs. More information on the properties of the CNFs can be found in Appendix A1.

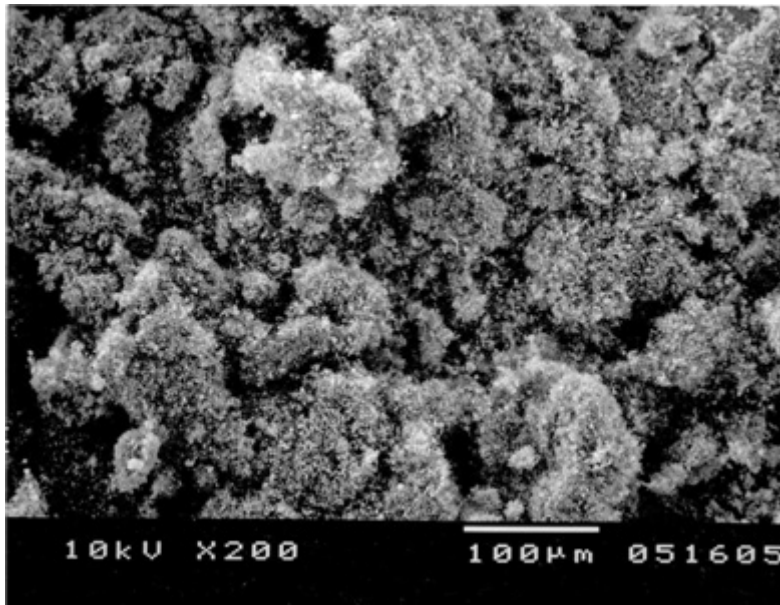


Figure 3.2. PR-19-XT De-bulked CNFs<sup>92</sup>

Silicon Carbide Whisker (SCW) was supplied by Pyromeral Inc. The trade name of SCW is Silar SC9M and its manufacturer is Advanced Composite Materials. These are de-agglomerated and very high modulus rigid nanofibers. Figure 3.3 is an enlarged view of a bulk of SCW as viewed in Scanning Electron Microscopy (SEM). The reported lengths of the fibers are 10-12µm, however while viewing in SEM it was found that most of the fibers were 25-30 µm. More information on the properties of SCW can be found in Appendix A2.

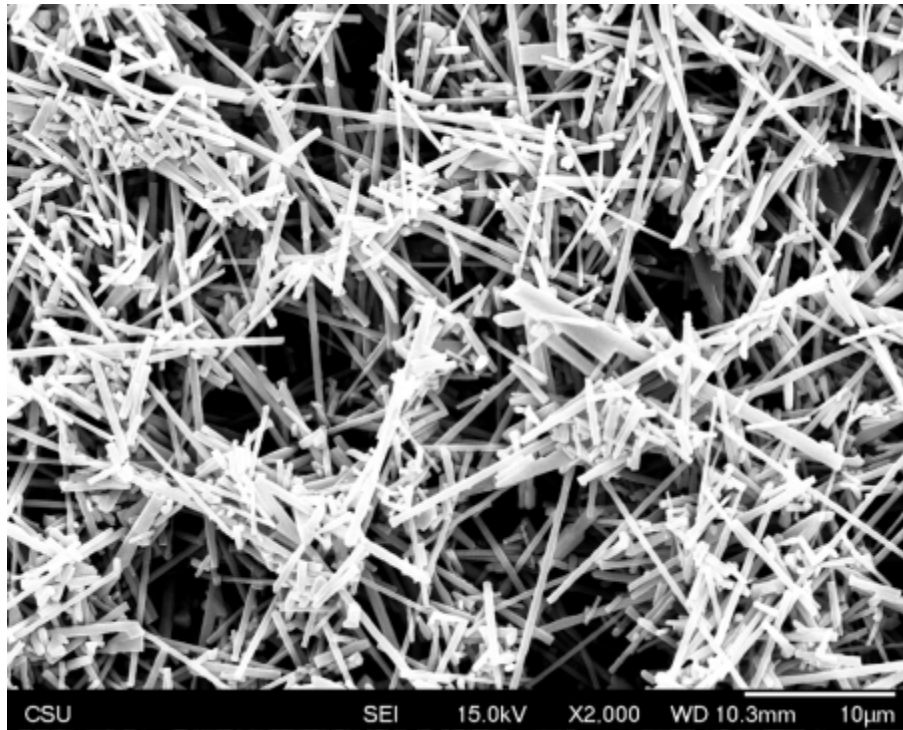


Figure 3.3. De-agglomerated bulk Silicon Carbide Whiskers

Silicon Carbide Particles (SCP) were supplied by superior graphite Inc. The trade name of this material is HSC ® Silicon Carbide Powder. This is beta rounded shape with average diameter of 0.45 µm. Detailed information on the properties of SCP can be found in Appendix A3 and A4.

The fibers involved in the composite fabrication are continuous roving Nextel 610 Alumina. The trade name of this fiber is 3M™ Nextel™ 610 ceramic fibers<sup>93</sup>. This fiber is composed of 99% fine grained, single phase Alpha-Al<sub>2</sub>O<sub>3</sub>. Details on the fiber are provided in Appendix A6. A summary of mechanical properties of Nextel 610 fibers is shown in Table 3.2. Nextel 610 fiber bundle was obtained as coated with an organic polymer sizing, which is intended to protect the fibers before matrix incorporation<sup>93</sup>. Two types of surface conditions were achieved on the fiber by heat treatment. The purpose of these variations in the surface was to investigate the effectiveness of reinforcements on the composites with the variations in the interfacial bond

strength between the major to constituents. Carbonaceous sizing was decomposed to inert atmospheres when exposed to elevated temperatures. Alternatively, the sizing was completely removed by oxidation to oxidative environment when the fiber was exposed to elevated temperatures and clean surface was obtained.

Table 3.2 Properties of the fiber used in the composite fabrication<sup>93</sup>

Type	Fiber Diameter (μm)	Fiber Density (g/cm <sup>3</sup> )	Tensile Modulus (GPa)	Tensile Strength (GPa)	Max Temp (°C)
Nextel 610	10-12	3.9	380	3.10	1000

### 3.4 Conclusion

Inorganic polymer, geopolymer of this investigation is a potassium based polysialate material with a combination of poly-condensed structure and unreacted particles. The material is different from conventional organic polymer because of the absence of carbon and the composition in the precursor materials. To understand the effect of aspect ratio all the nanomaterials were selected into two aspect ratios, such as 1 and ~40. The strength of ANF is lower compared to other two nanofillers of equal strength. This leads to investigate the effect of the strength of nanofillers on toughening inorganic geopolymer. Among all the nanomaterials, chemical configuration of alumina is closer to that of geopolymer, which suggests stronger interfacial bonding. Conversely carbon nanomaterials have a quite different chemical configuration compared to the geopolymer. Surface energies of alumina and silicon carbide nanomaterials are quite higher than that of

carbon nanomaterials. The differences in the chemical configurations and surface energies of these nanofillers enable the variations in the interfacial bond strength and therefore the effects of nano-reinforcement.

## 4 GEOPOLYMER PROCESSING OPTIMIZATION

The purpose of this preliminary study is to develop a repeatable baseline geopolymer samples with sufficient mechanical and thermal properties that allowed handling and testing. This study includes the search for optimum processing schedule in terms of process induced shrinkage, mechanical strength and stiffness. MEYEB was selected as the geopolymer for this study.

### 4.1 Processing of MEYEB for Evaluation of Cure Schedule

A detailed processing study is presented, which has already been performed to improve the baseline properties of neat MEYEB in preparation for ultimate evaluation of the addition of nano-reinforcements. The experimental approach was developed in an attempt to reduce the cracking of neat MEYEB samples, which had been a serious impediment to better understanding the fiber reinforced composite properties during previous laboratory experiments. To evaluate process-induced changes, neat resin specimens were prepared for the measurement of the shrinkage during cure and post-cure, and of the effects on the resulting mechanical properties. Tests were developed to evaluate the response, related to each of the stages of processing, including varying the cure time for polycondensation and the heating rates, dwell times and temperatures for the drying stage of the process. Initial curing was performed at 80 °C in the presence of moisture. Drying was conducted at temperatures up to 250 °C, while high temperature post cure would take place up to 650 °C . Tests were performed in two series, first evaluating the effect of initial cure time, prior to drying, on the polycondensation reaction, and then in the second series, measuring the results after various drying and post-cure schedules, as described in Table 4.1.

Table 4.1. Cure schedule, Series 2

Sch. Name	Cure Time 80 °C (hr)	1 <sup>st</sup> stage				2 <sup>nd</sup> stage	3 <sup>rd</sup> stage
		Dry Time 80 °C (hr)	Evaporation Schedule				Post cure Schedule
			100 °C	145 °C	175 °C	250 °C	650 °C
<b>A1</b>	2					R-5°C/min H-5hr	R-5°C/min H-5hr
<b>A2</b>	10	0.2				R-5°C/min H-5hr	R-5°C/min H-5hr
<b>A3</b>	10	2	R-0.1°C/min H-3 hr	R-1°C/min H-3hr		R-5°C/min H-5hr	R- 5°C/min H- 5hr
<b>A4</b>	10	10	R-0.1°C/min H- 3hr			R-1°C/min H-5hr	R-5°C/min H-5hr
<b>A5</b>	10	10	R-0.1°C/min H-3hr	R-1°C/min H-3hr		R-1°C/min H-5hr	R-5°C/min H-5hr
<b>A6</b>	10	10	R-0.1°C/min H- 3hr		R-1°C/min H-3hr	R-1°C/min H-5hr	R-5°C/min H- 5hr
<b>B1</b>	24	10	R-0.1°C/min H-3hr			R-1°C/min H-5hr	R-5°C/min H- 5hr
<b>B2</b>	24	10	R-0.1°C/min H-3hr	R-1°C/min H-3hr		R-1°C/min H-5hr	R-5°C/min H-5hr
<b>B3</b>	24	10	R-0.1°C/min H-3hr		R-1°C/min H- 3hr	R-1°C/min H-5hr	R-5°C/min H-5hr

In Table 4.1 R stands for ramp rate; H for hold or dwell time. The first series of test specimens were cured in a sealed environment to ensure that moisture was retained, not allowing the

specimens to prematurely dry. This group of specimens was cured at 80°C for times ranging from 1 hour to 30 hours. The second series of tests was designed to study the effects of variations in cure and drying schedules. The details of the process schedules used for this second series of trials are given in Table 4.1. Trials are labeled ‘A’ for cases with an initial cure stage of 10 hours or less and are labeled ‘B’ to represent cases where this stage was extended to 24 hours. Drying parameters varied with the specific case being considered. The 650 °C postcure was held constant, throughout all trials. Linear shrinkage and compression strength were measured to assess the effects of varying the process parameters. A minimum of five specimens were produced for each condition evaluated, in both test series.

#### ***4.1.1 Specimen Preparation***

Specimens were prepared by pouring the liquid MEYEB solution into tubular acetal resin molds with a nominal inside diameter of 6 mm and length of 20 mm. These molds were closed on both ends with vinyl caps and sealed with PTFE tape. To further ensure moisture retention, the molds were sealed in polyethylene (PE) bagging. Atmospheric pressure was maintained inside the bagging. The molds were kept vertical in order for any bubbles to freely escape from the liquid state. Six specimens in molds, supported in a holder to maintain the vertical orientation, and sealed inside bagging, are shown in Figure 4.1 . A schematic representing four specimens is also shown in Figure 4.2.



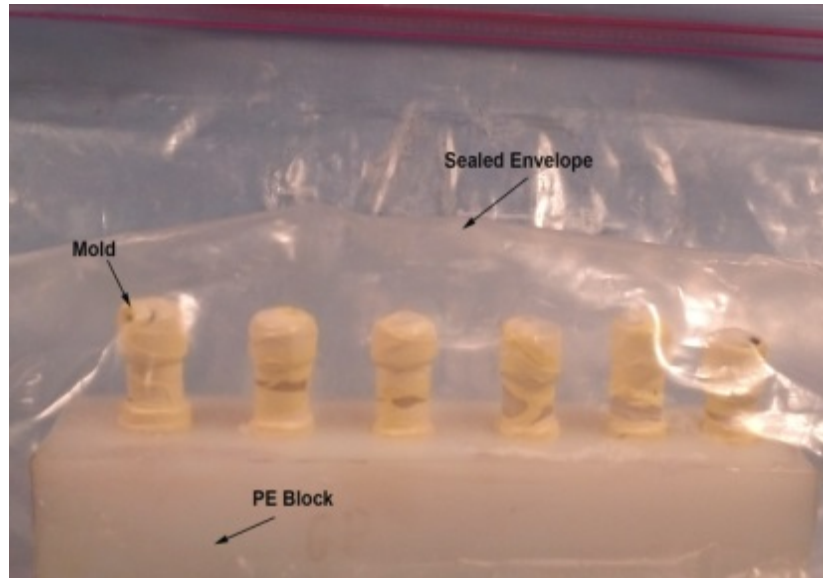


Figure 4.1. Mold preparation and curing of MEYEB in a sealed environment.

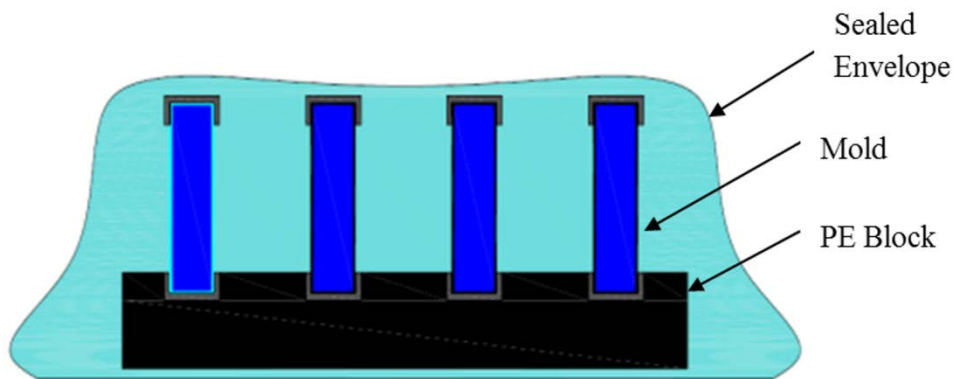


Figure 4.2. Schematic presentation of MEYEB curing inside the sealed molds.

To accomplish the initial cure, the samples were heated at 1 °C/min to 65 °C, then at 0.5 °C/min from 65 °C to 80 °C, and then held at 80 °C for a time ranging from 1 hour to 30 hours, in the sealed environment. The first series of specimens was tested immediately after this 80°C soak. For the second series of tests, processing was continued beyond the initial cure in the sealed environment. At the end of the initial cure in the sealed environment, the cylindrical samples were removed from the mold and dried in air at 80 °C for a predetermined time, ranging from

0.2 – 10 hours. Additional drying, at temperatures stepping up to 250 °C, was performed as detailed in Table 4.1. The final 650 °C de-hydroxylation stage was the same for all of the second series specimens. Elevated temperature (650 °C) postcures were performed in an oven in air and, for many of the specimens, in the thermo-mechanical analyzer with a nitrogen flow rate of 20 - 30 ml/min.

#### ***4.1.2 Evaluation of Effects of Process Variations***

To evaluate the effects of the process cycle variations, process-induced shrinkage and the resulting mechanical properties were measured. Process-induced shrinkage is a major factor in the development of residual stresses during fiber reinforced composite production, and thus understanding the shrinkage development during the processing of the neat inorganic polymer resin is of great interest. The mechanical properties were evaluated to assess the effects of process conditions on the degree of cure. Compression strength and modulus were measured, as these are relatively insensitive to small cracks and flaws that would negatively affect the measured tensile strength, but are representative of the intrinsic binding strength of the material.

### **4.2 Characterization Techniques**

#### ***4.2.1 Process-Induced Linear Shrinkage***

To determine the average linear shrinkage during the initial cure, the height of the liquid column and the length of the corresponding cured sample were measured using a caliper and averaged for a number of specimens. Average linear shrinkage was calculated using the following equation;

$$S_a = \frac{\sum_1^n \frac{L_0 - L}{L_0}}{n} \times 100\% \quad (10)$$

where,  $S_a$  is the average linear shrinkage,  $L_0$  is the length of mold,  $L$  is final length of sample after curing at the specified time, and  $n$  is the number of specimens for each curing schedule. Linear shrinkage, measured in this technique, is a close approximation of the real time measurement, which allowed to measure only the average total initial shrinkage that corresponds to the different sets of specimens as described in Table 4.1. Thermo-mechanical analysis (TMA) was performed to investigate drying and postcure related instantaneous shrinkage. A Seiko Instruments TMA/SSC120C automatic cooling dynamic load thermomechanical analyzer was used for this study. In this set of experiments, a constant load of 20 mg was applied on the quartz probe to maintain contact with the top of the sample. All samples were approximately 19 mm long and the tests were performed over the temperature range from 30 °C – 650 °C. The investigations were performed based on length change, which can be found using the following equation;

$$S_i = \frac{L_0 - L_i}{L_0} \times 100\% \quad (11)$$

Where,  $S_i$  is the instantaneous length change,  $L_0$  is the initial length before the start of experiment and  $L_i$  is the instantaneous length of the sample at any temperature.

#### **4.2.2 Thermo-gravimetric Analysis**

The equipment used for Thermogravimetry (TGA), Differential Thermogravimetry (DTG) & Differential Thermal Analysis (DTA) is a Seiko I SSC/5200 TG/DTA 220 by Seiko Instruments Inc. This instrument uses a highly sensitive cantilever-beam-balance system to measure mass change between the sample and the reference and thus enables the equipment to function as both TGA and DTA simultaneously. All samples were tested under 20-30 ml/min of nitrogen flow.

Aluminum sample pans were used for this experiment. Each test required 20-25 mg of crushed, cured sample, having average particle size of 50  $\mu\text{m}$  approximately.

### 4.2.3 Mechanical Properties

Compression strength was measured using an Applied Test Systems, Inc screw driven load frame. The tests were performed by placing cylindrical samples in an aluminum compression cage, as shown in Figure 4.3. Nominal specimen length and diameter were 17 mm and 6 mm, respectively. The crosshead loading rate was 0.5 mm/min until the failure load was attained. Compression strength was calculated using the following equation;

$$\sigma_c = \frac{F_b}{A} \quad (12)$$

Where,  $F_b$  is the ultimate breaking load due to compression and  $A$  is the initial cross-sectional area of the sample. The elastic modulus was calculated from the load-displacement data using the following equation,

$$E = \left(\frac{F}{l}\right) \times \left(\frac{L}{A}\right) \quad (13)$$

Where,  $E$  is the elastic modulus,  $\frac{F}{l}$  is the slope of the load-displacement plot in lbf/in,  $L$  is the gage length of the extensometer and  $A$  is cross-sectional area of the specimen. Calculation of the elastic modulus required finding the load-displacement relationships. Displacement measurement was performed using a clip gauge extensometer with a gauge length of 25.4 mm and travel of 7.62 mm (30%). A maximum load of 40% of the failure load was applied during the modulus measurement in order to stay in the elastic range and avoid damage to the extensometer. For modulus testing, additional specimens were prepared of greater size to allow attachment of the

clip gage extensometer. The length of these modulus samples was 33 mm and, in order to maintain the same aspect ratio as that of the compressive strength test specimens, the diameter was increased to 11.65 mm. Both strength and modulus measurement followed ASTM C 1424<sup>94</sup>. A typical setup of the load-displacement measurement, including the clip gage extensometer, can be seen in Figure 4.3.

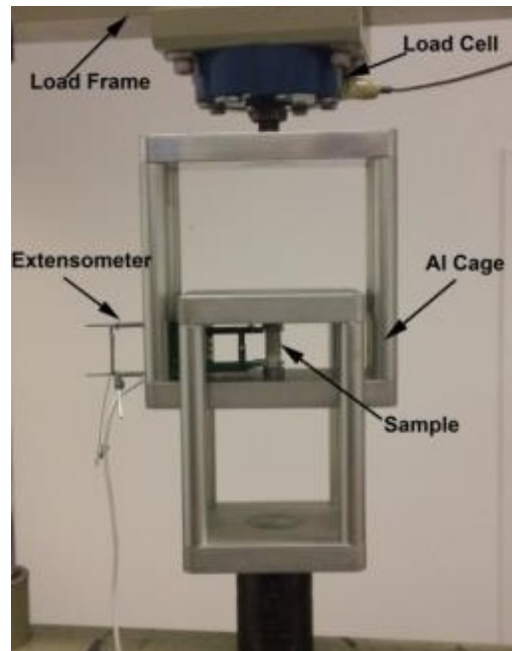


Figure 4.3. Experimental set up of load-displacement measurement with extensometer.

Failure load and load-displacement data were collected using computer data acquisition. Typically, five specimens were tested for each set of process conditions to calculate average compressive strength and modulus.

#### 4.2.4 Evaluation of Porosities and Voids

Due to rise in stress concentration, voids in the cured specimens are considered as detrimental to any mechanical performance of MEYEB. In order to investigate the voids formation, the external and fracture surfaces of both neat MEYEB specimens were observed using a stereo binocular microscope with a fiber optical light source as direct illumination. Measurement of open porosities is an effective tool for understanding the level of consolidation of the material. Apparent open porosity of the specimen is measured in terms of water absorption, which was performed by measuring the weight difference (in air) of completely dry specimens (heated at 150 °C) before and after submerging into water. The procedure is described in ASTM standard C-20-2010<sup>95</sup>. The following formula was used to measure the porosity of the samples

$$P (\%) = [1 - ((WD - WS) / \rho_w) / VT] \times 100 \quad (14)$$

Where, WD, dry mass of the specimen (g), WS is submerged mass of the specimen (g) and  $\rho_w$  is the density of water ( $\text{g}/\text{cm}^3$ ). The weight of the completely submerged specimen (WS) is measured using Archimedes principle<sup>96</sup> which can be presented using the assembly shown in Figure 4.4. Apparent porosities were also verified using a method described by Felipe Montes et al<sup>97</sup>.



Figure 4.4. Method for weighing sample submerged in water<sup>96</sup>

#### **4.2.5 Microstructural Analysis**

Micro structural analysis was performed using JEOL JSM-6500 Field emission scanning electron microscope (FESEM). Fracture surfaces of MEYEB specimens were coated in gold (10 nm thick) using a Hummer VII ion beam sputter coater to enable imaging. To obtain high-resolution images (less than 1  $\mu\text{m}$ ), a beam energy of 15 KV was applied on the samples (around 2 mm thick) inside the vacuum chamber which was maintained at  $9.63\text{E-}5$  Torr.

#### **4.3 Preliminary Results-Processing Evaluation**

The preliminary processing studies indicated the importance of controlling the process parameters. The results from the preliminary studies suggest how effectively a neat specimen can be prepared by controlling the parameters of curing and post processing so that the knowledge of processing can be applied to fabricate nano-reinforced specimens to state the hypothesis.

### 4.3.1 Effect of Cure Time on Shrinkage and Compression Strength

As described in the previous sections, the first series of tests involved evaluation of specimens immediately after the cure in a sealed environment, and before any process drying or postcure was initiated. A qualitative presence of liquid was monitored on the as-cured sample surface. Two of the as-cured samples are shown in Figure 4.5. Liquid droplets are observed on the surface of the sample cured for 1 hour (Figure 4.5(a)) while no liquid was present on the surface of the sample cured for 24 hours (Figure 4.5(b)). This suggests that the cure (the polycondensation reaction) was not complete after 1 hour, but was complete by 24 hours.

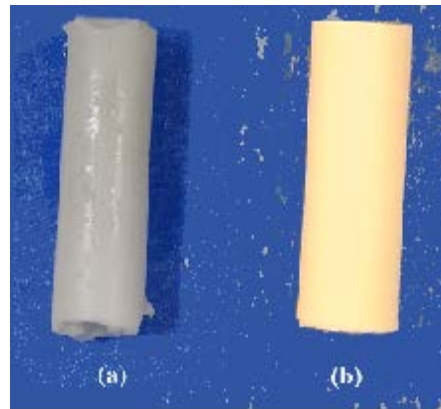


Figure 4.5. Samples cured in a sealed environment at 80°C for (a) 1 hr (b) 24 hr

Figure 4.6 and Figure 4.7 show the results of shrinkage measurement and compression strength testing for this first series of specimens processed at 80 °C, and only to the end of the initial cure in a sealed environment. While the cure shrinkage of 6.3% is low for the 1 hour cure, the corresponding compression strength, 26 MPa, is also low. These properties, along with the damp specimen surface and the observed soft nature of the material are consistent with an incomplete cure, indicating that this duration of the process needs to be extended. As the dwell time at 80 °C is increased to 5 hours, the shrinkage increases to 10.5%, with a corresponding increase in



compression strength to 55 MPa. The specimen surface at 5 hours is dry. These results suggest that the cure is essentially complete by 5 hours. However, increase in the dwell time at 80 °C in the sealed environment results in further changes in shrinkage and compression strength.

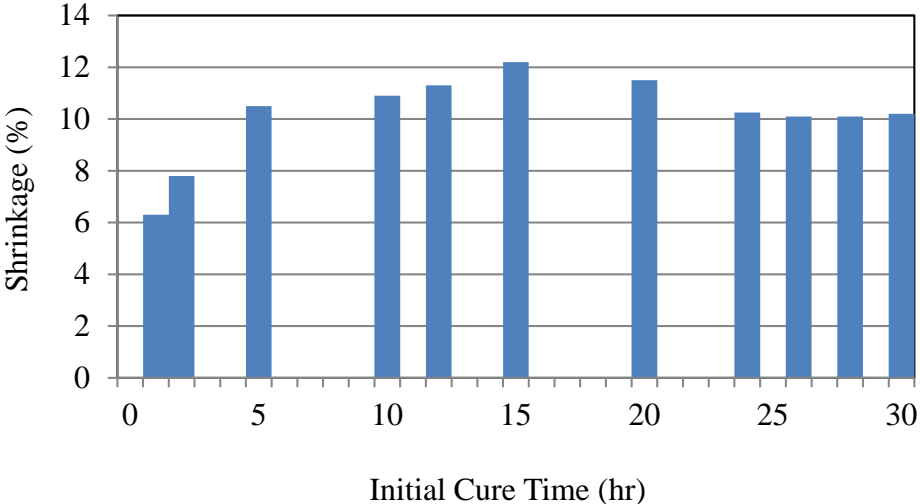


Figure 4.6. Average linear shrinkage after initial cure at various times

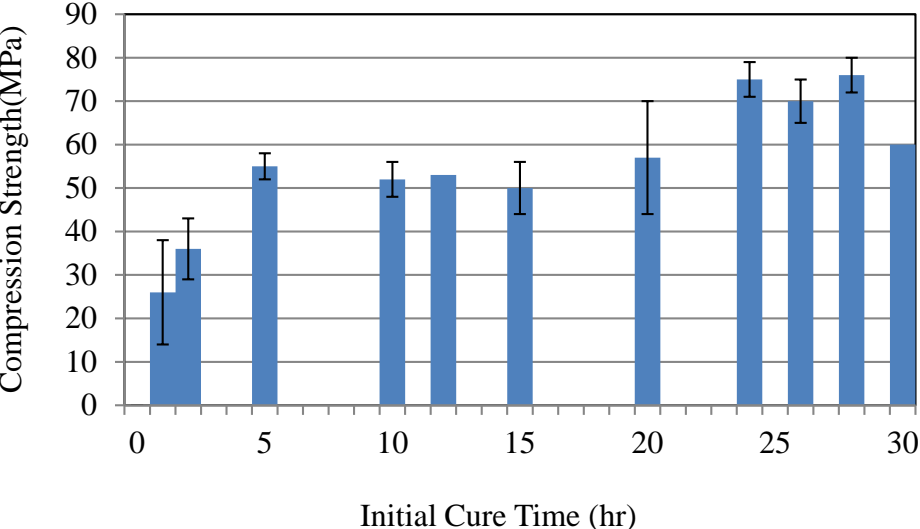


Figure 4.7. Compressive strength after cure in a sealed environment

The shrinkage increases to a maximum of 12.1% after 15 hours and then begins to drop, falling to a value of approximately 10.1%, after 24 - 26 hours. The corresponding compression strength values show a different trend, remaining statistically unchanged from 5 hours to 15 hours, and then increasing to a maximum of approximately 75 MPa by 24 – 26 hours. Again, the results of the 24 hour cure suggest that most of the potassium hydroxide (KOH) molecules have been used up in the poly-condensation reaction<sup>12</sup>. Thus, from this investigation, it can be summarized that, given enough time for initial cure, the cure shrinkage can be reduced and compressive strength increased. In addition, a 24 hour initial cure would be an important criterion in preparing fiber reinforced MEYEB composites with lower cure shrinkage and potentially higher mechanical performance. However, to fully understand the relationship between process-induced shrinkage and mechanical properties, specimens must be evaluated after a full cure, including the drying and postcure stages.

#### ***4.3.2 Effects of Drying and Postcure on the Shrinkage***

The results of the previous section clearly suggest that a 24 hour isothermal cure, at 80 °C, in a sealed environment is the preferred initial cure condition; however, this significantly extends the overall processing time. Rather than investigating the subsequent drying and postcure process parameters based solely on a 24 hour initial cure, it was decided to also include specimens, in this second series of tests, which are based on a 10 hour isothermal cure, as well as the baseline case, A1, which had only a 2 hour isothermal cure. 10 hour cure was chosen for this alternative initial cure time rather than 5 hours, to ensure a high degree of cure completion, but in retrospect, it seems that, in the future, it would also be of interest to evaluate specimens starting with an initial 5 hour isothermal cure at 80 °C, in the sealed environment.

Cure shrinkages of this second series of specimens (A1 through B3) were measured in the TMA. The results are presented in Figure 4.8, Figure 4.9 and Figure 4.10. Figure 4.8 and Figure 4.9 show the TMA measured shrinkages corresponding to each step of the drying and postcure processes. In each figure, (a) shows the heating profile with time and (b) is the corresponding length change, the negative sign indicating shrinkage. Figure 4.8 compares the shrinkages of the baseline, 2 hour isothermal cure, process schedule A1, to the 10 hour isothermal cure specimens, A2 – A6. While there is a variation in the shrinkage of the 10 hour cure specimens, the range is only from 2.6 to 3.4%, compared to the 5.1% linear shrinkage of the baseline, 2 hour isothermal cure, case. In comparing specimens A1 and A2, which both have relatively short postcure schedules (but much different isothermal cure times) the drying and postcure shrinkage is much smaller for the 10 hour isothermal cure, case A2, than for the baseline, A1, with only a 2 hour cure.

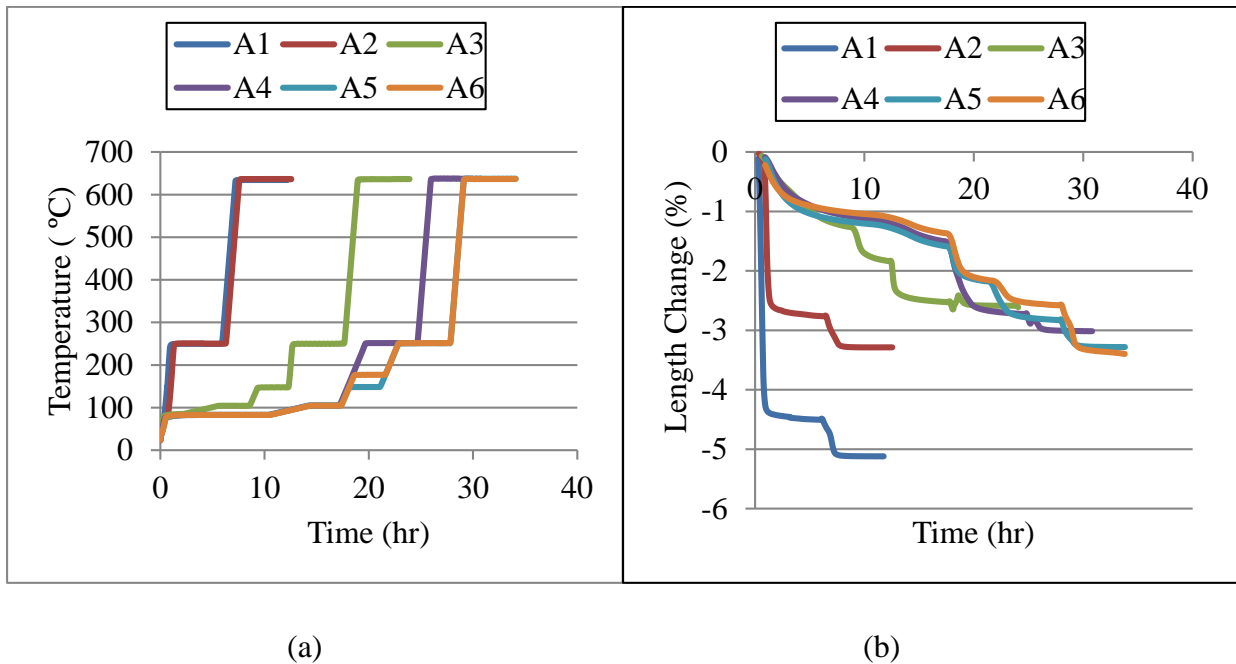
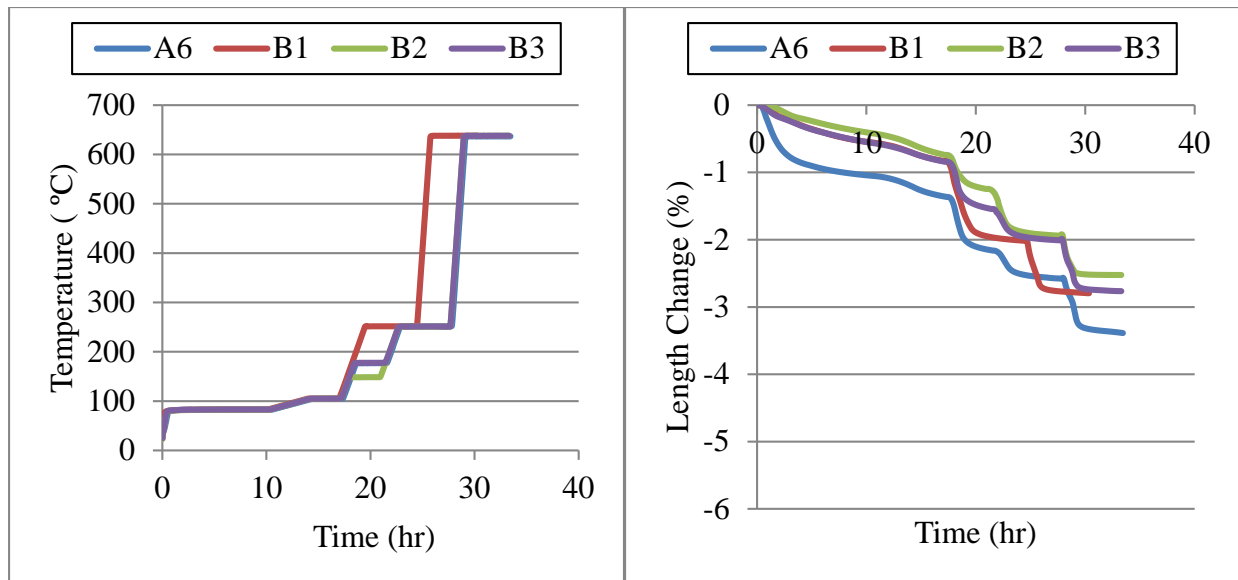


Figure 4.8. 2hr and 10hr cures followed by drying and postcure, (a) Temperature profile, and (b) Linear cure shrinkage



(a)

(b)

Figure 4.9. 24hr initial cures, drying & postcure, (a) Temperature profile (b) Linear cure shrinkage

Figure 4.9 compares the three cases that were cured for 24 hours, at 80 °C, in a sealed environment. There is little difference in shrinkage between the three cases, at each temperature increment. The final shrinkages have a narrow range of values, from 2.5 to 2.8%, suggesting that with the 24 hour cure, the specimen shrinkages are less sensitive to the drying and postcure schedules. Comparing results from cases B3 and A6, which have identical drying and postcure schedules, but differ in isothermal cure time in a sealed environment, it is noted that A6 has a larger final shrinkage of 3.4% vs. 2.75% for B3. However, it is interesting to note that essentially all of this difference in shrinkage occurs during the initial 10 hour drying at 80°C. After that, the increments of shrinkage with temperature are very similar. It is also important to realize, from Figure 4.8& Figure 4.9 that the majority of shrinkage occurs during the transitions between the processing temperatures, with little shrinkage developing during the extended temperature dwells for drying and postcure.

While Figure 4.8 and Figure 4.9 aid in understanding how the shrinkage accumulates with each step in the drying and postcure schedule, it is more convenient to compare the final shrinkages as displayed in Figure 4.10. Figure 4.10(a) clearly illustrates the effect of the various drying and postcure schedules on the linear shrinkage, showing the slightly lower shrinkages corresponding to the specimens isothermally cured in a sealed environment for 24 hours. Also obvious is the much higher drying and postcure induced shrinkage for the baseline case, with only the 2 hour isothermal cure.

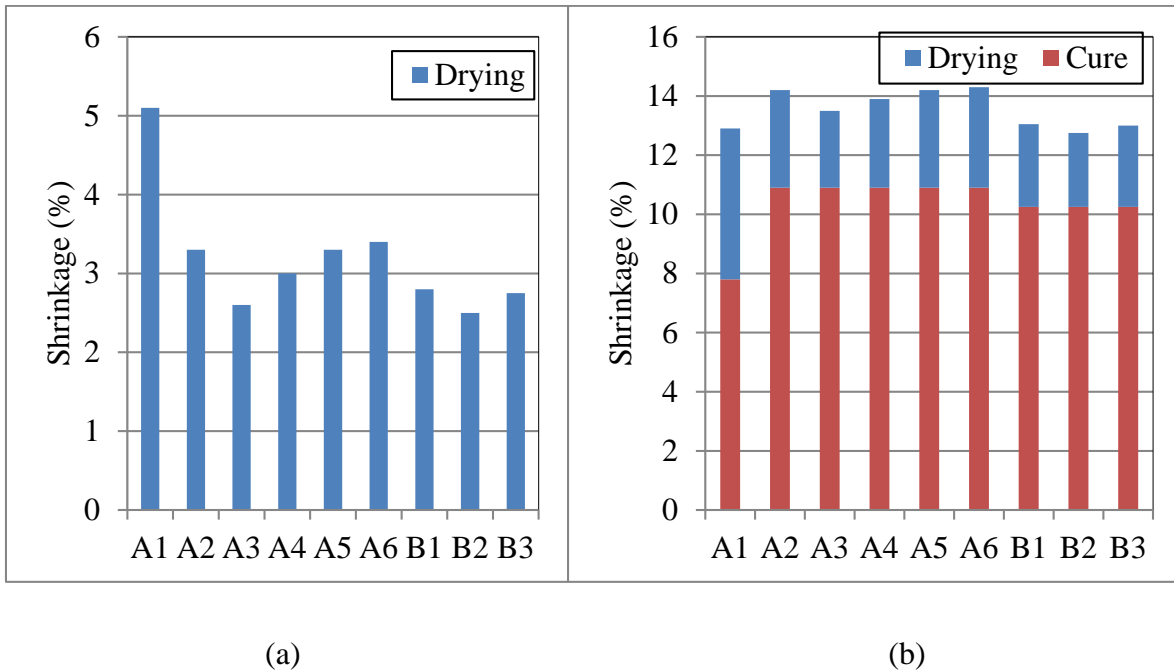


Figure 4.10. Cure shrinkage summary (a) Drying and post-cure component, (b) Total shrinkage

Figure 4.10(b) combines the results of the 80°C isothermal cure shrinkage (Figure 4.6) with the results of drying and postcure (Figure 4.10(a)) to allow comparison of the overall process-induced shrinkage. The overall process-induced shrinkage varies from 12.75 to 14.3%, with the

specimens cured in a sealed environment for 10 hours showing the highest overall shrinkages. The overall shrinkages of the specimens that were isothermally cured for 24 hours are clearly lower, but interestingly enough, so is the overall shrinkage of the baseline case, cured in a sealed environment for only 2 hours. The overall process duration for the baseline case, A1, is only 12 hours, compared to 50 hours for case B2, which had only a marginally lower total process-induced shrinkage. However, before assuming that there is no advantage to the extended process schedule, the corresponding mechanical performance of the various cases must be discussed.

### ***4.3.3 Mechanical Properties***

In attempting to address process-induced cracking of the neat MEYEB material, it is important to not only focus on the shrinkage, but also to better understand the corresponding changes in mechanical properties. In Figure 4.7, the compression strengths of the as-cured specimens were compared, clearly showing that extended cure times, in a sealed environment, resulted in higher mechanical performance. For the fully processed specimens it is also important to consider the effect of drying and postcure schedules on the mechanical properties. The primary comparison of mechanical properties again involves the compression strength, but data is also presented showing the evolution of the elastic modulus related to the degree of drying and postcure.

### ***4.3.4 Compression Strength Related to Process Schedule***

Compression strength of dried and postcured specimens is summarized in Figure 4.11. The as-cured strength, immediately after the 24 hour cure in a sealed environment, is shown in Figure 4.11 for reference. It is important to note that the dried and postcured compression strengths are substantially higher than those of the 24 hour as-cured specimens. Further, while few repetitions were performed, the associated differences in compression strength are statistically significant as

displayed by comparing the error bars. The compression strength increase due to drying and postcure is significant in magnitude as well, increasing from an average of 75 MPa for the 24 hour as-cured specimens to an average of 129 MPa for specimens processed with the B2 process schedule. Further, comparison of the compression strengths of specimen A1 to the average of specimens B2 shows an increase from 92 MPa to 129 MPa. This is an increase in strength of over 30%, while maintaining a statistically equal, and low, value of shrinkage. Thus, while a variety of process schedules seem to give similar values of process-induced shrinkage, as low as 12.75%, the compression strength clearly increases with increased intermediate temperature drying steps, such as schedule B2.

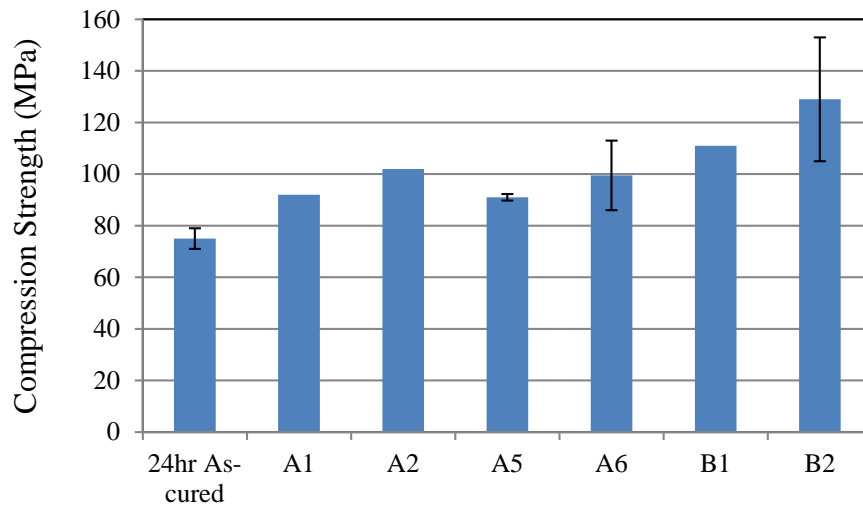


Figure 4.11. Compression strength comparison for the various process schedules

#### 4.3.5 Elastic Modulus Evaluation

Load-displacement profiles representative of as-cured specimens and of specimens postcured to 650°C are plotted in Figure 4.12. Using equation (5), the average modulus of the 80°C, as-cured, specimens was found as 12.43 GPa with a standard deviation of 0.64 GPa, while the average

modulus for the specimens postcured to 650°C was 20.63 GPa with a standard deviation of 4.9 GPa. This represents an elastic modulus increase of approximately 60%. This increase in the measured elastic modulus supports the argument of increasing crosslink density and dehydroxylation at higher temperature, as the elastic modulus is expected to be directly related to the interatomic bond strength and, therefore, to the degree of cure.

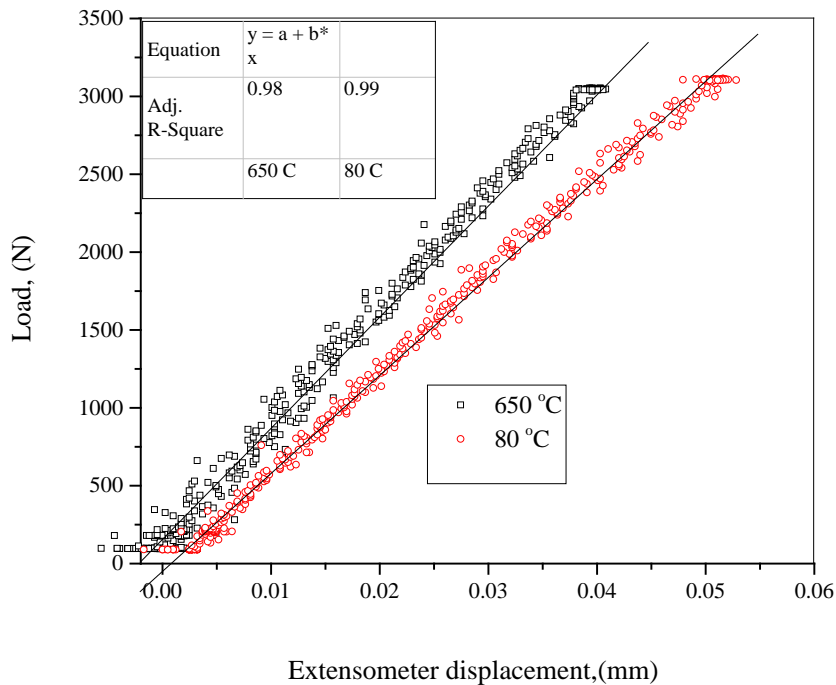


Figure 4.12. Clip gage displacement vs. load cell response during compression test.

#### 4.4 Conclusion

Combining the information gained from the measurements of the process-induced shrinkage and the mechanical properties, the results indicate that an extended 80 °C isothermal cure in a sealed environment, followed by a slow, stepwise drying process results in the best balance of cure shrinkage and mechanical properties. This combination is predicted to be the most resistant to



residual stress induced cracking as the matrix of a fiber reinforced inorganic polymer composite. Further, it is now clear that cracking of neat MEYEB inorganic polymer resin specimens, produced in earlier laboratory trials, was related to insufficient time in a humidity-sealed environment, leading to premature drying and incomplete poly-condensation. This realization has allowed the measurement of many neat resin properties necessary to better understand and predict the performance of the corresponding nanomaterials and fiber reinforced composites.

## 5 EVALUATION OF PROCESSED GEOPOLYMER

The goal of this study is to correlate the processing results with the changes in the inherent microscopic porosities and microstructure. To perform this study, baseline properties of MEYEB was measured at extended treatment temperature in both oxidative and inert environment. Both process related shrinkage and mechanical strength is suggested to have strong correlation with the microstructure. Thus, the current study was initiated to investigate the effects of varying the processing conditions, understanding the physical states of the materials determining suitable parameters to successfully produce neat inorganic polymer matrix specimens to gain an improved understanding the performance of the fiber reinforced geopolymer composites.

In order to evaluate the inherent mechanism on the morphological transformation associated with the corresponding shrinkage and mechanical properties of the matrix, the assessments of the apparent density and microstructure have been conducted with the variations in the process schedules that have been described in Table 4.1. Thermo-gravimetry and differential thermal analysis (DTA) have been undertaken with the aim of understanding the effect of chemical reactions on the thermodynamic stability at each stage of processing, which is related to process induced shrinkage and mechanical performance of the matrix materials. Thermal expansions have been investigated for the fully cured specimens at each process schedule elaborated in previous chapter (Chapter 4). Process induced shrinkage and thermal expansion of the processed geopolymer are key parameters that control the degree of thermal mismatch in the actual fiber reinforced geopolymer composites.

## **5.1 Specimen Preparation**

Thermal expansions of neat specimens were measured using cylindrical samples. The cylindrical sample preparation technique was described in earlier section. Flexure strength, fracture toughness and flexure modulus performed on neat samples treated at various temperature and environment. This test was performed on the specimens with rectangular cross sections. These specimens were prepared using liquid MEYEB poured in a plastic mold, which is designed according to the standard for notched fracture toughness<sup>98</sup> and un-notched flexure strength<sup>99</sup> test.

## **5.2 Mold Design for Non-Cylindrical Specimens**

The mold was designed to prepare enough solid MEYEB specimens using the liquid MEYEB with the dimensions specified for performing SEVNB test according to ASTM 1421-10 standard<sup>98</sup>. The design requires the selection of the compatible materials and ability to process liquid MEYEB in a sealed environment. Acetal copolymer was chosen as the mold material for curing the MEYEB specimens. This material was collected from Fort Collins Plastics Inc. In the liquid state, MEYEB is likely to react with various metals including aluminum, zinc and tin evolving hydrogen gas. Therefore, in order to cure this reactive polymer blend metallic mold is not a suitable medium. Alternatively MEYEB is not reactive with plastic materials. Among many plastic materials of choice, the one with high melting point and high glass transition temperature with reasonably low thermal expansion was a suitable choice for making this mold. Semi-crystalline Acetal plastic has these desirable properties. High chemical resistance of this plastic is also a desirable property. Some of the useful properties of this plastic are listed in Appendix A5.

The plastic mold was created in two parts. A 140x70x12.7 mm (5.5 x2.75x0.5 inch) acetal copolymer plastic block was used to make one part of the mold, which is shown in Figure 5.1. The other part was prepared with 8 separate slots each at 5x5.5x45 mm (0.196x0.216x1.77 inch) in dimensions. A rectangular slot with the dimension of 1.50x1.35 mm was machined around the periphery of each specimen slot, which was fitted with O-ring in order to prevent the specimen from entering air during the poly-condensation. The purpose of O-ring was also to prevent any spillage of liquid MEYEB out of the mold. The O-rings were prepared using silicone O-ring cord stock joining together using silicone adhesive. The other half of the mold is the flat Acetal block which is machined for 9 holes to tie with the slotted part using tie rods.



Figure 5.1. Molds for SEVNB specimens prepared using Acetal plastic

In order to prevent any buckling in the molds two aluminum backing plates were used on the opposite side of the mold stack, which is shown in Figure 5.2. The dimensions of the mold in assembled condition are shown in Figure 5.3 and Figure 5.4.

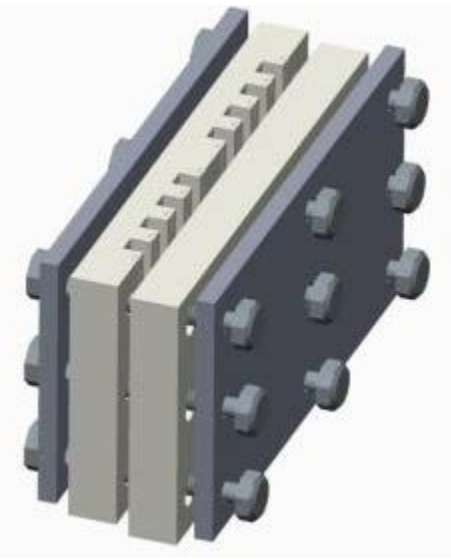


Figure 5.2. Mold assembly for initial curing of MEYEB in vertical orientation.

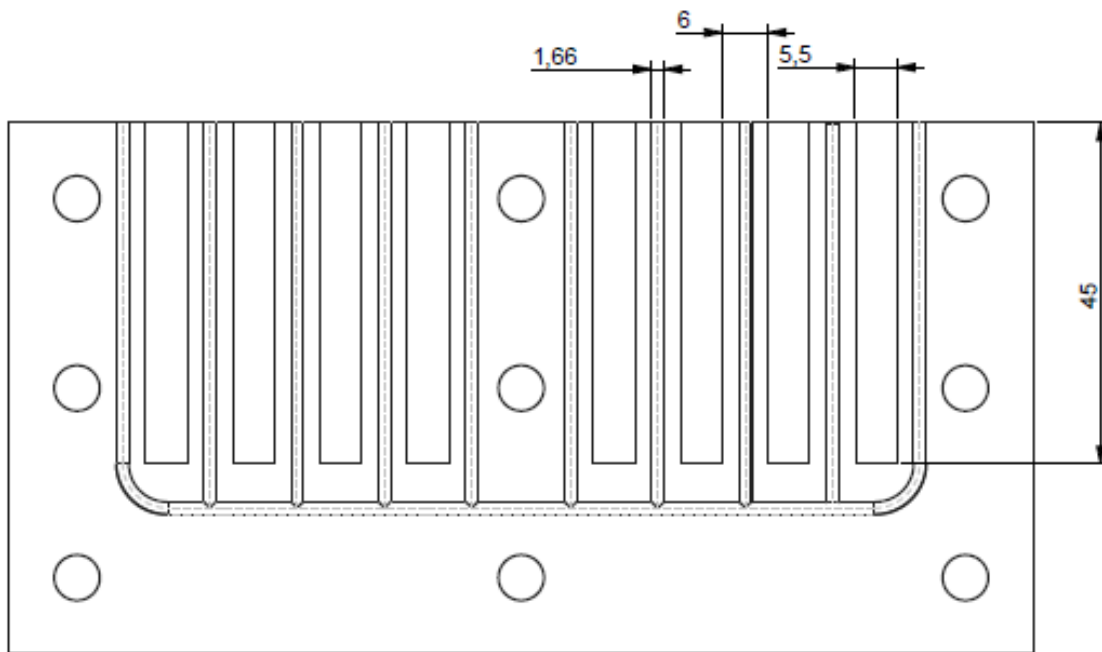


Figure 5.3. Slots for the samples in the mold and their dimensions (In millimeter).



Figure 5.4. Assembly of a mold with rectangular slots for curing MEYEB in vertical orientation.

### **5.3 Sample Degasification**

The degasification process is performed in a desiccator attached to a vacuum pump, which is shown in Figure 5.5. Degasification of liquid MEYEB is an important step of sample preparation. This step is performed to ensure the removal of entrapped air bubbles. Due to the rapid increase in viscosity at ambient temperature, it is difficult to perform the degasification of the entrapped bubbles in the nano-reinforced MEYEB. Therefore, during the degasification it is necessary to keep the ambient temperature as low as possible. In order to keep the MEYEB temperature low, the desiccator was placed on an ice bath as shown in Figure 5.5. Even though the degasification was performed on the ice bath, additional cooling was ensured by storing MEYEB during the intermediate period of degasification.

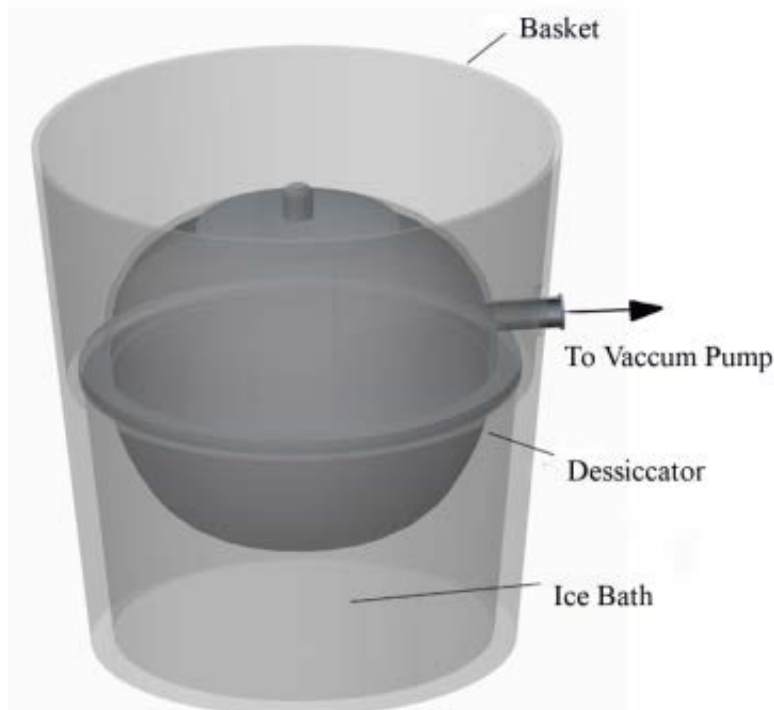


Figure 5.5. Sample degassing in a cold environment.

The effectiveness of the degasification process depends on many factors, of which two factors are important. One is the viscosity of the working liquid, which determines the amount of vacuum requirement for the degasification process. Normally for the degasification of a liquid with the viscosity close to the viscosity of water, the vacuum requirement is the half the atmospheric pressure at room temperature. Another important factor is the vapor pressure of the liquid which determines the maximum allowable vacuum during degasification without the evaporation of the liquid. Since MEYEB is water based polymer, its vapor pressure is assumed to be identical to that of water, which is around 31.74 Torr at 30 °C.

#### 5.4 Preparation of the Specimen

A typical assembly of the mold is presented in Figure 5.6. Once significant amount of the bubbles were removed the liquid MEYEB was ready to pour into the rectangular slot of the plastic mold. The amount of liquid MEYEB required to make one neat sample is approximately 2 gm. With the mold placing in vertical position (see Figure 5.4) half of the required liquid MEYEB was first poured into each slot. Then the mold was stored in the freezer. After freezing for two minutes, the rest of MEYEB was poured to fill each slot of the mold. The mold filled with MEYEB was then evacuated under vacuum to ensure the removal of the entrapped bubbles in the slot and liquid MEYEB. To ensure moisture retention, the molds were then sealed in polyethylene (PE) bagging. Atmospheric pressure was maintained inside the bagging. The complete assembly was then placed in the oven for initial cure. To perform the initial cure the oven was heated from 40 °C to 80 °C at 1c/min and then hold at 80 °C for 24 hours. After the initial cure was performed, the mold was allowed to cool before removing the samples. The required drying and post processing was performed by following the optimum processing schedule as described in the preliminary processing evaluation, which was schedule B2 (see Table 4.1). Five samples were prepared for testing samples treated at each type of combination of temperature and environment as mentioned in Table 5.1. The samples were treated at each combination for 5 hours. It is worth mentioning that the maximum processing and treatment temperature of the samples for each batch was limited by the temperature specified in Table 5.1, not by the maximum processing temperature as specified in schedule B2.





Figure 5.6 Assembly of the Mold with MEYEB in a sealed PE bagging.

Table 5.1 Mechanical tests performed on the neat MEYEB samples

Test Type	Temperature (°C ) and Environment					
	250	350	650		760	
	O <sub>2</sub>	O <sub>2</sub>	O <sub>2</sub>	N <sub>2</sub>	O <sub>2</sub>	N <sub>2</sub>
Un-notched Beam Flexure Test	✓		✓	✓	✓	✓
Notch Beam Fracture Test	✓	✓	✓	✓	✓	✓

The technique for the preparation of un-notched beam flexure test included minor grinding the surfaces of the samples to maintain the flatness. For preparing the SEVNB fracture test samples, an additional notch was made on the surface that is subjected under tensile loading. SEVNB

technique provides very reproducible results, however accurate measurement of fracture toughness using this technique requires a specimen preparation with close tolerance, parallel notch walls and very narrow notch tip with the diameter as close as the particle or grain sizes of the materials. The notch preparation station is shown in Figure 5.7. Fracture toughness measurement using this technique requires V-notches to be made on the surface of the specimens which is subjected to tension in 3-point bend beam test. At first, a 375-400  $\mu\text{m}$  wide notch was made using a diamond wafer blade and a notch preparation station.

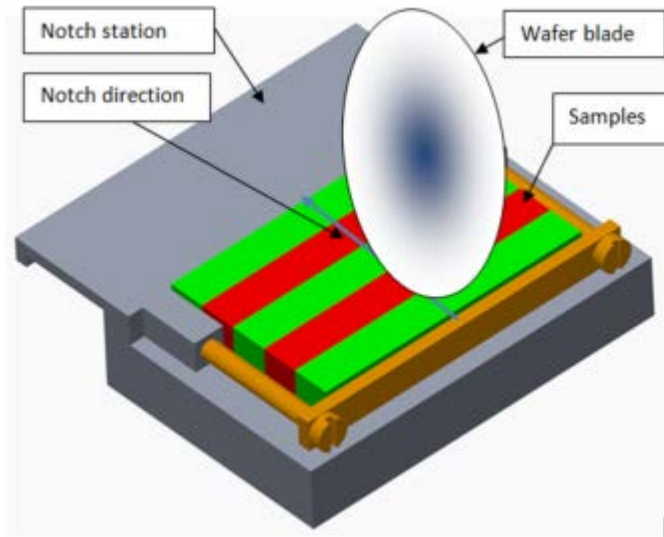


Figure 5.7. Notch preparations on the sample surface using a notch preparation station

The tip of notch was then sharpened using a 250  $\mu\text{m}$  thick razor blade sprinkled with diamond particle (7  $\mu\text{m}$ ) suspension. The suspension was first sprinkled on the blade to ensure the flow of diamond particles on the tip of the blade. In order to make the notch tip straight a fixture was used which is shown in Figure 5.8. The notched specimen was then heated to 170  $^{\circ}\text{C}$  in order to remove the suspension liquid and post heated at 650  $^{\circ}\text{C}$  for five hours to perform the remaining

3<sup>rd</sup> or de-hydroxylation stages of post processing as well as to eliminate the local residual stresses developed from the plastic deformation of the material due to the notch <sup>75</sup>.

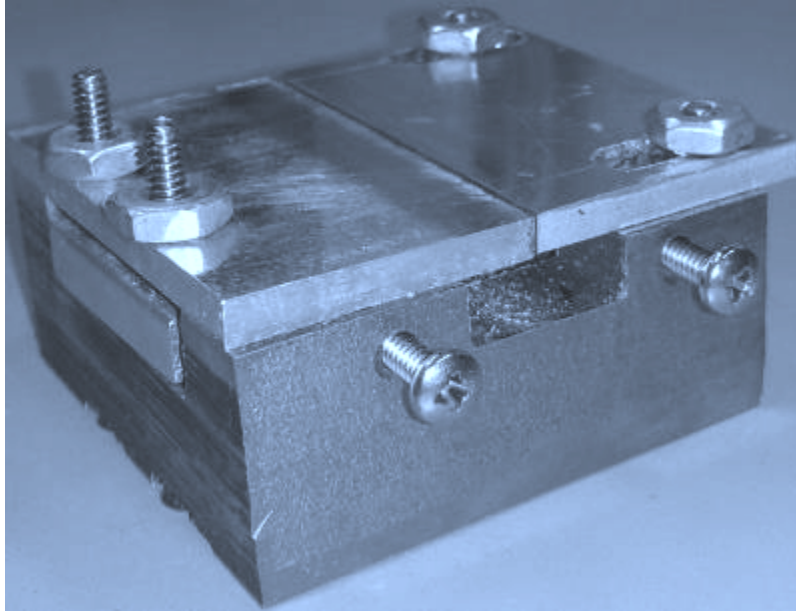


Figure 5.8. Fixture for the sharpening of the notch tip.

Notch was prepared on the tensile surface of the specimens with rectangular section. The microscope images of notch with unsharpened and sharpened tips are shown in Figure 5.9. It is found that the diameter of sharpened notch tip is less than 20  $\mu\text{m}$ . A tighter notch tip is a requirement for the SEVNB fracture toughness test. The current notch preparing technique is therefore expected to produce fracture toughness results with better accuracy and reproducibility.

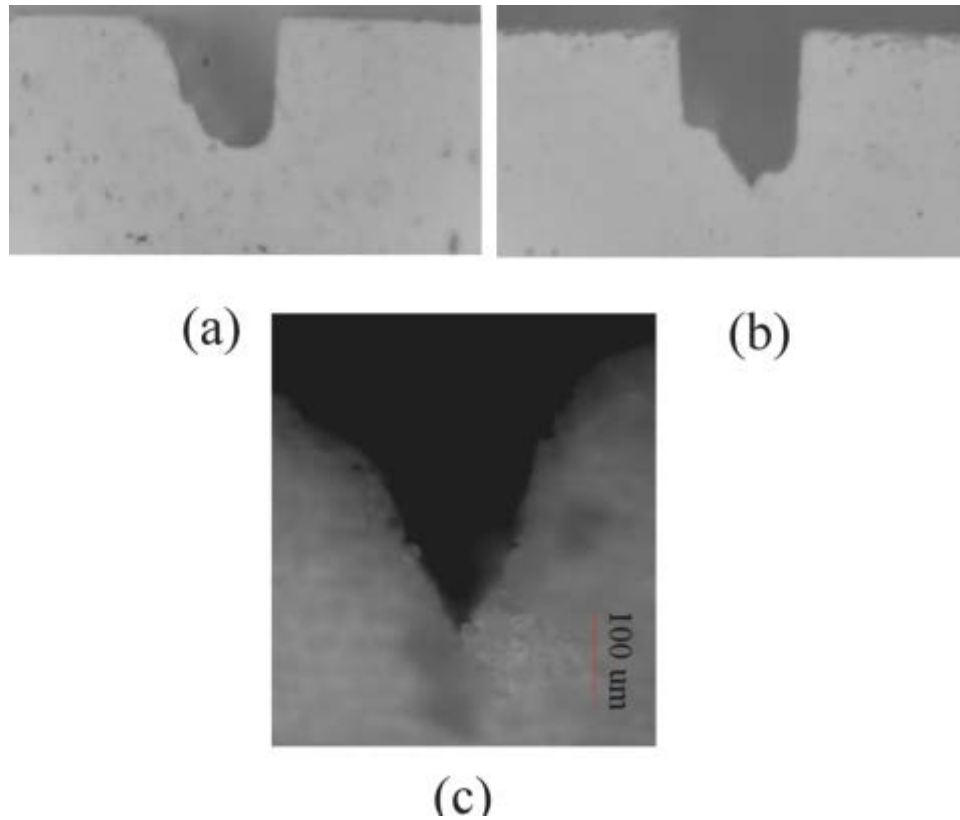


Figure 5.9. (a) Notch formation with diamond wafer blade and (b and c) notch tip sharpened using razor blade (250  $\mu\text{m}$  thick) sprinkled with diamond paste (7  $\mu\text{m}$ ).

### 5.5 Characterization Technique

Characterization of neat specimens involved notched and un-notched bend beam test. These test techniques were developed essentially to measure the effect of processing temperature and high temperature treatment on the flexure strength, toughness and modulus of neat MEYEB. The un-notched beam flexure test was also performed to verify the notched fracture toughness results.

### **5.5.1 Un-notched Bend Beam Test**

Following equation was used to perform un-notched bend beam test

$$S_b = \frac{3FL}{2bw^2} \quad (15)$$

Where,  $S_b$ =Flexural strength,  $F$ = breaking load,  $L$ =span length,  $b$ =specimen width,  $w$ =specimen depth. In order to validate the fracture toughness results the beam depth and width in both tests were kept constant.

### **5.5.2 Notched Bend Beam Test**

The expectation from the SEVNB test is to accurately measure the fracture toughness with direct loading on the pre-notched bend beam specimen. The geometry of the specimens is specified to measure fracture toughness using three point bend testing technique described in ASTM C1421-10<sup>98</sup>.

According the SEVNB technique, the fracture toughness is calculated from the fracture forces, test specimen size and measurement of the notch size. Fracture toughness testing was performed using Instron C1102 on a 3 point bend fixture with a span length  $S_0=30$  mm and test speed of 0.5 mm/min, under ASTM C1421-10<sup>98</sup>. The dimension of the overall notched specimen is presented in Figure 5.10.

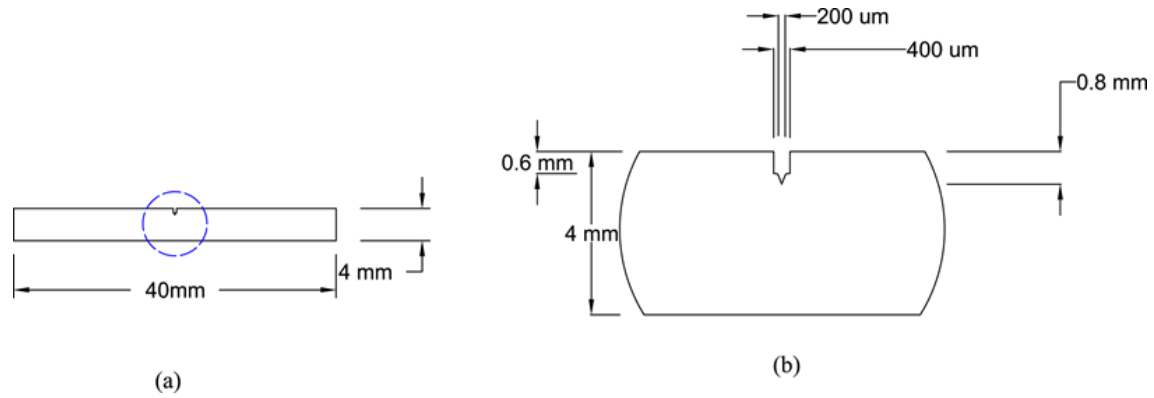


Figure 5.10. Notch geometry on a 30 mm span bend beam specimen (a) Overall view and (b) Expanded view of the notch in (a).

The fracture toughness was calculated, using the following equation:

$$K_{pb} = g \left[ \frac{P_{max} S_0 10^{-6}}{b w^{1.5}} \right] \left[ \frac{3[a/w]^{0.5}}{2[1-a/w]^{1.5}} \right] \quad (16)$$

Where,

$P_{max}$  = Maximum force, N

$S_0$  = Span length

$a$  = Notch length

$b$  = Width of the specimen

$w$  = Depth of the specimen

$$g = g(a/w) = A_0 + A_1 (a/w) + A_2 (a/w)^2 + A_3 (a/w)^3 + A_4 (a/w)^4 + A_5 (a/w)^5$$

The values of the polynomial,  $g(a/w)$  depends on the span to width ratio. The coefficients of the polynomial are suggested in the ASTM standard<sup>98</sup>. These are again shown here in Table 5.2.

Here, it is important to understand that, the values of the coefficients vary with the ratio of the span length-to-depth ( $S_0/W$ ) of the specimen. Therefore, this ratio for all the specimens is required to maintain within a consistent range. This ratio was maintained between 6 and 7.

Table 5.2. Coefficients for the Polynomial  $g(a/w)$  for Three-point Flexure

Coefficients	S <sub>0</sub> /W	
	6	7
A <sub>0</sub>	1.923	1.9322
A <sub>1</sub>	-5.1389	-5.1007
A <sub>2</sub>	12.6194	12.3621
A <sub>3</sub>	-19.551	-19.0071
A <sub>4</sub>	15.9841	15.4677
A <sub>5</sub>	-5.1736	-4.9913

According to ASTM standards 1421-10, the recommended notch depth to width ratio be  $0.3 < a/w < 0.5$ , however from the article by VAMAS round robin<sup>100</sup> it is found that with the small  $a/w$  and a range of  $a/w$  from 0.1 to 0.5 there was no significant influence of the notch depth on the fracture toughness of sintered silicon nitride ceramic. A typical dimension of the specimen for SEVNB test is shown in Table 5.3. The notch tip radius was sharpened to approximately 20  $\mu\text{m}$  and overall depth to notch ( $a/w$ ) ratio was cut to  $\sim 0.2$ . The actual depth of each notch was carefully measured for each sample and accurate  $a/w$  values were recorded. At least five specimens were tested for each type of sample.

Table 5.3. Typical dimensions of the specimen prepared for the SEVNB test

Dimension( $w \times d \times L$ )	Notch width (mm)	a/w	$S_0$ (mm)	$S_0/w$
$5 \times 4.5 \times 45$	0.3	0.15-0.2	30	6.6

L=Sample total length

### 5.5.3 Variations in the Sample Geometry

Neat MEYEB samples as prepared for compression and flexural strength tests are presented in Figure 5.11. Cylindrical specimens were prepared to measure compression strength and evaluate thermal expansion related properties. Rectangular specimens were prepared to measure flexural modulus. The dimensions of the samples are presented in Table 5.4.

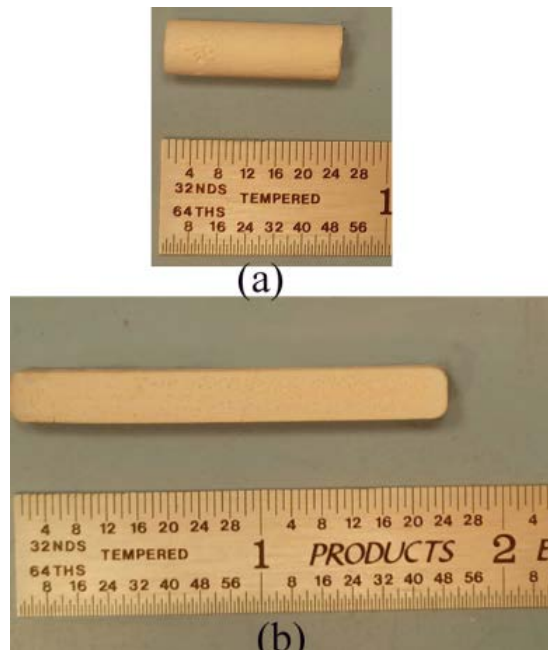


Figure 5.11. Neat MEYEB samples for (a) compression strength and (b) flexural strength measurement



Table 5.4. Dimensions of the compression and flexure test specimens

Specimen Type	Length, mm	Diameter, mm	Depth, mm	Width, mm
Cylindrical	19	6	-	-
Rectangular	45	-	4.5	5

#### 5.5.4 Flexural Modulus Measurement

In conjunction with compressive modulus it is necessary to measure flexure modulus of neat MEYEB. Compressive modulus was calculated using the actual linear deformation of the sample measured using the clip gauge. The technique on measuring the compressive modulus was described earlier (See Chapter 4). The scope of the current study is to measure the flexure modulus.

Modulus measurement requires the elastic deformation of the specimen. When this deformation cannot be measured using a strain gage, it is usually measured using the cross head displacement<sup>101</sup>. The Measurement using the cross head displacement is normally calibrated by accounting the machine compliance,  $C_m$ . In order to measure  $C_m$ , the flexure test can be performed on a stiff metallic sample with known modulus. A three point flexure test was performed by applying loads from 0-65 lb (0-290 N) where the machine cross head displacement was calculated using the cross head displacement rate ( $\delta$ ). Ideal load carrying capacity of the known sample,  $A_I$  for this investigation at the cross head displacement ( $\delta$ ) was calculated using the following equation-

$$F_{Al} = \left( 4 * b * d^3 * \frac{E_{Al}}{L} \right) * \delta \quad (17)$$

Where, b= Sample width

d=Sample depth

L= Span length of 3 point flexural test

$E_{Al}$ = Modulus of aluminum 6061 T6= 68.9 GPa

Compliance of the aluminum sample ( $C_{Al}$ ) and the machine ( $C_m$ ) were calculated from the slope of theoretical load and actual load at the cross head displacement, respectively, which are shown in Figure 5.12.

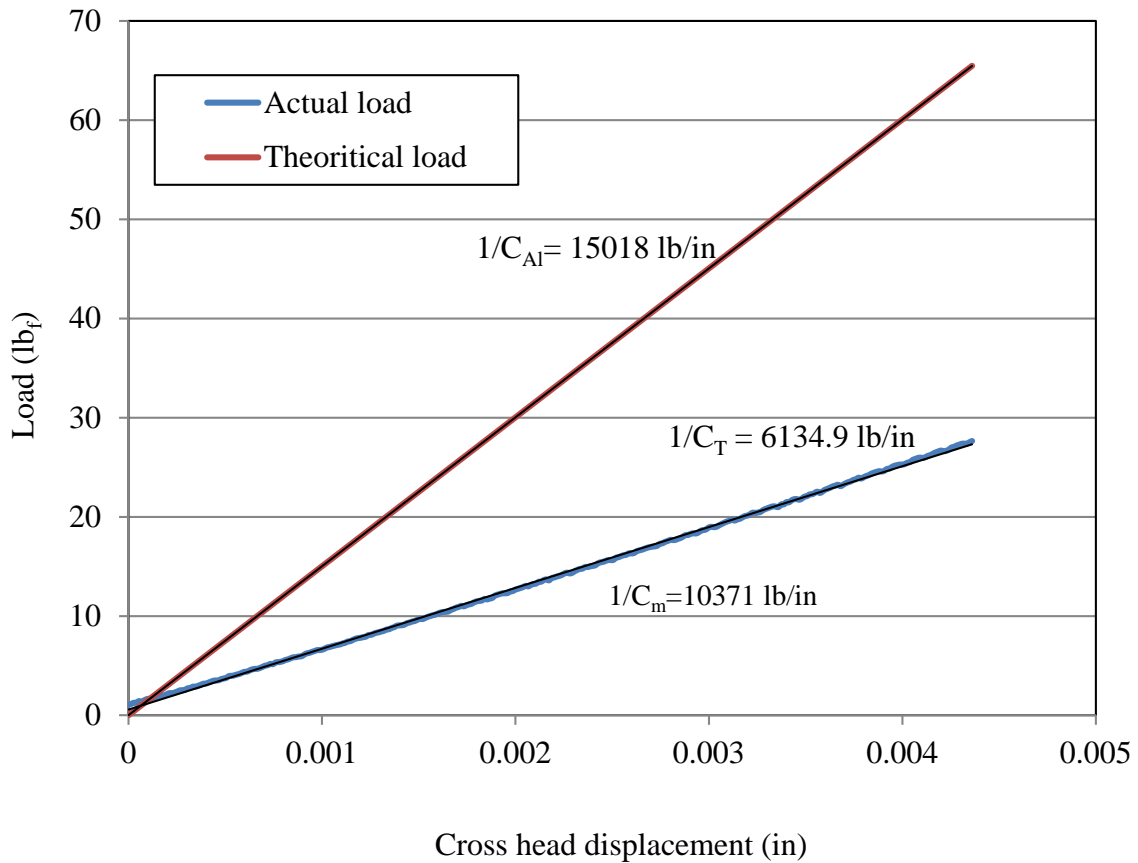


Figure 5.12. Comparison of theoretical and average load displacement profile for

Al-6061

Total compliance ( $C_T$ ) is the sum of the compliance of the sample with known modulus ( $C_{Al}$ ) and the compliance of the machine ( $C_m$ ) which can be shown in the following equation-

$$C_T = C_m + C_{Al} \quad (18)$$

Using equation (18) compliance of the sample can be rearranged

$$\frac{1}{C_{Al}} = \left( \frac{F_{Al}}{\delta} \right) = E_{Al} * \left( \frac{4 * b * d^3}{L} \right) \quad (19)$$

By rearranging the total compliance and machine compliance one can re write equation (18) in the following manner-

$$\frac{1}{E_T} = \frac{1}{E_m} + \frac{1}{E_{Al}} \quad (20)$$

Using the total and sample compliance the measured modulus of Instron C1102 machine is 100 GPa. This modulus value can be used as a correction factor to find the flexure modulus of unknown sample ( $E_s$ ) using the following rearranged formula –

$$E_S = \frac{E_T * E_m}{E_m - E_T} \quad (21)$$

This technique can be applied to any type of testing including tensile, compressive and flexure, however compliance must be calibrated separately for each of the test type. Once the modulus is found, actual deformation of the unknown specimen can be measured from the load-cross head displacement profile.

### ***5.5.5 Analysis of Thermal Stability***

Thermogravimetry (TGA) tool was used to measure the thermal stability of fully cured neat MEYEB. A Seiko I SSC/5200 TG/DTA 220 (by Seiko Instruments Inc) was used for this analysis. This instrument uses a highly sensitive cantilever-beam-balance system to measure mass change between the sample and the reference and thus enables the equipment to function as

both thermogravimetry and Differential Thermal Analyzer simultaneously. Differential Thermal Analysis (DTA) results were obtained from the difference in temperatures between the sample and the reference. All samples were tested in aluminum sample pan under 20-30 ml/min of nitrogen flow. Each test required 20-25 mg of crushed, cured sample, having average particle size of 50  $\mu\text{m}$ .

### **5.5.6 *Microstructure Analysis***

Microstructures of neat MEYEB were investigated JEOL JSM-6500 Field emission Scanning Electron Microscope (FE-SEM). Fracture surfaces of the specimens were coated in gold (10nm thick) using a Hummer VII ion beam sputter coater to enable imaging. To obtain high-resolution images (less than 1  $\mu\text{m}$ ), a beam energy of 15 KV was applied on the samples (around 2 mm thick) inside the vacuum chamber which was maintained at 9.63E-5 Torr.

## **5.6 Results**

This section deals with the results of mechanical strength, thermal stability, thermal expansion and microstructure evaluation associated with the effect of processing temperature and high temperature treatment neat MEYEB. The results will lead to understand the applicability of this geopolymer as a matrix of continuous fiber reinforced composites.

### **5.6.1 *Effect of Extended Heat Treatment on Compressive Strength***

Figure 5.13 is the presentation of compressive strength of neat MEYEB measured at extended temperature in oxygen. It is seen that, compressive strength gradually increased upto 760  $^{\circ}\text{C}$  and then decreased at 870  $^{\circ}\text{C}$ . With the increase in temperature from 80 – 760  $^{\circ}\text{C}$ , the increase in compressive strength is almost 100%. The results indicate that extended temperature heat

treatment made the geopolymer stronger which resulted in the further improvement in the compressive strength. However, beyond 870 °C this geopolymer is no longer strong, which is seen from the drop in compressive strength.

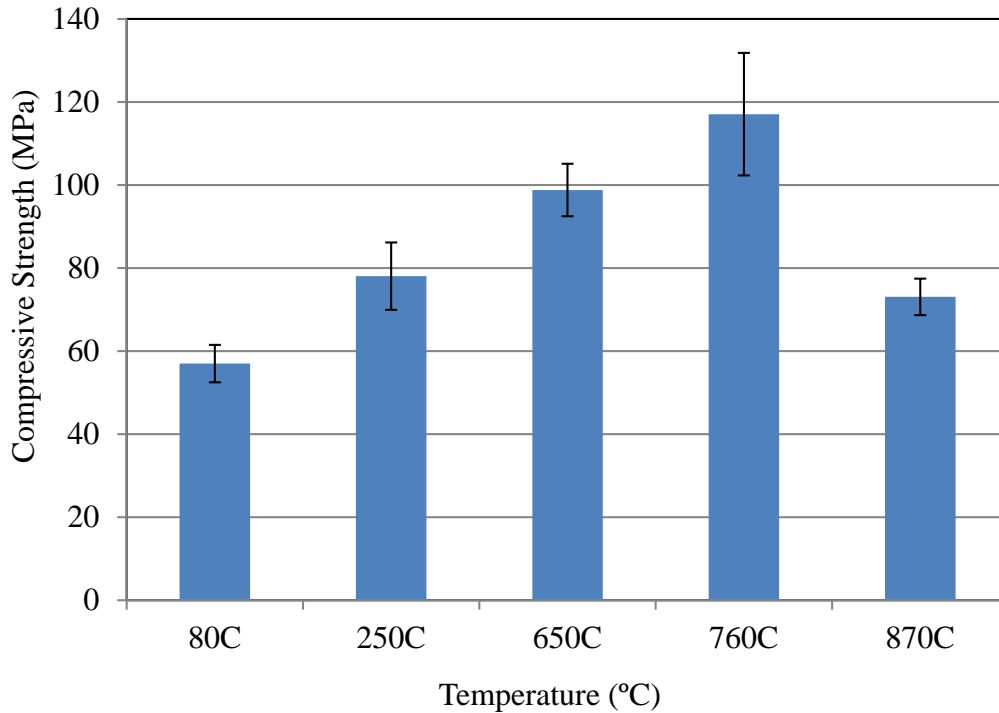


Figure 5.13 Effect of temperature on compressive strength of MEYEB in oxygen

### 5.6.2 Effect of Extended Heat Treatment on Flexural Strength

Figure 5.14 is the presentation of flexure strengths of neat MEYEB treated separately in oxygen and nitrogen at various temperatures. While temperature increased from 250 °C to 650 °C Flexure strength increased by 35.8% and 54.3% in oxygen and Nitrogen, respectively. Further increase in temperature from 650 °C to 760 °C in respective environment resulted in increase in flexure strength only by 1% and 10%, respectively. It is found that, the increase in the flexure strength in non-reactive environment is higher than in the reactive environment, which follows the trend in compressive strength in the respective temperature range.

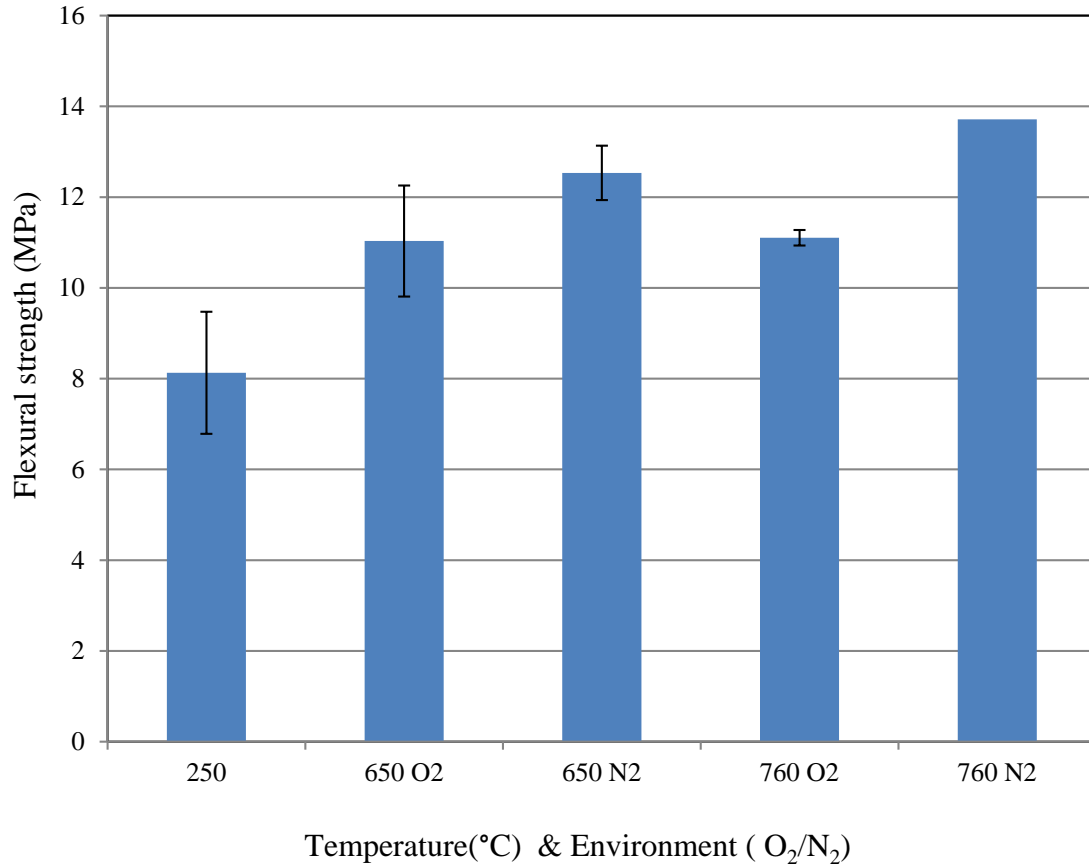


Figure 5.14 Effect of temperature and environment on flexural strength of MEYEB

### 5.6.3 Effect of Extended Heat Treatment on Fracture Toughness

Figure 5.15 is the presentation of the fracture toughness ( $K_{IC}$ ) of neat MEYEB. While temperature increased from 250 °C to 650 °C fracture toughness increased by 70% and 84% in oxygen and nitrogen, respectively. From 250 °C to 350 °C toughness increased by 65%, which is almost 92% and 78% of the total increase in the 250°C- 650 °C range. Further increase in temperature from 650 °C to 760 °C resulted in increase in fracture toughness by 50 % and 16 %, in oxygen and nitrogen, respectively. The improvements in toughness again followed similar pattern as in compressive and flexure strength.

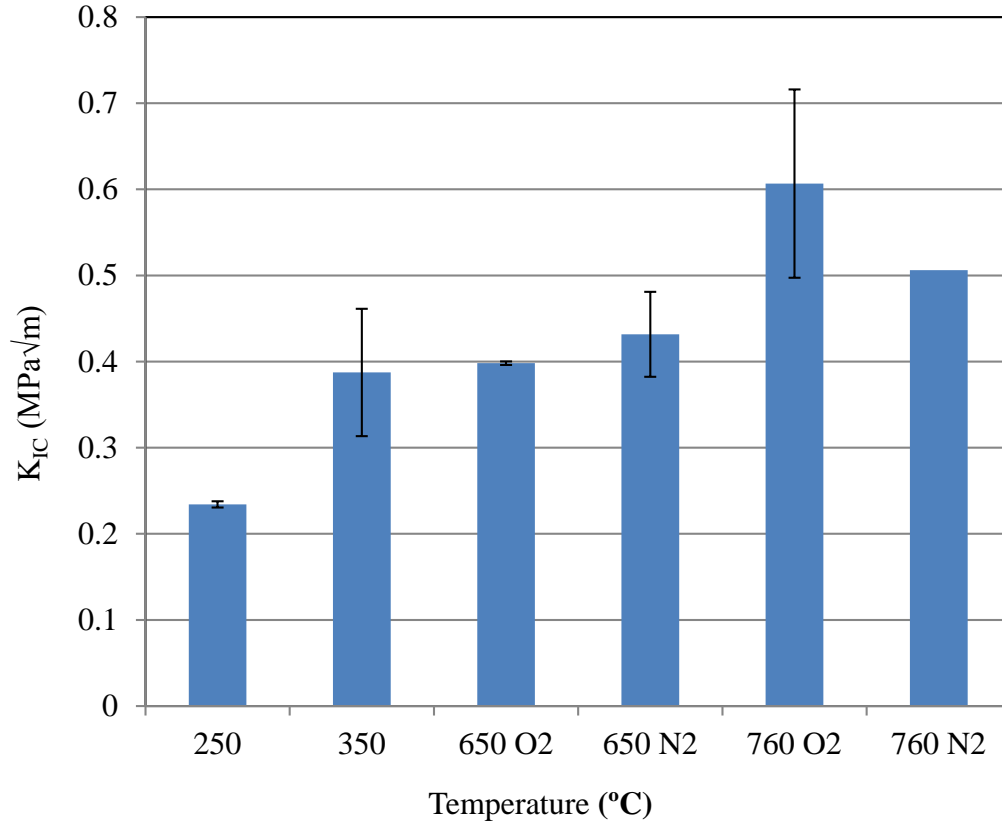


Figure 5.15. Effect of temperature and environment on fracture toughness of neat MEYEB

The variations in the fracture toughness of neat MEYEB with temperature is again presented in Figure 5.16. It is found that the increase in toughness in non-reactive environment follows exponential relations. This exponential relation is equivalent to the temperature dependent diffusion which follows Arrhenius relationship<sup>102</sup>. It is also found that in the reactive environment the changes in toughness differ from the changes in non-reactive environment. This difference suggests that in the reactive environment the increase in toughness is resulted from diffusion and high temperature reactions.

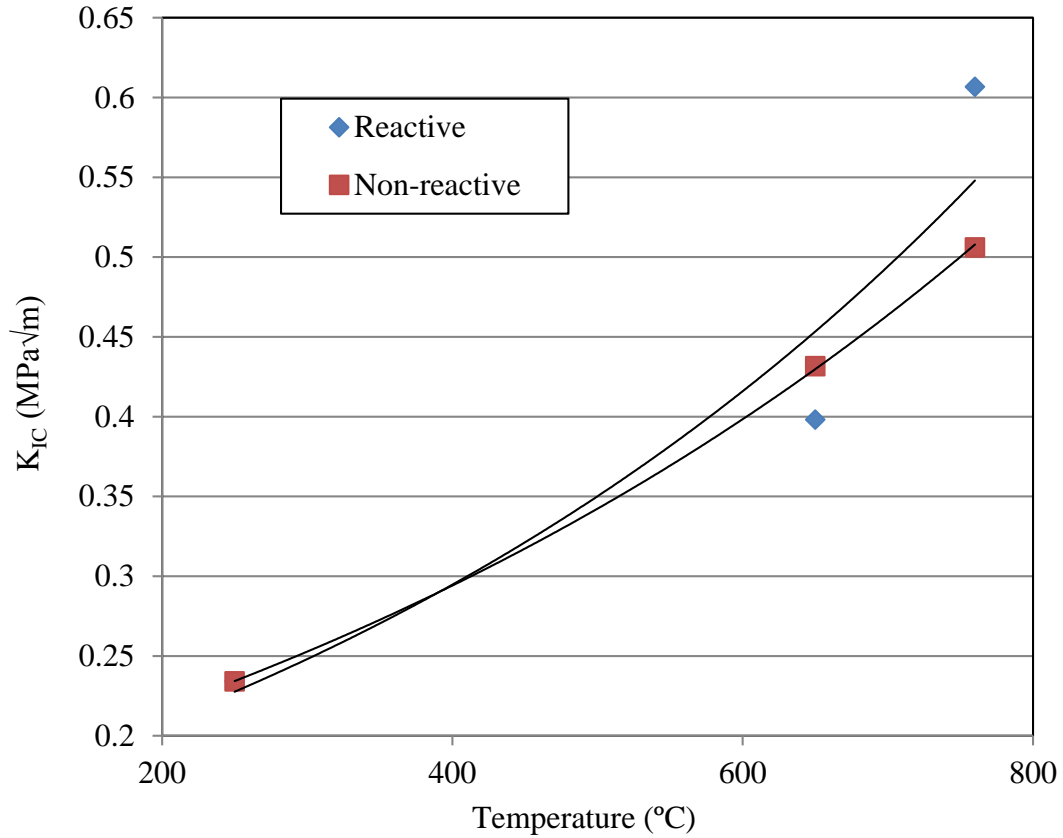


Figure 5.16. Fracture toughness of neat MEYEB at various temperatures in reactive and non-reactive environment.

#### 5.6.4 Effect of Extended Heat Treatment on Flexural Modulus

Figure 5.17 presents flexural modulus of neat MEYEB treated over extend temperature. It is found that the modulus of neat MEYEB gradually increased with increasing the treatment temperature. Flexural modulus of neat MEYEB increased 70% and 34% while the treatment temperature increased from 250 °C to 650 °C and 760 °C, respectively.



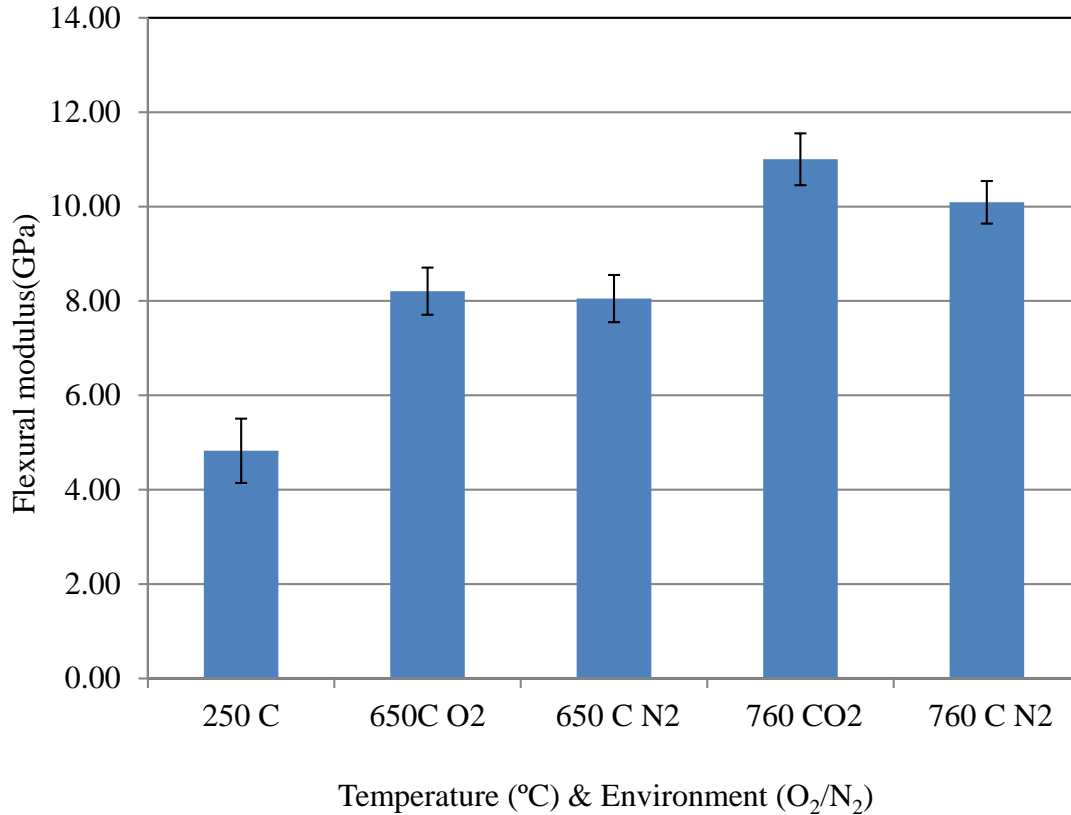


Figure 5.17. Flexural modulus of neat MEYEB processes at various temperatures and environments.

This increase in flexural modulus is in coherence with the improvement in compressive modulus presented in Figure 4.12. The result suggests the increase in bonding strength with the increase in the treatment temperatures. The increase in flexural modulus is the resultant effect of the increase in cross link density<sup>11</sup>, de-hydroxylation<sup>12</sup> and probably inter-particle diffusion. At 760 °C there is slight increase in modulus in oxidative environment; however the differences in the modulus at each temperature (650 °C and 760 °C) are less than 5%, which may suggest that the differences are statistically insignificant. The increase in modulus with the treatment temperature is in similar manner with the changes in the flexural strength.

Evaluation of the modulus of neat MEYEB is one of the important finding of this study. Previously attempted various nano and micro reinforcement for toughening of MEYEB was unsuccessful in providing expected results because it was assumed that the modulus of neat MEYEB is as high as the modulus of many sintered ceramics. Now it is found that even though the modulus of neat MEYEB is higher compared to the modulus of organic polymer but it is much lower compared to conventional sintered ceramics. This low regime of modulus indicates that nanofillers with high interfacial bond strength and high modulus are effective in strengthening and toughening of MEYEB.

#### ***5.6.5 Thermal Stability of Cured and Post Processed MEYEB***

TGA and DTA of freshly cured neat MEYEB ( at 80 °C ) is presented in temperature domain in Figure 5.18, which are representative of the thermal characteristics of the drying at 80 °C to the post cure followed by the post processing part of the optimum process schedule B2 (see Table 4.1). Figure 5.19 presents the similar thermal characteristics in time domain. As seen in Figure 5.19, during 80 °C drying, a weight loss is approximately 6.5 %. Further weight loss of 3.5 % and 1.2 % occur during the drying at 250 °C and post processing to 600 °C, respectively. The weight loss in the range of 250-600 °C is found as 1.2 %, which is almost 3 times lower than that observed from 100-250 °C range (3.5%).

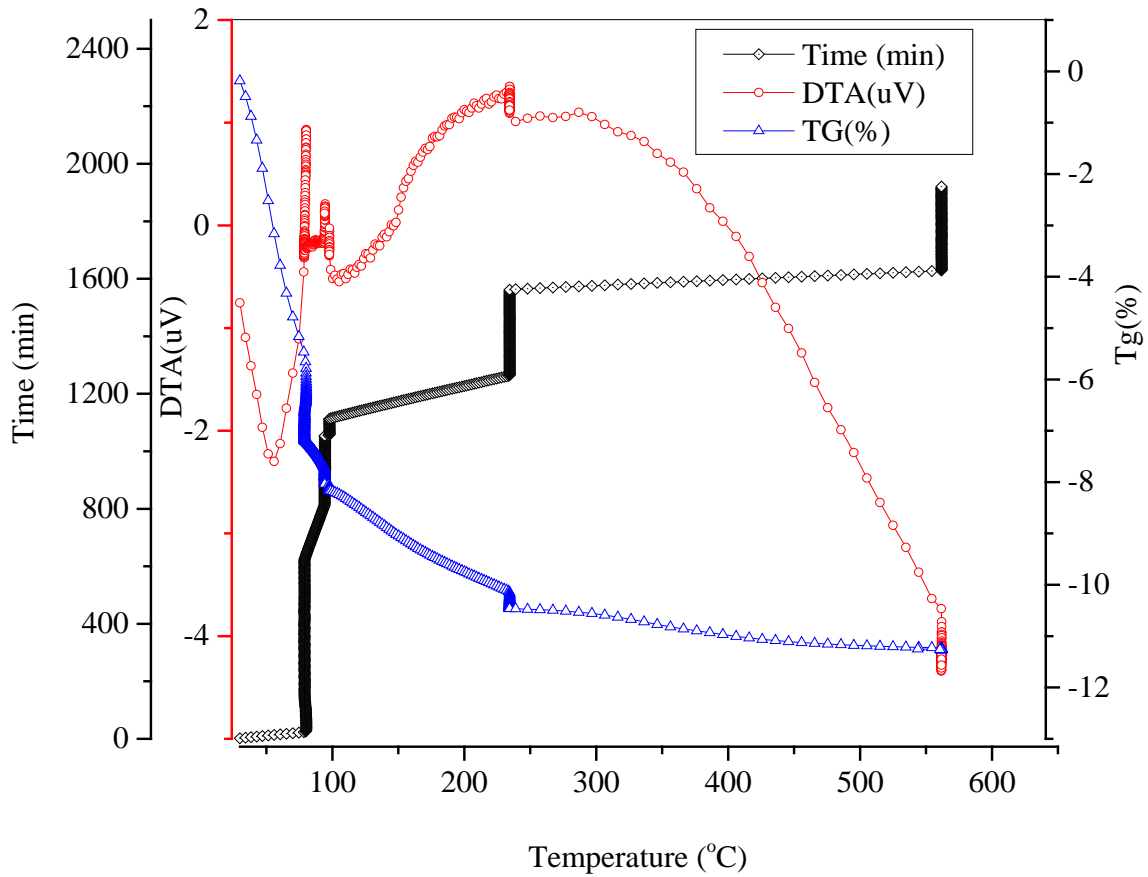


Figure 5.18. TGA and DTA of neat MEYEB treated through schedule B2 after initial cure at 80 °C

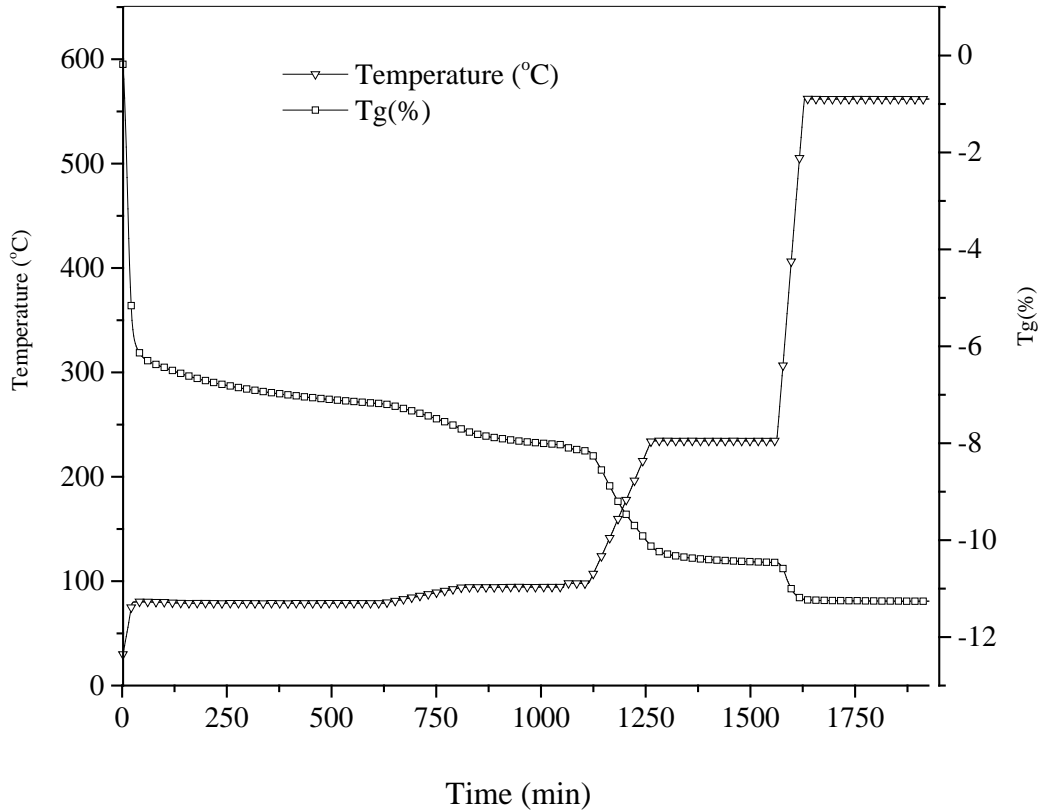


Figure 5.19. TGA of neat MEYEB treated through schedule B2 after initial cure at 80 °C ( in time domain)

The weight loss during the 80 °C drying stage starting after the initial cure is associated with the evaporation of liquids from the freshly cured sample. Further two step weight losses in 80-250 °C and 250-650 °C ranges suggest the removal of chemically bonded liquids and dehydroxylation of OH<sup>-</sup> atoms from the inorganic polymer networks, respectively <sup>12</sup>. Gradual reduction of weight loss in 250-650 °C range compared to 80-250 °C range suggests that, with the 650° C processing , MEYEB gradually reaches to the state of thermal stability. Thermal studies with the similar inorganic polymer<sup>13</sup> suggest that, with the post processing at 600 °C the geopolymer reaches to a state of thermal stability which is good till 900 °C. Overall this thermal analysis indicates the effectiveness of the cure schedule and post processing on the structural

stability of the geopolymer. Figure 5.20 presents similar 80-650 °C post treatment TG and DTA of freshly cured neat MEYEB (see Figure 5.18) followed by uncontrolled schedule similar to schedule A1, with just by heating at a rate of 5 °C/min and no intermediate hold. Total weight loss from this observation is only ~7%.

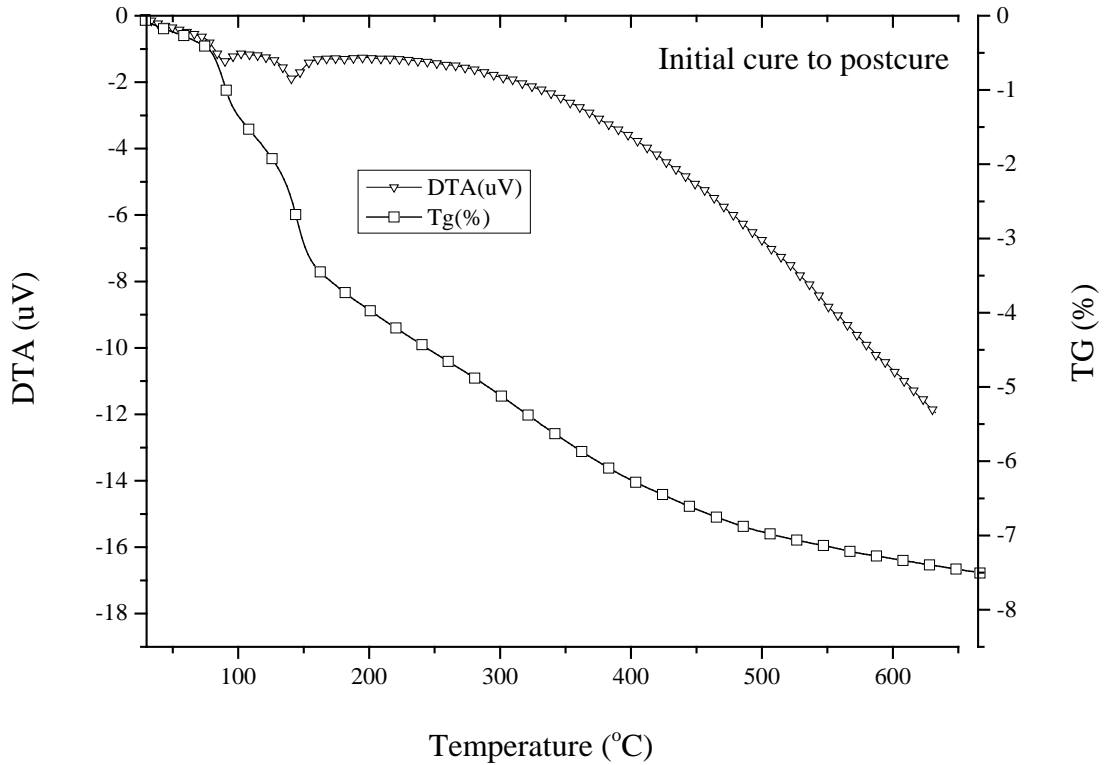


Figure 5.20 TGA and DTA of neat MEYEB at 80-600 C (after initial cure at 80 °C) followed schedule A1 (ramp of 5 °C/min )

While total weight loss during the controlled drying and post processing (followed by schedule B2 in Table 4.1) was approximately 12% (see Figure 5.18) the weight loss is only ~7% in the case of uncontrolled post processing (see Figure 5.20). Higher weight loss corresponds to the prolong dry at 80 °C.

The DTA of both controlled and uncontrolled schedules are presented in Figure 5.21. Both schedules present two endothermic peaks at 100 and 144 °C, which indicate loss of physically attached liquid during post processing.

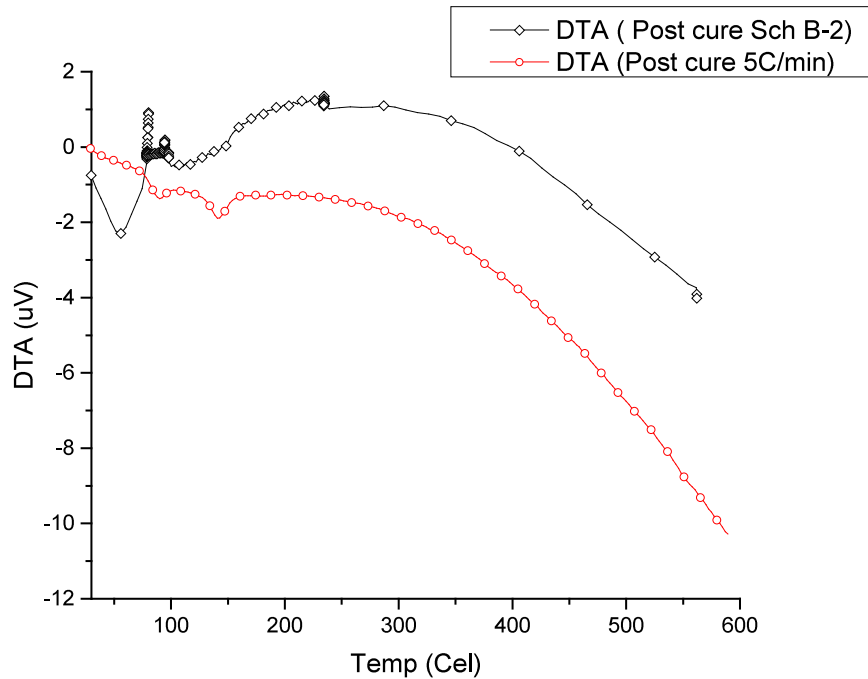


Figure 5.21 DTA of freshly cured samples while postcured (a) following schedule B-2 and (b) at 5 °C/min

Two endothermic peaks in DTA of both controlled (schedule B2) and uncontrolled (schedule A1) post processing schemes indicate the loss of physically attached liquid during post processing<sup>103</sup>. Below 300 °C, higher weight loss occurs in schedule B2 than in schedule A1 by just heating at 5 °C/min, which indicates better processing through controlled ramp and hold at different critical temperatures. This demonstration suggests optimum dehydration and dehydroxylation of water molecules through the controlled process schedule.

Figure 5.22 presents the TGA and DTA of the reheating cycle (80 °C-650 °C) of MEYEB post heat treated upto 650 °C. This result does not include any data related to cure or post processing. DTA of post heat treated (Figure 5.22) MEYEB shows one broad endothermic peak (First peak before 100°C) indicating early removal of moisture. It does not show any other endothermic peak at around 144 °C or further, which was seen in the post processing schedule (see Figure 5.21). Broad endothermic peak of post processed MEYEB (Figure 5.22) indicates removal of environmental moistures adsorbed in the post processed sample which was just physically attached. No chemical reaction occurs during this moisture removal period. This evidence suggests that the fully cured and post heat treated MEYEB is secured from environmental degradation upto 650 °C.

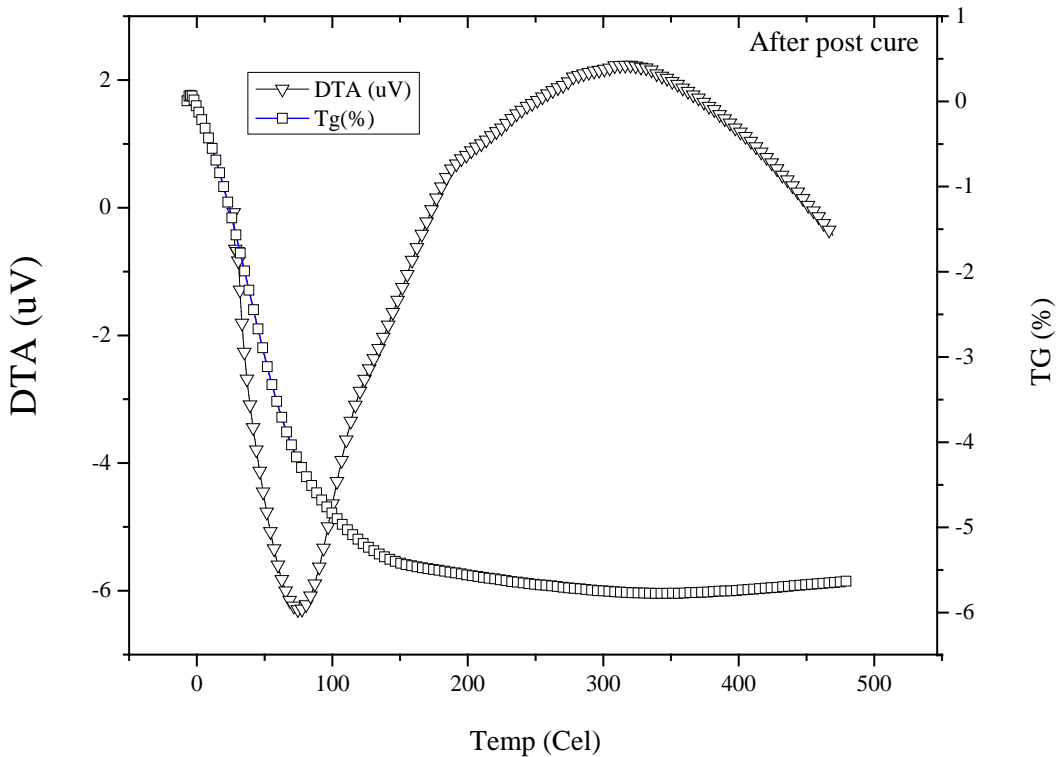


Figure 5.22 TGA and DTA of neat MEYEB while reheated at 5° C/min after post heat treatment at 650 °C

In summary, both TGA and DTA of MEYEB share some useful information that can help to understand the changes in neat MEYEB through the different stages of processing .With the help of this thermal analysis it is possible to interpret the state of thermal reactions between potential nano-fillers and MEYEB at various stages of processing. These reactions have the potential to control the interfacial strength. During the post cure processing majority of weight loss occur below 300 °C and after 300 °C minor weight losses occur until the temperature reached to 650 °C. After 300 °C material starts consolidated till the high temperature processing continues. If nanofillers are added to MEYEB there is a potential that the interfacial strength between MEYEB and nanofillers increases during this consolidation period of MEYEB. Also at 300 °C some critical changes might occur in MEYEB structure and the interfacial strength between MEYEB and nanofillers.

#### ***5.6.6 Evaluation of Density through the Processing***

Density change during the curing process depends on the changes in both weight and dimension. Due to the evaporation of the liquid, weight loss of freshly cured MEYEB is faster in the beginning of curing process. In this study the density change is measured as a simultaneous function of weight change obtained from TGA and length change obtained from dilatometry (TMA) during the drying and post cure process, after initial cure. The following equation is used for the calculation of the density change ( $\%x_\rho$ )-

$$\%x_\rho = \left( \frac{1 - \frac{\%x_m}{100}}{3 \times \% \left( \frac{\Delta L}{L_0} \right)} \right) \times 100 \quad (22)$$



Where  $\%x_m$  is the weight loss or TG% and  $\%(\frac{\Delta L}{L_0})$  is the linear cure shrinkage (Dilatometry) obtained from TGA and TMA analysis, respectively. According to equation (22), the changes in density with temperature are the function of both weight loss and linear shrinkage. The changes in density through the process variations in cure schedule A and B are shown in Figure 5.23. The data from the drying and post processing stages of two representative samples A1 and B2 are shown in this investigation. It is worth mentioning that, this study does not include the density variations during the initial cure stage when MEYEB was in liquid condition.

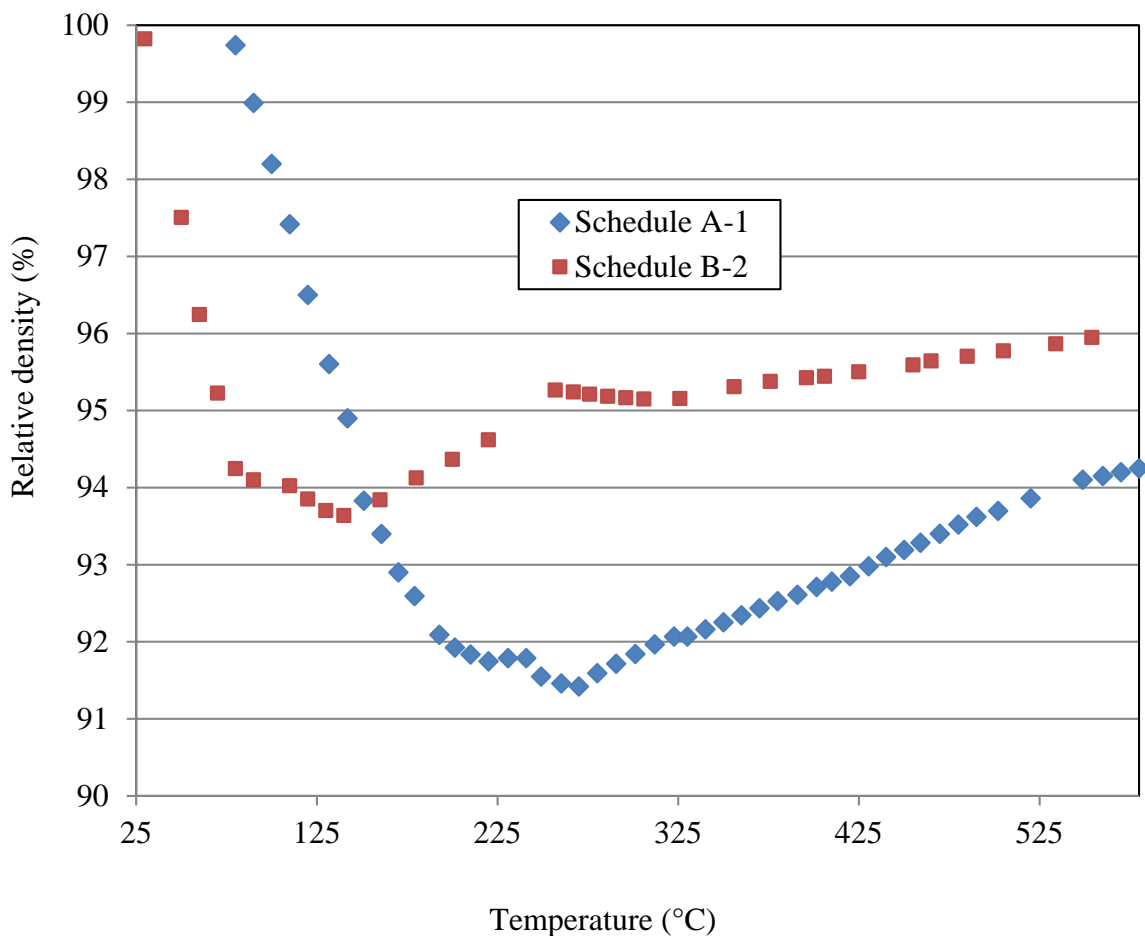


Figure 5.23 Density change of MEYEB during post cure as a function of temperature

As shown in Figure 5.23, in both processing schedule, density of MEYEB rapidly reduced during the initial part of drying and then increased with temperature. This reduction took place upto 250 °C and 180 °C for samples processed using schedule A1 and B2, respectively. The density reduction of the sample dried through schedule B2 is 3.2 % lower than the sample dried through schedule A1. Initial reduction in the density indicates the evaporation of physically attached moisture. Since the schedule B2 has allowed more time during the initial cure process than schedule A1, a slow removal of moisture is found during the drying stages through schedule B2. As the temperature further increased, the rate of size reduction went over the weight change, which resulted in an increase in density or the density recovery in both schedules. However, the density recovery of samples from schedule A1 is lower compared to the samples from schedule B2. This suggest that, due to the incomplete cure through the schedule A1, more moisture that didn't take part in the poly-condensation reaction was dried out/evaporated in the drying stage leaving some large voids and porosities in the cured materials. The evidence of porosities can be seen in microstructure investigation. Due to the presence of large pores, further post heating from 280 °C to 580 °C didn't facilitate in any significant consolidation of the materials processed through schedule A1. As seen in Figure 5.18, major weight loss in the 80-250 °C range plays significant role in the density change. Since this temperature range is crucial for the density change phenomena, a slow drying is suggested to control the consolidation of the material, which is obtained using schedule B2.

### ***5.6.7 Evaluation of Thermal Expansion with Processing Schedules***

The study of the coefficient of thermal expansion the matrix material is essential for the high temperature continuous fiber reinforced composite applications. Mismatch of thermal expansion coefficients between the fiber and matrix can introduce residual stresses, which limit the life of

the composite. Figure 5.24 presents a dilatometer [  $\left(\frac{\Delta L}{L_0}\right) \times 100\%$  ] curve of the thermal expansion and contraction of fully cured inorganic polymer processed following schedule B2. Figure 5.24 (a) shows expansion and contraction of the sample in one cycle, representing a contraction/shrinkage around 0.2% while heating in the 100-200 °C range. This shrinkage at relatively low temperature suggests the removal of the moisture. In order to verify whether this shrinkage is related to the diffusion of atmospheric moisture, a second heating and cooling cycle was performed. This cycle was performed immediately after the completion of the first heating cycle (Figure 5.24 (c)) and after a room temperature hold for 24 hours (Figure 5.24(b)), respectively. With the 24 hours room temperature hold, similar shrinkage (Figure 5.24(b)) was observed in the second heating cycle, which was not observed when the second heating cycle was performed immediately. Therefore, this shrinkage is indicative to the loss of atmospheric moisture uptake. From the dilatometer profile of the second heating (Figure 5.24(d)) it is found that the measured coefficient of thermal expansion of the cured inorganic polymer is 4.23  $\mu\text{m}/\text{m}/^\circ\text{C}$  over the temperature range of 30-600 °C as demonstrated by a  $R^2$  value of 0.99. The linear thermal expansion results of MEYEB suggest that, this geopolymer is compatible as the matrix with the conventional continuous ceramic fibers including alumina<sup>104</sup> and silicon carbide<sup>105</sup>.

Thermal expansion or the dilatometer profiles of the cured specimens as processed in various schedules are presented in Figure 5.25. The heating and cooling were repeated for each sample for at least two times and the profile from the second heating is presented in order to avoid the early shrinkage (see Figure 5.24(a)). Out of five specimens tested, three specimens ( A-1, A-3, A-6) were chosen from the set A which had seen initial cure for only 10 hours or less dry cure and remaining 2 specimens (B-2, B-3) from set B which had been processed with 24 hours of initial cure.

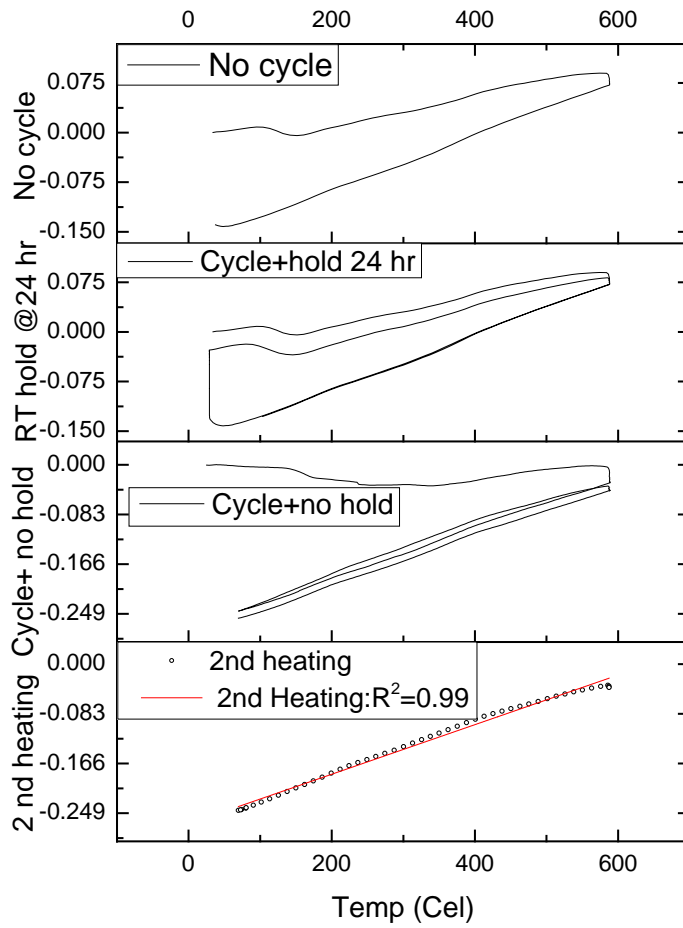


Figure 5.24 Dilatometer profile of sample B2 after post cure with (a) heating and cooling (b) cyclic heating & cooling with intermediate hold (c) no hold and (d) second heating

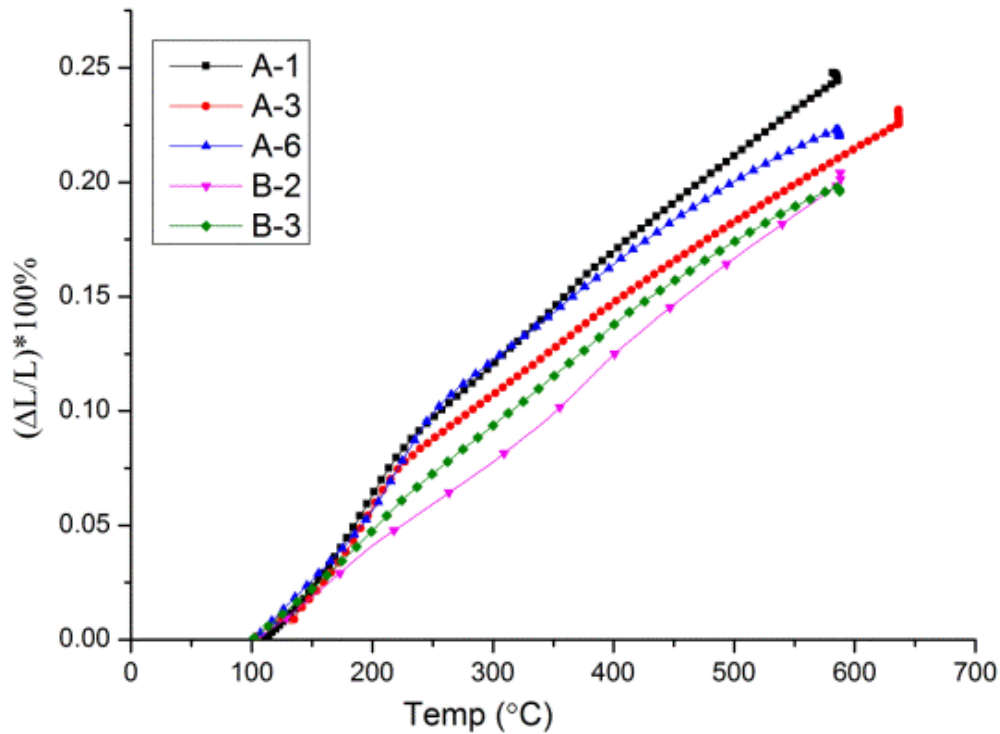


Figure 5.25 Thermal expansions of fully processed specimens followed by various schedule

CTEs of cured and post processed specimens followed by schedule A1, A3 and A6 (10 hour or less initial cure followed by a 10 hour of dry postcure ) were found to vary between the 100-200 °C and 250-650 °C temperature ranges. Average CTEs of those specimens over the two temperature ranges were 6.48  $\mu\text{m}/\text{m}/^\circ\text{C}$  and 3.75  $\mu\text{m}/\text{m}/^\circ\text{C}$ , respectively. Conversely, the CTEs of the specimens from set B were constant over the 100-600 °C temperature range, with an average value of 4.20 $\mu\text{m}/\text{m}/^\circ\text{C}$ . This indicates a reduction in thermal expansion of set B specimens by over 35% in the 250-650 °C temperature range. The reported<sup>83,50,106</sup> thermal expansion data for a typical poly-sialate geopolymer also matched with this value. This result indicates that, with sufficient hold time for isothermal cure and drying the inorganic polymer materials present a stable and constant thermal expansion over a wide temperature range.

### ***5.6.8 Understanding the Curing Process through Microstructure Evaluations***

Figure 5.26 is the presentation of the microstructure of specimens at various stages of processing (80 °C & 650 °C) followed by schedule B2 and post treatment at 870 °C. Figure 5.27 presents the diameter of unreacted particle and the inter-particle porosities in the MEYEB matrix with the heat treatment temperature. Detail procedure of measurement and distribution of the diameter of particles and porosities are presented in Appendix B3. According to the microstructure, the fracture surface of 80 °C cured specimen (Figure 5.26 (a)) can be described as the particles of unreacted materials distributed over the poly-condensed network of MEYEB matrix. It appears that the particles are bonded to each other on the surface. The average sizes of the un-reacted particles are in the range of  $0.45 \pm 0.2 \mu\text{m}$ . The wide distribution in the particle size is due to the heterogeneity in the formation of precipitation. From Figure 5.26 (a) & (b) it is found that sample treated at both 80 °C and 250 °C contain inter-particle porosities, however, higher pore densities are found in the sample treated at 80 °C. This suggests weak particle to particle bonding and incomplete poly-condensation reaction. While MEYEB is processed at 250 °C particles became more interconnected to each other with more poly-condensed structure. The poly-condensed structure in the 250 °C treated sample (see Figure 5.26 (b)) is approximately 20-30 vol%, which is higher compared to the sample cured at 80 °C (see Figure 5.26 (a)). The changes in morphology suggests that in 80-250 °C temperature range more ions are dissolved into liquid and creates more geopolymer network until the complete drying of unreacted liquid occurs. It is also suggested that the polycondensation reaction does not complete at 80 °C rather it completes at elevated temperature.

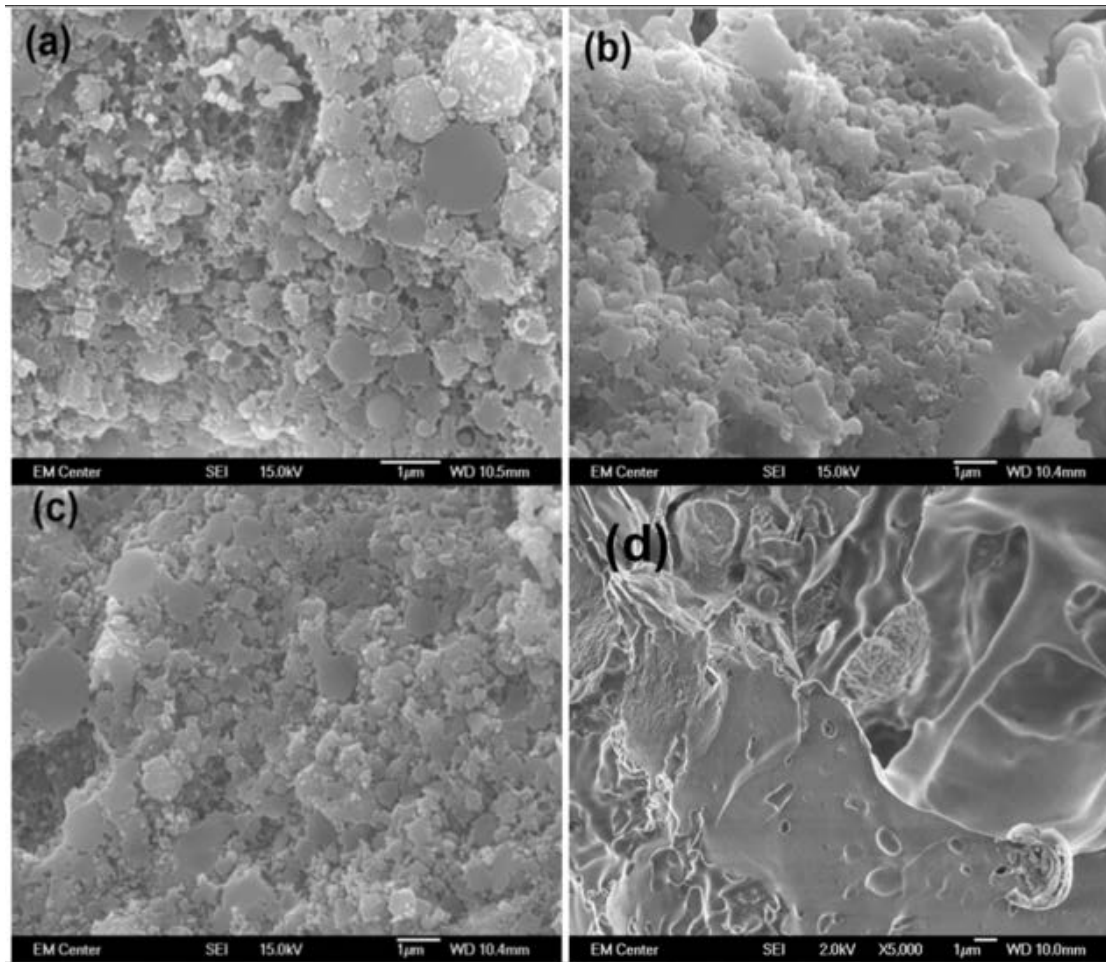


Figure 5.26 SEM images of MEYEB followed by schedule B2 (a) cured at 80 °C, post processed at (b) 250 °C, (c) 650 °C and (d) treated at 870 °C.

With successive treatment at 650 °C and 870 °C the spherical particle nature of MEYEB reduced and more homogeneous structure appeared, which is seen in Figure 5.26 (c) & (d). This suggests thermal diffusion of particles that results into coalesced materials. Un-reacted particles are expected to work as reinforcement in the geopolymer and therefore to increase mechanical strength. Since there is no particle nature at 870 °C, geopolymer at this temperature behaves like a weak monolithic sintered material. This evidence therefore verifies the drop in compressive strength as seen in previous section.

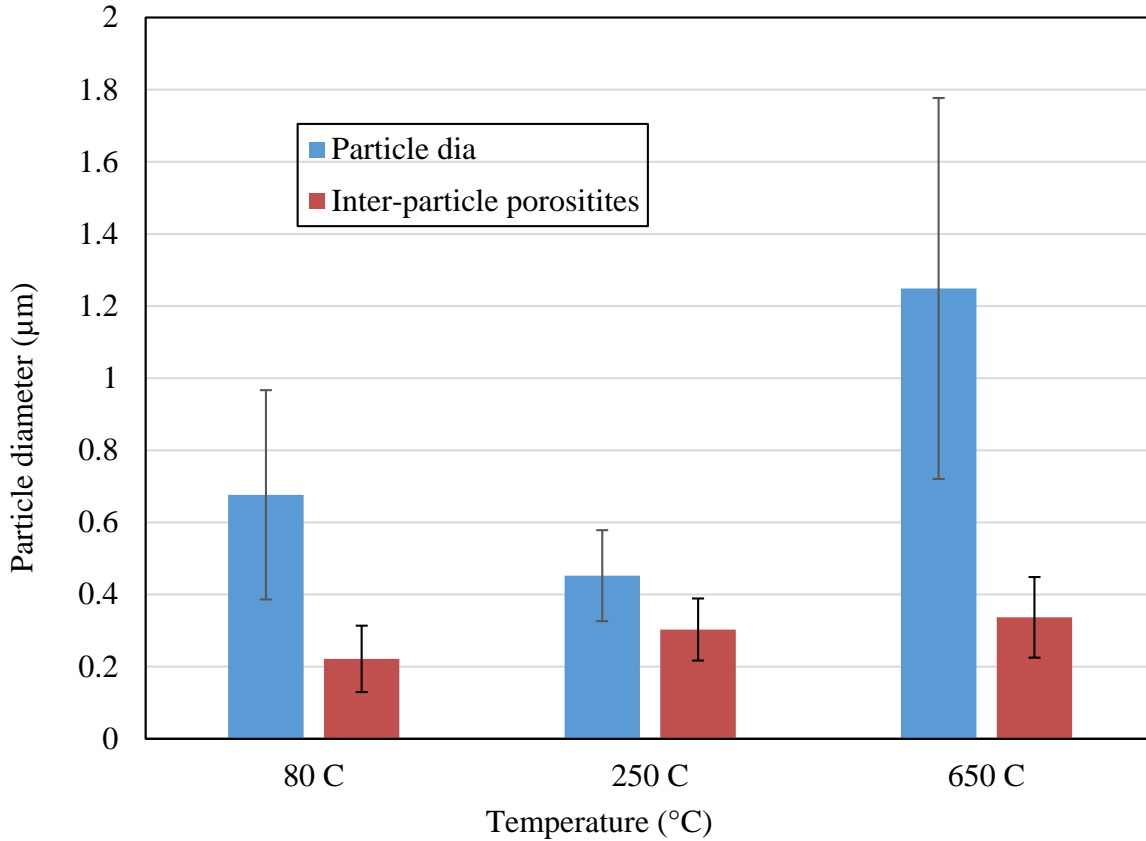
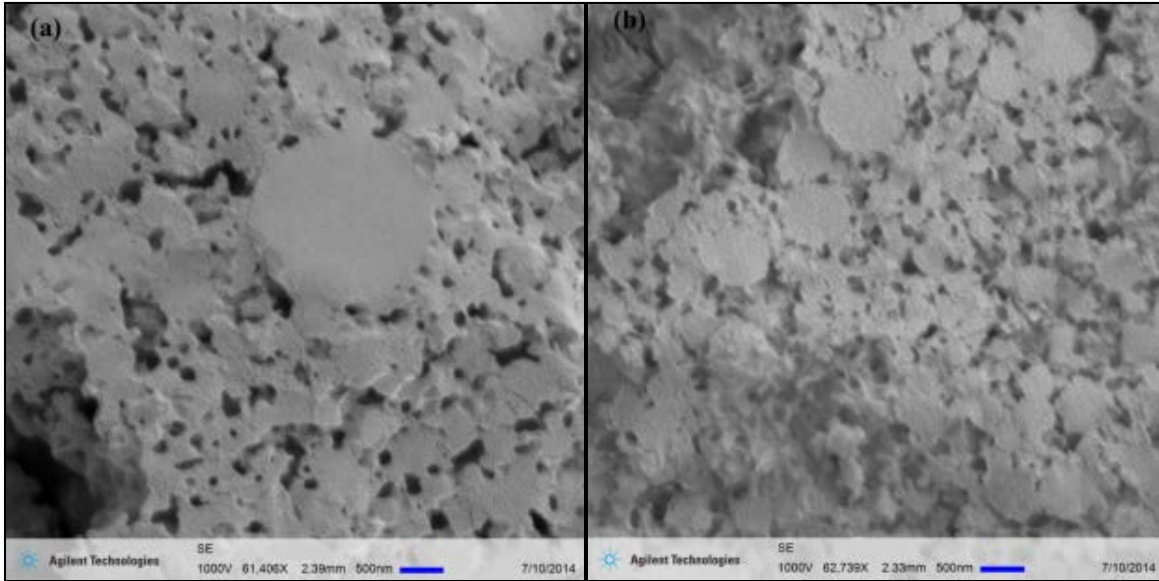


Figure 5.27 Diameter of particles and porosities of neat MEYEB with temperature

SEM micrographs of the fracture surfaces of post processed specimens followed by schedule A1 and B2 are shown in Figure 5.28(a) & (b), respectively. The images present particle nature of MEYEB with some inherent porosity. The average pore size of each sample was measured using average grain intercept method<sup>107</sup>. From the measurement it was found that the pore sizes of the samples processed using schedule A1 and B2 are images are  $237 \pm 140$  um and  $75 \pm 23$  nm, respectively. Therefore this result indicates the variations in the pore size with the variations in the process schedule. It also suggests that smaller pore size is indicative to better process schedule.





(a)

(b)

Figure 5.28 SEM images of sample followed by schedule (a) A1 and (b) B2 after processed at 650 °C (O<sub>2</sub>).

It is previously mentioned that geo-polymerization process follows three steps such as dissolution, poly-condensation and precipitation. Geo-polymerization starts with the dissolution of Si and Al from Si and Al rich starting materials which are normally in spherical shape. In the presence of alkali medium the dissolution process of Si and Al ions starts with the size reduction of the large spherical particles of alumino-silicate rich materials. Later these ions are suggested<sup>36</sup> to take part in the formation of the complex geopolymer network through the process called poly-condensation. As soon as the poly-condensation process completes the undissolved remnant of the starting materials precipitate in the form of dispersed particles. The size and homogeneity of the dispersed particles depend on the initial cure time. Sufficient dissolution of the starting materials occur with longer initial cure, which results in the smaller and uniformly distributed precipitates on the poly-condensed structure. This results in the smaller inter-particle porosity. On the other hand, if the initial cure time is insufficient, larger particles precipitate in a

heterogeneous manner which results into higher inter-particle porosity. SEM micrographs therefore verify this hypothesis on the difference in the porosity and particle size with the variations in the process schedule from A1 to B2.

Overall the microstructure evaluation assists in sufficient understanding on the effect of structural variations in the strength of geopolymer. It helps to understand that gradual increase in optimum processing and treatment temperature increases bond strength of particles and reduces inter-particle porosities of particles that simultaneously assist in increasing resistance to particle pullout and strength. Further increase in treatment temperature reduces structural inhomogeneity and retention of the particles to act as reinforcement.

## **5.7 Conclusion**

Combining the information gained from the measurements of the process-induced shrinkage and the mechanical properties, the results indicate that an extended 80 °C isothermal cure in a sealed environment, followed by a slow, stepwise drying process results in the best balance of cure shrinkage and mechanical properties. This combination is predicted to be the most resistant to residual stress induced cracking as the matrix of a fiber reinforced inorganic polymer composite. The reduction of thermal expansion through the optimized processing also minimizes the cracking due to thermal loading. Further, it is now clear that process related changes are directly related to the inherent microstructure of the materials. This realization has allowed the measurement of many neat resin properties including thermal stability and thermal expansion, which are necessary to better understand, and predict, the performance of the corresponding nano and fiber reinforced composites.

Thus, future processing studies involving nano and continuous fiber reinforced/MEYEB composites will need to further investigate the development of residual stresses during processing as the state-of-cure progresses in the sealed environment, and during the subsequent drying and post-cure.

Neat MEYEB cures and solidifies at 80 °C; however the sufficient strength does not develop at this early stage of processing. Drying and post processing upto 250 °C reduces the un-reacted and physically attached water molecules. The removal of attached water molecules completes at 250-350° C range. Chemically bonded water molecules start to remove at 350 °C and continue till 650 °C. Removal of physically attached liquid has more influence on mechanical properties compared to the removal of chemically bonded liquid. Therefore the improvement of mechanical properties in 250-350 °C range is much higher compared to 350-650 °C range. Further treatment at 650-760 °C is the potential regime for thermal diffusion of the particle phases which causes further increase in mechanical strength.

Compressive strength gradually increased upto 760 °C, however compressive strength dropped down at 870 °C as a result of the elimination of particle reinforcement. Flexural strength, fracture toughness and modulus all increased gradually with the increase in treatment temperature upto 760 °C. The responses to all the mechanical properties are similar in both inert and oxidative environment. Therefore, it can be suggested that thermal response of this alumino-silicate based geopolymer to mechanical properties are not affected by oxidative environment and this geopolymer is suitable in an oxidative environment to a maximum operating temperature of 760 °C. Thus it is now possible to evaluate the effectiveness of nanofillers on the geopolymer whose baseline properties are documented in the suitable temperature and environmental conditions.

## 6 EFFECTIVENESS OF NANOFILLERS ON TOUGHENING

Optimal processing was the preliminary method on developing sufficient properties of MEYEB before the addition of nanofillers. This section focuses on the effect of nanomaterials on toughness of MEYEB. Various nanomaterials as presented in the previous materials section are implemented in the geopolymer according to several test matrices. One test approach was developed using the variables associated with the variations in nanomaterials and treatment environment which followed general procedure of a factorial design of experiments. In order to investigate the effect of nano-reinforcement at high temperature, this test approach included upper use temperature range of MEYEB ranged from 650 °C to 760 °C. The key purpose of this experiment is to find the limits where the variables have the significant effect on fracture toughness. To perform this experimental study two types of nanofillers (of low and high aspect ratios), carbon (C) and alumina ( $\text{Al}_2\text{O}_3$ ) were chosen with the differences in the interfacial strength, tensile strength and oxidation stability. The test matrix and the design of experiments are introduced in the preliminary study of nano-reinforcement. The procedures for sample and notch preparation are described in the subsequent sections.

Later a comprehensive test matrix was developed to investigate the nano-reinforcement effect using three types of nanofillers ( of low and high aspect ratios), carbon (C), silicon carbide (SiC) and alumina ( $\text{Al}_2\text{O}_3$ ) in a wide temperature range from 250 °C to 760 °C. Two of these three nanofillers have similarities in the tensile strength and oxidation stability but differences in interfacial strength (see Table 3.1). The test matrix and associated studies with these three nanomaterials are presented after the study with preliminary test matrix.

## 6.1 Evaluation of Interfacial Strength

An evaluation is required especially to investigate the effect of interfacial strength between the proposed nanomaterials and the inorganic matrix material, because this variable has one of the most significant roles in toughening of geopolymer. Among two types of nanofillers of the preliminary study, alumina has closer chemical network with MEYEB than CNF, which indicates stronger alumina/MEYEB interface. Due to the inorganic nature, third nanofiller of the comprehensive study, silicon carbide is expected to have sufficient interfacial bond strength with MEYEB. No direct approach was made to measure the interfacial strength but was evaluated using the fracture surface investigation of nano-reinforced MEYEB. To perform this evaluation 2 vol% of all high aspect ratio nanofillers (CNF, SCW and ANF) were separately mixed with MEYEB. The interfacial strength of the following nanomaterials were therefore evaluated-

Carbon -C

Silicon carbide-SiC

Alumina –Al<sub>2</sub>O<sub>3</sub>

## 6.2 Preliminary Study on the Nano-reinforcement

It is hypothesized that, the high aspect ratio nanofillers with high interfacial strength is more effective in toughening than nanoparticles with low interfacial strength. To verify this hypothesis an approach is undertaken to investigate the relative importance of aspect ratio and interfacial strength on the fracture toughness,  $K_{IC}$  at any given volume fraction at various operating temperature and environment. This approach is generally termed as full factorial design.

### 6.2.1 Full Factorial Design

Full factorial design is developed to investigate the potential effects of several independent variables on the fracture toughness ( $K_{IC}$ ) of MEYEB. These variables are Aspect Ratio (AR), Interfacial Strength (IS) and Volume Fraction (VF), Temperature (T) and Environment (E). These variables are expected to have combinations of linear and non-linear effects on the dependent variable, fracture toughness. For the simplicity in the design, the linear effects of aspect ratio and environment are investigated with nonlinear effects of interfacial strength, volume fraction and temperature. Linear effects can be measured with the 2 level values, low and high. However non- linear effects can be estimated with several intermediate levels along with low and high. By combining all these linear and non-linear effects, a full factorial design is normally performed with the combinations of two, three and four level variables whose values are shown in Table 6.1.

Table 6.1. Variables and their levels for investigations of fracture toughness

<b>Variables</b>	<b>Variables Name</b>	<b>Levels</b>	<b>Level Types</b>	<b>Values</b>	<b>Units</b>
A	Aspect ratio(AR)	2	Low, High	1, ~40	
B	Interfacial strength(IS)	3	Low, medium, high		MPa
C	Volume fraction (VF)	3	Low, medium, high	0, 0.5, 2	Vol %
D	Temperature (T)	4	Low, medium high	250, 350,650, 760	°C
E	Environment (E)	2	Inert, reactive	N <sub>2</sub> , O <sub>2</sub>	% O <sub>2</sub>

With the levels of variables mentioned in Table 6.1, the total number of experiments to run for a full factorial design are,  $2 \times 3 \times 3 \times 4 \times 2 = 144$ . This would allow the investigations of main effects and 5 way interactions of the independent variables.

### 6.2.2 Fractional Design

Performing of the full factorial design requires large amount of resources and time. A fractional design would allow the reduction of experiments from the full factorial with the sacrifice in minor higher level interaction and nonlinearity effects. These higher level interactions can be neglected by choosing an alias structure with some assumptions. This alias structure determines the effects which are confounded with each other. At first, with considering the linear effect, all the independent variables can be set at only low and high level, which are shown in Table 6.2.

Table 6.2. Variables with 2 levels for investigations of fractional factorial design

<b>Variables</b>	<b>Variables Name</b>	<b>Levels</b>	<b>Level Types</b>	<b>Values</b>	<b>Units</b>
A	Aspect ratio	2	Low, High	1, ~30	
B	Interfacial strength	2	Low, high		MPa
C	Volume fraction	2	Low, high	0.5, 2	Vol %
D	Temperature	2	Low, high	650 , 760	°C
E	Environment	2	Inert, reactive	N <sub>2</sub> , O <sub>2</sub>	

In order to perform the factorial design with only the 2 level variables the study requires performing  $2^5 = 32$  experiments. Performing these 32 experiments would also require significant

amount of time and resources. By reducing the number of experiments a balanced fractional factorial design can be performed at  $\frac{1}{2}$  or  $\frac{1}{4}$  replicate form which accounts for upto second order interactions among aspect ratio, interfacial strength, volume fraction, and effects of temperature and environment. An orthogonal array matrix is taken to perform the fractional factorial design with the  $\frac{1}{2}$  replicate, which require a total of  $2^{(5-1)} = 16$  experiments as shown in Table 6.3. The investigation of these 16 experiments eliminates any possible 3, 4 or 5 way interactions between these independent variables, but it still maintains the ability to extract information regarding major interactions. In Table 6.4, the alias structure is shown with the confounding of the variables in higher order.

### **6.2.3 Test Matrix**

Test matrix was developed to test the effect of nanomaterial addition into MEYEB on  $K_{IC}$  using fractional factorial design. A half ( $\frac{1}{2}$ ) fractional factorial design was performed to investigate the simultaneous effect of five variables with their high and low values, which is shown in Table 6.2. These variables are re-stated as aspect ratio, volume fraction, interfacial strength, operating environment and temperature. The fractional factorial design was performed with carbon and alumina nanomaterials. Two types of carbon nanomaterials with high and low aspect ratio are CNF and CNP, respectively. Similarly the two types of alumina nanomaterials are ANF and ANP, respectively. All the nanomaterials are to be mixed separately. The test matrix is shown in Table 6.3.



Table 6.3. Test matrix for nanomaterials reinforced MEYEB to perform (1/2) fractional factorial

Materials		V <sub>f</sub>		Temp		Environment		Temp		Environment	
Name	L	Vol %	L	°C	L	Type	L	°C	L	Type	L
ANF	+1,+1	0.5	-1	650	-1	Reactive	+1	760	+1	Inert	-1
	+1,+1	2	+1	650	-1	Inert	-1	760	+1	Reactive	+1
ANP	-1,+1	0.5	-1	650	-1	Inert	-1	760	+1	Reactive	+1
	-1,+1	2	+1	650	-1	Reactive	+1	760	+1	Inert	-1
CNF	+1,-1	0.5	-1	650	-1	Inert	-1	760	+1	Reactive	+1
	+1,-1	2	+1	650	-1	Reactive	+1	760	+1	Inert	-1
CNP	-1,-1	0.5	-1	650	-1	Reactive	+1	760	+1	Inert	-1
	-1,-1	2	+1	650	-1	Inert	-1	760	+1	Reactive	+1

L= Level; high means +1 and low means -1. ANF-Alumina Nanofiber; ANP-Alumina Nanopowder; CNF-Carbon Nanofiber; CNP- Carbon Nano-powder.

#### 6.2.4 Alias and Confounding

With the fractional factorial design some higher order effects are not possible to estimate separately, which are termed as confounded. In that case higher order effects are confounded with comparatively low order effect which means those higher order effects are aliased with the low order effects. Table 6.4 summarizes those alias structures. In this study all three ways

interactions are aliased with some of the two way interactions. This may reduce the capability of finding the effects of all variables in all combinations; however it significantly reduces the number of experiments compared to the full factorial design and potentially indicates the variables and their combinations that have more significant effects than the others.

Table 6.4. Alias structure with confounding in the 1/2 replicate fractional factorial designs

Alias Number	Alias Structure
1	AB=CDE
2	AC=BDE
3	AD=BCE
4	AE=BCD
5	BC=ADE
6	BD=ACE
7	BE=ACD
8	CD=ABE
9	CE=ABD
10	DE=ABC

In Table 6.4, A=Aspect ratio, B=Interfacial strength, C=Volume fraction, D=Temperature, and E=Environment. Previously shown Table 6.3 involves 16 different combinations of these variables. Each row of the test matrix presents two nano-reinforced samples prepared following the prescribed treatment conditions. Two types of such samples as in the first row of Table 6.3 are, 0.5 vol% ANF reinforced MEYEB treated at 650 °C in reactive environment (O<sub>2</sub>) and 0.5 vol% ANF reinforced MEYEB treated at 760 °C in inert environment (N<sub>2</sub>), respectively The specimens for each test type were treated for 5 hours at each treatment condition. Finally fracture

toughness was measured for each type of samples and compared. In summary, fractional factorial design assists in finding the more significant variables and eliminates such variables from the full factorial design that have less significant effects. Fractional design is the starting point of the investigation which directs/regulates the operation of the full factorial design effectively with relatively fewer variables.

### 6.3 Comprehensive Approach with Nano-reinforcement

This study is developed based on the full factorial design that is centered on the investigation of the interactions between Interfacial strength, aspect ratio, temperature and environment at a fixed volume fraction. This study involved three nanomaterials with the aim of better understanding the effect of interfacial strength. Additional nanomaterials used in this study were silicon carbide with low and high aspect ratios such as SCW and SCP, respectively. This study involved a wider temperature range, where MEYEB is practically applicable as the matrix of continuous fiber reinforced composite. The framework of the comprehensive test plan is shown Table 6.5.

Table 6.5. Comprehensive test plan

Variables	Level		
VF	Constant		
IS	Low	Medium	High
AR	Low		High
T	Low	Medium	High
E	Low		High

According to Table 6.5, a constant loading of all the nanofillers were separately added to MEYEB by following optimum processing schedule B2 as described in previous section ( See Table 4.1) . The nanomaterials that were added in various samples are mentioned in the following section. All the nano-reinforced samples were first processed upto 250 C of the processing schedule B2 (see Table 4.1). Then the samples were divided into the groups for treatment at various temperatures and environments as mentioned in the test matrix in Table 6.6. Finally fracture toughness was measured for each type of samples and compared.

### ***6.3.1 Nanomaterials for comprehensive test Plan***

SCW-Silicon carbide whisker

SCP-Silicon carbide particles

ANF-Alumina nanofiber

ANP-Alumina nanoparticles

CNF-Carbon nanofiber

CNP-Carbon nanoparticles

### ***6.3.2 Matrix for Comprehensive Test Plan***

Test matrix for the extended test plan is presented in Table 6.6. Item 1 in Table 6.6 allows the investigation with the variations of interfacial strength and aspect ratio at 250 °C. According to this item 2 vol % of all nanomaterials were reinforced in MEYEB to directly compare with each other and with neat MEYEB. Item 2 was introduced in this Table 6.6 to compare the toughness of neat MEYEB with 2% SCW reinforcement at 350 °C, since the thermal analysis of neat MEYEB (see Figure 5.20 and Figure 5.21) showed some critical changes in the neighborhood of this temperature.

Table 6.6. Combined & extended test plan including full factorial plan

Item	Temp. And Env.	Neat	2% ANF	2% ANP	2% SCW	2 % SCP	2% CNF	2% CNP
1	250 °C	✓	✓	✓	✓	✓	✓	✓
2	350 °C	✓			✓			
3	650 °C (N <sub>2</sub> )	✓	✓	✓	✓	✓	✓	✓
4	650 °C (O <sub>2</sub> )	✓	✓	✓	✓	✓		
5	760 °C (N <sub>2</sub> )	✓	✓	✓	✓	✓		
6	760 °C (O <sub>2</sub> )	✓	✓	✓	✓	✓		

Items 3,4,5 and 6 were suggested to compare the effectiveness of three types of nanomaterials at reasonably high temperatures ( 650 °C and 760 °C ) and two environment conditions ( reactive and non-reactive), however the effectiveness of CNF and CNP were only investigated in non-reactive environment at 650 °C. The reason for this is the possibility of complete degradation of CNF and CNP in reactive environment. Also at higher than 650 °C, CNFs becomes thermally unstable<sup>91</sup>, so no carbon nanomaterials reinforced sample were prepared with heat treatment at 760 °C.

## 6.4 Sample Preparation Technique

### 6.4.1 Mixing of Nanomaterials

Pre-weighed nanomaterials were separately mixed in MEYEB for making nano-reinforced MEYEB of each type. The mass percentage of required amount of nanomaterials (wt. %) were calculated based on the required volume and density of particular nanomaterials as shown in the following equation-

$$wt\% = \frac{V_n\% * \rho_n\%}{V_n\% * \rho_n\% + (1 - V_n\%) * \rho_m\%} * 100\% \quad (23)$$

Where,  $V_n\%$  is the amount of nanomaterials in volume percentage,  $\rho_n$  &  $\rho_m$  is bulk density of dry nanomaterials and liquid density of MEYEB in  $g/cm^3$ , respectively. Bulk densities of various nanomaterials are listed in Table 3.1. The reported density of liquid MEYEB<sup>82</sup> is  $1.79 g/cm^3$ .

For mixing nanomaterials in MEYEB a slow shear mixing was performed using a rolling mill. The shear mixing was achieved by placing the mixing jar in appropriately angled inside a two piece 4-6 inch diameter foam block inserted into a PVC tube, which is shown in Figure 6.1. The Tube-foam-mixing jar assembly was placed on the roller of the rolling mill which was rotated at a speed of 200-300 RPM.

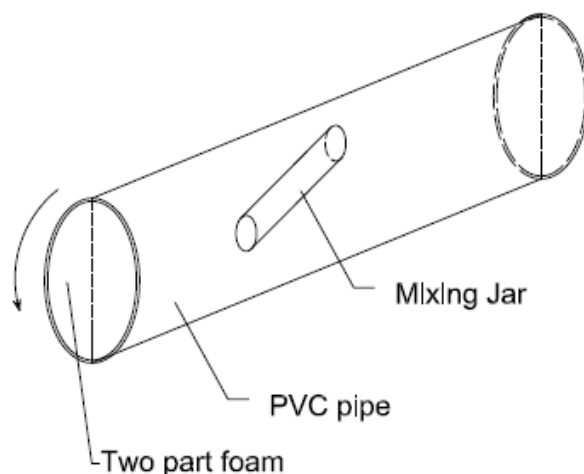


Figure 6.1. Nanoparticle mixing in MEYEB using a Rolling mill

#### **6.4.2 Processing and Curing of Nano-Reinforced Sample**

Acetal mold was used for preparing nano-reinforced samples. The processing and curing of nano-reinforced samples was exactly similar to the one for neat MEYEB samples. The required drying and post processing was performed by following the optimum processing schedule as described in the preliminary processing evaluation, which was schedule B2 (see Table 4.1). Five samples were prepared for each type of test to perform at each combination of temperature and environment as mentioned in Table 6.6. It is worth mentioning that the maximum processing and treatment temperature of the samples for each batch was limited by the temperature specified in Table 6.6, not by the maximum processing temperature as specified in schedule B2.

#### **6.4.3 Sample Preparation for XRD**

XRD study can play important role in investigating the phase transformation and nano-induced nucleation of neat and nano-reinforced MEYEB with the variations in the treatment temperatures and types of nano-fillers. XRDs were performed on neat MEYEB separately treated at 250 °C, 650 °C (O<sub>2</sub>) and 870 °C (O<sub>2</sub>). Additional XRDs were performed in 19-30 degree range on neat

MEYEB separately treated at 650 °C and 760 °C in oxygen. The particular interest was to investigate any XRD peak more closely with high signal to noise ratio. The XRD was performed on 2% SCW reinforced MEYEB in order to investigate the toughening mechanism through the possibilities in phase transformations. The sample that was selected for this study was heat treated at 650 °C in oxygen. All the samples were crushed separately to make fine powder.

## **6.5 Characterization Technique**

### ***6.5.1 Un-notched Bend Beam Test***

This technique is described earlier in chapter 5 for testing neat samples. Similar technique is followed for testing of nano-reinforced samples.

### ***6.5.2 Notched Bend Beam Test***

SEVNB technique is used to measure fracture toughness. This technique is described earlier for testing neat samples. Similar technique is followed for testing of nano-reinforced samples.

### ***6.5.3 Verification of the Notch Effect in the Notched Bend Beam Test***

It is important to investigate whether the breaking load in the SEVNB test represents the actual fracture toughness of the specimens. Since the notches are made on the tensile surface of the specimens, in order to validate the toughness results, the effect of notch tip must be verified. In order to verify this, the breaking load of the notched beam was calculated using the strength measured from the un-notched beam with equivalent thickness deducting the notch depth using equation 24. Then this load was compared with the breaking load of the beam with the notch. The effect of notch can be validated if the breaking load of the notched beam becomes smaller



than the calculated breaking load for the untouched beam of equivalent thickness, because in the notched beam no additional load is required to create a sharp notch or starter crack.

Equivalent thickness ( $w_{eq}$ ) of a notched beam with thickness  $d$  can be calculated using following equation -

$$w_{eq} = \text{Equivalent thickness} = \left(1 - \frac{a}{w}\right) \times w \quad (24)$$

Breaking load ( $F_{eq}$ ) of the beam with equivalent thickness can be calculated using following equation -

$$F_{eq} = \frac{2 \times b \times w_{eq} \times S_b}{3 \times L} \quad (25)$$

Where,  $b$ = specimen width,  $S_b$ = Bending strength from un-notched bend beam test.

#### **6.5.4 Flexural Modulus Measurement**

Using the similar testing technique as described in chapter 5, flexural modulus of neat and nano-reinforced MEYEB was measured in order to investigate the effect of various nanomaterials on the variations in the bonding strength and their relations with the changes in the toughness. Since MEYEB is a low modulus inorganic material, in order for this material to utilize as a matrix for fiber reinforced composites, it is highly necessary to investigate the potential of nano-reinforcement in increasing the modulus of MEYEB. It is also important to compare the flexural modulus of neat MEYEB with the compressive modulus previously measured in chapter 5.

#### **6.5.5 Thermogravimetry Analysis**

The purpose of the study of thermogravimetry of nanofiller materials was to understand the interface condition between MEYEB and nanofillers through the knowledge of diffusion, sublimation and chemical reactions of the materials themselves at the temperature and

environment chosen for preliminary and comprehensive study associated with the nano-reinforcement.

In order to perform the thermogravimetry, nano-materials were heated in silver pan at 5 °C/min and treated at the specified temperatures for 5 hours. Treatment was performed in both oxygen and nitrogen. The purpose of using silver pan was to perform the analysis at as high as 760 °C.

#### **6.5.6 Fractography**

Fractography is an essential characterization tool in evaluating brittle materials. The primary interest in fractography is evaluating the fracture surface. The evaluation of the fracture surface enables in collecting many important information including the changes in microstructure with temperature, the dispersion of nanomaterials, the bonding nature (weak or strong) between the nanofillers and geopolymer, the difference in the pull out length of different types of nanofibers from the matrix and possible sites for nucleation due to the presence of nanofillers. Fractography study was performed using Scanning Electron Microscopy (SEM). Detail on the SEM technique was described chapter 5.

#### **6.5.7 EDS**

Energy dispersive X ray spectroscopy (EDS or EDX) allows the identification of the particular elements in different phases of neat and nano-reinforced MEYEB and their relative proportions (Atomic % and weight %). EDS is a chemical microanalysis technique that adopts the backscattered electron images in the SEM. When the sample is bombarded in the SEM, the electrons eject from the sample. The electrons in higher energy state then fill the electron vacancies by releasing its energy in the form of X-ray, which is detected as the signal from a specific element of the sample. X-rays generated from various elements of the sample depend on

the energy of the bombarded electron needed to eject the electron from the atom. The X-rays of those elements are specific to the elements present in the sample. The detector of EDS is capable of detecting those X-ray energies with a high accuracy and better resolution from the subsurface volume in a few micrometer depths. In order to minimize the noise level and identify closely packed x-ray peaks the accepted practice is to specify the EDS resolution at  $MnK\alpha$  energy<sup>108, 109</sup>.

EDS was performed in SEM equipped with AMTEK EDAX, Model: Octane super with 60 mm<sup>2</sup> detector<sup>110</sup> at the Central Instrumentation Facility in Colorado State University. The detector has a resolution of 130 eV at  $MnK\alpha$ . The detail on the EDS detector can be found in Appendix A7. The x-ray peaks were collected from the pre-specified points on the sample SEM image at the maximum 15 kV SEM electron beams.

### **6.5.8 XRD**

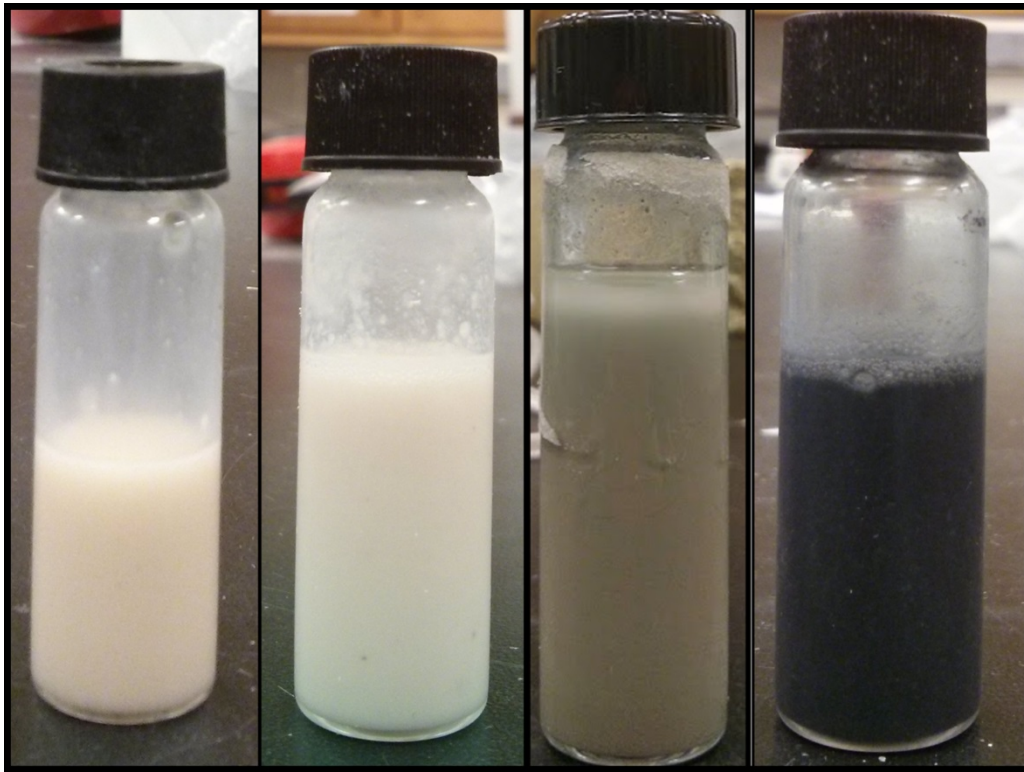
The x-ray diffractogram of MEYEB at various post processing temperature were measured using Scintag X-2 X-ray powder diffractometer. The 0.1542 nm wavelength  $CuK\alpha$  radiation was used in this experiment to measure the intensity peaks of samples in a stationary sample stage in the range of 5 to 85 degree with a step size of 0.02 deg.

## **6.6 Results of the Nano-reinforcement Study**

### **6.6.1 Evaluation of the Nanofiller Dispersion**

Dispersion of 2 vol% alumina nanofibers, silicon carbide whiskers and carbon nano-fibers were primarily evaluated by observing the mixture of nano-reinforced MEYEB (5-7 ml) in the glass vials using a point and shoot camera. During this observation no agglomeration was found the mixture. This confirms the effectiveness of the nanofiller mixing technique. The images are

shown in Figure 6.2. From Figure 6.2 it is found that the color of alumina nanofiber (ANF) mixed MEYEB is uniform and white throughout the geopolymer suspension volume. Similarly for SCW and CNF mixed MEYEB the colors were found as gray and black, respectively. Overall, the uniform color of the individual nanofiller mixed MEYEB suggests an effective dispersion of those nanofillers. The similarities in the chemical structure between the respective nanofibers and nanoparticles (SCW and SCP for example) suggest that the nanoparticles are dispersed in a similar manner as the respective nanofibers or whisker.



(a)

(b)

(c)

(d)

Figure 6.2 (a) Neat MEYEB & (b-d) MEYEB mixed with 2 vol% (b) ANF & (c) SCW (d) CNF in a suspension

Furthermore, the fracture surfaces of the cured and post processed samples were investigated using stereo-viewer at x16 magnification. The fracture surfaces were imaged from the samples treated at 250 C. The images are shown in Figure 6.3. The images further suggest that ANF, SCW and CNF are dispersed uniformly in MEYEB.

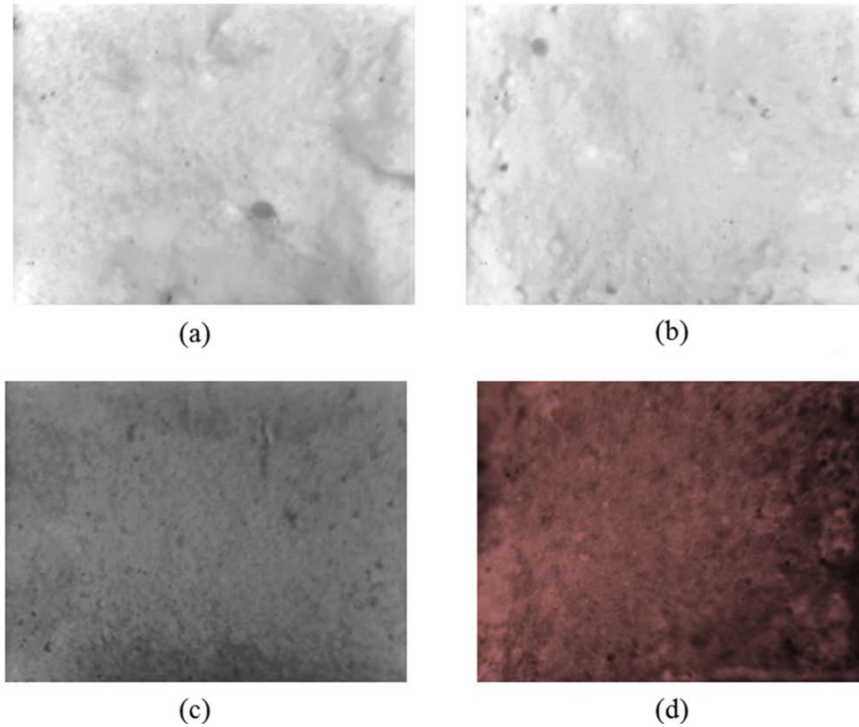


Figure 6.3 Fracture surfaces of (a) neat (b) 2vol% ANF (C) 2vol% SCW and (d) 2vol% CNF added MEYEB ( At x16 magnification)

### **6.6.2 Evaluation of Interfacial Strength**

The purpose of this study is to interpret the interfacial strength between the surface of nanofiller and MEYEB from the study of fracture surface. Fracture surfaces of 2 vol% CNF, SCW and ANF reinforced MEYEB are presented in Figure 6.4 (a), (b) and (c), respectively. Nanomaterials are clearly identifiable in the respective images. In the fracture surface it is observed that

alumina nanofibers are difficult to separate from the matrix. In contrast, CNFs are easily separable from the matrix. CNFs also have long pull out. SCW are attached to the particles of MEYEB. SCW also has torturous surface. Alumina nanofibers are embedded into the polycondensed phase of MEYEB and only interpretable through the appearance of needle like structures. Therefore, ANF and SCW are expected to have strong interactions with MEYEB and CNFs have weak interaction with MEYEB.

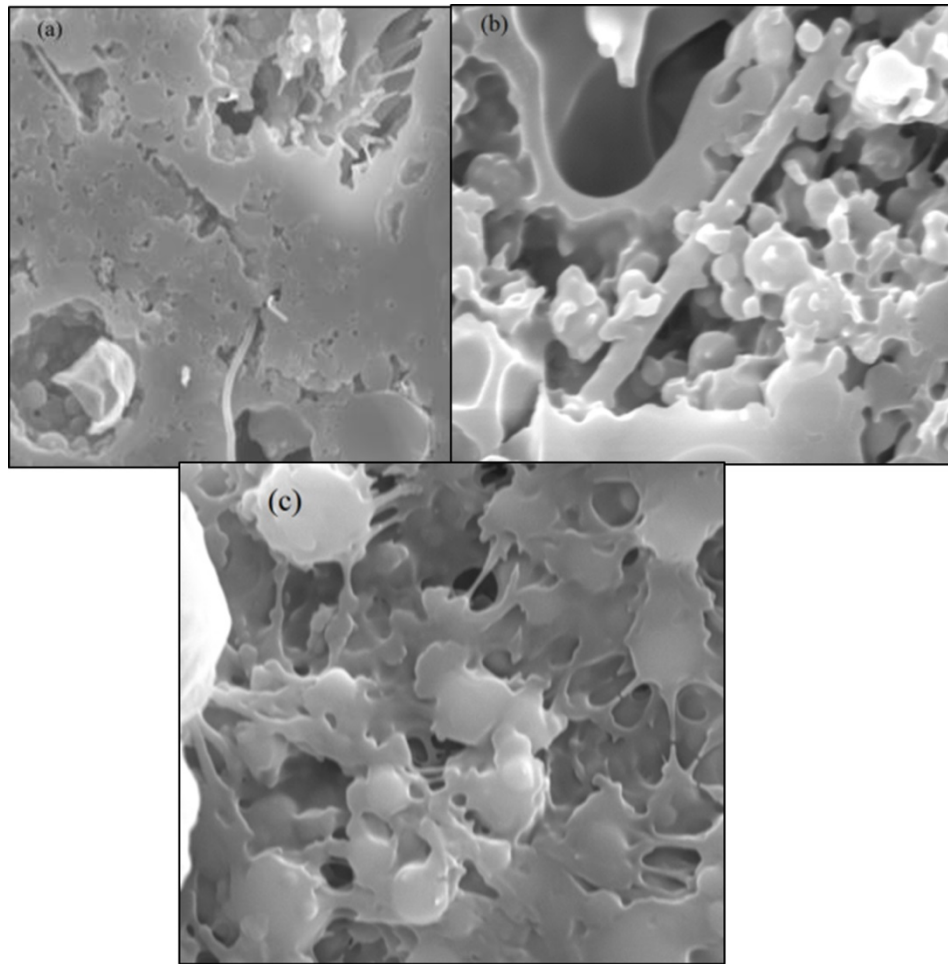


Figure 6.4. Fracture surface of (a) Carbon Nanofiber (CNF) (x2000 magnification) (b) Silicon Carbide Whiskers (SCW) (x10,000 magnification) and (c) Alumina nanofiber (ANF) (x10,000 magnification) reinforced MEYEB.

### **6.6.3 Thermal Analysis of the Nanomaterials**

The purpose of this study is to investigate the thermal stability of the proposed nano-materials with the understanding of the weight gain/losses at various stages of processing and treatment of nano-reinforced MEYEB. This study involved Thermogravimetry of individual nanomaterials before reinforcement into MEYEB. The expectation from the thermogravimetry study is the interpretation of structural integrity, reduction in strength and possible changes in interfacial bond strength with MEYEB.

#### **6.6.3.1 Thermogravimetry of ANF**

Figure 6.5 is the presentation of Thermogravimetry (TGA) of Alumina nano-fibers (ANF) in the 30 -650 °C and 30-760 °C ranges. The key interest of this study is the weight losses at 650 °C and 760 °C at different environmental condition. Total weight losses from the TGA are summarized in Table 6.7 . The weight losses of ANF at 650 °C in nitrogen and oxygen environment are similar. These losses indicate the potential of calcination and oxidation of surface and OH- bonds, respectively. Weight losses also indicate potential reduction in tensile strength of ANF which reduces its effectiveness in toughening of MEYEB. While compared the thermogravimetry upto 760 °C, it was found that the total weight loss is 25% higher in nitrogen environment than in oxygen environment. This possible reason for the higher weight loss in nitrogen is unknown and needs further investigation. This result indicates the reduction in the strength of ANF with the sublimation of ANF surface atoms and a potential reduction in interfacial strength between alumina nanofiber and MEYEB in nitrogen environment.

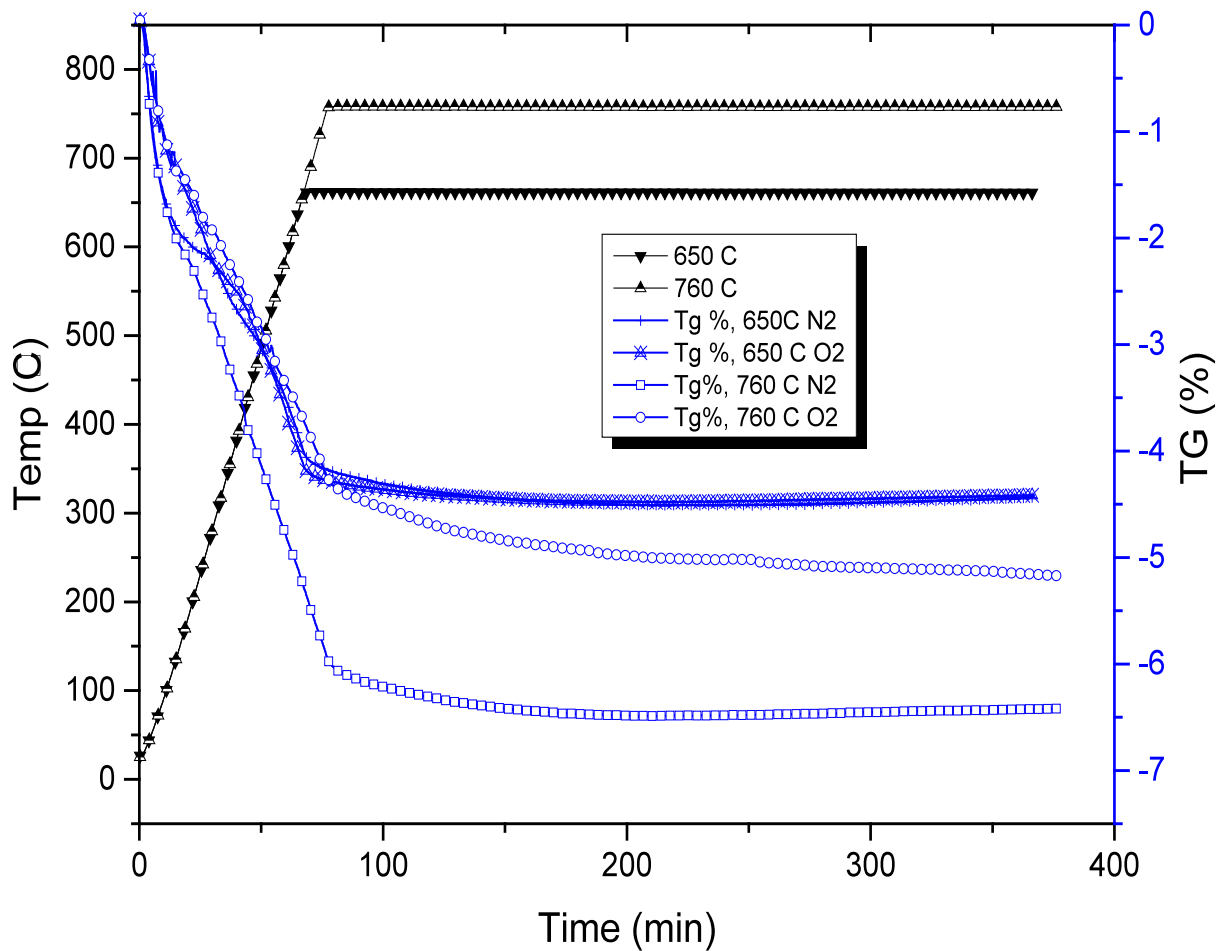


Figure 6.5. Thermal degradation (TG%) of alumina nanofibers (ANF) at 650 °C and 760 °C in oxygen and nitrogen, respectively.

Table 6.7. Weight loss of Alumina nanofiber (ANF) at different temperature and environment

Material	Maximum treat temp, °C	Environment	Weight loss,%
ANF	650	N <sub>2</sub>	4.0
	650	O <sub>2</sub>	4.0
	760	N <sub>2</sub>	6.5
	760	O <sub>2</sub>	5.0



### 6.6.3.2 Thermogravimetry of SCW

Thermogravimetry of Silicon Carbide Whisker (SCW) is presented in Figure 6.6. The analysis was also performed in the 30-650 °C and 30-760 °C temperature ranges. The weight losses in nitrogen at 650 °C and 760 °C were approximately 1.5% and 2.2 %, which indicate the reduction of moisture below 200 °C and the decomposition non-crystalline free carbon<sup>111</sup> starting at 350 °C<sup>112</sup>. While treated in oxygen, the weight gradually drops until temperature is reached to the maximum and then weight gradually increases with the hold times. The gain in weights in oxygen at those temperatures (especially at 760 °C) indicates silicon dioxide layer formation. SiO<sub>2</sub> layer formation is suggested to occur at 760 °C which should protect the whiskers until about 1900 °C<sup>113</sup>. Total weight loss SCW at each TGA are shown in Table 6.8.

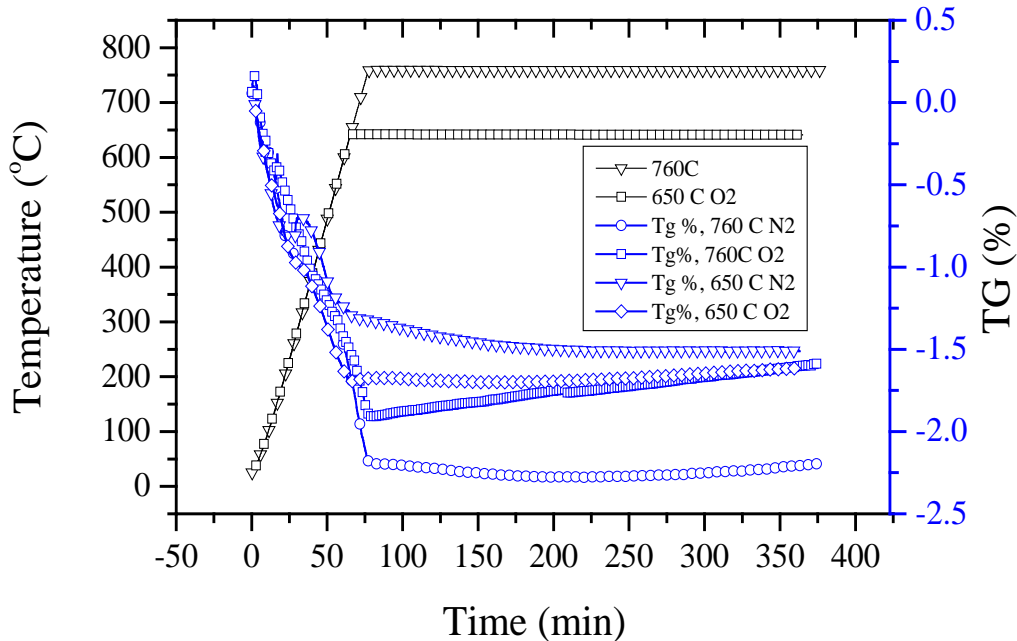


Figure 6.6. Thermal degradation (Tg%) of Silicon Carbide Whisker (SCW) at 650 °C and 760 °C in oxygen and nitrogen, respectively.

Table 6.8. Weight loss of SCW at different temperature and environment

Material	Maximum Treat temp, °C	Environment	Weight loss, %
SCW	650	N <sub>2</sub>	1.5
	650	O <sub>2</sub>	1.6
	760	N <sub>2</sub>	2.25
	760	O <sub>2</sub>	1.6

#### 6.6.4 Results-Preliminary Studies

##### 6.6.4.1 Investigations of the Fracture Surfaces

The purpose of presenting the fracture surfaces after SEVNB test was to have a visual observation of the origin of crack and co-linear crack propagation. Fracture surfaces of neat and nano-materials reinforced MEYEB specimens are shown in the Figure 6.7- Figure 6.10. The fracture surfaces of the specimens in those figures are representative of the test matrix in Table 6.3.

Fracture surfaces of ANF and ANP reinforced samples are presented in Figure 6.7 and Figure 6.8. It is found that the surface of the samples treated in oxygen (Figure 6.7(a) Figure 6.8 (a)) remained white; however in nitrogen (Figure 6.7(b) and Figure 6.8(b)) the surfaces became partially gray from outside. The reason for this change in color was may be due to some contamination on the samples from the mold and polishing of the surfaces. Treatment of the samples in nitrogen at high temperature allowed the depletion of this unknown material as a thin layer on the sample. It is clear from the figures (Figure 6.7 (b) and Figure 6.8 (b)) that the

contamination did not propagate through the entire thickness of the specimen. Once the notch was created on the tensile surface of the samples the color of the subsurface materials was found as expected. It is seen in Figure 6.7 (b) and Figure 6.8 (b) that the tips of the cracks are free from contamination, which confirms no effect of surface contamination of fracture toughness. The faces perpendicular to the notch still have contamination and can possibly affect the toughness results. To verify this with confidence four surfaces of some samples were grounded to remove the contamination and performed notched bend beam test. The notched bend test on the grounded samples did not show any statistically significant differences in the fracture toughness. This test confirmed that the dark or gray appearance on the surfaces of the samples treated in nitrogen did not affect the toughness results.

The fracture surfaces of carbon nanomaterials reinforced specimens are shown in Figure 6.9 and Figure 6.10. The surfaces were found as expected except the CNF reinforced specimen treated in oxygen. The dark appearance on the surface was due to the insufficient exposure of the light source while photographs were taken.



Figure 6.7. Fracture surfaces of ANF reinforced and treated at 760 °C in (a) oxygen and (b) nitrogen.



(a)

(b)

Figure 6.8. Fracture surface of ANF reinforced and treated at 650 °C in (a) oxygen and (b) nitrogen.



(a)

(b)

Figure 6.9. Fracture surface of CNF reinforced and treated at 650 °C in (a) oxygen and (b) nitrogen.



(a)

(b)

Figure 6.10. Fracture surface of Carbon nanofiber reinforced and treated at 760 °C in (a) oxygen and (b) nitrogen.

CNF reinforced specimen treated at 650 °C in oxygen did not turn completely white, which may indicate that some nanofibers still remained intact. At 760 °C in oxygen the specimen turned completely white. This suggests that nanofibers were completely burnt out of the MEYEB matrix at 750 °C in oxygen.

#### **6.6.4.2 Fracture Toughness Evaluation**

The Purpose of this study is to measure the fracture toughness of MEYEB reinforced with various nanofillers and treated at various thermodynamic conditions. The results presented in this section directly represent the study of fracture toughness with the specimens related to the preliminary investigation with alumina and carbon nanomaterials.

##### **6.6.4.2.1 Evaluation Based on Material Analysis**

Fracture toughness results of neat, alumina and carbon nanomaterial reinforced MEYEB samples are presented in Figure 6.11 and Figure 6.12 . These results correspond to the studies of fractional factorial design in Table 6.3. It is found that the fracture toughness of neat MEYEB treated at 650 °C & 760 °C in N<sub>2</sub> is  $0.51 \pm 0.028 \text{ MPa}\sqrt{\text{m}}$  and  $0.6 \pm 0.05$ , respectively.

An increasing trend in fracture toughness was observed in 0.5 vol% and 2 vol% alumina nanofiber (ANF) reinforced MEYEB treated at 650 °C in oxygen and nitrogen, respectively (Figure 6.11). It is found that fracture toughness increased by over 20% and 32% while MEYEB was reinforced with 0.5 and 2 vol% ANF, respectively. This means that, fracture toughness of 2 vol% ANF reinforced MEYEB is approximately 12% higher ( $0.72 \text{ MPa}\sqrt{\text{m}}$  vs  $0.63 \text{ MPa}\sqrt{\text{m}}$ ) compared to 0.5 vol% ANF reinforced MEYEB. With the similar amount of ANP reinforcement no improvement in fracture toughness found.

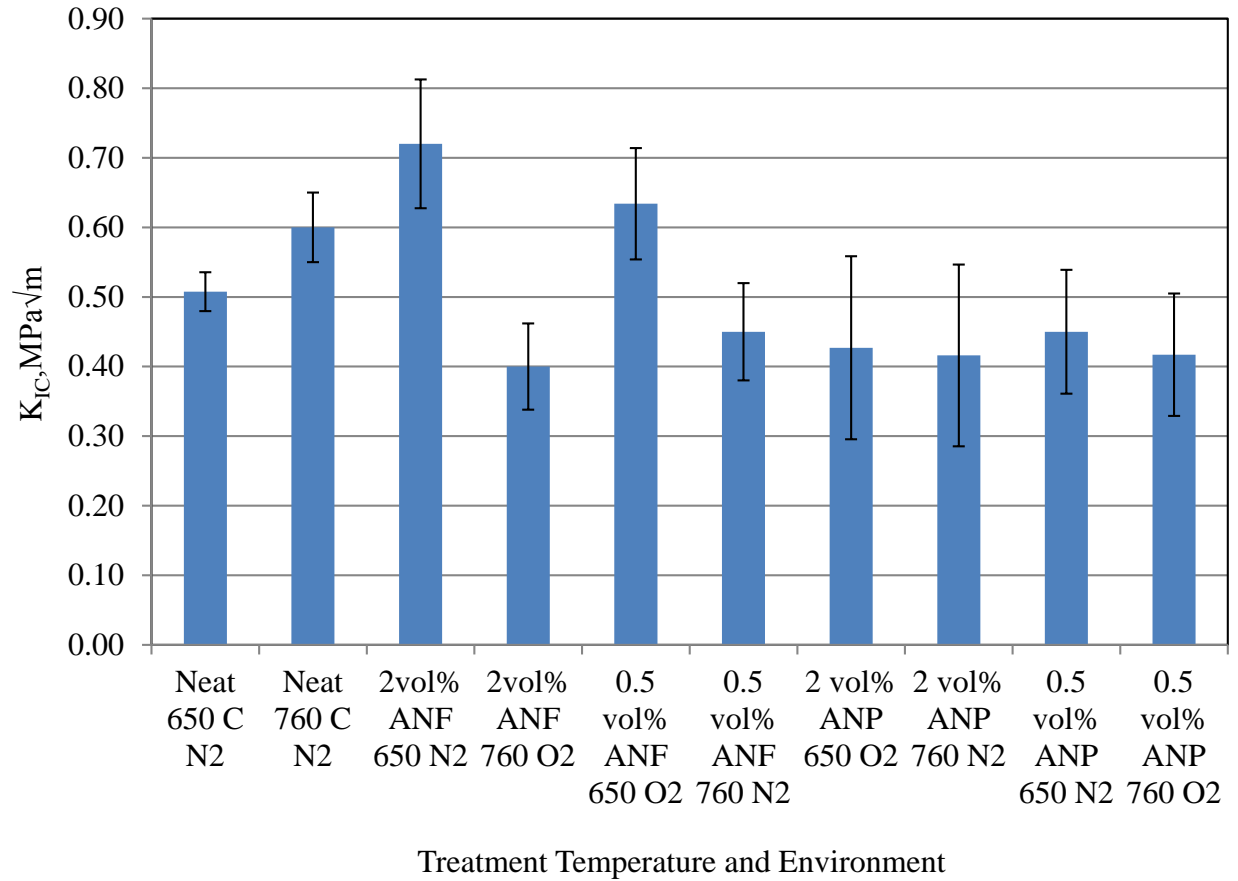


Figure 6.11. Fracture toughness of neat and ANF and ANP reinforced MEYEB with various volume fractions of nanomaterials.

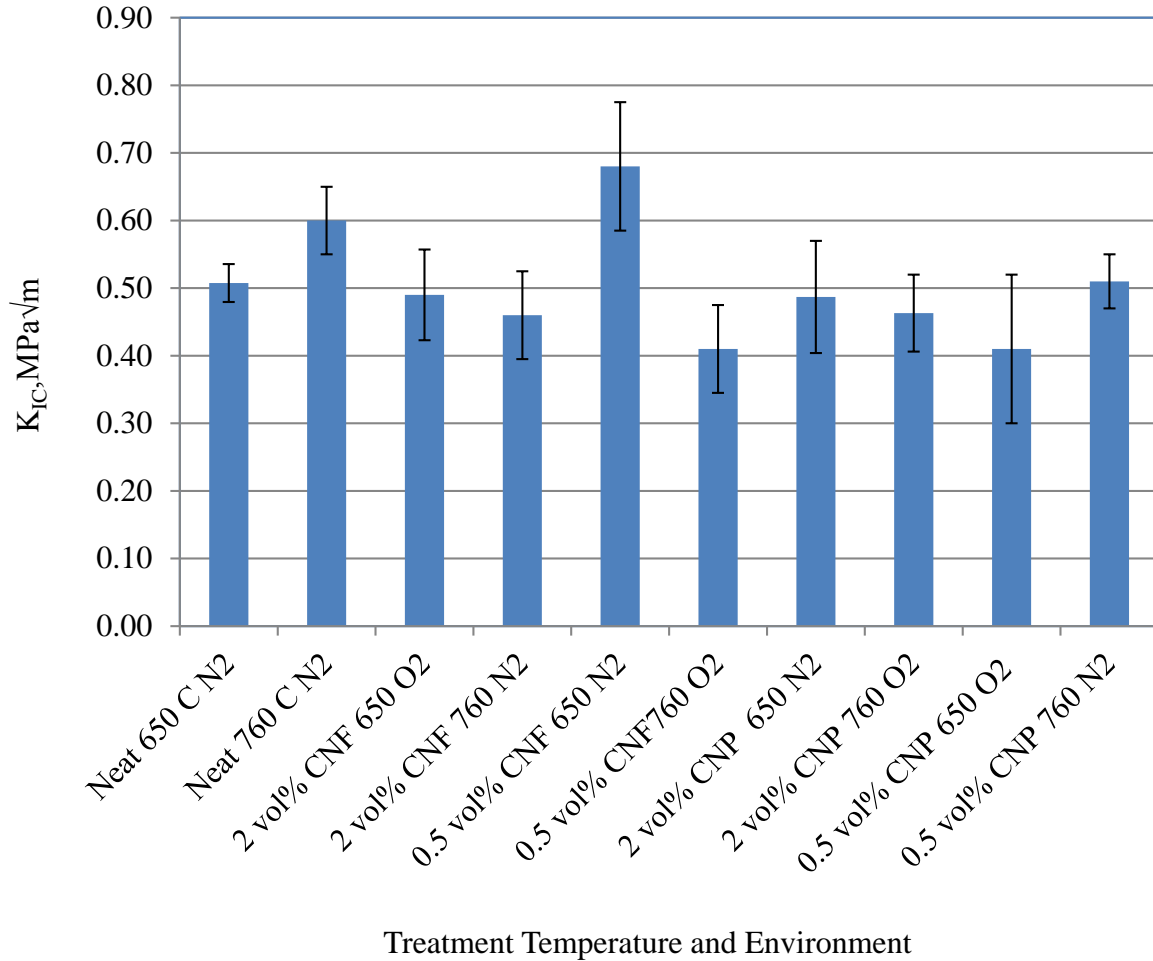


Figure 6.12. Fracture toughness of neat and CNF and CNP reinforced MEYEB with various volume fractions.

When MEYEB was treated at 760 °C the response in the fracture toughness was found to be different. Toughness of 2 vol% ANF reinforced MEYEB treated at 760 °C (O<sub>2</sub>) reduced by approximately 18% compared to neat MEYEB treated at 650 °C (N<sub>2</sub>). Fracture toughness of various CNFs reinforced MEYEB specimens are presented in Figure 6.12. It is found that, 0.5 vol% CNFs reinforced MEYEB in oxygen at 760 °C did not show any increase in fracture toughness. CNFs treated in inert environment remain intact and contributed to increase in toughness. Therefore, 0.5 vol % CNFs reinforced MEYEB treated in nitrogen showed some

increase in fracture toughness, which is around 27.8% higher than neat MEYEB treated at 650 °C in N<sub>2</sub>. When 2% CNF reinforced MEYEB treated in oxygen at both 650 °C and 760 °C, no improvement in toughness was found, rather some loss in toughness was found in the sample treated in oxygen at 760 °C. 2 vol% CNF reinforced MEYEB treated at 760 °C in N<sub>2</sub> did not have any increase in fracture toughness; rather the toughness decreased from the neat MEYEB at 650 °C treated in N<sub>2</sub>. Similarly the toughness of 0.5 vol% CNFs reinforced MEYEB treated at 760 °C in oxygen was found lower than neat MEYEB at 650 °C.

Load-cross head displacement profiles of neat, 0.5 vol% ANF and 2 vol% ANF reinforced MEYEB are presented in Figure 6.13. It is worth mentioning that the displacement data in Figure 6.13 are for comparison only. The actual opening of the crack or the crack extension can be measured from the clip gage extensometer. It is seen that, in the linear elastic regime, 2 vol% ANF contributed to the increase in the slope of load –displacement profile. Later it is shown that 2 vol% ANF actually led to increase the flexural modulus of MEYEB.

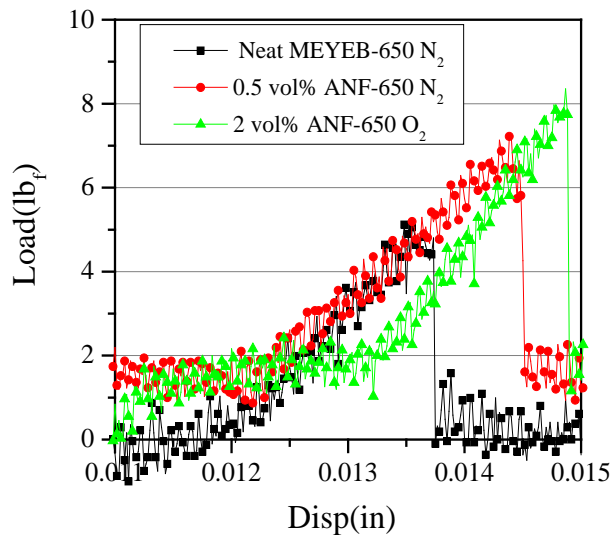


Figure 6.13. Load-cross head displacement profiles of neat and Alumina nanofiber reinforced MEYEB specimens in notched beam flexural strength (SEVNB) test



Some key results from ANF and CNF reinforcement are summarized in Table 6.9. In summary, while ANF reinforcement is considered, two samples performed better than neat MEYEB, which are 2 vol% ANF reinforced MEYEB treated at 650 °C (N<sub>2</sub>) and 0.5 vol% ANF reinforced MEYEB treated at 650 °C (O<sub>2</sub>). Similarly when CNF reinforcement is considered, only one sample performed better than neat MEYEB, which is 0.5 vol% CNF reinforced MEYEB treated at 650 °C (N<sub>2</sub>). The results are further analyzed in the following section.

Table 6.9. Summary of toughness results from preliminary studies

Sample	Treatment	K <sub>IC</sub> , (MPa*m <sup>1/2</sup> )	Change, %
Neat	650 °C N <sub>2</sub>	0.51±0.028	
Neat	760 °C N <sub>2</sub>	0.6±0.05	
2vol% ANF	650 °C N <sub>2</sub>	0.69±0.09	+35%
2vol % ANF	760 °C O <sub>2</sub>	0.41±0.06	-20%
0.5vol% ANF	650 °C O <sub>2</sub>	0.61±0.06	+20%
0.5vol% CNF	650 °C N <sub>2</sub>	0.65±0.09	+27%
0.5% CNF	760 °C O <sub>2</sub>	0.43±0.065	-28%

#### 6.6.4.2.2 Analysis of Preliminary Results

The proportional increase in fracture toughness with the increase in ANF (see Figure 6.11) suggests strong interface effect in both nitrogen and oxygen environments. Increase in fracture

toughness with the increase in ANF content in MEYEB indicates the positive effect of high aspect ratio nanofillers. From the presentation of the load–cross head displacement (Figure 6.13) it is clear that the slopes of the load-displacement profiles within the elastic limits are constant for neat and ANF reinforced specimens and ANF led to increase modulus of MEYEB.

The variations in the toughness of neat MEYEB at 650 °C and 760 °C suggest gradual increase in toughness with temperature. But with ANF toughness is reduced at 760 °C. This suggests that at this high temperature ANF losses its structural integrity and effectiveness in toughening. CNFs are known as the high performance nano-filler for toughening of organic polymer matrix. However due to low thermal stability CNFs are not expected to retain the toughness of the matrix at high temperature and reactive environment. CNFs treated in inert environment remain intact and contribute to increase in toughness. CNFs reinforced sample treated in oxygen lost CNFs completely and was left with more voids, which resulted in lower toughness compared to neat samples treated at 760 °C. Moreover, the decrease in toughness of 2% CNF reinforced MEYEB at 760 °C in nitrogen and oxygen suggests the structural loss of MEYEB and complete loss of CNFs, respectively.

#### 6.6.4.3 Statistical Presentation of Preliminary Results

The results presented in Figure 6.11 and Figure 6.12 are combined and represented with various statistical tools such as Pareto, ANNOVA Table and effect plots. Pareto chart presents the cumulative effect of individual variables and their interactions on the fracture toughness of MEYEB. The Pareto effects can be calculated using the following equation-

$$E_i\% = \frac{E_{i-1}+E_i}{\sum_{i=1}^n E_i} \times 100\% \quad (26)$$

Where  $E_{i-1}$  and  $E_i$  stand for the effect of any variable and the effect of next one, where all the effects are ordered from high to low. Pareto charts of the effects of the variables are presented in Figure 6.14. Pareto chart shows that the cumulative effects of 5 variables contribute to the 80% of the total effects of toughening. These are VF, AR\*T, AR, T and E. Among these variables, volume fraction (VF) has only main effect and no interaction effect. ANNOVA chart shows the comparison between the effects without summing them up. ANNOVA chart is presented in Table 6.10. The key understanding from this ANNOVA chart (Table 6.10) is the p-value. The lower p-value for a main or interaction effect indicates that the probability of that particular effect is significant. Main and interaction effects of the variables are presented in Figure 6.15 and Figure 6.16.

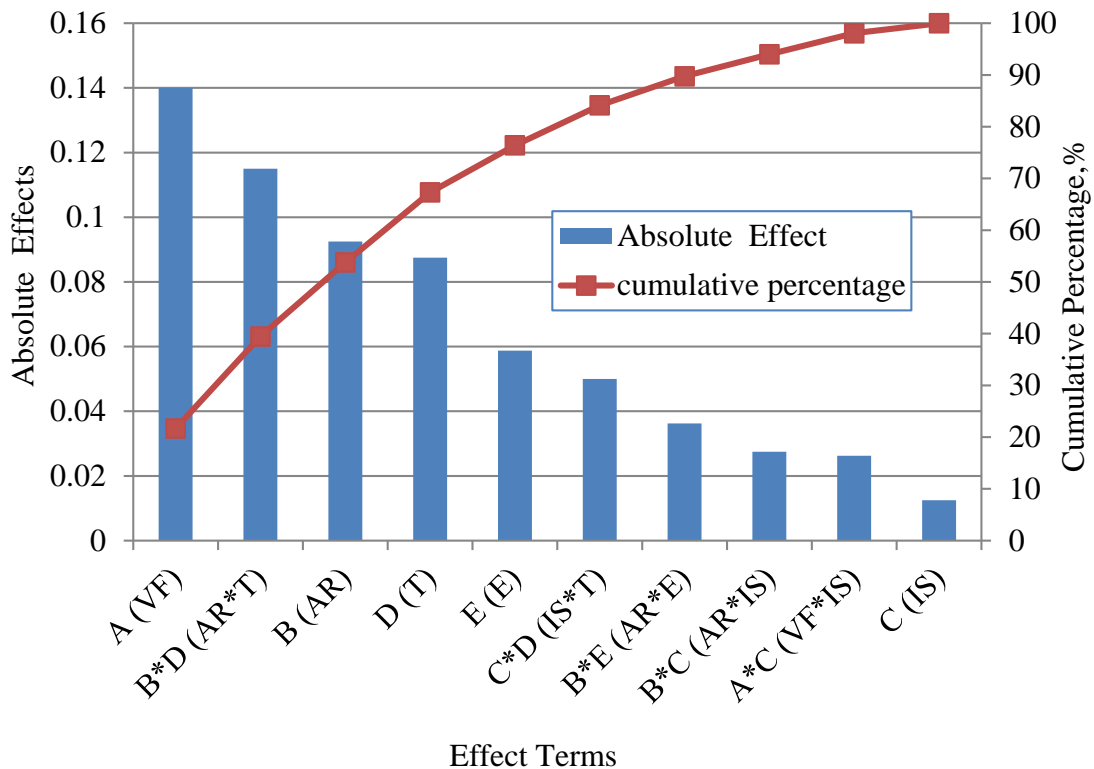


Figure 6.14 PARETO chart showing the main and interaction effects of the variables

Table 6.10. ANNOVA chart showing the results from the design of experiments

Source	DF	SS	MSS	F	p-value
Model	10	0.31	0.031	43.55	9E-12
A (VF)	1	0.0036	0.0036	5.074	0.035
B (AR)	1	0.068	0.0684	96.15	2.7E-09
C (IS)	1	0.001	0.0012	1.75	<b>0.199</b>
D (T)	1	0.061	0.0612	86.03	7.1E-09
E (E)	1	0.027	0.0276	38.78	3.5E-06
AC (VF*IS)	1	0.0055	0.0055	7.74	0.0111
BC (AR*IS)	1	0.006	0.006	8.498	0.0083
BD (AR*T)	1	0.105	0.1058	148.61	5.4E-11
BE (AR*E)	1	0.0105	0.0105	14.77	0.0009
CD (IS*T)	1	0.02	0.02	28.093	3E-05
Residual Error	21	0.015	0.0007		

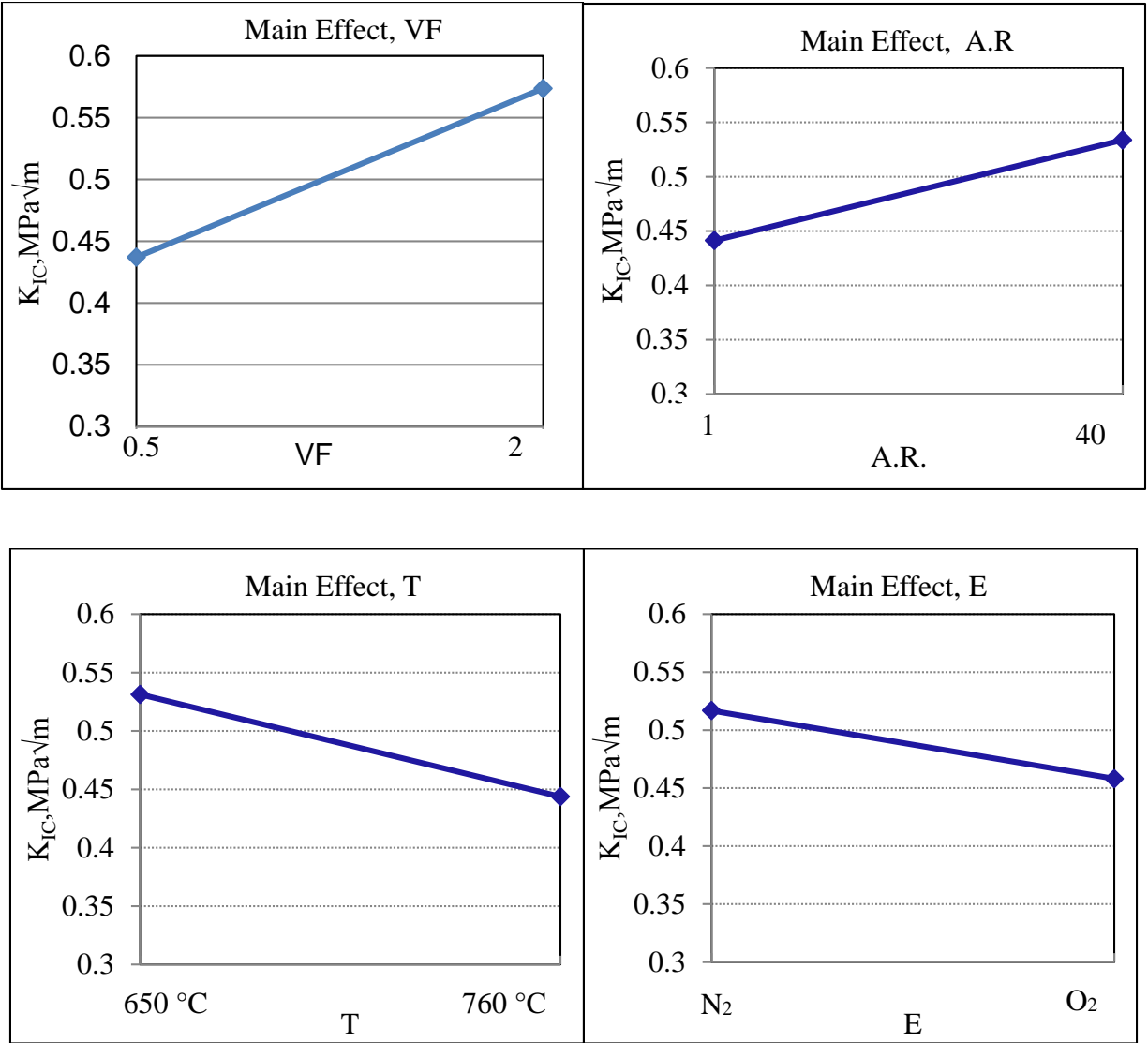


Figure 6.15. Experimental results of the main effect of A- Volume Fraction, B- Aspect Ratio, D-Temperature and E-Environment.

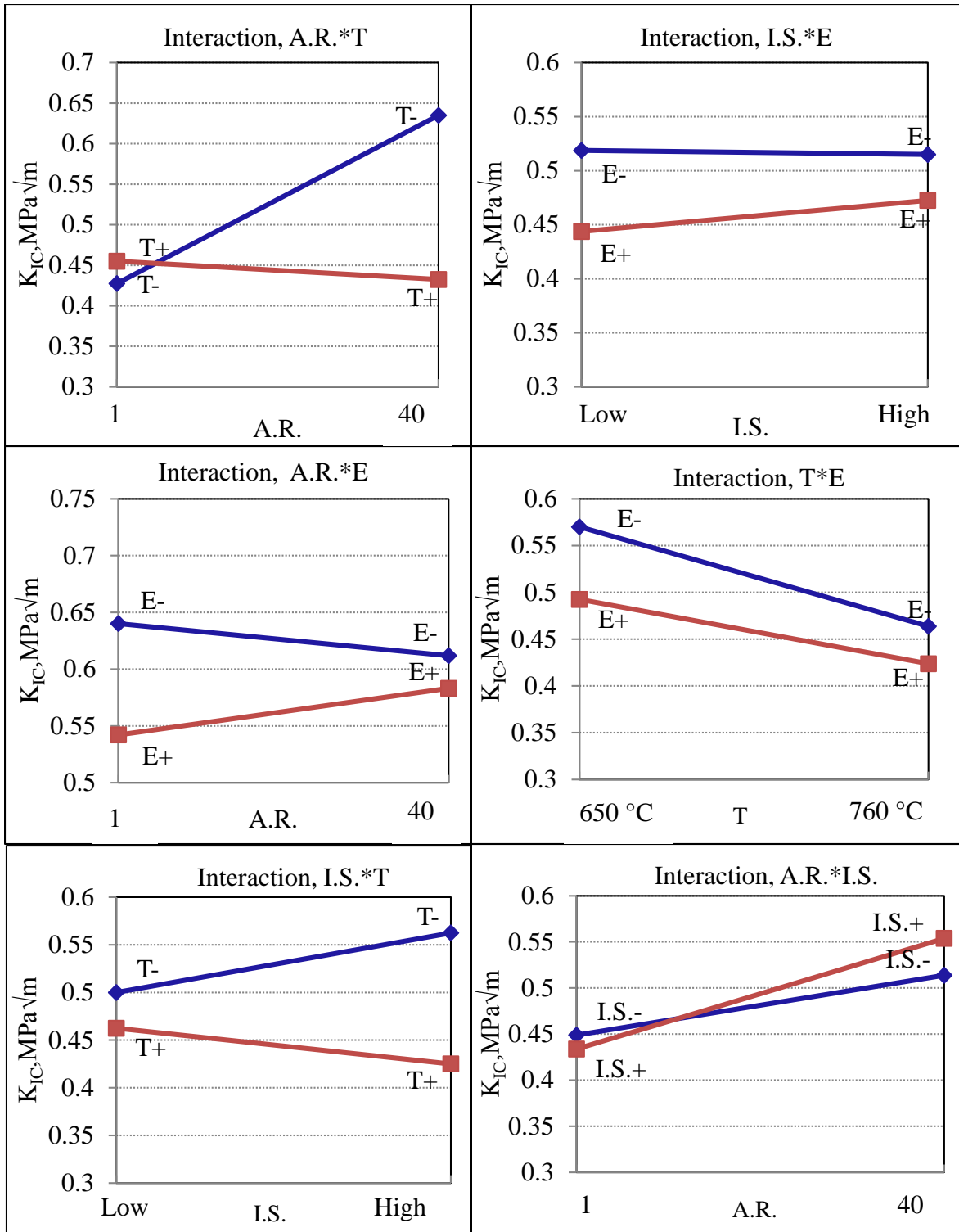


Figure 6.16. Experimental results of the combined effect of A- Volume Fraction, B-Aspect Ratio, C-Interfacial Strength, D-Temperature and E-Environment.

Findings from the Pareto chart (Figure 6.14, ANNOVA table ( Table 6.10) and effect charts (Figure 6.15 and Figure 6.16 ) are summerized as follows-

1. Interaction effect of Aspect Ratio (B) and Temperature (D) is significant. Main effects of those two variables are also significant. High aspect ratio (B) and low operating temperature (D) is favorable for high fracture toughness.
2. Variables that have significant effects on fracture toughness are Volume Fraction (VF), Aspect Ratio (B), Temperature (D) and Environment (E).
3. Variable that has minimum effects on fracture toughness is Interfacial Strength. (C). Low main effects is obtained from this variable.
4. ANNOVA Table (Table 6.10) presents p values of the main and interaction effects. It is mentioned that, lower p value means that the effect of a variable is significant. The following variables have significant effects-Aspect ratio & Temperature (A.R.\*T); Aspect Ratio & Interfacial Strength (A.R.\*I.S.); Interfacial strength & Temperature ( I.S.\*T) and Interfacial strength & Environment (I.S.\*E).

These effects are significant, but I.S. has the lowest main effect and highest p value. Therefore, according to the ANNOVA analysis, the effect of interfacial strength (C) is insignificant. Also the bar charts presenting the fracture toughness results of nano-reinforced samples (Figure 6.11 and Figure 6.12) have shown no direct comparison between the materials with high and low interfacial strength. It is previously stated that, between the two nano-materials, alumina nanomaterials have stronger interfacial strength with MEYEB than carbon nano-materials. However, from this preliminary study the effect of nanofillers/MEYEB interfacial strength could not be measured with statistical significance. The probability value of the effect of interfacial

strength was the highest ( $P=0.2$ ) of all the main and interfacial effects, which suggests that new studies with a new test matrix is required. Also the baseline neat specimens were not compared for all treatment temperatures and environments. It is therefore highly important to evaluate the properties of neat MEYEB at various processing and treatment temperatures at reactive and non-reactive environment, respectively.

The study based on the comprehensive test plan was able to verify the effects of interfacial strength, environment and temperature in a more direct way. A preliminary test was performed in this respect, to show the effect of SCW reinforcement on the toughness of MEYEB and judgment of using silicon carbide nanomaterial in the comprehensive test plan. The results from the preliminary study and comprehensive test plan were presented in the subsequent sections.

#### 6.6.4.4 Justification for Studying in a Single Volume Fraction

Effect of volume fraction of SCW on toughness of MEYEB is presented in Figure 6.17.

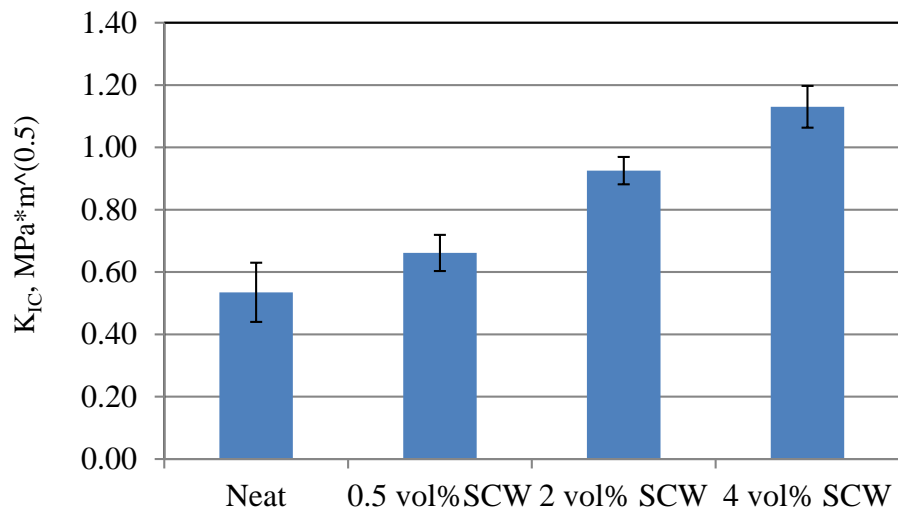


Figure 6.17. Variations in toughness of MEYEB with the addition of SCW nano-fillers in different volume fractions and treated at 350 °C.



From this initial study of 0.5 and 2 vol% SCW reinforced MEYEB it is found that with two volume fractions (0.5 and 2 %) added the toughness increased by 24.5 % and 73%, respectively. Toughness is found to increase with further loading of SCW. With 4% SCW addition toughness increased by 113%. The increase in toughness is close to linear with the  $R^2= 0.97$  which is shown in Figure 6.18.

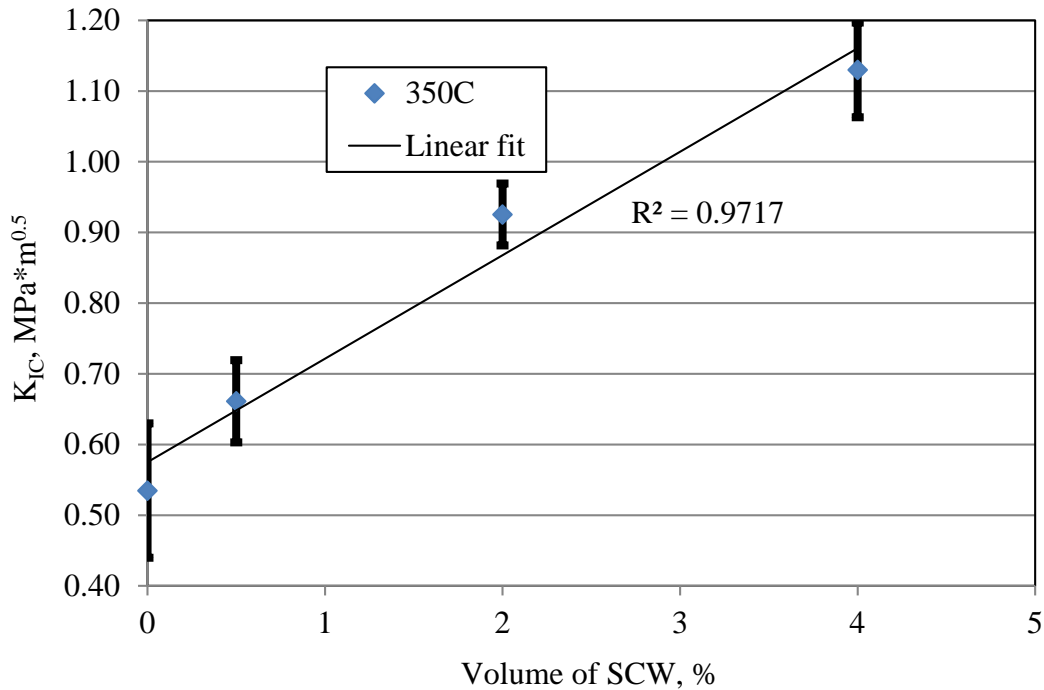


Figure 6.18. Variations in toughness of MEYEB with addition of SCW nanofillers.

The proportional increase in toughness with the addition of SCW suggests that there is a good chance of increase in the toughness with the addition of SCW at loading rates higher than 4 vol%. This linear relationship indicates that volume fraction of SCW has only main effect on the fracture toughness and there is no interaction of the effect of volume fraction with the effects of other variables mentioned in Table 6.1. Therefore the performance of the listed variables (see Table 6.1) can be investigated by keeping the loading of nanomaterial at a single volume

fraction. High loading of nano-materials reduces the loading of MEYEB while the investigation of continuous fiber reinforced composite is performed. In addition, organic nanofillers, CNF and CNP with high volume fractions are difficult to disperse uniformly into inorganic geopolymer. Therefore, the comprehensive study is performed with the loading of nanofillers at 2 vol%.

### **6.6.5 Results- Comprehensive Studies**

The purpose of the comprehensive study is to measure the fracture toughness and flexural strength of neat MEYEB and MEYEB added with various nanofillers and treated at various thermodynamic conditions. The results presented in this section directly represent the study of fracture toughness with the specimens related to the comprehensive test plan (Table 6.6) with silicon carbide, alumina and carbon nanomaterials.

#### **6.6.5.1 Effect of Aspect Ratio on $K_{Ic}$ of MEYEB**

Fracture toughness,  $K_{Ic}$  of neat and various high aspect ratio nanofillers reinforced MEYEB at 250 °C is presented in Figure 6.19.

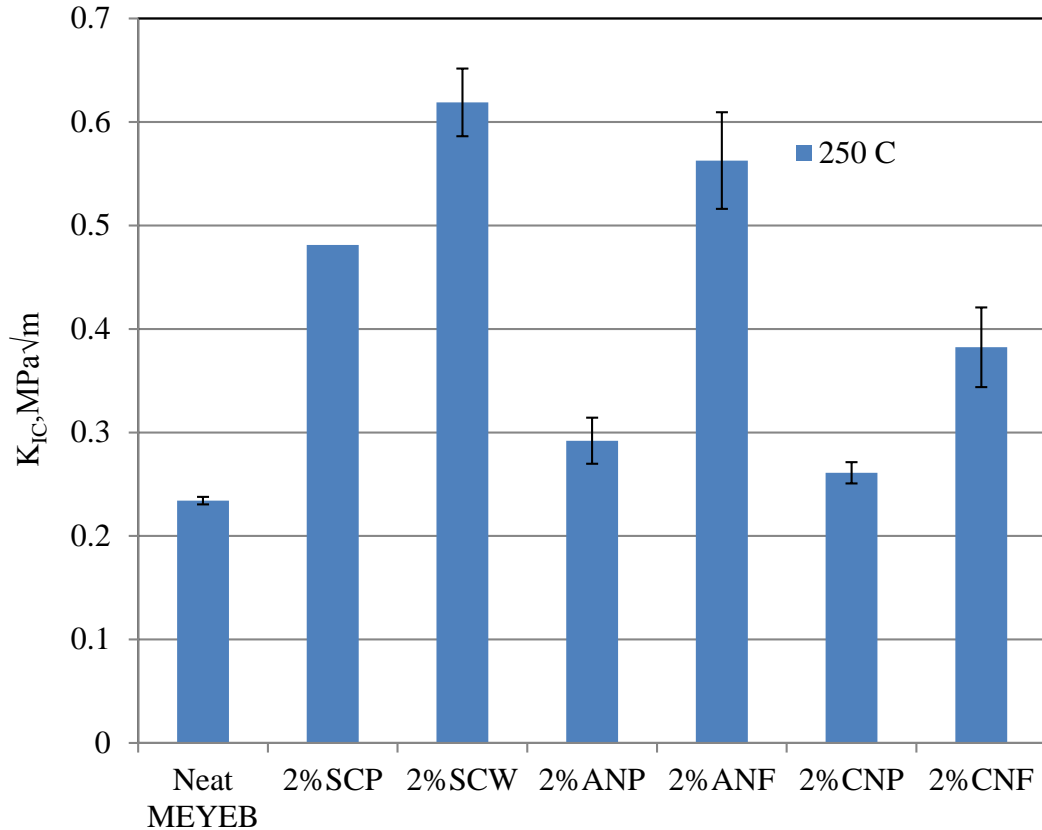


Figure 6.19 Toughness of neat and various nano-fillers (low and high aspect ratio) reinforced MEYEB treated at 250 °C.

As seen in the data presented in Figure 6.19, the higher aspect ratio versions of each nanomaterial show higher fracture toughness values than the particulate form. In fact, among the nanoparticles, only the SCP and ANP show statistically significant improvements over the neat MEYEB. However, all of the high aspect ratio nano-fillers or nanofibers showed a measurable improvement in fracture toughness over the neat MEYEB, with the 2% SCW showing, by far, the highest fracture toughness.

### 6.6.5.2 Effect of Temperature on $K_{IC}$ of Nanofibers Reinforced MEYEB

Figure 6.20 presents  $K_{IC}$  of high aspect ratio nanofillers reinforced MEYEB treated at various temperature and environments.

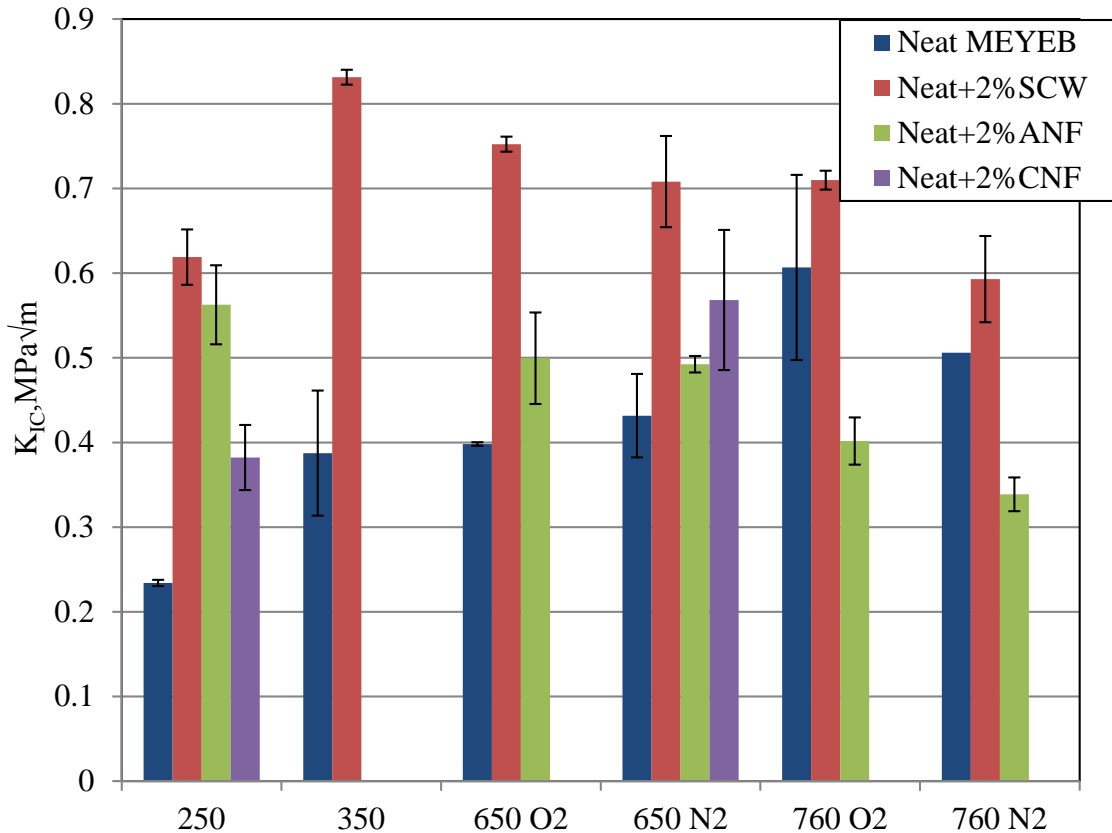


Figure 6.20. Toughness of neat and various high aspect ratio nano-fillers reinforced MEYEB at various temperatures and environments.

It is found that at 250 °C and 650 °C, SCW and ANF results in higher improvements in fracture toughness of MEYEB compared to CNF. At 250 °C, the improvement in toughness with 2 vol% loading of SCW, ANF and CNF compared to respective neat samples at 250 °C were by 0.38, 0.33 and 0.15 MPa\*m<sup>1/2</sup> or 165%, 143% and only 65%, respectively. At 650 °C in nitrogen, the improvement in flexural strengths with 2 vol% loading of SCW, ANF and CNF compared to the

respective neat samples were 0.27, .06 and 0.13 MPa\*m<sup>1/2</sup> or 62%, 14% and 32%, respectively. Therefore, high aspect ratio nanofillers seem to be more effective in strengthening MEYEB at 250 °C compared to the respective effects at 650 °C in nitrogen. In oxygen the improvement with 2vol% SCW loading the improvement in flexural strength is 232%, which is higher compared to the improvement in the respective sample treated at 250 °C.

Fracture toughness results at 350 °C are interesting. At 350 °C, 2% loading of SCW resulted in toughness improvement by 0.45 MPa\*m<sup>1/2</sup> compared to respective base line, whereas the improvement of the similar system at 250 °C was only 0.38 MPa\*m<sup>1/2</sup>. With the same loading, toughness dropped a small amount while treatment temperature increased from 350 °C to 650 °C.

Findings of Figure 6.20 can be summarized in a different way. It is found from Figure 6.20 that, with 2% SCW reinforcement the increase in toughness from neat MEYEB is almost 160% at 250 °C, however there is only 92% increase from neat MEYEB at 650 °C. The increase in toughness with SCW reinforcement is the highest at 350 °C. There is also 70% increase in toughness of neat MEYEB itself while the treatment temperature was increased from 250 °C to 650 °C in nitrogen. Therefore it seems that the contribution of SCW reinforcement in toughening of MEYEB is fairly constant at both 250 °C and 650 °C.

#### **6.6.5.2.1 Environment Effects K<sub>IC</sub> of Nanofibers Reinforced MEYEB**

Part of Figure 6.20 is separately presented here in Figure 6.21 to show the effect of environment on toughness variations on neat and nanofibers reinforced MEYEB.

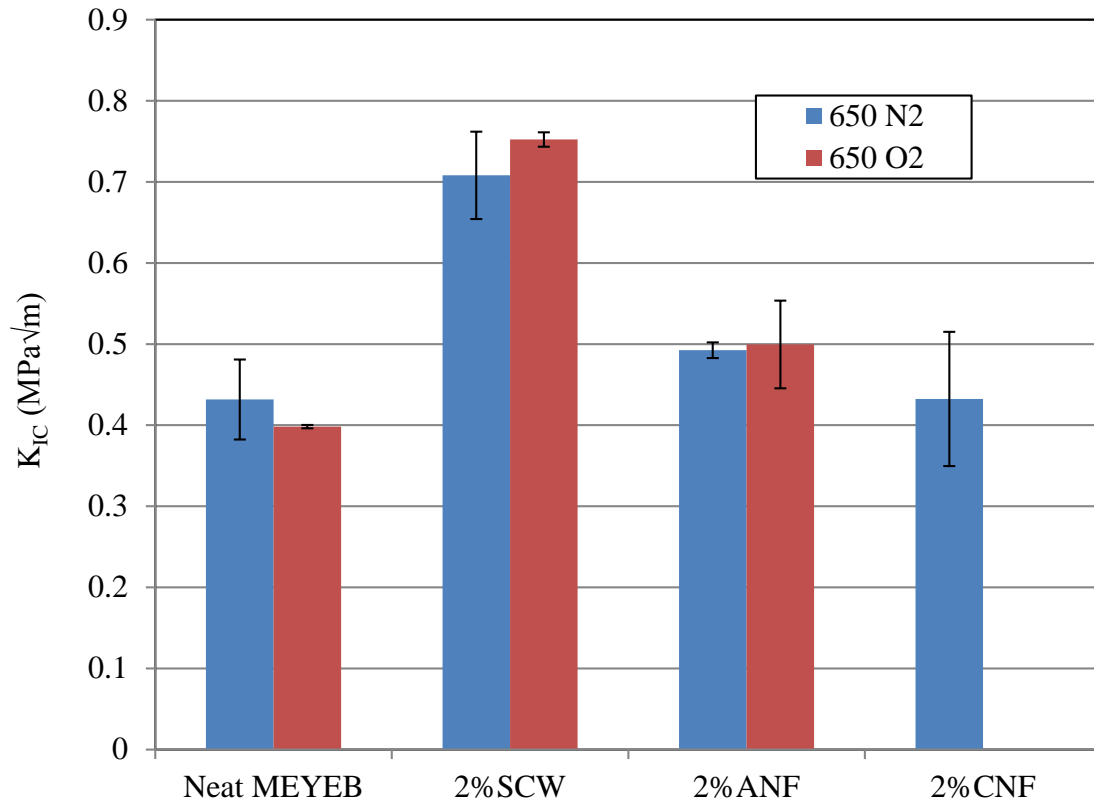


Figure 6.21. Toughness of neat and various high aspect ratio nano-fillers reinforced MEYEB at 650 °C in oxygen and nitrogen.

The difference observed in fracture toughness in both reactive (oxygen) and inert (nitrogen) environment is not significant. Fracture toughness responses of neat and nano-reinforced MEYEB at various temperatures and environment suggest that nanomaterials with high aspect ratio and high interfacial strength are favorable in improving properties at both reactive and inert environment.

### 6.6.5.3 Effect of Nano-Reinforcement on Flexural Strength

#### 6.6.5.3.1 Effect of Aspect Ratio Flexural Strength

Figure 6.22 is the presentation of the bending strengths of nanofilled MEYEB treated at 250 °C.

Flexural strength of neat specimen is added in the chart for comparison.

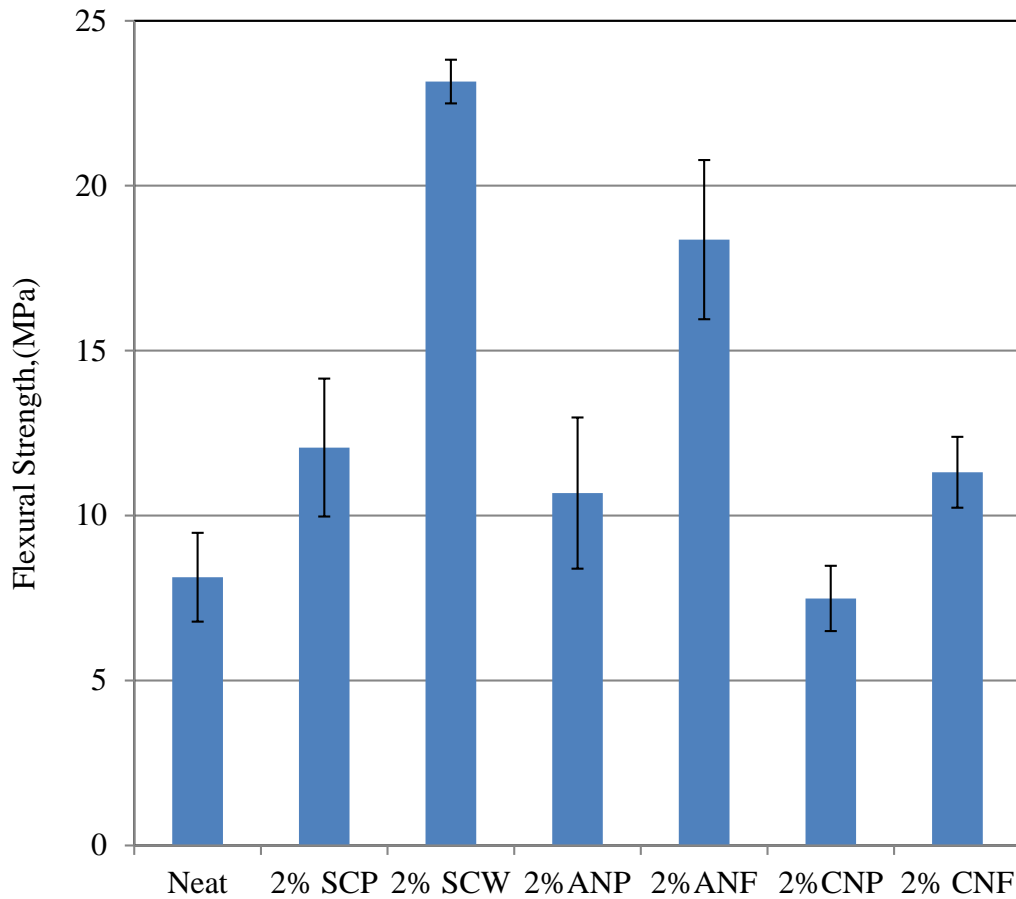


Figure 6.22. Flexural strength of neat MEYEB and MEYEB reinforced with low and high aspect ratio nanofillers treated at 250 °C.

As seen in the data presented in Figure 6.22, the higher aspect ratio versions of each nanomaterial show higher flexural strength values than the particulate form. In fact, of the nanoparticles, only the SCP shows a statistically significant improvement over the neat MEYEB.

However, all of the high aspect ratio nano-fillers showed a measurable improvement in flexural strength over the neat MEYEB, with the 2% SCW showing, by far, the highest flexural strength.

#### 6.6.5.4 Thermal Effect on Flexural Strengths of Nanofibers Reinforced MEYEB

Flexure strength of neat MEYEB and high aspect ratio nanofillers reinforcement are presented in Figure 6.23. It is found that at 250 °C and 650°C, SCW and ANF resulted in the higher improvement in the strength of MEYEB compared to CNF. At 250 °C the improvement in flexure strengths with 2vol% loading of SCW, ANF and CNF compared to respective neat samples at 250 °C were found as 183%, 126% and only 39%, respectively.

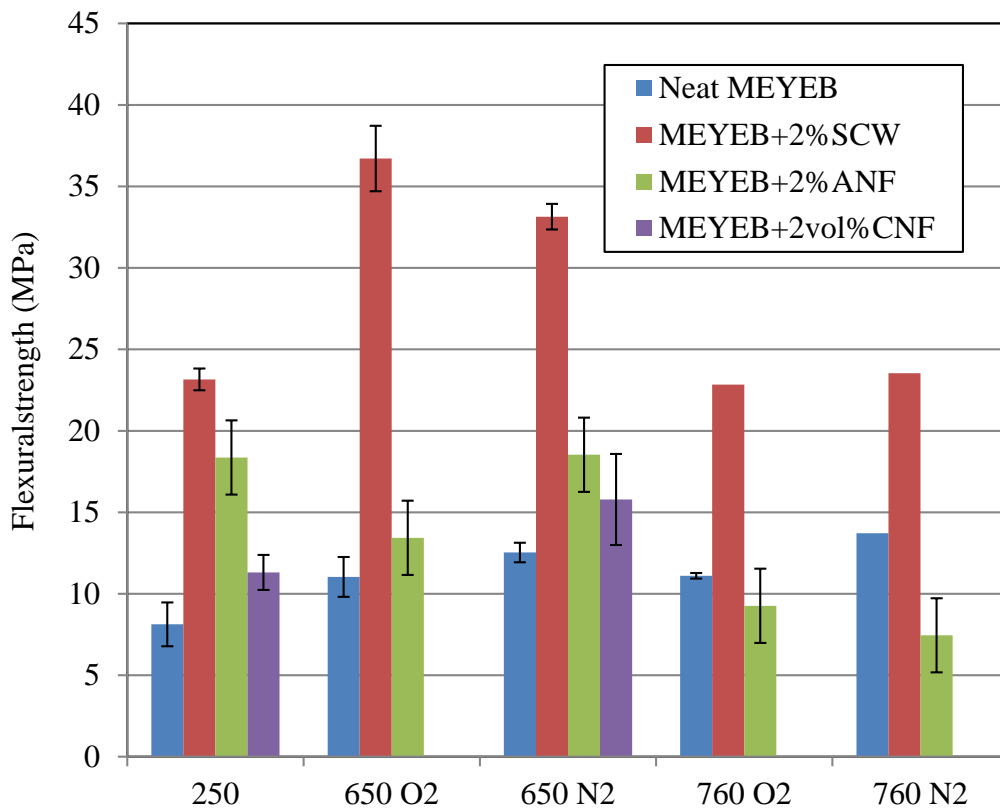


Figure 6.23. Flexural strength of neat and various high aspect ratio nanofillers reinforced MEYEB at various temperatures in nitrogen and oxygen environment.



At 650 °C in nitrogen, the improvement in flexure strengths with 2 vol% loading of SCW, ANF and CNF compared to the respective neat samples were 164%, 47.8% and 26%, respectively. Therefore, high aspect ratio nanofillers seem to be more effective in strengthening MEYEB at 250 °C compared to the respective effects at 650 °C in nitrogen. However, in oxygen the improvement with 2vol% SCW loading the improvement in flexure strength is 232%, which is higher compared to the respective improvement at 250 °C. At 760 °C in oxygen and nitrogen, respectively, the improvement in flexural strengths with 2vol% loading of SCW compared to the respective neat samples were 107% & 71%. However with 2vol % ANF, flexural strength reduced by 16% and 45%, in oxygen and nitrogen, respectively.

#### **6.6.5.5 Thermal Effects on Flexural Strengths of Nanoparticles Reinforced MEYEB**

Flexural strengths of the low aspect-ratio-nanofiller reinforced MEYEB samples at various temperatures and environments are presented in Figure 6.24.

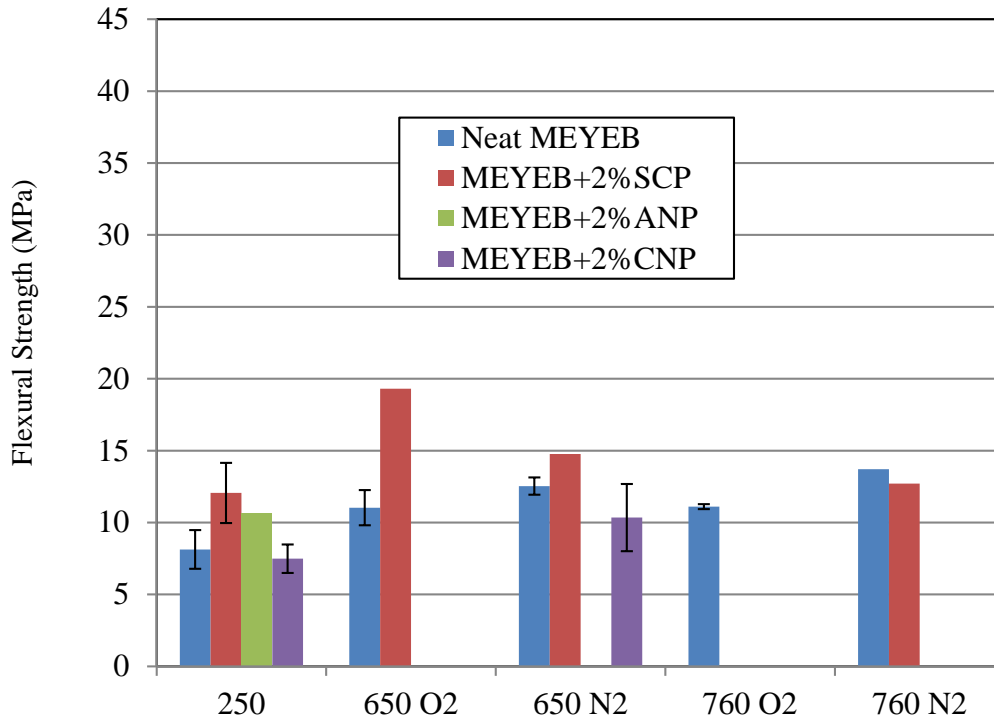


Figure 6.24. Flexural strength of neat and various low aspect ratio nano-fillers reinforced MEYEB at various temperatures nitrogen and oxygen environment.

Low aspect ratio nano-fillers are less effective in increasing flexural strength compared to high aspect-ratio nano-fillers. Among these nanomaterials SCP has the largest effect in flexural strength of MEYEB at 250 °C and 650 °C (in both reactive and non-reactive environment).

#### 6.6.5.6 Environment Effect on Flexural Strength

Figure 6.25 present flexural strengths of neat and high aspect nanofillers reinforced MEYEB treated in oxygen and nitrogen environment at 650 °C, respectively. The results give insight about the simultaneous effect of high aspect ratio of the nanofillers and treatment environment on the strength of MEYEB.

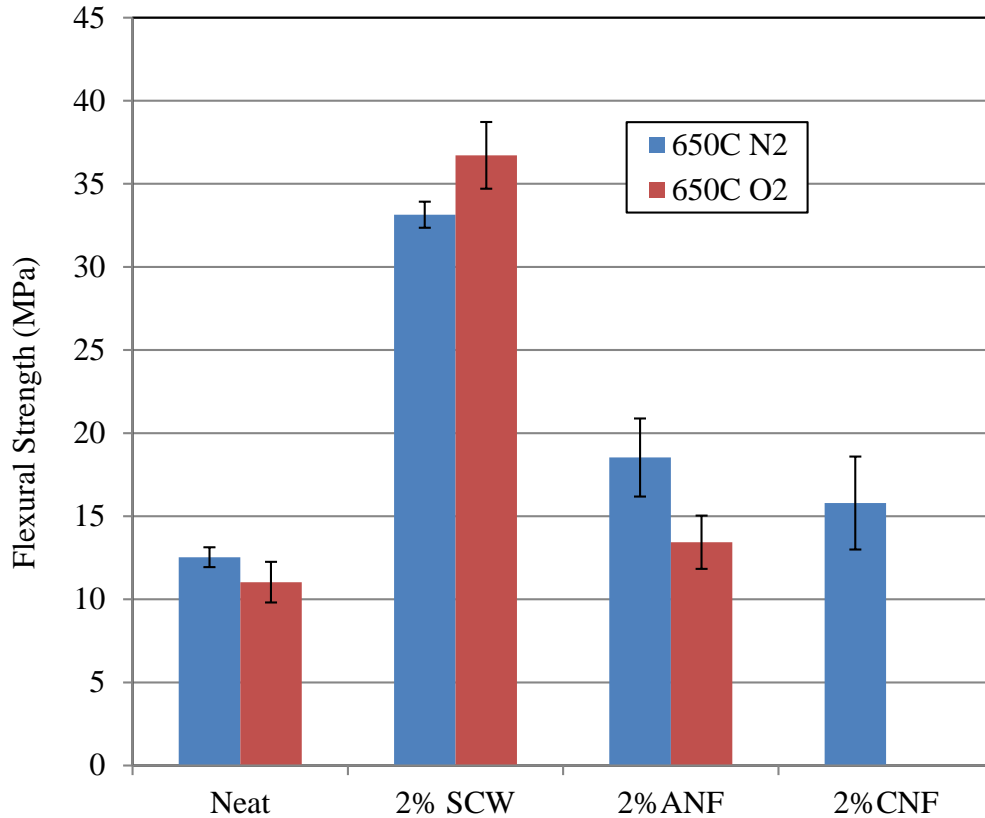


Figure 6.25. Flexural strength of neat and various high aspect ratio nanofillers reinforced MEYEB at 650° C in reactive and non-reactive environment.

From Figure 6.25 it is found that, non-reactive environment (nitrogen) is favorable for the strength of MEYEB compared to the reactive environment. The reactive environment causes partial oxidation at 650 °C which causes little reduction in the strength of MEYEB. At 650 °C, SCW significantly improves the strength of MEYEB. Also at reactive environment, SCW recovers the loss in strength of MEYEB due to oxidation. It is also found that the largest improvement in the flexural strength was achieved with SCW reinforcement.

#### **6.6.5.7 Effects of Nanofillers on the Flexural Modulus of MEYEB**

Figure 6.26 is the presentation of the effectiveness of SCW and ANF in improving the flexural modulus of MEYEB. It has been found 2vol % SCW is effective in improving the baseline flexural modulus of MEYEB at all thermodynamic conditions except for 760 °C (O<sub>2</sub>). ANF contributed to the improvement of the baseline flexural modulus upto 650 °C. At 760 °C (O<sub>2</sub> & N<sub>2</sub>) ANF did not contribute to the improvement of the baseline flexural modulus, rather the modulus decreased at those thermodynamic conditions. From this investigation it can be summarized that small amount of nanofillers are capable in improving the modulus of low modulus MEYEB which is an important improvement of inorganic geopolymer matrix to be more compatible with high modulus ceramic fiber.

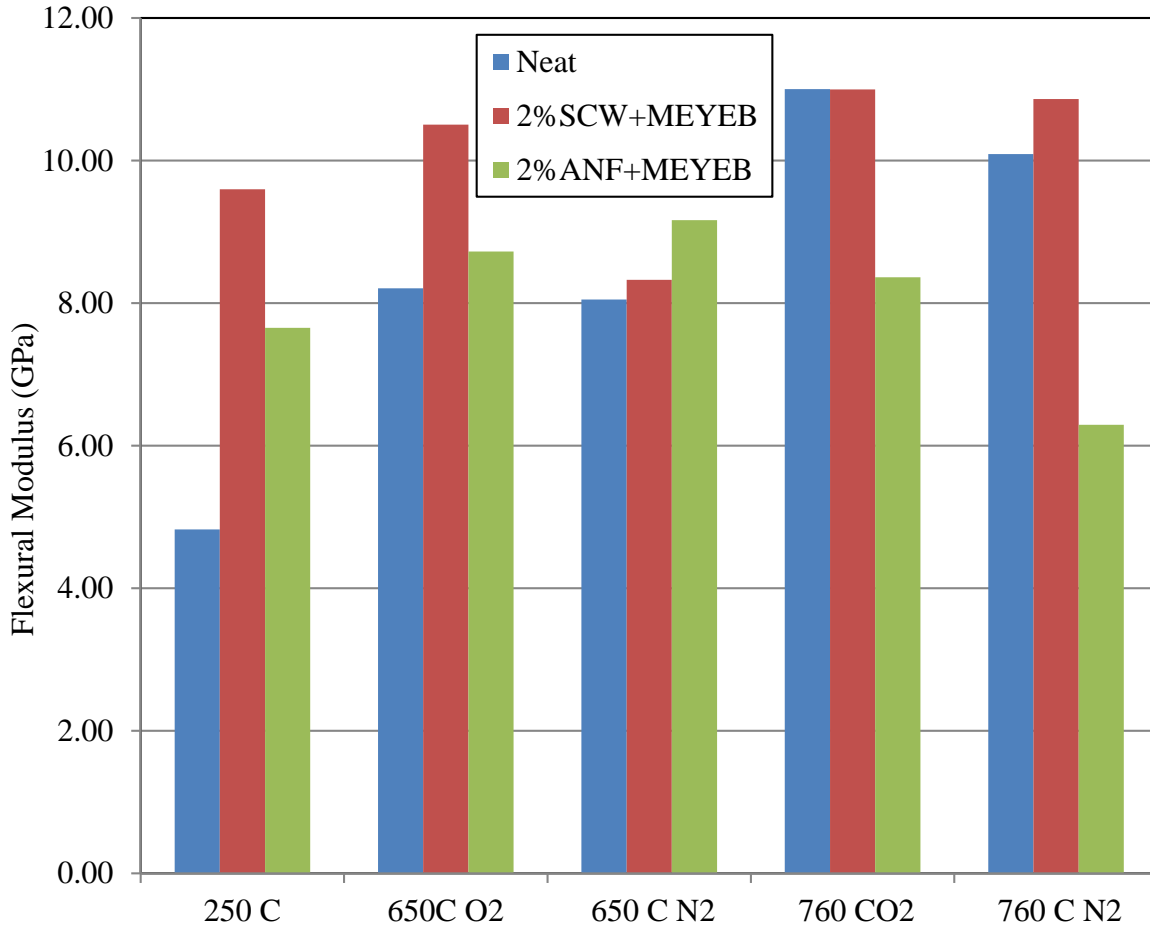


Figure 6.26. Variations in the flexural modulus of MEYEB with the addition of 2vol % nanofillers.

#### 6.6.5.8 Effect of $a/w$ on $K_{IC}$

For neat and nano-reinforced MEYEB samples,  $K_{IC}$  measurement was performed with some variations in the notch length to depth ( $a/w$ ) ratio. The variations in the  $K_{IC}$  with ( $a/w$ ) for some of those samples are presented in Figure 6.27. From this figure it can be stated that, with the variations in  $a/w$ ,  $K_{IC}$  did not clearly follow any increasing or decreasing trend. This observation suggests that, within the  $a/w$  range investigated, there is no crack growth resistance in the materials.

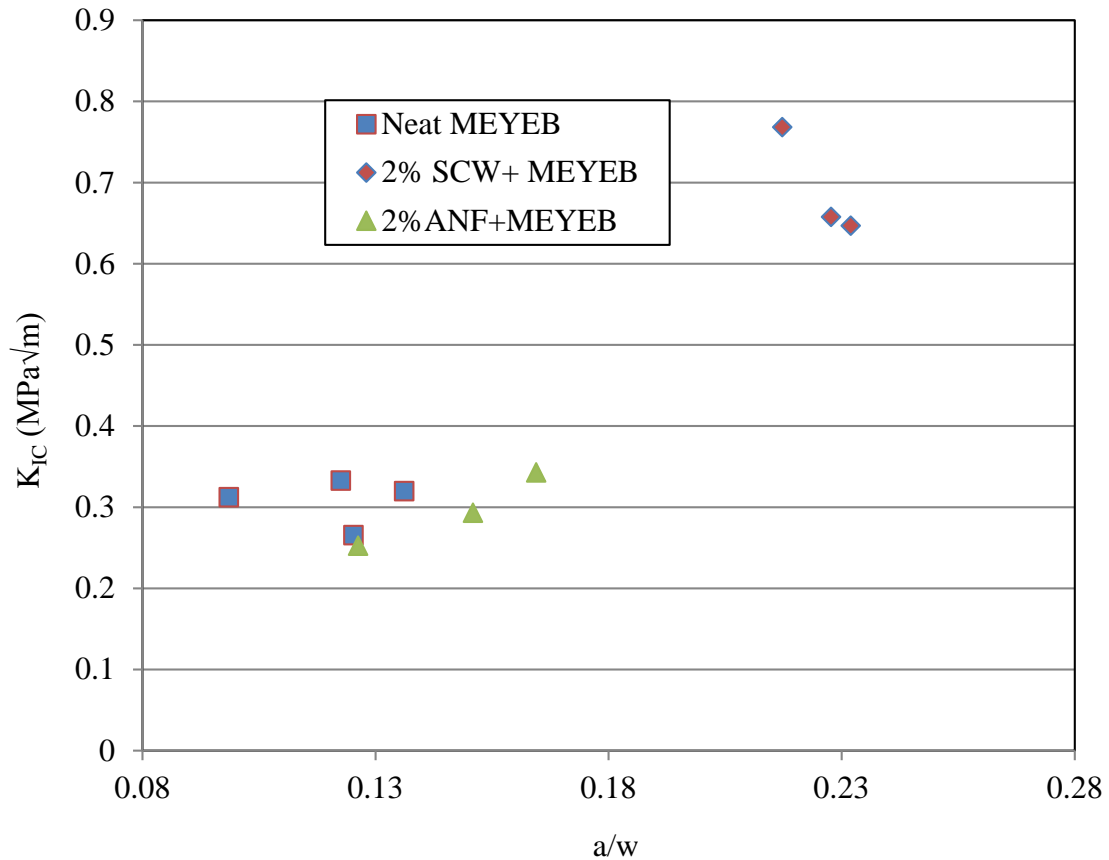


Figure 6.27. Variations in the fracture toughness with the variations in the ratio of notch length to depth ( $a/w$ ) of the samples treated at 650 °C ( $O_2$ ).

### 6.6.5.9 Verification of the Fracture Toughness Test Results

Table 6.11 shows some of the comparisons to the breaking loads of equivalent notched and un-notched beam samples. All the samples involved in this comparison were treated at 650 °C in oxygen.

Table 6.11. Breaking loads of the notched and un-notched beam of equivalent thickness

Types	a/w	L	b	w <sub>eq</sub>	S <sub>b</sub>	F <sub>eq</sub>	F <sub>notch</sub>	Notch effect
Units		in	in	in	Psi	lbf	lbf	
Neat MEYEB	0.14	1.20	0.21	0.15	1755	4.91	3.24	Yes
2%SCW+ MEYEB	0.19	1.20	0.19	0.15	5328	12.97	7.05	Yes
2%SCW+ MEYEB	0.23	1.20	0.19	0.15	5328	12.78	6.35	Yes
2%SCP+ MEYEB	0.15	1.20	0.21	0.16	1705	4.68	4.52	Yes

F<sub>notch</sub>= Breaking load measured from the notched beam test.

From the Table 6.11 it is found that, the breaking loads of neat and 2 vol% nanofillers reinforced samples from the notched beam fracture strength test are lower than the loads carried by the samples from un-notched beam fracture toughness test of equivalent thicknesses, respectively. Therefore it can be stated that the starter notch on the tensile surface of the notched beam is able to initiate the crack propagation and generate accurate fracture toughness results. Similar observations were found in all the samples prepared and tested for the verification of nano-reinforcement effect. Therefore, it can be summarized that the experimental fracture toughness results measured from the notched beam fracture test are valid.

#### 6.6.5.10 Summary of Comprehensive Test Results

The flexure strength results are summarized first. Possible reason for the increase in flexural strength using high aspect ratio nanofillers (see Figure 6.22) is that high aspect ratio nanofillers have more potential in increasing sliding friction between the clusters of MEYEB and the ability to resist the crack formation. Possible reason for the improvement in flexure strength using nanoparticles is the improvement in only the sliding friction. Unless pure flexural moment is achieved, 3 point flexural test measures some shear component of the involved samples. Particulate type nanofillers improve these shear properties of the geopolymer. Nanofibers and whiskers are more effective in improving this shear resistance compared to nanoparticles which was evidenced with the improvement in the flexural strength.

Possible reason for the increase in fracture toughness with high aspect ratio nanofillers at 250 °C (see Figure 6.19) is that high aspect ratio nano-fillers have more potential in increasing sliding friction between the clusters of MEYEB and crack bridging across the crack length. Possible reason for the improvement in toughness using nanoparticle is the crack deflection and crack pinning as a result from the presence of more rigid and high modulus nano material across the crack propagation. The toughness results from the high aspect ratio nanofillers need to be verified with the baseline properties and microstructure of MEYEB and interactions of MEYEB along with several variables including environment and thermal effect.

It is previously mentioned that SCW has higher interfacial strength compared to CNF. In line with the interfacial strength comparison, it is understandable that high aspect ratio and high interfacial strength nanofillers are more effective in toughening of MEYEB. With 2% SCW reinforcement, the improvement in toughness was higher at 350°C compared to similar system at



250 °C. Also with 2% SCW reinforcement the highest toughness was found at 350 °C. The reason for this type of behavior can be related to the competing effect of the changes in interfacial strength of SCW/MEYEB interface and gradual improvement on the strength of neat MEYEB as seen in Figure 5.15. With the changes in temperature from 250 °C to 350 °C the interface between SCW and MEYEB becomes perfect, but properties of MEYEB still get improved upto 650 °C. Therefore, Properties of neat MEYEB leads to the further improvement in the toughness of SCW reinforced MEYEB.

The interaction between the improvement of neat material property and the effect of SCW reinforcement with the treatment temperature is interesting. It is important to understand the effects of additional variables that play some roles in toughening. It is possible that modulus and tensile strength of some nano-fillers play more significant roles than the interfacial strength itself, because interfacial strength might be sufficient enough and its effect on MEYEB is fairly constant within that temperature ranges. Moreover, with the heat treatment at 760 °C the strength and toughness of ANF reinforced MEYEB dropped down compared to neat MEYEB. Later, upon the investigation it was found that this small improvement in the strength and toughness was associated with the low modulus and strength of ANF. At 760 °C, Alumina acts as the site of nucleation for the geo-polymerization process<sup>52</sup>. Nucleation at high temperature reduces the structural integrity of nanofillers and toughness of nano-reinforced geopolymer. The ability of the nanofillers in improving modulus depends on the degree of cross linking. Therefore there is a scope of discussion about the multivariable effects in combination with the baseline properties and microstructure of MEYEB and interactions of MEYEB along with several variables including environment and thermal effect.

## 6.7 Conclusion

TGA of alumina nanofibers showed some weight loss which may cause the reduction in mechanical performance of this material. TGA of silicon carbide whiskers showed some weight gain in oxygen at high temperature which indicates the formation of silica layer and constant mechanical properties of this material. Fractography of CNF and ANF reinforced MEYEB indicates the difference in the interfacial strength. MEYEB/CNF interface can be interpreted as lower compared to MEYEB/ANF interface. MEYEB/SCW interface have the intermediate strength. Based on the fractograph ANF, ANP, SCW and SCP make stronger bonding with MEYEB than CNF and CNP.

Fracture surfaces of the SEVNB tested samples presented co-linear crack propagation. The crack started from the notch tip and the crack front propagated in parallel to the notch length. Also the flexural strength results were compared with that of fracture toughness. Co-linear crack propagation is an indication of perfect failure due to the starter notch which is also verified by the flexural strength measurement.

Preliminary results suggest that nano-fiber reinforcement is effective in toughening MEYEB. Volume fraction has main effect, which means at any volume fraction the effects other variables on nano-reinforcement will be similar. It is also found that aspect ratio and temperature both have sufficient main and interaction effects. However the comparison between the effectiveness of high & low interfacial strength was inadequate. This limitations lead to investigate with comprehensive set of experiments. From the comprehensive study, the following observations were found-

1. With the increase in the treatment temperature mechanical properties (strength, toughness and modulus) of neat MEYEB gradually increased and the effect of toughening through the use of nanofillers either increased or decreased depending on the interfacial strength between MEYEB and nanofillers.
2. With particular nanofiller reinforcement the improvement in flexural strength of the geopolymer is similar compared to the improvement in fracture toughness with a minor variation in the case of alumina nanofibers.
3. High aspect ratio nanofillers such as whiskers and nanofibers show some improvement in flexural strength and toughness which needs to be verified with the baseline properties of geopolymer.
4. Among two nanofillers with similar interfacial strength, nanofiller with low strength and modulus found to be less effective in toughening compared to the nanomaterials high strength and modulus.
5. Effectiveness of SCW, ANF and CNF all were reduced at high temperature in both oxygen and nitrogen environment.
6. Small amount of several high aspect ratio nanofillers are capable in improving the modulus of MEYEB.

## 7 OVERALL DISCUSSION

The following discussion interprets the results of the current study to verify the proposed hypothesis. It summarizes specific aspects of the processing of neat geopolymer that interacts with the toughening mechanism associated with the nanofiller reinforcement. This discussion takes effect in highlighting the comparison between the effectiveness of nanofillers with the variations in aspect ratio and interfacial bond strength. The discussion also highlights the effects of other variables related to the chemical configurations and issues related to the thermal stability of nanofillers. Various arguments in the discussion are supported by the investigations using fractography, elemental analysis and phase transformation.

The hypothesis that was proposed as one of the criteria for toughening geopolymer using nanofillers is mentioned as follows-

“High aspect ratio nanofillers are more effective than nanoparticles. High interfacial strength at the nano-filler/ geopolymer interface improves toughness of nano-filler/ geopolymer system”.

Effectiveness of nano-reinforcement in toughness is equal to the improvement of toughness of nano-reinforced materials beyond the baseline properties of the neat materials. Improvement in toughness ( $dK_{IC}$ ) & percentile improvement in toughness ( $\% dK_{IC}$ ) for each type of nano-fillers can be calculated using the following equation-

$$dK_{IC} = K_{IC}(NF) - K_{IC}(N) \quad (27)$$

$$\% dK_{IC} = \frac{dK_{IC}}{K_{IC}(N)} \times 100 \quad (28)$$

Where,  $K_{IC}$  (NF) &  $K_{IC}$  (N) are toughness of nanofilled and neat geo-polymer respectively.

Nano-based toughness evaluation requires finding of the toughness of neat materials.

## 7.1 Evaluation of Neat Geopolymer

It is essential to evaluate the response of the baseline mechanical properties and the microstructure of the neat geopolymer to variations in thermal treatment. Variations in this microstructure depend on the thermal treatment, which influences the mechanical properties of the geopolymer. Once solidified the resultant microstructure of geopolymer is equivalent to an inhomogeneous distribution of particles in a poly-condensed matrix, as shown in the model in Figure 7.1. Inhomogeneity in the cured neat matrix occurs due to the formation of un-reacted particles in the poly-condensed poly-sialate matrix, compositional variations in poly-condensed structure, and unreacted particles. The formation of this type of inhomogeneous structure depends on the cure temperature, time and moisture content during the solidification process. The inhomogeneity in the neat matrix influences the reinforcing capability of various nanofillers. In the case of nano-reinforcement it is important to understand that the nanofillers should be capable in being attached to the particle as well as the poly-condensed structure.

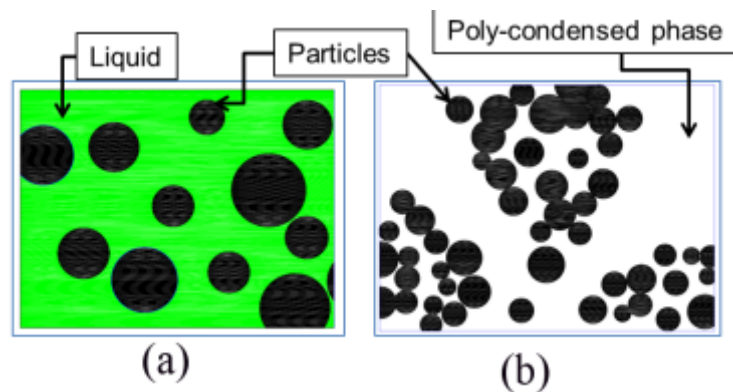
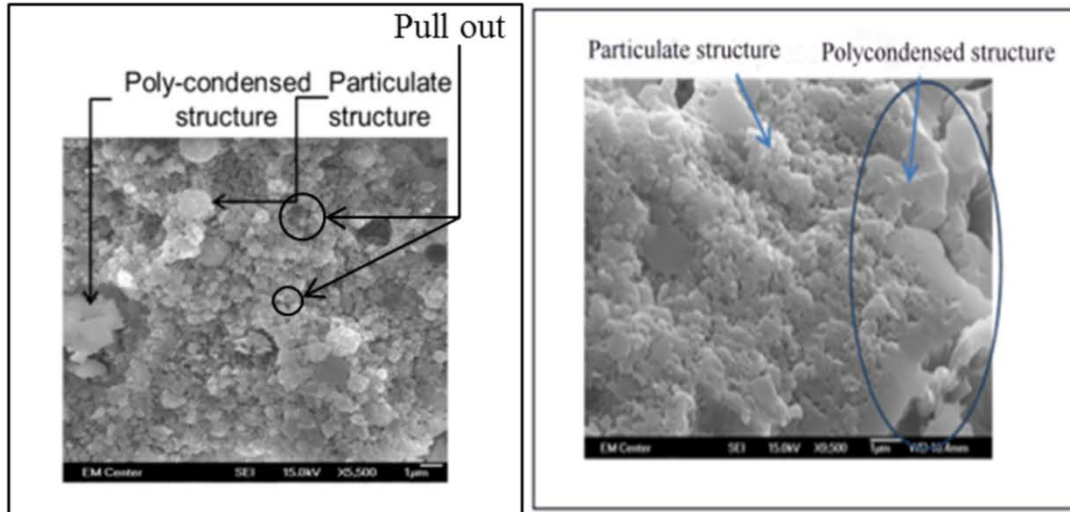
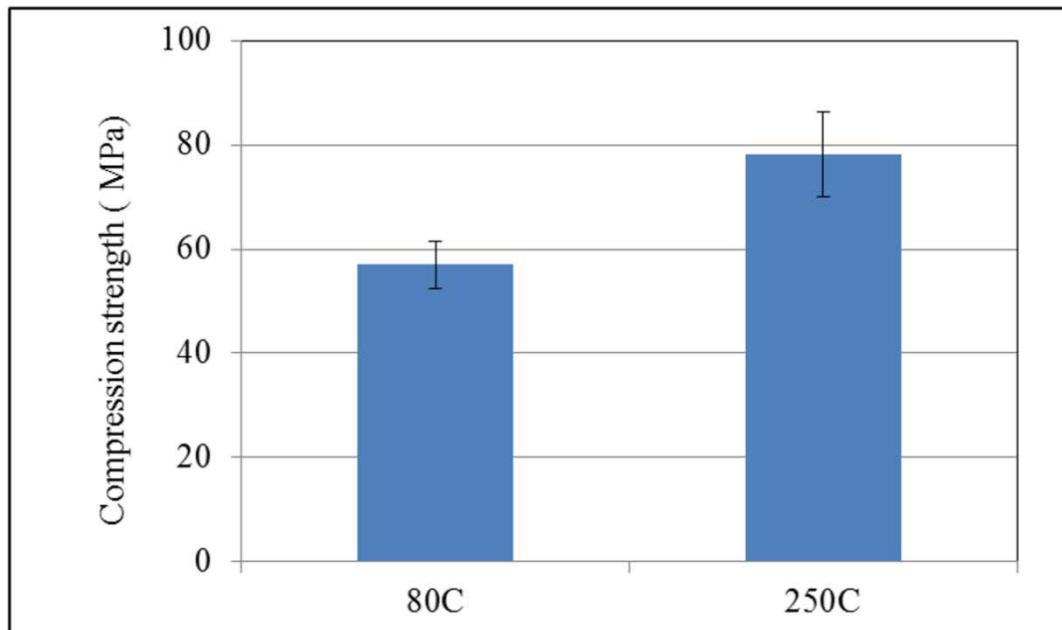


Figure 7.1. Solidification process of neat MEYEB in (a) liquid form with particles and (b) solid form after cured for 24 hr at 80 °C



(a)

(b)



(c)

Figure 7.2. Various phases present in neat geopolymer cured (a) 24 hr at 80 °C (b) post processed at 250 °C and (c) response to corresponding compression strength cured 24 hr at 80 °C and post processed at 250 °C.

Post cure heat treatment temperature affects the structural inhomogeneity and the mechanical properties of the overall composite. As seen in Figure 7.2 , post processing at 250 °C results in

more poly-condensed matrix and a reduction in the amount of particles pulled out. The phenomenon of less particle pull out is directly related to the increased bond strength and increased mechanical strength which is seen in Figure 7.2(c).

Increased bonding and reduced particle pull out indicate improved mechanical properties. However, this improvement in mechanical properties is limited by the structural inhomogeneity of the materials. It is shown, previously in SEM images (Figure 5.26) and here in Figure 7.3, that with the increase in treatment temperature to 870 °C un-reacted particles diffuse into poly-condensed part of geopolymer and form a coalesced material.

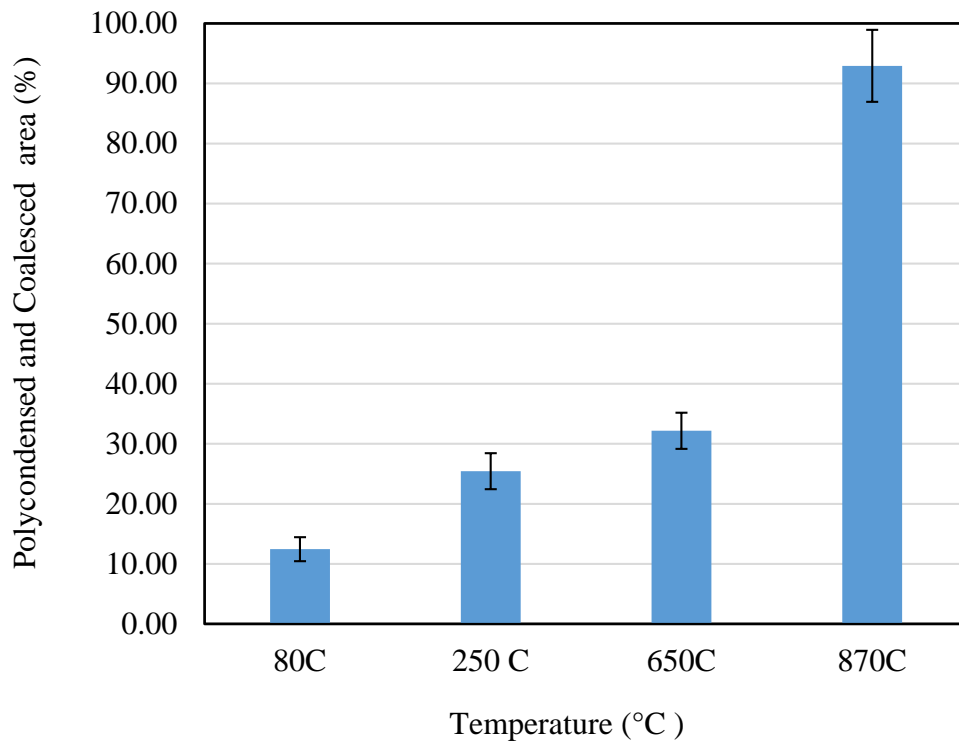
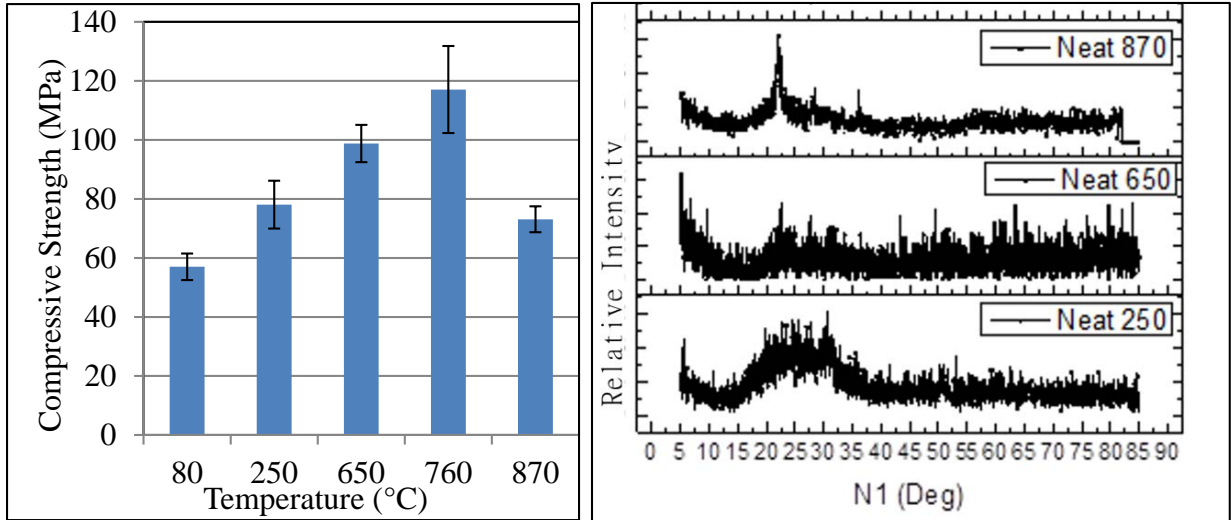


Figure 7.3 Area of Poly-condensed structure of neat MEYEB heat treated at various temperatures. (Detailed analysis with subsequent SEM images can be found in Appendix C2)

From Figure 7.3 it is found that, at 870 °C the poly-condensed and coalesced structure increased to 92%, i.e. the particle structure reduced to only 8%. This significant reduction in particle essentially reduces self-reinforcement of geopolymer and therefore the mechanical strength. Mechanical properties are also limited by the phase stability of the materials. The variations in the mechanical properties i.e. compressive strength and phases i.e. X-ray diffractogram of neat geopolymer at various thermodynamic conditions are shown in Figure 7.4(a) & (b), respectively. From Figure 7.4 (a) it is found that, the strength of this material increases with temperature up to 760 °C and after that the strength decreases. Alternatively, XRD results at 870 °C (see Figure 7.4 (b)) show high intensity narrow at around ~24, ~ 29 and ~36 deg, respectively. Among those peaks the one at ~24 deg is prominent. These peaks clearly indicate some degree of crystalline nature in the geopolymer. These peaks indicate the formation of zeolite phases in the geopolymer at higher temperature<sup>44</sup>. Similar crystalline peaks were not seen at other treatment temperatures lower than 870 °C. The result suggests that the decrease in strength at 870 °C is related to the onset of crystallization (Figure 7.4 (b)). It is therefore clear that the reduction in particle reinforcement and phase transformation of geopolymer occur in coincidence, which affects mechanical performance of geopolymer. Among the treatment and operating temperature ranges the phase and morphological transformations are unexpected since the physical and chemical interactions of the nano-fillers with the amorphous geopolymer are different from the interaction with crystalline geopolymer. Therefore, for the purpose of investigating the effectiveness of nano-reinforcement the maximum treatment temperature was limited to 760 °C to avoid the crystalline transformation.





(a)

(b)

Figure 7.4. Variations in the (a) compression strength and (b) phase transformation of geopolymer with the variations in treatment temperature.

Fracture toughness and compression strength of neat material at various temperatures are shown, combined, in Figure 7.5. It is seen that toughness follows a similar trend as the compression strength, up to 760 °C. Therefore, from the fracture toughness perspective, 760 °C can be considered as the maximum treatment temperature for nano-reinforced geopolymer. Beyond that temperature, the geopolymer crystallizes, and thus responds to the incorporation of nanofillers in a different way.

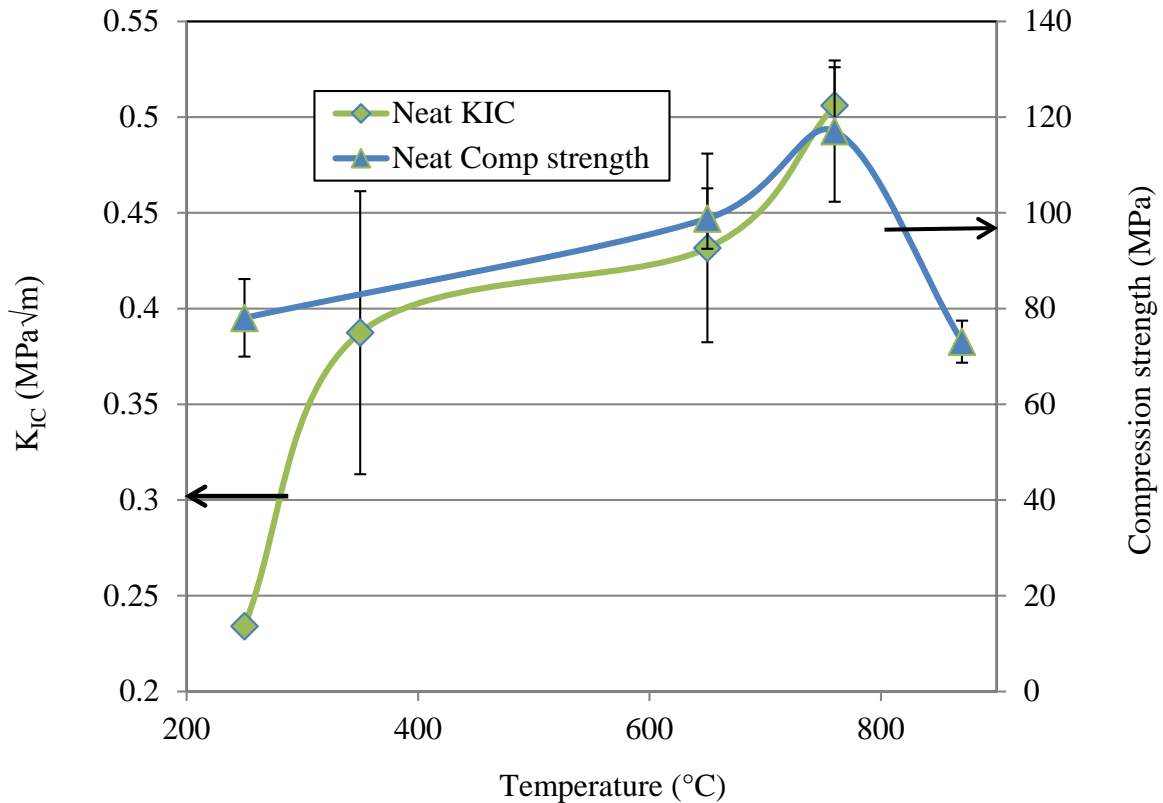


Figure 7.5 Toughness and compression strength variations with temperature

## 7.2 Effect of Nano-reinforcement

This discussion is about the investigation that considered the effectiveness of various nanofillers in additional improvement in toughness of geopolymer in the useful temperature range which is found as 250 °C-760 °C. Three types of nanomaterials were chosen with variations in aspect ratio and interfacial bond strength. Those are alumina, carbon and silicon carbide nanomaterials. It was possible to evaluate the effectiveness of those nanofillers by varying the volume fraction or keeping the volume fraction constant. A preliminary study was performed in order to investigate the effects of variables including Aspect ratio (AR), Interfacial strength (IS) and Volume fraction (VF), Temperature (T) and Environment (E) on toughness ( $K_{IC}$ ) of geopolymer with the addition of 0.5 and 2 vol% Alumina and carbon nanomaterials. From the preliminary study, it has been

found that at all thermodynamic conditions volume fraction has only linear effect and very small interaction with aspect ratio (AR), treatment temperature (T), environmental conditions (E) and interfacial bond strength (IS) with geopolymer. The results are again shown in the PARETO chart in Figure 7.6. This chart includes main effects (VF, AR, IS, T & E) and two way interaction effects (AR\*T, IS\*T, AR\*E, AR\*IS & VF\*IS) of those variables. The summary of this chart in terms of the main and interaction effects is presented in the following order from highest to lowest-

$$VF > AR * T > AR > T > E > IS * T > AR * E > AR * IS > VF * IS > IS \quad (29)$$

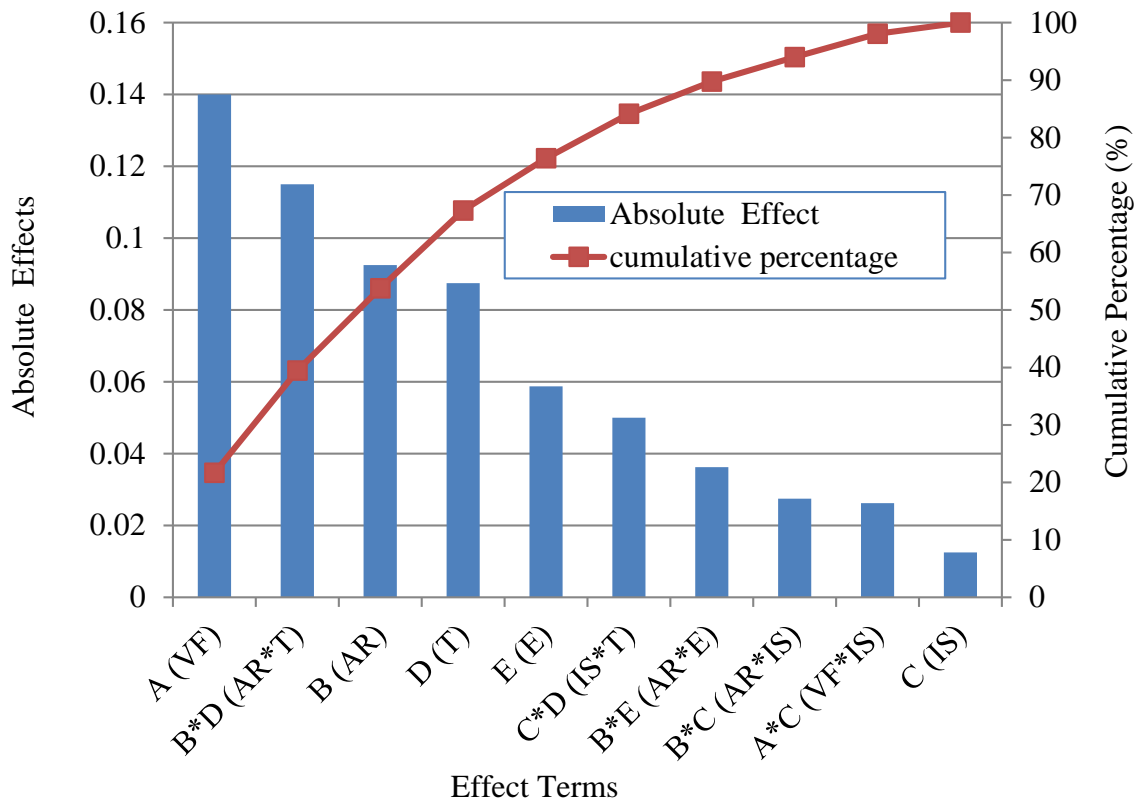


Figure 7.6. Pareto effect chart showing the effects of the variables on fracture toughness of MEYEB.

PARETO chart shows that volume fraction has the highest main effect followed by the interaction effect of aspect ratio and temperature, main effect of aspect ratio and so on. Therefore from the results for alumina and carbon nanomaterial reinforcements, it can be stated that the relative effects of other variables on toughness do not change at any volume fraction.

Addition of SCW also found to increase the toughness of neat matrix. The effectiveness of SCW nano-fillers with the volume fraction is linear which is shown at a constant thermodynamic condition (Figure 7.7(b)). The main effect of 0.5 and 2 vol% alumina and carbon nanomaterials in all thermodynamic conditions are also shown in parallel with the effectiveness of SCW (Figure 7.7(a)). Within this range it is found that SCW has an almost linear effect on the toughness. Since the increase in toughness with increase in volume fraction is linearly proportional, it is possible to evaluate the effectiveness of the variations in the physical properties of the nanofillers at a single volume fraction with the expectation that the effect will scale with volume fraction. Therefore, a nano-material volume fraction of 2 vol% is sufficient to investigate the effectiveness of nanofillers in toughening of geopolymer.

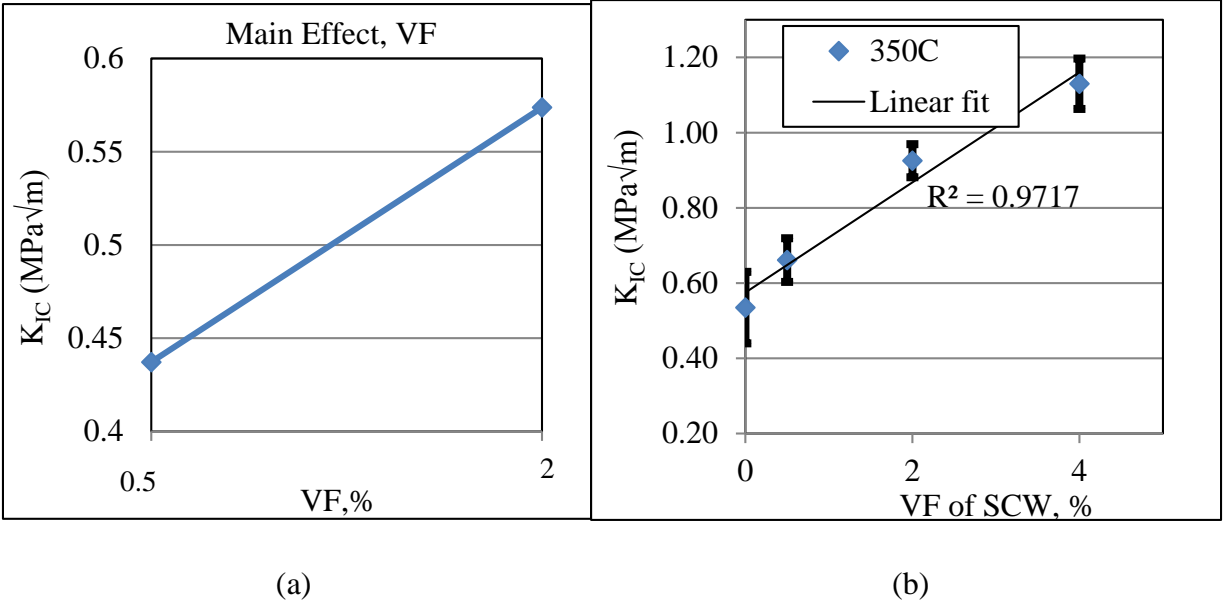


Figure 7.7. (a) Main effect of volume fractions of alumina & carbon nanomaterials and (b) Effect of volume fractions of SCW at constant thermodynamic conditions on  $K_{IC}$ .

### 7.3 Effectiveness of Aspect Ratio of Nano-filler

The effectiveness of the aspect ratio on the toughness was investigated for all the nanomaterials at a single volume fraction of 2 vol%. Two thermodynamic conditions, non-reactive and reactive, were also investigated. The results are presented in Figure 7.8. It is found that among the post heat treated thermodynamic conditions high aspect ratio nanofillers are more effective compared to nanoparticles. High aspect ratio nanofillers are more effective in bridging the cracks compared to nanoparticles. This crack bridging is an active mechanism in toughening with high aspect ratio nanofillers. This investigation validates part of the proposed hypothesis which relates to the effectiveness of high aspect ratio nanofiller. Another part of the hypothesis is related to the interfacial strength between nanofillers and geo-polymer.

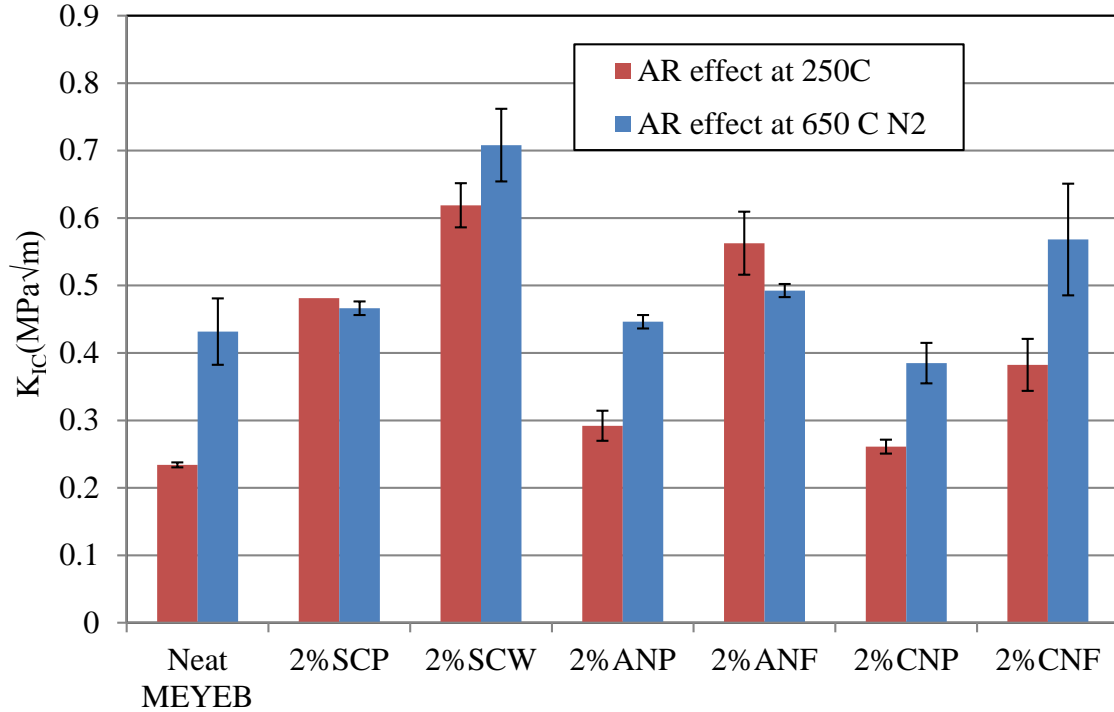


Figure 7.8. Effect of aspect ratio at low and high temperature in nitrogen.

#### 7.4 Effectiveness of Interfacial Strength

Since high aspect ratio nanofillers, including nanofibers and whiskers, are more effective than nano-particles, it was decided to focus on the evaluation of the effectiveness of the interfacial strengths of high aspect ratio nanofillers only. High aspect ratio nanofillers for this evaluation are CNF, SCW and ANF. Such an evaluation is valid if there is a good dispersion of nanofillers in all cases. The dispersions of 2 vol% of CNF, SCW and ANF are presented in Figure 7.9. A model microstructure with 2 vol% nanofillers is presented alongside in Figure 7.9(d) to compare the effectiveness of the dispersion of CNF, SCW and ANF in the respective nano-filled geopolymer. It is found that each type of nanofiller in the respective nano-reinforced geopolymer closely represents the model with the simulated nanofillers which amount almost 2 vol%. This

investigation suggests that all the nanofillers dispersed uniformly in the matrix and that the volume fraction seems consistent with the simulation.

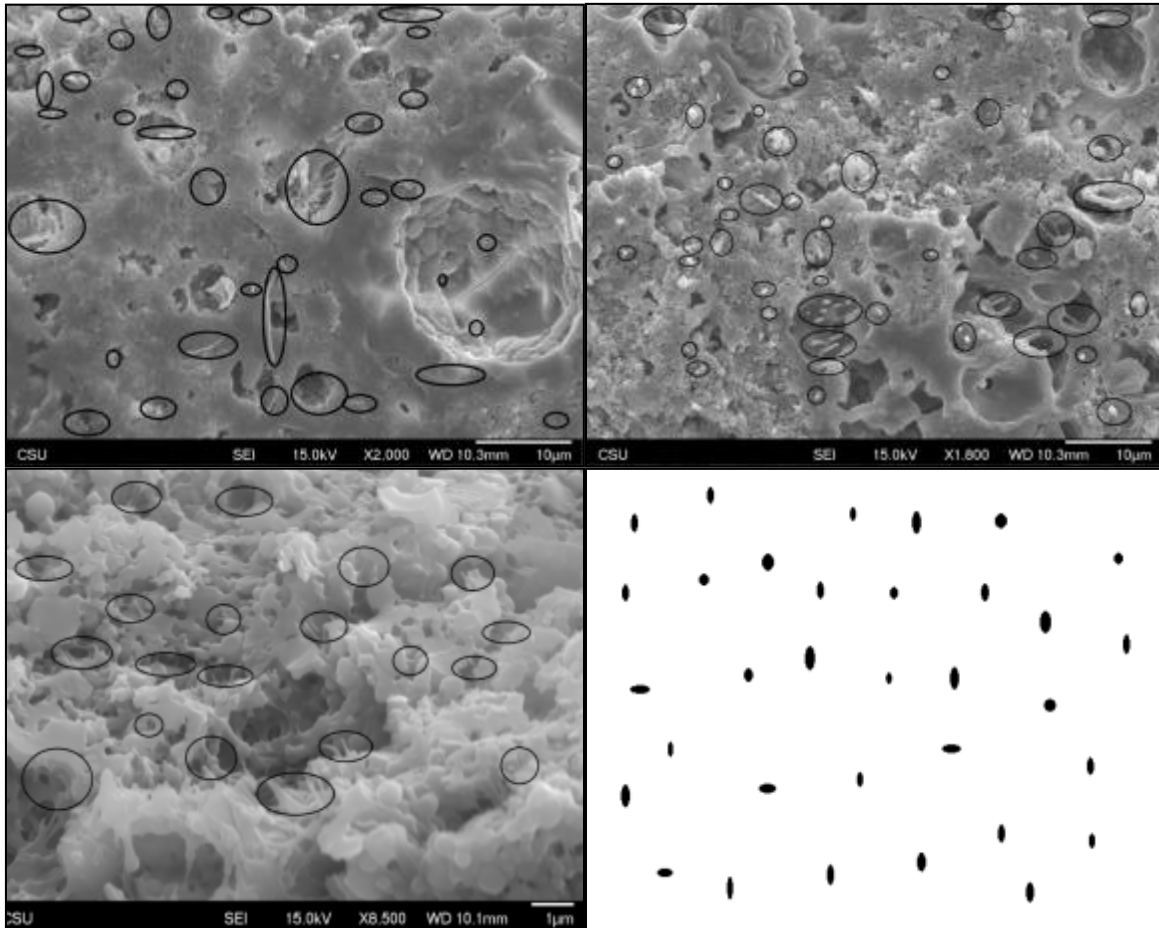


Figure 7.9. Dispersion of 2 vol% (a) CNF (b) SCW (c) ANF and (d) Simulated model representing 2 vol% nanofillers at 650 °C.

The next step of the discussion is to compare the interfacial bond strength of two nano-materials with similar mechanical properties and their effectiveness in toughening geopolymer. For the comparison to the effectiveness of interfacial bond strength, it is important to keep the tensile strength of nanofillers constant, because effectiveness of nanofillers in toughening partly depends on these properties<sup>9</sup>. Tensile strength and modulus of CNF and SCW are comparable;

however, CNFs are expected to have low interfacial strength with geopolymer compared to SCW<sup>114</sup>. The evaluation of the microstructures, as seen in Figure 7.10, supports the interpretation of the expected interfacial bonding strength between geopolymer and these two nano-fillers. The clean separation of CNFs from the geopolymer matrix, indicated by the clean nanofiller surface, is consistent with the statement that CNFs have low interfacial strength. Conversely the bonding of SCW with the geopolymer particles and the resulting amount of matrix material attached to the SCW surface indicates high interfacial bond strength. Pullout lengths of CNF and SCW (see Figure 7.10 (a) & (b)) are also important observations for drawing any conclusion about interfacial strength. This pull out length is approximately 5-10  $\mu\text{m}$  vs 1-2  $\mu\text{m}$  for CNF and SCW, respectively. Higher pull out length suggests that CNFs have weaker interfacial bond strength<sup>115</sup> with geopolymer than does SCW.

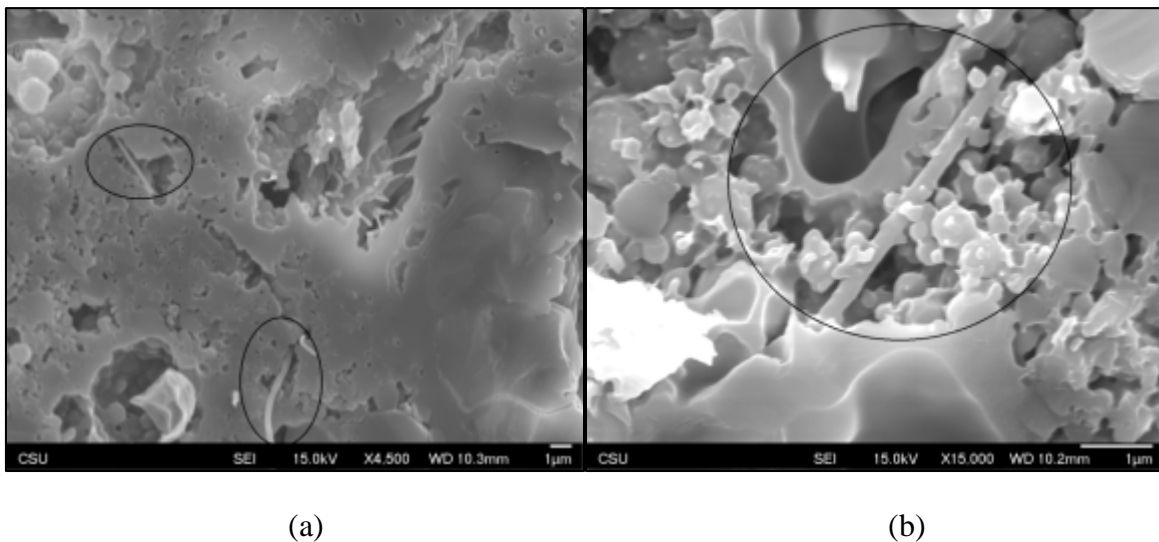


Figure 7.10. Evaluation of interfacial strength of (a) CNF/geopolymer and (b) SCW/geopolymer interface.

To compare the effectiveness of the high aspect ratio nano-fillers the toughness contribution i.e.  $dK_{IC}$  and %  $dK_{IC}$  for each type of nano-fillers were calculated at each of the two temperatures



evaluated, 250 °C and 650 °C, using equations (25) & (26). Figure 7.11 is the presentation of  $K_{IC}$  and %  $dK_{IC}$  of CNF and SCW at low and high temperature.

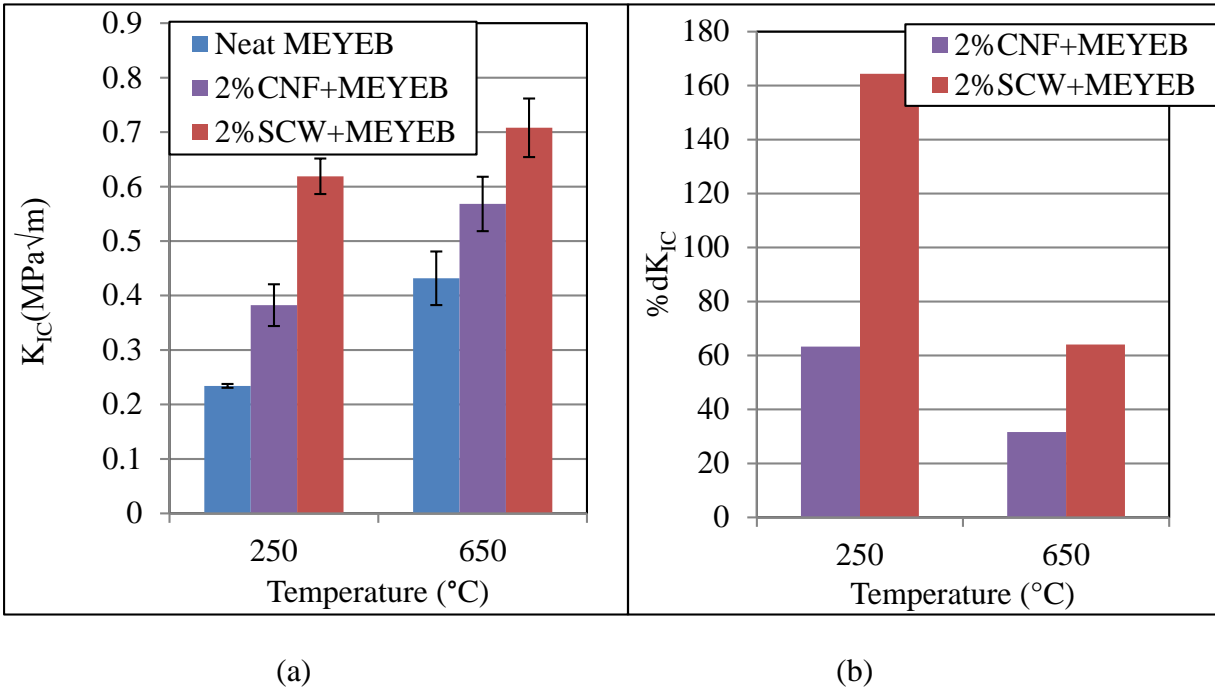


Figure 7.11. Toughness contributions of low and high interfacial strength nanomaterials at low and high temperature in nitrogen.

From Figure 7.11, it is found that, at both temperatures (250 °C and 650 °C), SCW is more effective in toughening the geopolymer than CNF. It has been previously stated that the interface of SCW/geopolymer is stronger compared to CNF/geopolymer interface. Therefore, the data supports the hypothesis statement related to the effect of nanofiller/matrix interface strength, showing improved toughness with increasing interface strength.

High interfacial strength is effective in bridging MEYEB geopolymer. ANF and SCW nanofillers make stronger interfaces with polycondensed and particle structures of geopolymer respectively and create bridging, which is shown in Figure 7.12. Strong bridging between particles and SCW helps deflecting cracks which is perpendicular to the SCW orientation.

Similar mechanism can happen in ANF reinforced geopolymer, however ANF is found to perform this mechanism in the poly-condensed region. Overall, strong bridging is the effective toughening mechanism in this particular type of geopolymer.

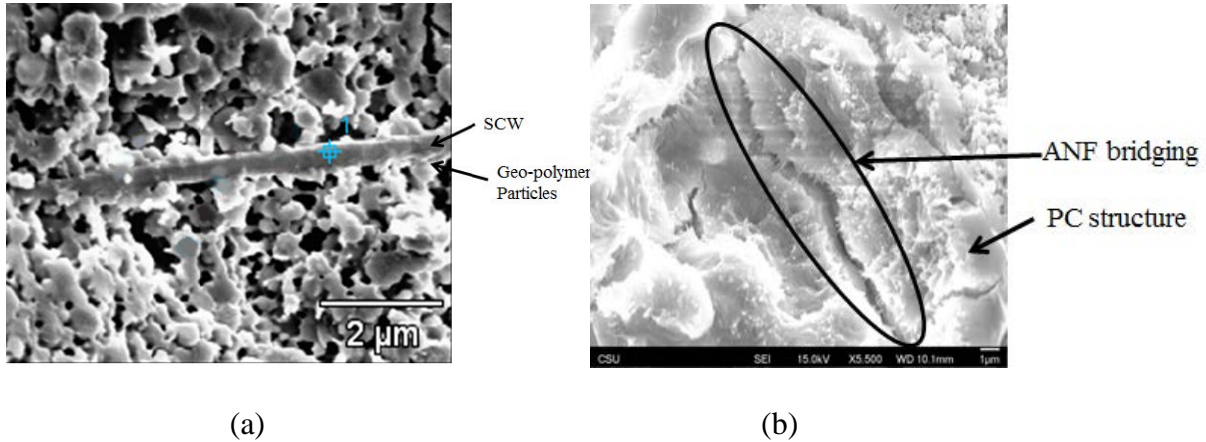


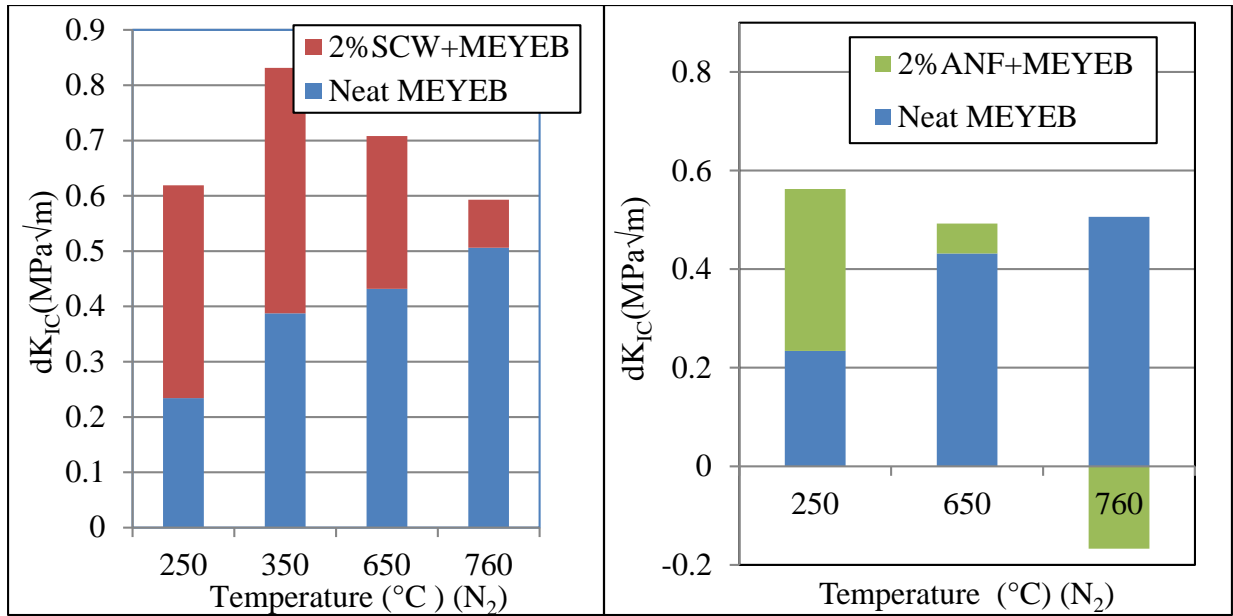
Figure 7.12. Bridging of SCW and ANF with the structure of geopolymer.

### 7.5 Thermal Effects on the Nanofiller's Stability and Interfacial Strength

Besides interfacial strength there are number of variables that control the effectiveness of toughening through nano-reinforcement. Matrix morphology and nanofiller's ability to interact with the structure of that matrix material determines the nanofiller's reinforcing capability. Variations in the physical dimensions and chemical configurations between ANF and SCW affect their ability to interact with, and therefore reinforce the geopolymer. Thermal and oxidative stability of nanofillers plays an important role in effective reinforcement of the geopolymer at high temperature. CNFs are not applicable for high temperatures and oxidative environments due to rapid reaction with oxygen. Conversely SCW and ANFs have excellent thermal and oxidation stability. The tensile strength of the nanofillers is also a limiting factor in improving the toughness of this nano-reinforced geopolymer<sup>116</sup>. Strength of ANF is lower than that of SCW and CNF (see Table 3.1). This lower strength is expected to limit the performance

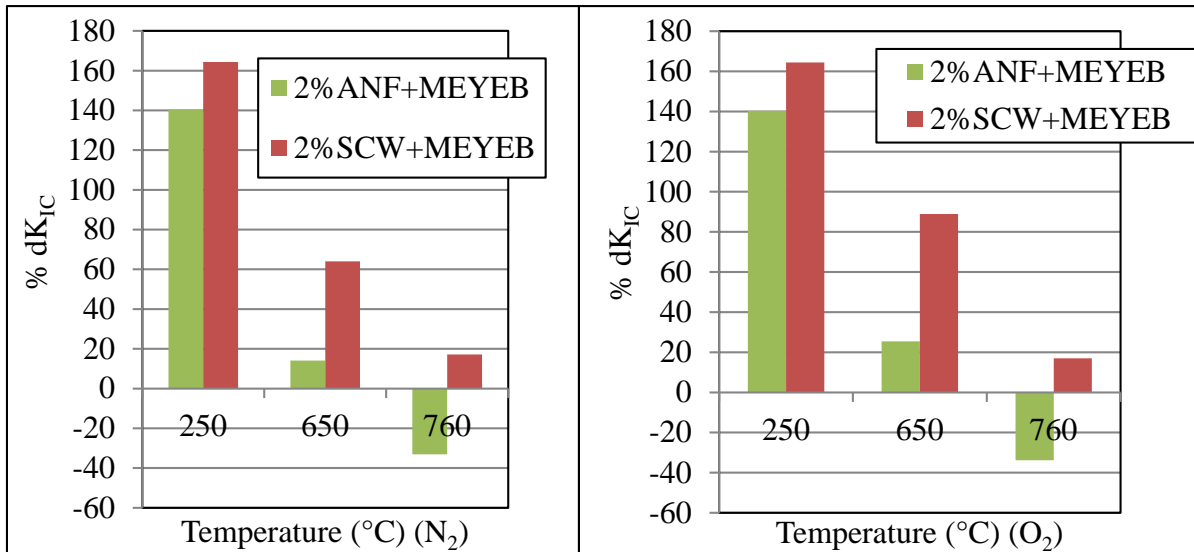
of ANF as reinforcement in the geopolymer, since the crack breaks ANF at a lower load than would be need to break SCW. Thermal diffusion is another factor affecting the structural integrity of nanofillers and their effectiveness in toughening the geopolymer. Diffusion driven adsorption drastically reduces the structural integrity of nano fillers when the nanaofillers contain similar chemical structure to that of the geopolymer matrix. The similarity in chemical structure is why the thermal degradation of ANF is expected when used as reinforcement in the aluminosilicate based geopolymer matrix. High temperatures can also lead to the formation of an interface layer which can affect the performance of nanofillers and of the nano-composite<sup>117</sup>. The following discussion highlights the effects of these variables on the toughness of geopolymer.

Effects of temperature on the effectiveness of SCW and ANF as toughening additions are shown in Figure 7.13 as the magnitude of the toughness, ( $dK_{IC}$ ). It is found that the  $dK_{IC}$  of SCW and ANF at low temperature (250-350 °C) are different from the contributions at high temperature starting at 650 °C in N<sub>2</sub>. SCW contribution to toughness reaches a maximum at 350 °C and then gradually drops until 760 °C. However, in all thermodynamic conditions  $dK_{IC}$  of SCW is positive. This means that, SCW improves toughness of geopolymer in all thermodynamic conditions investigated. This is not the case for the ANF reinforced geopolymer. At low temperature  $dK_{IC}$  of ANF is positive but lower than the  $dK_{IC}$  of SCW. However, at high temperature  $dK_{IC}$  of ANF is negative. These results suggest that, thermal treatment affects the interface in theses nanomaterials and thus affects the toughness. The effectiveness of SCW and ANF with the variation in temperature is explained in the following section with the investigation of the morphology of nano-reinforced geopolymer.



(a)

(b)



(c)

(d)

Figure 7.13. Toughness contribution,  $dK_{IC}$  of (a) SCW and (b) ANF at low and high temperature in nitrogen and %  $dK_{IC}$  of SCW and ANF in (c) nitrogen and in (d) oxygen.

Toughness contribution ( $dK_{IC}$ ) of SCW in both nitrogen and oxygen environments are similar, which is found from Figure 7.13 (c). Similarly,  $dK_{IC}$  of ANF shows similar trend in both environments (Figure 7.13(d)). This indicates no variations in the effectiveness of ANF and SCW with the variations in the environment.

SEM and EDS were performed to investigate the effectiveness of SCW and ANF with the variations in temperatures. Figure 7.14 presents SEM micrographs, which show the morphology of ANF and SCW reinforced geopolymer after 250 °C cure, but with no further high temperature heat treatment. From Figure 7.14 (a) it is found that ANF is mostly dispersed within the poly-condensed structure; however, Figure 7.14 (b) shows that SCW is dispersed within both the poly-condensed and particulate regions of the structure. To verify the concentration of ANF in the poly-condensed region EDS on both regions was performed, which is shown in Figure 7.15(a). Similarly the presence of SCW in both regions was verified using EDS, which is shown in Figure 7.15(b).

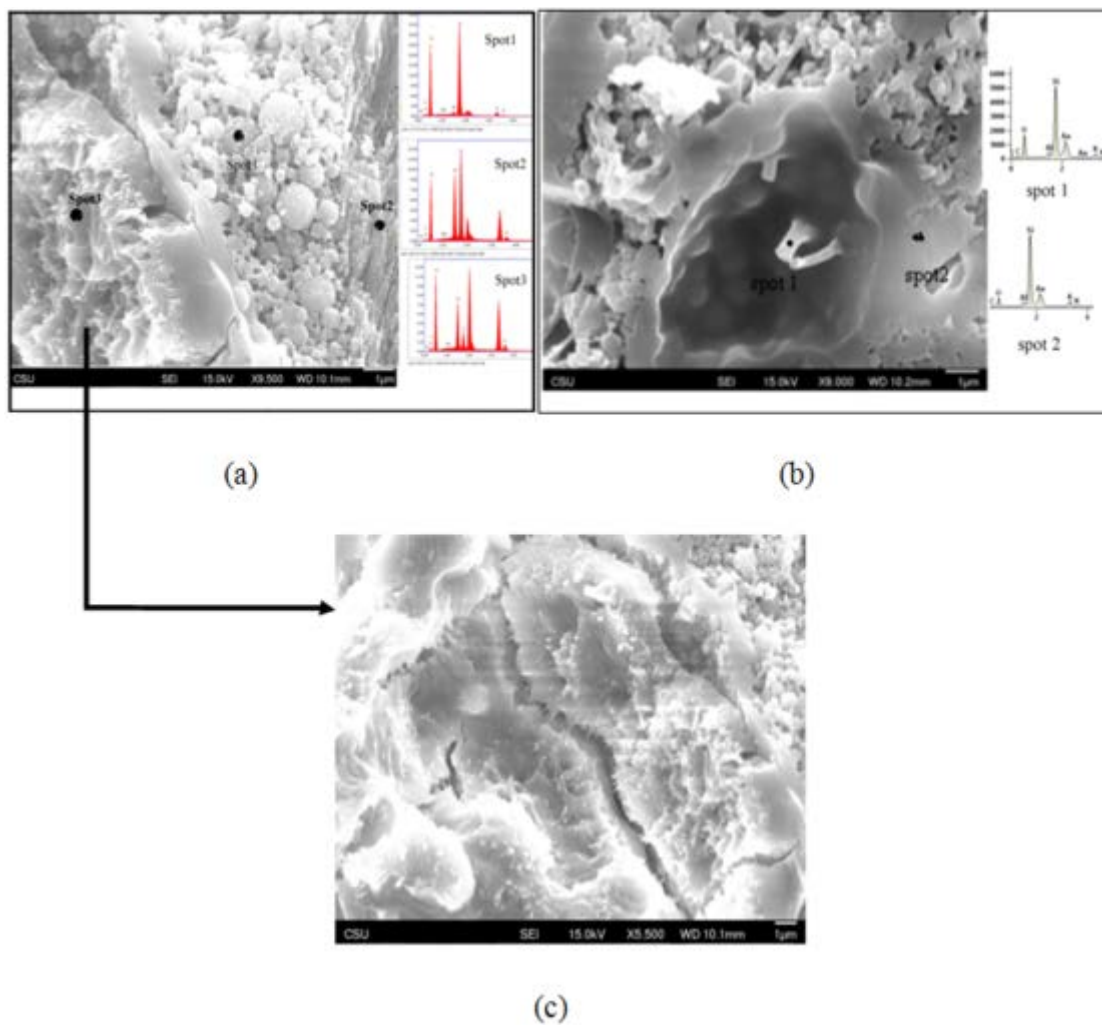
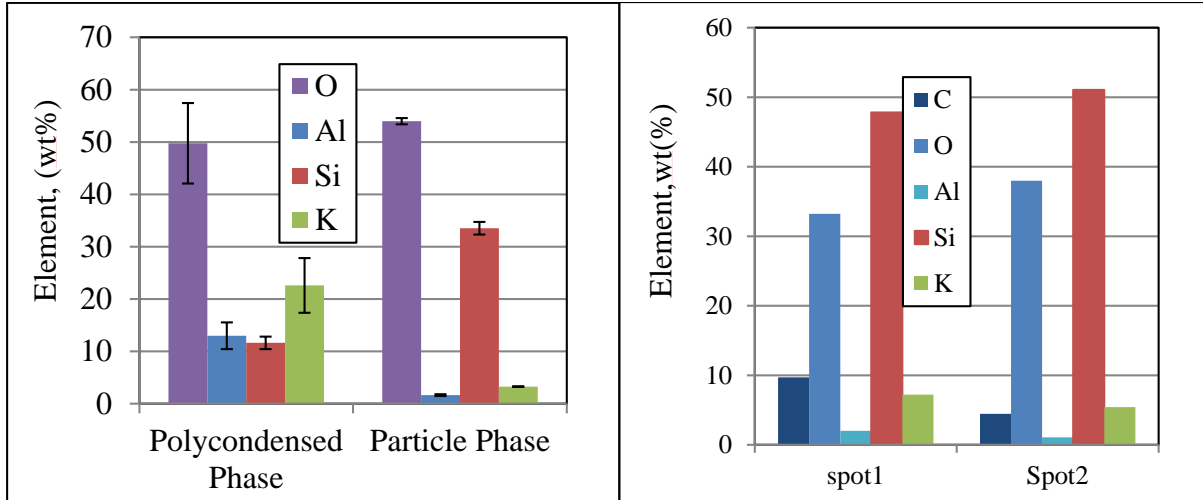


Figure 7.14. Morphology of (a) ANF and (b) SCW reinforced geo-polymer at low temperature (250 °C). (c) Enlarged view of ANF reinforced poly-condensed structure.



(a)

(b)

Figure 7.15. Atomic wt % of elements on the (a) poly-condensed and particle structures & (b) on the nano-fillers and poly-condensed structure of ANF and SCW reinforced geo-polymer, respectively (The atomic wt% represents the respective EDS spectrums shown in Figure 7.14.)

The EDS data presented in Figure 7.14(a) shows that the poly-condensed network contains much higher Aluminum and Potassium concentrations than the particle structure. This suggests that the Potassium balanced poly-condensed network of geopolymer contains a higher concentration of ANF. This evidence of higher ANF concentration in poly-condensed structure supports the features as seen in the microstructure of ANF reinforced geopolymer (see Figure 7.14) and further suggests that ANF is not contained in the structure formed by the particles and is thus not available to toughen the geopolymer in those regions. Poly-condensed gel nucleates on the ANF surfaces<sup>52</sup> which help in partial reinforcement of the matrix. From the EDS of SCW reinforced geo-polymer (see Figure 7.14(b)), it is found that carbon on the surface of rigid nano-sized SCW fibers is much higher compared to the overall geopolymer materials. This confirms the

nanofibers as SCW. This evidence along with the microstructure of SCW reinforced geopolymer (see Figure 7.14 (b)) suggests that SCW is more capable in reinforcing both the particulate and poly-condensed regions of the geopolymer structure.

To better understand the difference between the microstructures of the ANF and SCW reinforced MEYEB at low temperature, a descriptive model is presented, which is shown in Figure 7.16. It is expected that these models, describing different interactions between SCW and ANF nano-reinforcements and the geopolymer will be useful in discussing the difference in the effectiveness of these two types of nanofillers. According to this model, the neat geopolymer consists of residual particles embedded into poly-condensed matrix. The SCW reinforced geopolymer model shows that, SCWs disperse homogeneously and form a scaffold structure to hold residual particles in place. The presence of SCW increases the sliding friction of particles and crack resistance around the particles. However ANF reinforced geopolymer model shows the dispersion of ANFs only in the poly-condensed matrix. It is also shown that, the lengths of ANFs are small to bridge multiple particles and hold them in place. This suggests that nanofillers are required to have some minimum length in order to hold particles against pulling out. Therefore according to the models presented (see Figure 7.16), it is possible to state that, SCWs have better reinforcing capability compared to ANF which allows these nanofillers to effectively reinforce the complete geopolymer structure and perform better in toughening. This is also supported by the toughness results shown in Figure 7.13 .



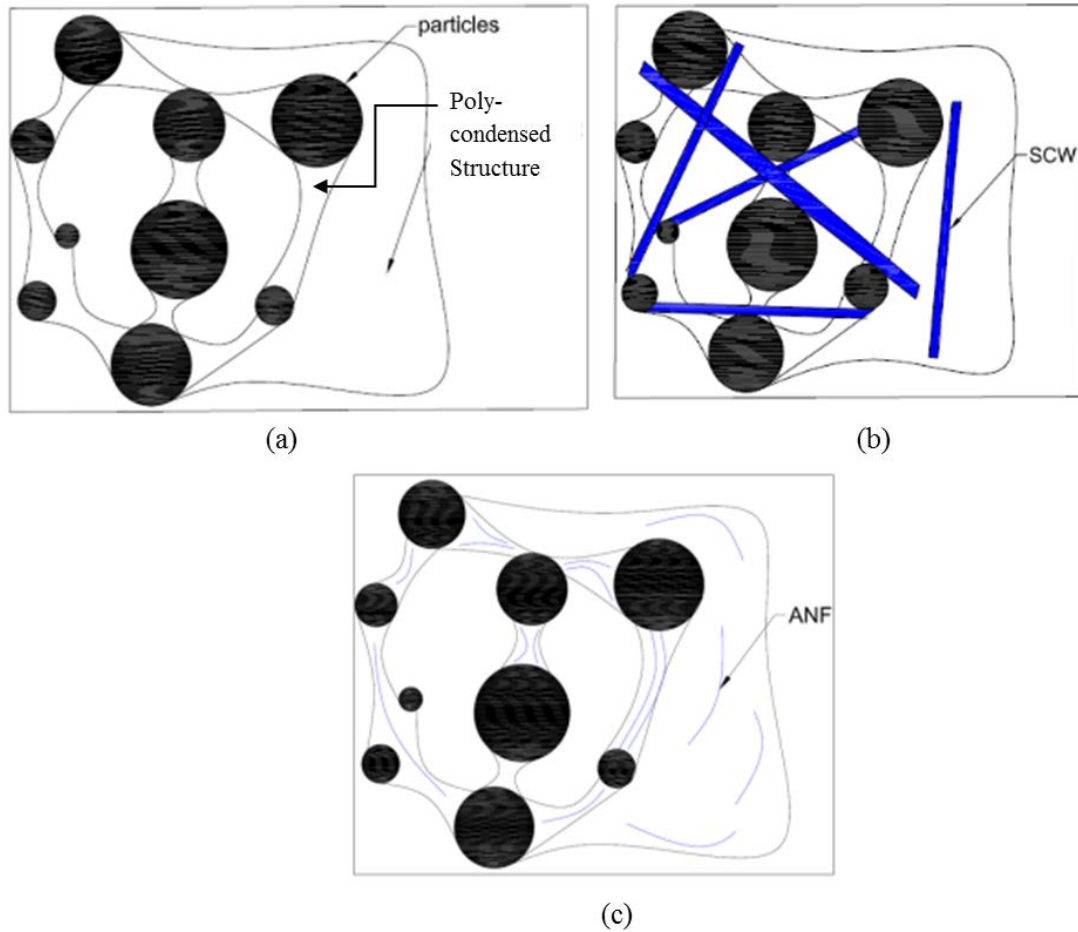


Figure 7.16. Descriptive model showing the dispersion of (b) SCW and (c) ANF in the geopolymer matrix.

In order for effectively reinforcing geopolymer of this type the minimum length ( $l_{nf}$ ) of the nanofiller is suggested as higher than twice the sum of particle size and inter-particle distance. The relationship can be expressed in the following equation

$$l_{nf} > 2(D_p + SD_d + I_p + SD_l) \quad (30)$$

Where,  $d_p$ ,  $I_p$ ,  $SD_d$  and  $SD_l$  are diameter of the particles, inter-particle distance and standard deviation in particle diameters and inter-particle distances, respectively. According to Figure 5.27 the minimum length of nanofillers to reinforce MEYEB at 80 °C, 250 °C and 650 °C should be at least 2.56, 1.94 and 4.5  $\mu\text{m}$ . The detailed calculation is presented in Appendix B4. It

is worth mentioning that, standard deviations in the particle diameter and the inter-particle distances were added in order to make a statistically viable estimation in the length of the nanofiller.

## **7.6 Effectiveness of Nanofillers at High Temperature**

The variations in the effectiveness of SCW and ANF at high temperature are explained here.  $dK_{IC}$  of 2 vol% SCW and expected  $dK_{IC}$  of 4 vol% SCW is presented in Figure 7.17. As explained before, with the high temperature treatment the effectiveness of SCW is reduced in the case of both 2 and 4 vol% reinforcement. The reduction in toughness suggests the variations in the interfacial strength at high temperature.

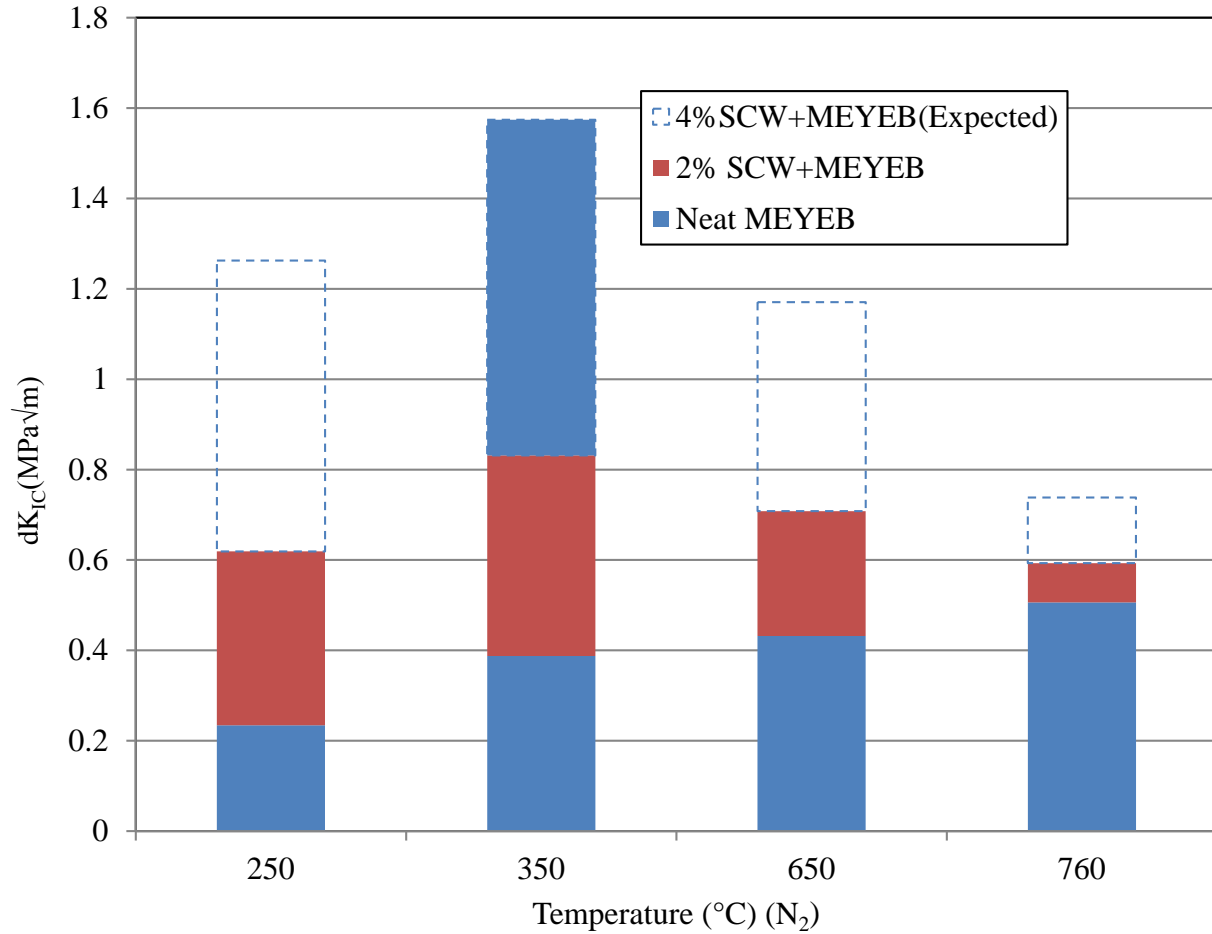


Figure 7.17. Net increase in toughness using 2% SCW and expected net increase in toughness using 4% SCW in various treatment temperatures.

Variations in the interface strengths between SCW and geopolymer are observed in terms of the variations in the pull-out lengths when SCW reinforced geopolymer is heat treated at different temperatures. Figure 7.18 is representative of some SEM images of such samples treated at 250° C and 650 °C. The SEM observation shows that at 650 °C the pull out length of SCW is almost three times higher than samples heat treated at 250 °C. Some more representative SEM images can be found in Appendix C3. Even though greater pull out length is often consistent with higher toughness in some conventional ceramic matrix composites (CMC)<sup>2,9</sup>, in this case higher

pull out length indicates that the load transfer between the weak geopolymer matrix and strong nano-filler, and crack bridging strength, are low. Due to weak interfacial strength sufficient load is not transferred to nano-filler, which causes the geopolymer to fail at lower load. This lower failure load is associated with lower fracture toughness. Therefore it can be stated that weaker interface strength causes the reduction in the effectiveness of SCW in toughening of geopolymer. The possible reason for the weaker interface is the formation of a separation layer on the surface of nano-fillers. The variations in the interfacial strength are investigated using EDS and XRD, which is described in the following section.

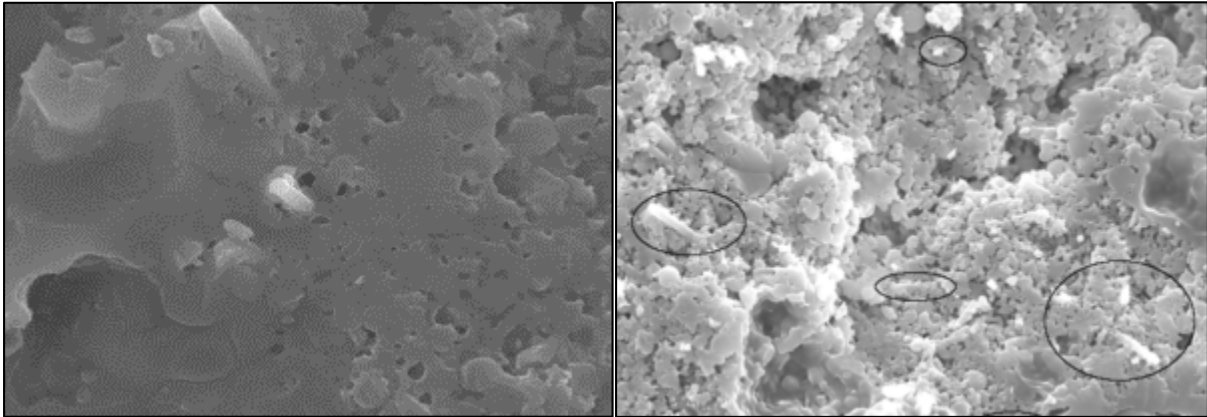


Figure 7.18. Pull out of SCW at (a) 250 °C & (b) 650 °C in N<sub>2</sub> (x2000 magnification).

EDS analyses were performed to quantify the elements on the interface surface of bulk, as-received, SCW and on the surface of SCW in SCW reinforced geopolymer treated at 250 °C and at 650 °C. The representative EDS of the elements on those surfaces of SCW are presented in Figure 7.19 and the average wt % of those elements are presented in Figure 7.20. Raw wt.% data of EDS are presented in Appendix C4. It is found that with the increase in temperature upto 650 °C, the atomic wt% of oxygen, aluminum and potassium increased and that of carbon & silicon

decreased. This increase in temperature and reduced silicon environment<sup>118</sup> in the SCW reinforced geopolymer is suggested to favor the formation of  $Al_4C_3$  due to the reaction between free aluminum ion and carbon<sup>117</sup>. Once this  $Al_4C_3$  layer is formed it stops further reactions that would thicken the layer<sup>119</sup>. Therefore further increase in the layer thickness does not occur with the increase in temperature. If this  $Al_4C_3$  could get thicker (but actually not) the interfacial strength might stop being reduced and actually increase. Therefore, with further increase in temperature to 760 °C interfacial strength stays in the lower state which results in the corresponding lower fracture toughness.

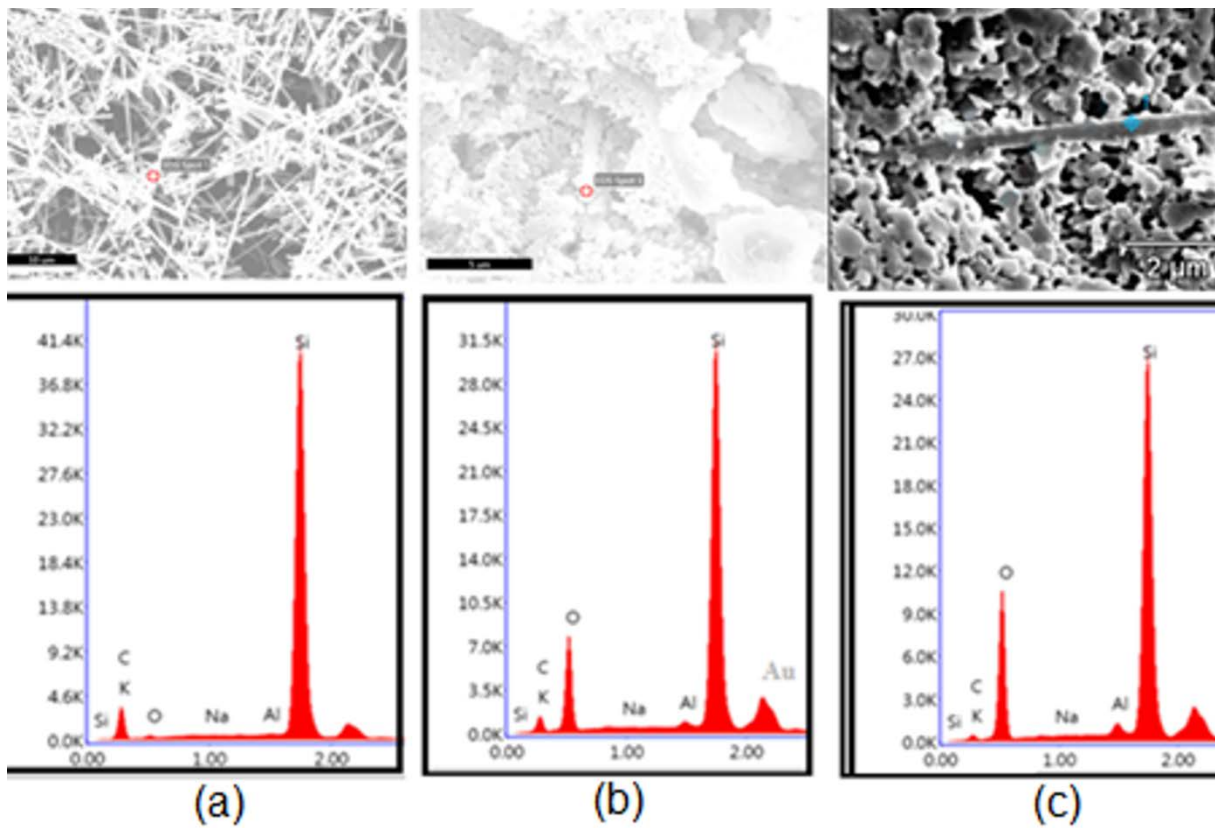


Figure 7.19. EDS of (a) bulk SCW & 2 vol% SCW in MEYEB at (b) 250 °C and (c) 650 °C.

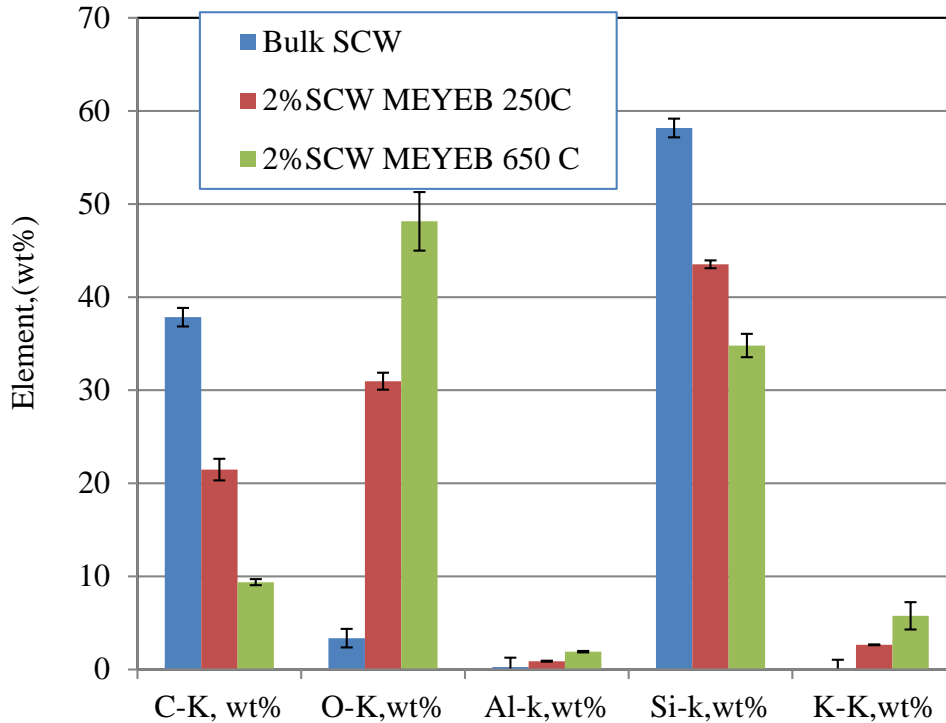


Figure 7.20. Elements of SCW on (a) bulk SCW, (b) 250 °C and (c) 650 °C.

XRD was performed to verify the formation of  $Al_4C_3$ . XRD analysis of 4% SCW reinforced geopolymer (see Figure 7.21) suggests that a new crystalline  $Al_4C_3$  phase is formed. This  $Al_4C_3$  layer is expected to form in the interface between the matrix and SCW, because the surface of SCW is the source of free carbon and matrix is the source of  $Al^+$  ions. A model showing the formation of this  $Al_4C_3$  layer at the interface of SCW and geopolymer is presented in Figure 7.22.  $Al^+$  ions leach out of the geopolymer precursor particles and take part in the polycondensation reactions. Excess  $Al^+$  ions react with the surface carbon of SCW to form  $Al_4C_3$ <sup>118</sup>. The formation of  $Al_4C_3$  depends on the proper thermodynamic condition (high temperature) and chemical environments (Reduced Si). Thus, the interface between geopolymer to  $Al_4C_3$  is weaker compared to the interface between  $Al_4C_3$  to SCW. This weak interface affects the toughening mechanism associated with strong bridging between SCW and geopolymer.

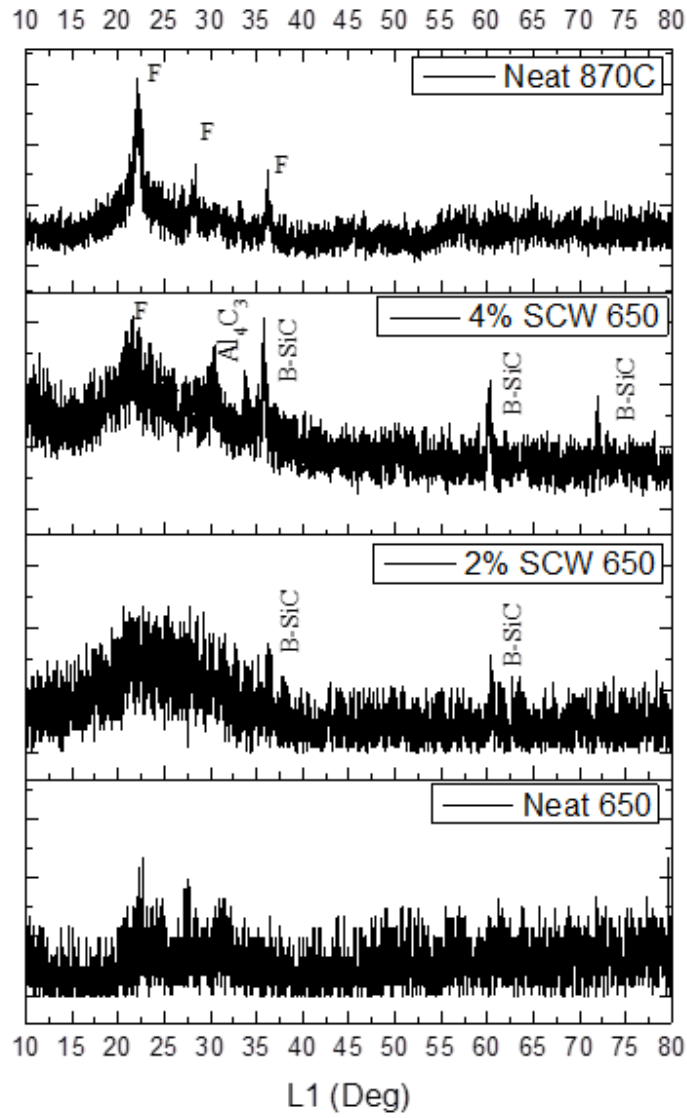


Figure 7.21. XRD of neat MEYEB at (a) 650 °C ( $O_2$ ) and (b) 870 °C ( $O_2$ ) & 2 % and 4% SCW reinforced MEYEB at (a) 650 °C ( $O_2$ ) (All treated for 5 hours).

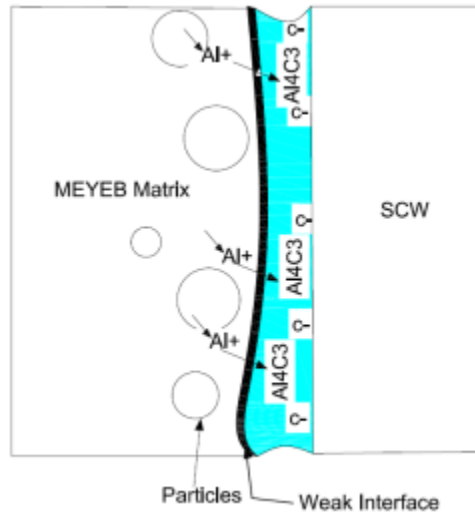


Figure 7.22. A model presenting the interface layer formation at high temperature (Not drawn in scale; weak interface is shown as a black solid layer).

The effectiveness of ANF in toughening ( $dK_{IC}$ ) was also reduced at high temperature (see Figure 7.13(b)). This is described with the mechanism of the morphological transformation of 2vol% ANF reinforced geopolymer from 80 °C to 650 °C. Figure 7.23 (a) & (b) present the microstructures of ANF reinforced geopolymer treated only at 80 °C and post heat treated upto 650 °C in oxygen, respectively. The microstructures of the materials clearly show the reductions in the ANF concentrations with increasing treatment temperature. This evidence is also supported by the elemental analysis of the two microstructures, ANF reinforced geopolymer treated at only 80 °C and post heat treated upto 650 °C, which is shown in Figure 7.24. Images of EDS spectrums with area and point analysis can be found in Appendix C4. Aluminum could not be found in the EDS of ANF reinforced geopolymer treated at 650 °C. This reduction suggests strong diffusion of ANF into the like geopolymer matrix. With the thermal treatment at 650 °C atomic weight % of Aluminum reduced by almost 70% (13wt. % vs 4wt. %) and that of silicon increased by almost 132% (11.62 wt. % vs 27.46wt. %). The depletion of aluminum and



prominence of silicon suggest that ANF has diffused into the silica rich geopolymer matrix. ANF with high surface energy<sup>85</sup>, opposite to bulk alumina which has low surface energy, may be favored by this diffusion into chemically similar geopolymer matrix, however, more study and thermodynamic analysis are required to validate if the diffusion is the key factor behind the depletion of ANF. The reduction in the toughness of ANF reinforced geopolymer with high temperature treatment therefore indicates the reduction in the structural integrity and effectiveness of ANF.

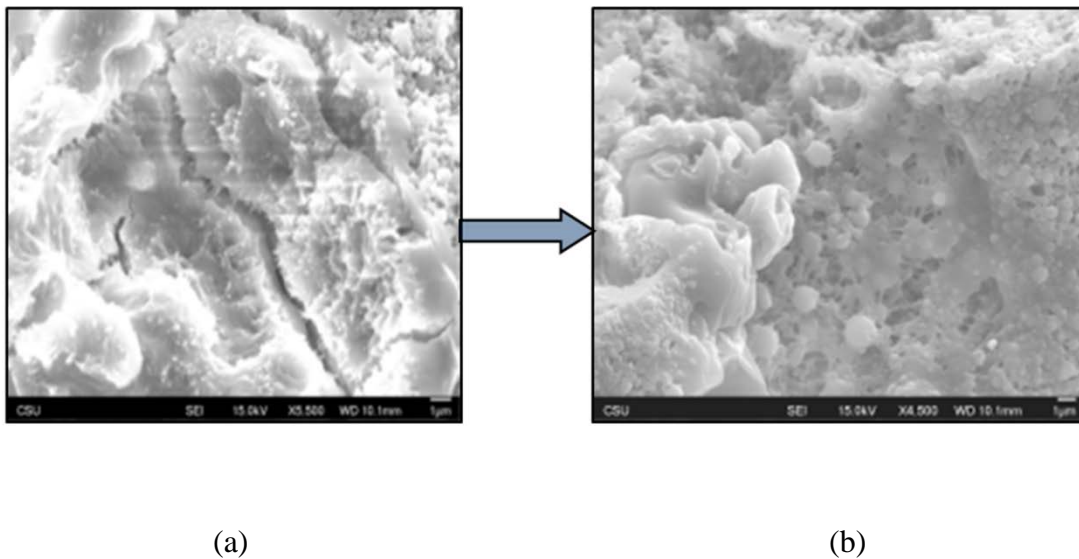


Figure 7.23. Morphological transformation showing diffusion of ANF with thermal treatment from (a) 80 °C to (b) 650 °C (O<sub>2</sub>).

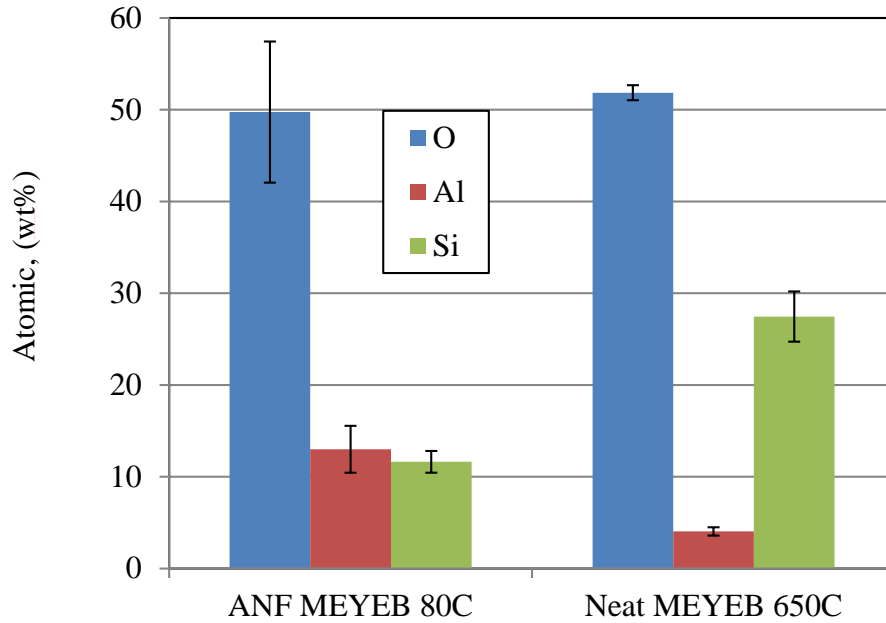


Figure 7.24. Various elements of 2vol % ANF reinforced geopolymer at 80 °C and 650 °C (in O<sub>2</sub>).

Diffusion continues at an even more rapid rate at 760 °C which causes further reduction in the effectiveness of ANF (see Figure 7.13(b)) in toughening. At this high temperature ANF completely diffuses and acts as defects in the geopolymer matrix. Therefore at 760 °C, ANF negatively affects the toughness of the geopolymer.

## 7.7 Future Works

Several recommendations can be made along the line with the continuation of the current research for improving the effectiveness of nano-reinforcement in toughening of geopolymer. Some of these are recommendations can be listed as follows,

1. Investigate the effectiveness of nano-fillers reinforcement into the geopolymer at intermediate treatment temperatures between 350 ° and 650 °C to gain more understanding on the thermal effects on the performance of nanofillers.

2. Modify the interface conditions between nanofillers and the geopolymer in order to prevent thermal diffusion of nanofillers. This can be done by applying surface coating on the nanofillers, heat treating nanofillers before application and by controlling the surface chemistry of the nanofillers.
3. Apply more than one type of nanofillers into geopolymer in combination that toughen poly-condensed network & deflects cracks around the residual geopolymer particles simultaneously.
4. The mechanism of Aluminum carbide formation in the Silicon carbide whisker (SCW) and geopolymer interface needs lot more validation. In order for the formation of continuous layer of SCW, SCW reinforced geopolymer is required to heat treat for extended period of time and anneal in the furnace. It is suggested that the thickness of this type of layer can be 50-60 nm, approximately<sup>119</sup>. SEM can be performed to view this layer at the interface.
5. Further evaluation is needed to observe ANF in ANF reinforced geopolymer at 650 °C. It is important to understand why ANF was not observed in SEM and EDS at 650 °C. ANF should be structurally stable at this temperature. It requires more thermodynamic analysis including Gibbs surface energy, chemical kinetics of the diffusion between geopolymer and ANF and characterizations using SEM and EDS.

From the overall discussion it can be stated that nanofillers with high aspect ratio and high interfacial strength are effective in toughening of geopolymer. 2 % SCW has been found to most effective in toughening in all the thermodynamic conditions investigated. The study presented in the next chapter will verify the effectiveness of the nanofiller in continuous fiber reinforced composites (GPC).

## 8 FIBER REINFORCED COMPOSITES

This study verifies the effectiveness of the 2 vol% SCW nano-filler in toughening continuous fiber reinforced MEYEB. Fibers used in this investigation are Nextel 610 with clean and carbon coated surfaces, respectively. Two types of surface treatments were used to demonstrate the effectiveness of optimum nano-reinforcement in two opposite interfacial strength between the fiber and matrix while keeping the effect of aspect ratio of nanofillers and interfacial strength between nanofiller/matrix interfaces constant. The mechanical tests involved in this investigation were to measure flexural strength and short beam shear.

### 8.1 Experimental Technique

Continuous fiber reinforced geopolymer composites were prepared using Nextel 610 unidirectional fiber and MEYEB. Chemical configurations of the fiber surfaces were modified in order to prepare composites with the variations in the interfacial strength between the major constituents. Four types of composites were prepared using 0 and 2% SCW reinforced MEYEB as matrices and clean and carbon coated Nextel 610 as fibers. The designations of the samples are presented in Table 8.2.

#### 8.1.1 Carbon Coated and Clean Fiber Processing

Carbon coating was produced by placing Nextel 610 fibers in the chamber of chemical vapor deposition (CVD) which is shown in Figure 8.1. To perform this process the chamber of CVD was evacuated, then backfilled with nitrogen at a pressure of 760 torr. The chamber was heated to 700 °C at 5 °C/min. The chamber was maintained at 700 °C for 15 minutes. To end this process the heater was then turned off and the chamber was allowed to cool down to room temperature.

To obtain Nextel 610 fiber tows with clean surface the coating or sizing was removed in refractory oven following the same respective temperature schedule with maintain the flow of air in the chamber of the oven. Clean and carbon coated Nextel 610 fiber tows are presented in Figure 8.2.



Figure 8.1. CVD furnace used to modify the sizing of the surface of fiber tow into a carbon deposited layer.



Figure 8.2. Nextel 610 fiber with (left) clean and (right) carbon deposited surface.

## 8.2 Preparation of the Mold for Composite Processing

A steel mold with the compression bar is presented in Figure 8.3. The mold has the capability of preparing samples with two different types of minimum thicknesses required for different tests. The dimensions of the cavities of the mold assembly are shown in Table 8.1.



Figure 8.3. Steel mold & T-bar for the fabrication of fiber reinforced composites.

Table 8.1. Dimensions of the cavities in the mold assembled with the T-bars.

Cavity Type	Length (mm)	Width (mm)	Thickness (mm)
Thick	203	7.5	2.5
Thin	203	7.5	5.5

### 8.3 Calculation of the Required Fiber Amount

In order for evaluating the performance of various fiber reinforced composites a generally accepted approach is to maintain a constant fiber volume fraction in all the samples. Before fabricating the sample, the amount of fiber was estimated based on this constant fiber volume fraction, which is maintained at 50%. Appendix B5 presents the calculation of the total number of fiber tows required for a sample with expected dimensions of the thin cavity (Table 8.1) and fiber volume fractions of 50%. The required fiber amount was total 33 tow of lengths equal to the length of the cavity.

### 8.4 Composite Preparation Technique

In order to prepare the composite, the surface treated fiber tows were first cut to the length of the die cavity. Once the particular surface condition was achieved fiber tows were cut to the length of the die cavity. The number of tows used was measured to achieve a 50 percent volume fraction. The tows were separated into six groupings and wet out by hand. The MEYEB resin was poured onto the fibers and worked in by applying pressure via a paint roller. More MEYEB was poured out as necessary until the fibers appeared to be wet out. Before placing the fibers longitudinally in the die cavity a small amount of resin was poured into the die cavity. It was

then spread out over the entire length and sides of the cavity which achieved a very thin coating on its base and walls.

After placing the fibers the in the die cavity, a light layer of resin was spread over the top of the fibers. Using this technique to wet out fibers was very time consuming. This limited the number of samples that could be created because of the working time of the resin, which was about 30 to 40 minutes. After placing all fiber samples in the die, it was then fully enclosed using the side plates and T-bars. The die was then sealed in a bag, and placed under vacuum. Vacuum was held for two to three minutes. The die was then moved to a different bag, placed in the hot press, and pressure was applied. Starting from 40 °C the die was ramped at 1 °C/min up to 80 °C and held for one hour. For curing the samples for curing more than 1 hour, additional moisture was added to the bag to aid the curing process. Then the bag was placed in the oven and cured for additional 23 hours at 80 °C. After the initial cure, the die was allowed to cool and the samples were removed. Samples were then subjected to the post cure regime followed by treatment schedule shown in Table 8.2. This Table also presents the designation of the types of the samples that were prepared.



Table 8.2. Test matrix of the fiber reinforced composite samples.

Sample No.	Sample Type	Fiber Type	Surface condition	Matrix	Treatment schedule	Test technique	
						Flexural	SBS
1	N-CL610-M250	Nextel 610	Clean	0%SCW MEYEB	Dry at 80 °C (10hr) →100°C (3hr) →250°C(5hr)	✓	✓
2	N-CL610-SCW-M250	Nextel 610	Clean	2%SCW MEYEB		✓	✓
3	N-CC610-M250	Nextel 610	Carbon coated	0%SCW MEYEB		✓	✓
4	N-CC610-SCW-M250	Nextel 610	Carbon coated	2%SCW MEYEB		✓	✓

### 8.5 Volume Fraction Calculation

Actual fiber volume fraction was calculated using the following equation-

$$v_f = (m_f / \rho_f) / V_c \quad (31)$$

Where,  $m_f$  = Mass of fiber

$\rho_f$  = Density of fiber

$V_c$  = Volume of Composite

This volume fraction was then compared with the volume fraction calculated using the theoretical mass of the fibers based on the total tows used to make the composite. The calculation is shown in Appendix B5.

### 8.6 Characterization

Both bend beam and short beam shear composite specimens were prepared to investigate the effect of nano-reinforcement on the specific mechanical properties. Any increase in pure

flexural strength of the composite can be directly co-related to the improvement in the tensile strength. Three point bend beam test with high span to depth (L/d) ratio is a preferable technique to evaluate the flexural strength of the composite. Conversely short beam shear test can be performed to investigate the improvement of pure shear resistance due to nano-reinforcement. Due to the short length of the beam, the stress field through the beam in the short beam shear test is significantly disturbed by the local forces at the loading and support point and the plane of high shear stress becomes the failure plane, which is the mid-plane along the entire beam between the supports. The short beam test eliminates the possibility of the failure under bending stress in which is dominated by the failure of the fibers. In this test specimen fails purely under shear stress which is dominated by the ability of the matrix to resist the failure. This is also denoted as inter-laminar shear strength<sup>120</sup> which is purely the matrix property. The smaller the span to depth ratio is maintained, the higher is the possibility of getting pure shear response. According to standard <sup>121</sup> the span to depth (L/d) ratio for short beam test is maintained as 4.

Flexural strength tests were conducted in ATS load frame at a displacement rate of 0.012 in/min. The test fixture had a support span of 45.4 mm producing a span-to-specimen thickness ratio of 15-to-1. Force was recorded as a function of time. SBS tests were conducted on the same load frame using a modified setup of the same test fixture producing span-to-thickness ratio of 4-to-1. The sample span, thickness and total length for SBS test were 12mm, 3mm and 20 mm, respectively. Testing was conducted in accordance with ASTM D2344<sup>121</sup> at a displacement rate of 0.012 in/min. Once again, force was recorded as a function of time.

## 8.7 Results

Weight, densities and volume fraction of the fibers in the composites are presented in Table 8.3. Here it is seen that, fiber volume fraction of all types of composites are almost 40%. The difference in the volume fraction of neat and nanofilled composites are less than 3 %, which is acceptable for any comparison based on flexural and shear strength. Volume fractions of all the composites were compared with the respective volume fractions calculated based on the theoretical mass of the fiber based on the tow numbers and it was found that there were no differences between the volumes fractions measured in these two techniques.

Table 8.3. Compositions of Nextel 610 fiber reinforced MEYEB composites with and without nano-reinforcement.

Fiber surface	Matrix	Fiber weight, gm	Density of fiber, g/cc	Composite Weight, gm	Composite vol,cm <sup>3</sup>	Actual fiber , $v_f$
Clean	0% SCW MEYEB	7.41	3.88	11.46	4.62	0.414
Clean	2% SCW MEYEB	7.45	3.88	11.81	4.78	0.401
Carbon coated	0% SCW MEYEB	7.4	3.88	11.41	4.6	0.412
Carbon coated	2% SCW MEYEB	7.36	3.88	11.86	4.72	.404

### 8.7.1 Effect of Nano-reinforcement on the Flexural Strength

The images of the bend beam specimens of the fiber reinforced neat and nano-filled MEYEB composites are shown in Figure 8.4. Both neat and nano-filled specimens were processed at 250 °C. There is a clear difference in the appearance of the specimens, which is similar to the differential appearance as found in the neat and SCW reinforced MEYEB matrix. The lengths to depths (L/d) ratio for all the specimens are maintained as 15, which is in accordance to the standard ASTM C1341<sup>122</sup>.

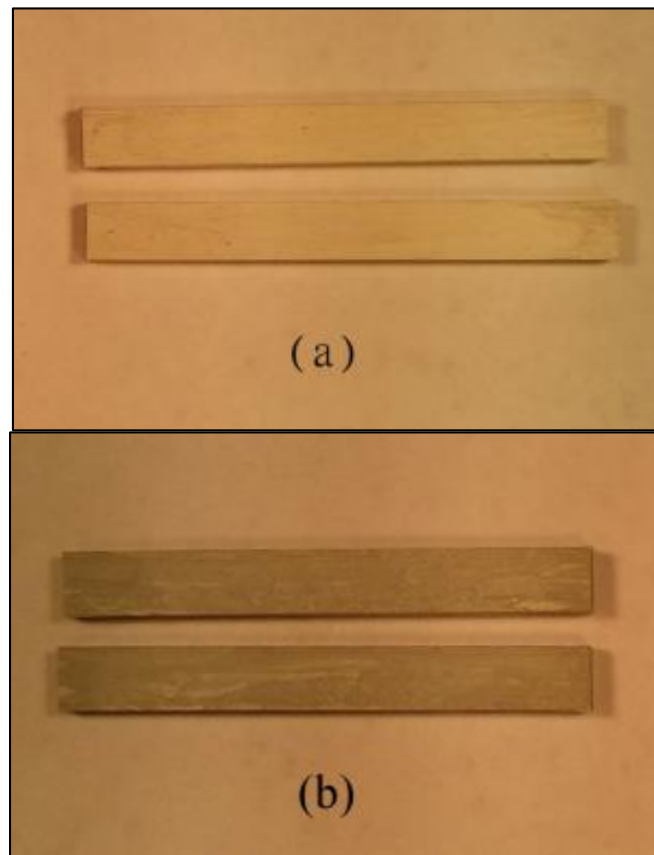


Figure 8.4. Clean Nextel 610 reinforced (a) Neat and (b) 2 vol% SCW nanofilled MEYEB composites treated at 250 °C.

Figure 8.5 presents the flexural strengths of clean and carbon coated Nextel 610 reinforced MEYEB with 0% and 2 vol% SCW nano-reinforcement. It is clearly demonstrated that 2% SCW nano-reinforcement increased the flexural strength of the composite by 35%. Possible mechanisms are the increase in the matrix tensile strength and partly the increase in inter-laminar sliding friction due to improved shear resistance.

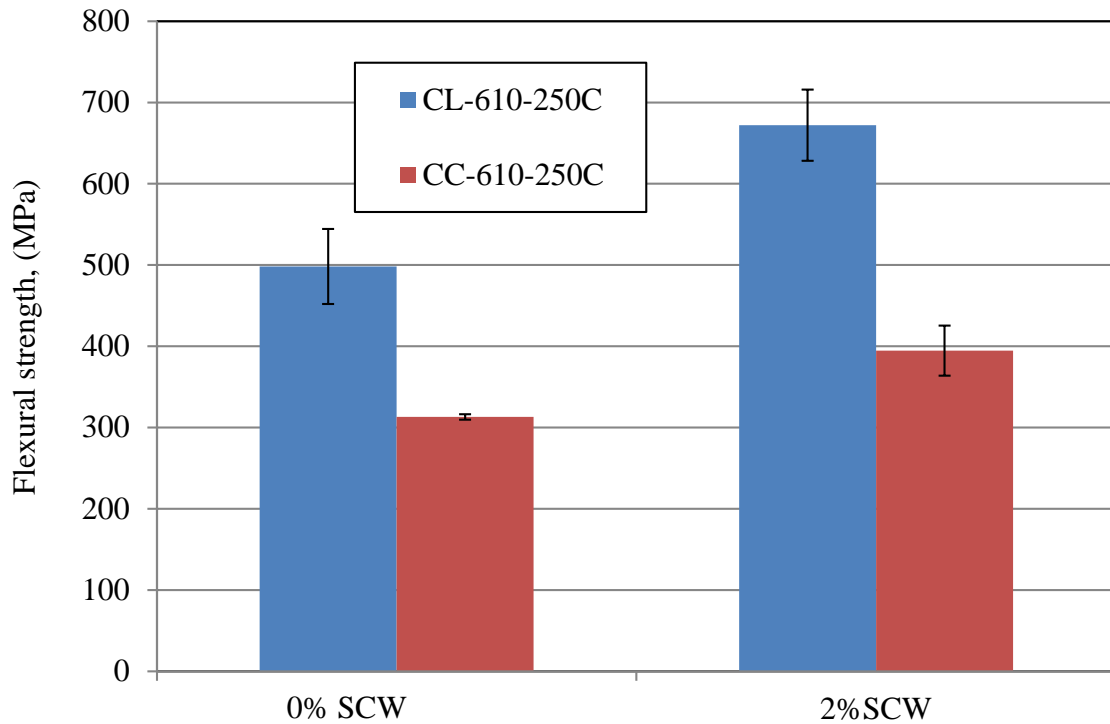


Figure 8.5. Flexural strength of 0% and 2% SCW nanofilled MEYEB reinforced with clean Nextel 610 fiber treated at 250 °C.

### 8.7.2 Effect of Nano-reinforcement on the Shear Strength

The images of the short beam specimens of neat and nanofilled MEYEB composites are presented in Figure 8.6. The span-to-depth (L/d) ratios of these specimens are 4. The surface nanofilled specimens look darker than that of the specimens with no nanofillers. Overall the dark

appearance of the nanofilled samples suggests that nanofillers are uniformly distributed into the geopolymer matrix.

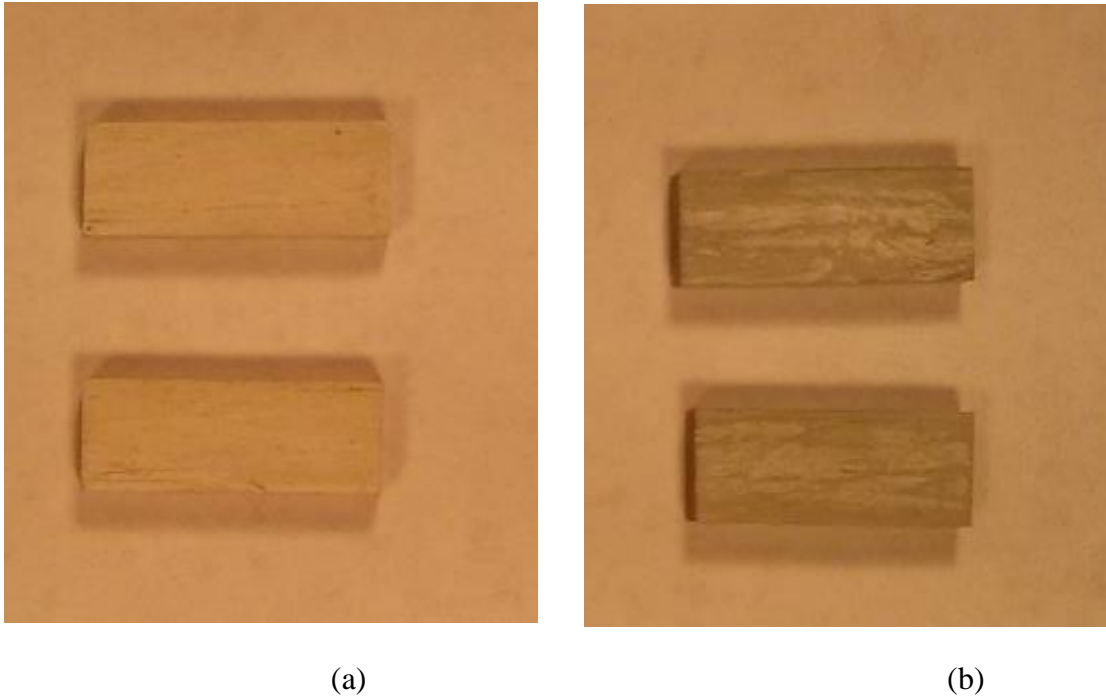


Figure 8.6. Short beam test specimen prepared from clean Nextel 610 reinforced (a) 0 vol% and (b) 2 vol% SCW nanofilled MEYEB composites treated at 250 °C.

The short beam shear strength of 0% and 2% SCW nanofilled MEYEB clean & coated Nextel 610 composites are presented in Figure 8.7. The study shows that with 2%SCW reinforcement, shear strength of the composite increased by approximately 39.5%. The increase in short beam shear strength is the direct indication to the increased resistance to inter-laminar separation of the composite.

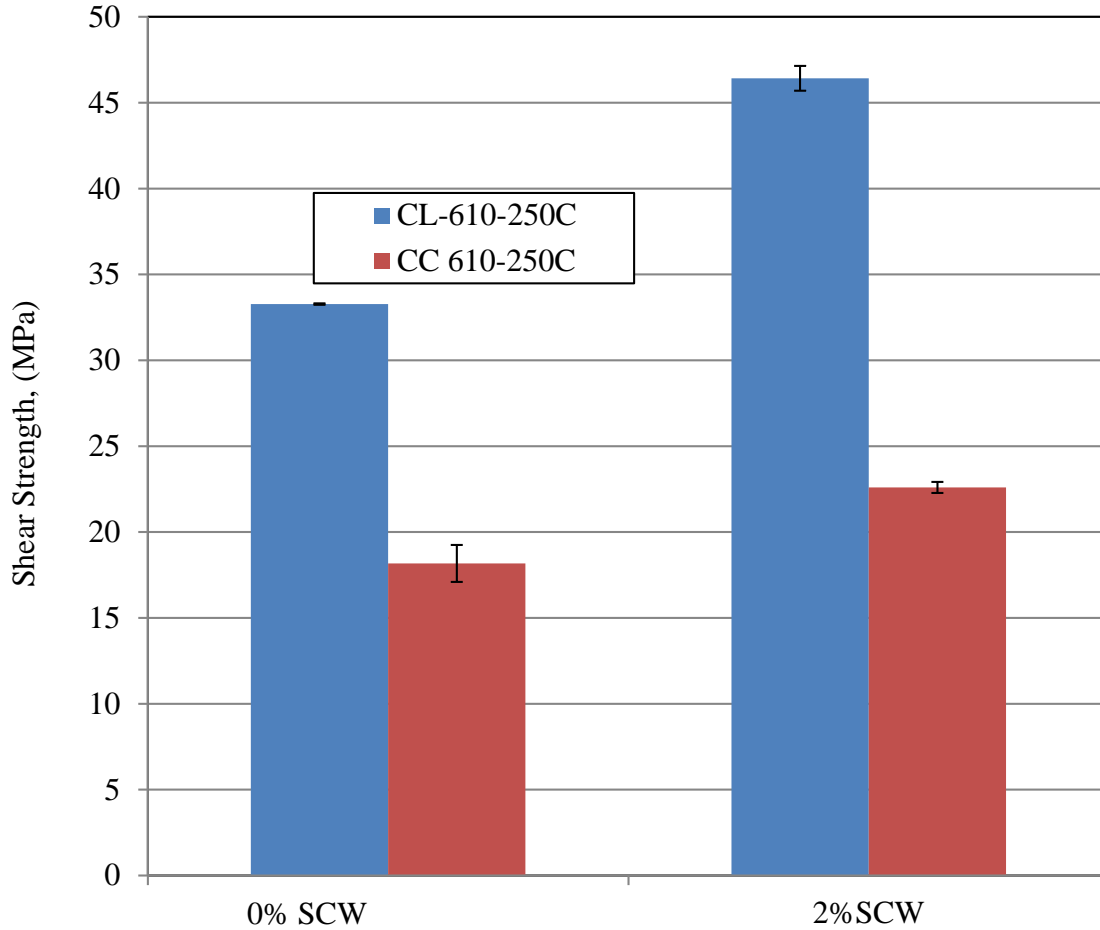


Figure 8.7. Short beam shear strength of neat and 2% SCW nanofilled MEYEB reinforced with clean Nextel 610 fiber treated at 250 °C.

## 8.8 Discussion

Composites were made using 0 vol% and 2 vol% SCW reinforced geopolymer matrix with either clean or carbon coated continuous fiber in pairs. The flexural and shear strength of neat and 2 vol% SCW reinforced composites are presented together in Figure 8.8. Percentile improvements in flexural strengths with 2 vol% SCW are presented alongside in Figure 8.9. From the results, the loading of 2 vol% SCW is found to be effective in strengthening both continuous coated and continuous clean fiber reinforced composites, respectively. With 2 vol% SCW addition, the

flexural strengths of the matrix, clean fiber and coated fiber reinforced composite improved by ~15, ~174 and ~81 MPa, which are 184%, 35% and 21 %, from the respective baseline specimens , respectively. Similarly shear strength of two versions of composites (clean and coated fiber reinforced) were improved by 39.5 % and 24%, respectively. Small flexural strength improvement in the nanofilled matrix (~15 MPa) therefore shown to have resulted in a large improvement in the fiber reinforced composites. The improvement in the flexural and shear strength suggests both high tensile properties and improved inter-laminar shear strength of the nanofilled composites with both versions of continuous fiber.

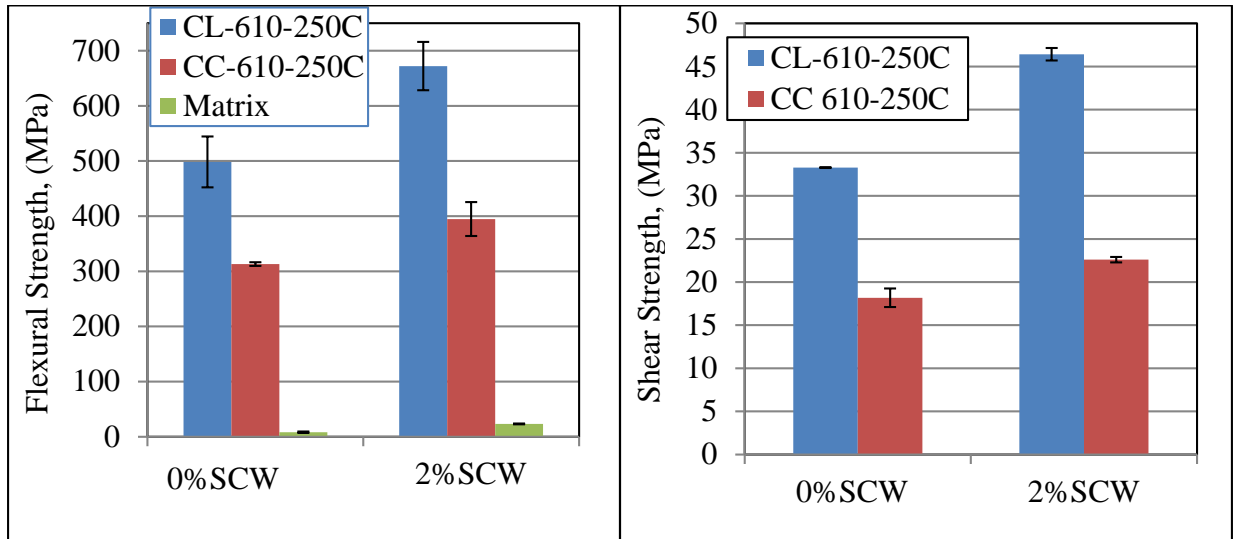


Figure 8.8. (a) Flexural and (b) Shear strengths of neat matrix & clean fiber, 2%SCW reinforced matrix & clean fiber, neat matrix & coated fiber and 2%SCW reinforced matrix & coated fiber composite.



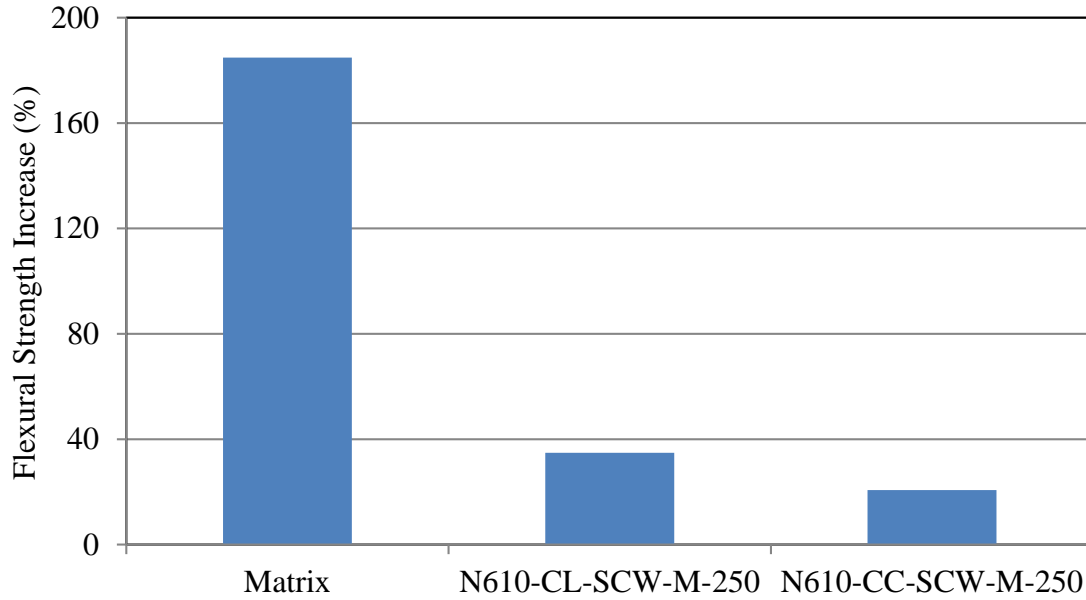


Figure 8.9. Net improvement in flexural strength of geopolymers matrix, continuous clean and coated fiber reinforced geopolymers matrix composites with the additions of 2% SCW nano-fillers.

Crack propagations during the short beam shear test were photographed as shown in Figure 8.10. According to this figure the top edge of the sample was in tension. The photographs show the cracks immediately after the specimens failed at the maximum breaking load. From the photographs it is clear that, the crack in the 0 vol% SCW reinforced matrix directly propagated through the length of the specimen along the mid-span without much damage to the matrix, however in case of 2 vol% SCW reinforcement, the matrix revealed more damage near the loading pin on the tensile surface, which is an indication of crack energy absorption.

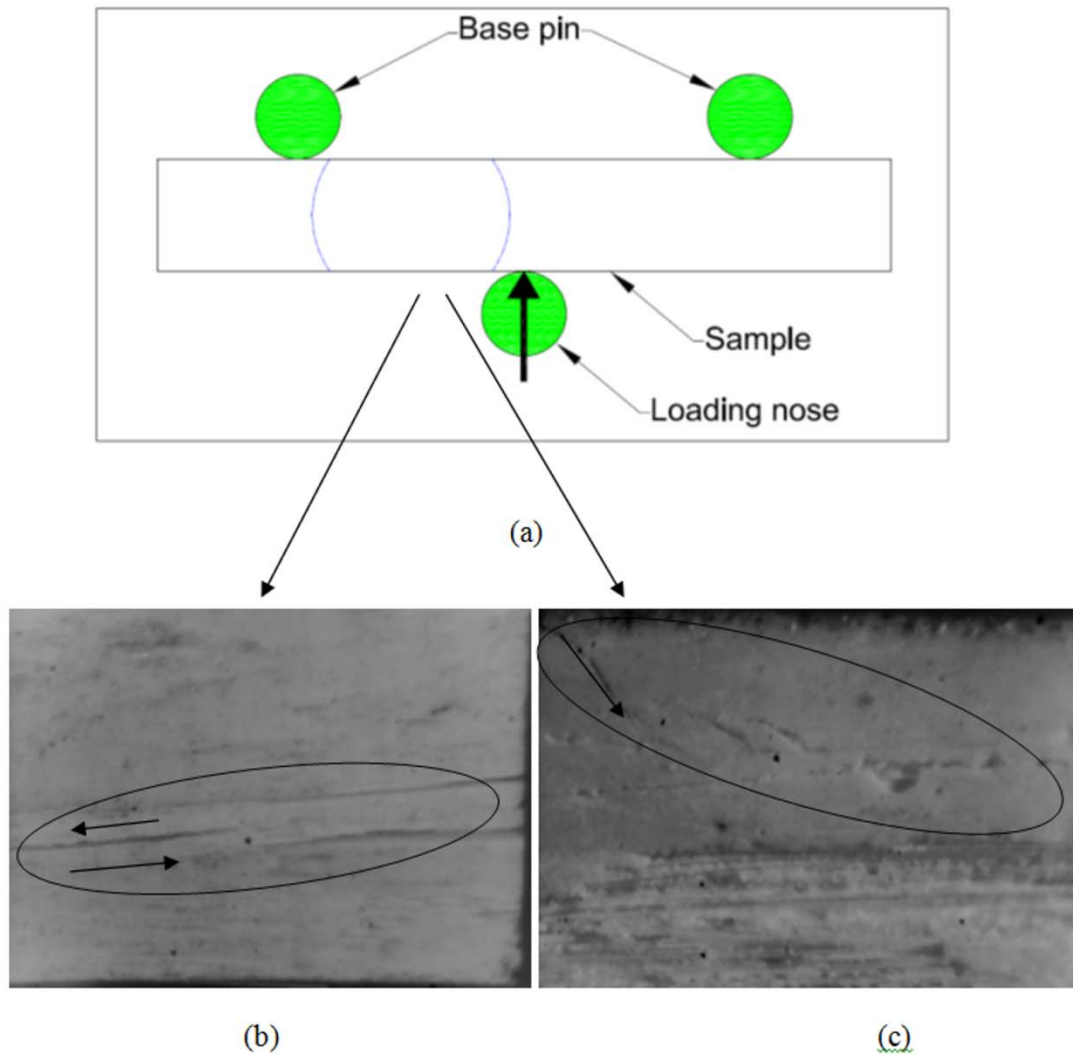


Figure 8.10. Crack propagation of (b) neat (c) 2% SCW reinforced composite through the length of short beam specimen (c) viewing perpendicular to the thickness (at 16x magnification). (The direction of the crack is shown using the arrow).

Figure 8.11 is also the clear representation of the difference in the crack propagation between 0 vol% and 2 vol% SCW reinforced composites with clean fiber. In the neat composite the crack directly propagated through the length of the specimen all the way to the end. However, in the nano-reinforced specimens no crack was observed as directly propagated to the end. This

indicates that nano-reinforcement facilitates in high energy absorption and inter-laminar shear strength and less catastrophic failure of the structure.

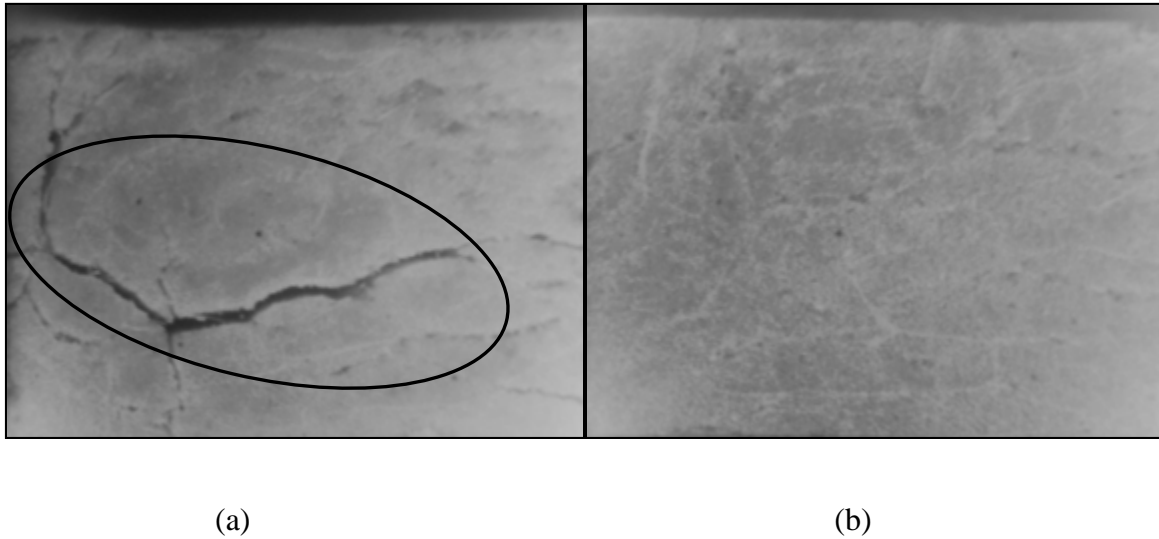


Figure 8.11. The representation of the crack that propagated through the length to the end of (a) clean neat (N-CL610-M250) (b) clean fiber and 2% SCW reinforced specimen (N-CL610-SCW-M250) (at 16x magnification).

Figure 8.12 is the presentation of the crack propagation through the coated fiber & 0 vol% SCW reinforced geopolymer matrix and coated fiber & 2% SCW reinforced geopolymer matrix composite. The pattern of the matrix damage in the 2% SCW reinforced composite again suggests the improvement in the absorption of energy related to the crack propagation. Therefore, it can be stated that the optimum nanofiller are effective in strengthening continuous fiber reinforced composites. This effectiveness is the outcome of the improved tensile and inter-laminar shear strength.

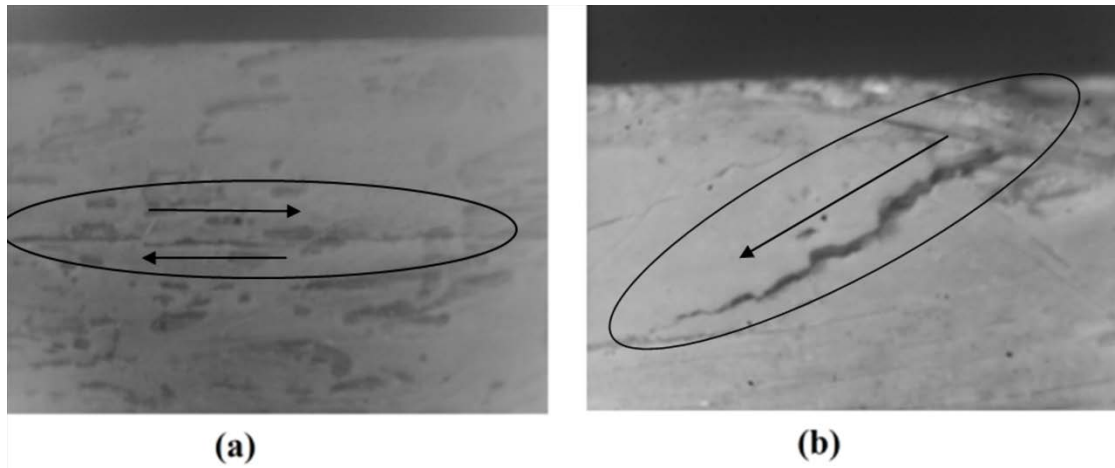


Figure 8.12. Crack Propagation of coated fiber reinforced neat ( N-CC610-M250) and coated fiber& 2%SCW reinforced (N-CC610-SCW-M250) MEYEB matrix composite. (The direction of the crack is shown using the arrow).

## 8.9 Conclusion

The effectiveness of optimum nanofiller has been demonstrated with the continuous fiber reinforced geopolymer composites. The resultant synergetic effect of the interfacial strength between nanofibers/geopolymer and continuous fiber/ geopolymer interface is the key controlling factor in toughening geopolymer matrix composites. The effectiveness of high aspect ratio and high interfacial strength nanofiller has been verified in this investigation, which is primarily the outcome of the improved inter-laminar shear strength and de-lamination resistance. High interfacial strength between nanofiber/geopolymer interface leads to the improvement in the strength of the continuous fiber reinforced geopolymer matrix composites.

## 9 OVERALL SUMMARY

Previous studies suggest that continuous fiber reinforced inorganic polymer composites has potential as high temperature capable structural member. However limited information on the processing of neat polymer and its evaluation based on mechanical and thermal properties hindered further investigation on the capability of inorganic polymer composites in retaining mechanical performance at high temperature and reactive environment. This study has been laid out to derive sufficient information to bridge the gap between the processibility and potential for toughening of neat polymer for the application to fiber reinforced composites.

In the present study inorganic polymer, geopolymer has been processed with optimum parameters that enabled preparing geopolymer samples for evaluating various mechanical, thermal and microstructural properties. The external toughening study has been performed at various operating temperature and environmental conditions using the nanofillers with the variations in the interfacial strength and aspect ratio. Studies showed that at all thermodynamic conditions nanomaterials with high aspect ratio are more effective in toughening compared to nanoparticles.

Further investigations have shown that at various thermodynamic conditions, effectiveness of high aspect ratio nanofillers is a dependent variable which depends on the interfacial strength, tensile strength, reinforcing capabilities, oxidation stability and thermal diffusion. Effectiveness of nano-reinforcement also has been found to be influenced by the in-homogeneity in the geopolymer matrix. Alumina nanofiber (ANF) has been found to create a strong bonding with polycondensed structure of geo-polymer however, due to short length and morphology it didn't

effectively reinforce the overall structure. Conversely, Silicon carbide whisker (SCW) has been found to be capable in reinforcing both particle and poly-condensed structure and therefore act as crack deflectors around the particles surfaces. Due to this improved reinforcing capability SCW is effective in toughening of geo-polymer even though ANF has stronger interfacial strength.

It also has been found that toughness and strength of nano-reinforced geopolymer is strongly limited by the strength and volume fractions of the nanofillers. The evidence shows that stronger SCW is more effective compared to weaker ANF. At high temperature effectiveness of different nanofillers are affected in different manner. Thermal diffusion and formation of separation layer have been found to influence the effectiveness of SCW and ANF, respectively. Therefore it can be stated that the effectiveness of nanofillers depends on the ability to prevent thermal diffusion and formation of weak interfacial bonding.

By keeping all the variables constant silicon carbide whisker with strong interfacial strength has been found to perform better in toughening of geopolymer compared to carbon nanofiber (CNF) with weak interfacial strength. It has been proposed that high aspect ratio and high interfacial strength of nanofillers increased toughness by crack bridging and crack deflection mechanism. Therefore it can be demonstrated that high aspect ratio nanofillers with high interfacial strength are more effective in toughening geopolymer.

Effectiveness of the optimum nanofillers has been verified on the continuous fiber reinforced composites with the variations in the interfacial bond strength between the fiber and matrix. Optimum nanofiller, silicon carbide whisker with 2 vol% loading have been found to be effective in strengthening continuous fiber reinforced composites. Nanofillers with small volume fraction have shown a significantly large improvement in strength of the fiber reinforced composites

which are largely due to the improved tensile and inter-laminar shear strengths. In summary it can be stated that in toughening of geopolymer using randomly oriented nano-fillers crack deflection and strong bridging mechanism plays more important role than pull-out and debonding mechanism.

## REFERENCES

1. Lutgard C De Johghe, Mohamed N Rahman. "Sintering of ceramics". In, Handbook of advanced ceramics. Elsevier Inc, 2003.
2. Narottam P Bansal, Jacques Lamon, In "Ceramic matrix composites: Materials, Modeling and Technology". October 2014, page 219.
3. "Thermal degradation of polymeric materials", Rapra Technology Limited, UK, 2005.
4. Michael Welter, "Unidirectional fibre reinforced geopolymer matrix composites", PhD Thesis.
5. Bridge, J.W., Grabher, A.E., Radford, D.W. "Preliminary investigation of geopolymer matrix-ceramic fiber composites for high temperature structural applications", TEAM 2008, Oct. 6-9, 2008, Istanbul, Turkey.
6. Donald W. Radford, Andrew Grabher and John Bridge, " Inorganic Polymer Matrix Composite Strength Related to Interface Condition", *Materials* 2009, 2(4), 2216-2227; doi:10.3390/ma2042216.
7. D.W. Radford and P.T. Nivala, "DMA as a method of measuring toughness in inorganic polymer matrix composites", The 19th International Conference on Composite Materials.
8. Maximilien E Launey and Robert O. Ritchie. "On the fracture toughness of Advanced Materials", *Adv Mater*, 2009, 21, 2103-2110
9. Anthony G. Evans. "Perspective on the development of high-toughness ceramics." *J Amer Cer Soc*, 1990, 73(2), 187-206.
10. Radford, D.W. and Nivala, P.T. "Dynamic Mechanical Analysis Assessment of the Effectiveness of Toughness Modifications of Inorganic Polymer Matrix Composites". *SAMPE 2010*, Seattle, WA, May 2010.
11. Rahman Samsur and Radford, D.W. "Inorganic polymer matrix materials processing optimization", *SAMPE Tech 2013*, Wichita, KS, Oct 2013
12. Davidovits, J. In "Geopolymer Chemistry and Applications". Saint-Quentin, France, Institut Geopolymere, 2011
13. Grabher, A.E. "Processing Techniques and Evaluation of Geopolymer as a Matrix Material in Fiber Reinforced Composite Engine Exhaust Valves". *Thesis*, Colorado State University, 2008.



14. Nivala, P.T. and Radford, D.W. “The Effectiveness of Toughness Modifications of Inorganic Polymer Matrix Composites as Measured by Static Flexure Testing”. 42<sup>nd</sup> International SAMPE Technical Conference, Salt Lake City, UT, Oct. 12, 2010.
15. F. J. Silva and C. Thaumaturgo. “Fiber reinforcement and fracture response in Geopolymeric mortars”. *Fatigue Fracture Eng Mater Struct*, 26, 167-172.
16. E. Rill, D.R. Lowry and W.M. Kriven. “Properties of Basalt fiber reinforced geopolymer composites”. Strategic materials and computational design. 34<sup>th</sup> international conference on advanced ceramics and composites, 2010.
17. Kazuo Ueno, Satoshi Sedeoka, “Fracture toughness of SiC whisker reinforced Si<sub>3</sub>N<sub>4</sub> ceramics”, *Int J High Tech Ceramics*.198, 3(3), 254.
18. Terry Tiegs. SiC Whisker reinforced alumina. In “Handbook of ceramic composites”. Edited by Narrottam P. Bansal, 2005 Kluwer Academic Publishers.
19. P. F. Becher, C. H. Hsueh, P. Angelini and T. N. Tiegs. “Toughening Behavior in Whisker Reinforced Ceramic Matrix Composites”. *J. Am. Ceram. Soc.*, 71 [12]1050–61(1988).
20. Ai KahSoh, Dai-Ning Fang, Zhao-Xu Dong, “Analysis of Toughening Mechanisms of ZrO<sub>2</sub>/Nano-SiC Ceramic Composites”. *J compos mater*, 2004, 38(3), 227-241.
21. T. N. Tiegs and K. J. Bowman. “Fabrication of Particulate-, Platelet- and Whisker-Reinforced Ceramic Matrix Composites”. pp. 91–138 in Handbook on Discontinuously Reinforced Ceramic Matrix Composites, *Am. Ceram. Soc.*, Westerville, OH (1995).
22. Sriharsha Pasupuleti ,RamseshuPeddetti , Sridhar Santhanam, Kei-Peng Jen et al. “Toughening behavior in a carbo nanotube reinforced silicon nitride composite”. *Mater Sci Eng*, A 491 (2008) 224–229
23. Kazuya Shimoda, Tatsuya Hinoki, Akira Kohyama. “Effect of carbon nanofibers (CNFs) content on thermal and mechanical properties of CNFs/SiCnanocomposites”. *Compos SciTechnol*, 2010, 70(2), 387-392
24. Luke S. Walker, Victoria R. Marotto, Mohammad A. Rafiee, Nikhil Koratkar and Erica L. Corral. “Toughening in Graphene Ceramic Composites”. *J Amer Chem Soc*, 5(4), 3182-3190, 2011. doi. 10.1021/nn200319d
25. “Advanced Materials by design”, U.S. Congress office of Technology Assessment, OTA-E351, Washington, DC: US government printing Office, June 1988
26. J.K. Wells, P.W.R. Beaumont. “De-bonding and pull-out processes in fibrous composites”. *J Mater Sci*, 20(1985)
27. P F Becher, C H Hsueh, P Angelini, T N Tiegs. “ Toughening behavior in whisker reinforced ceramic matrix Composites ”, *J. Am. Ceram Soc*, 1988, 71[12],1050-61

28. Anthony G. Evans, "Perspective on the Development of High-Toughness Ceramics", *J. Am. Ceram Soc.*, 73 (21), 187-205 (1990)
29. Joseph Millis Brown. "High Temperature Composite Materials and Structures". PhD Thesis. Department of Aerospace Engineering University of Bristol July 2013
30. Narottam P Bansal, Jacques Lamon, "Ceramic Matrix Composites: Materials, Modeling and Technology". page 53, John Wiley & Sons, Oct 27, 2014.
31. A.G. Evans, S. Williams, P.W.R. Beaumont, "On the toughness of particulate filled Polymers", *J Mater. Sci.*, 1985, 20, 3668-3674
32. B.B. Johnsen, A.J. Kinloch and A.C. Taylor, "Toughness of syndiotactic polystyrene/epoxy polymer blends: microstructure and toughening mechanisms", *Polymer*, 2005,46, 7352–7369
33. W. M. Kriven, J. L. Bell, S. W. Mallicoat and M. Gordon, "Intrinsic Microstructure and Properties of Metakaolin-Based Geopolymers," contributed chapter to Proc. of Int. Workshop on Geopolymer Binders – Interdependence of Composition, Structure and Properties, Weimar, Germany, 71-86 (2007).
34. Zhen-Yan Deng, Jihong She, Yoshiaki Inagaki, Jian-Feng Yang, Tatsuki Ohji, Yoshihisa Tanaka, "Reinforcement by crack-tip blunting in porous ceramics". *Journal of the European Ceramic Society*, 24 (2004) 2055–2059.
35. Sriharsha Pasupuleti, Ramseshu Peddetti, Sridhar Santhanam, Kei-Peng Jen et al., "Toughening behavior in a carbo nanotube reinforced silicon nitride composite", *Mater Sci Engg A*, 2008,491, 224–229
36. A. Fernández-Jiménez, A. Palomo, M. Criado. "Microstructure development of alkali-activated fly ash cement: a descriptive model", *Cement and Concrete Research*, 35 (2005) 1204–1209.
37. Zosin, A.P., T.I. Priimak, and K.B. Avsaragov. "Geopolymer materials based on magnesia-iron slags for normalization and storage of radioactive wastes". *Atomic Energy*, 1998. **85**(1): p. 510-514.
38. Palomo, A., M.W. Grutzeck, and M.T. Blanco, "Alkali-activated fly ashes - A cement for the future", *Cement and Concrete Research*, 1999. **29**(8): p. 1323-1329.
39. Swanepoel, J.C. and C.A. Strydom, "Utilization of fly ash in a geopolymeric material", *Applied Geochemistry*, 2002. **17**(8): p. 1143-1148.
40. Cheng, T.W. and J.P. Chiu. "Fire-resistant geopolymer produced by granulated blast furnace slag", *Minerals Engineering*, 2003. **16**(3): p. 205-210.

41. M.L. Wilson, S.H. Kosmatka. In “Design and Control of Concrete Mixtures. Chap03- Fly Ash , Slag, Silica Ffume and Natural Pozzolans”. *Portland Cement Association*, 15<sup>th</sup> Edition, January 30, 2011.
42. Frantisek Skvára, Tomas Jilek, Lubomir Kopecky, “Geopolymer materials based on fly ash. Ceramics”. *silikaty 49* (3) 195-204 (2005).
43. W.M. Kriven, M. Gordon, J.L. Bell. ,“Geopolymers: nanoparticulate, nanoporous ceramics made under ambient conditions”, *Microscopy and Microanalysis '04, Proc. 62nd Annual Meeting of the Microscopy Society of America*,10 (2004): 404– 405.
44. Pre De Silva and Kwesi Sagoe-Crenstil,“The Role of Al<sub>2</sub>O<sub>3</sub>, SiO<sub>2</sub> and Na<sub>2</sub>O on the Amorphous → Crystalline Phase Transformation in Geopolymer Systems”. *Journal of the Australian Ceramic Society* Volume 45[1], 2009, 63-71
45. J.L. Provis, G.C. Lukey, J.S.J. Van Deventer, “Do geopolymers actually contain nanocrystalline zeolites? A re-examination of existing results”. *Chemistry of Materials*,17 (2005): 3075–3085.
46. Palomo, M.T. Blanco–Varela, M.L. Granizo, F. Puertas, T. Vazquez, M.W. Grutzeck. “Chemical stability of cementitious materials based on metakaolin”. *Cement and Concrete Research*, 29(1999): 997–1004.
47. Fernandez–Jimenez, A. Palomo. “Composition and microstructure of alkali activated fly ash binder: effect of activator”. *Cement and Concrete Research*, 35(2005):1984–1992.
48. P. Duxson, S.W. Mallicoat , G.C. Lukey , W.M. Kriven b, J.S.J. van Deventer. “The effect of alkali and Si/Al ratio on the development of mechanical properties of metakaolin-based geopolymers”.
49. J.L. LaRosa, S. Kwan, M.W. Crutzeck. “Zeolite formation in class F fly ash blended cement pastes”. *Journal of the American Ceramic Society* 75(6) (1992) 1574–1580.
50. V. F. F. Barbosa and K. J. D. MacKenzie, “Thermal Behaviour of Inorganic Geopolymers and Composites Derived from Sodium Polysialate”, *Material Research Bulletin*, 38(2003): 319–331.
51. Jonathan L. Bell, Patrick E. Driemeyer and Waltraud M. Kriven, “Formation of Ceramics from Metakaolin-Based Geopolymers. Part II:K-Based Geopolymer”, *J. Am. Ceram. Soc.* , 92 (3) (2009): 607–615, DOI: 10.1111/j.1551-2916.2008.02922.
52. Catherine A. Rees, John L. Provis , Grant C. Lukey, Jannie S.J. van Deventer , “The mechanism of geopolymer gel formation investigated through seeded nucleation”, *Colloids and Surfaces A: Physicochem. Eng. Aspects*, 318 (2008): 97–105.

53. Nouari Saheb, Najam Ul Qadir, Muhammad Usama Siddiqui, Abul Fazl Muhammad Arif, Syed Sohail Akhtar and Nasser Al-Aqeeli, “Characterization of Nanoreinforcement Dispersion in Inorganic Nanocomposites: A Review”, *Materials* 2014, 7(6):4148-4181: doi:10.3390/ma7064148.
54. Xiaoming Li, Wei Liu, Lianwen Sun, Katerina E. Aifantis, Bo Yu, Yubo Fan, Qingling Feng, Fuzhai Cui, and Fumio Watari, “Resin composites reinforced by nanoscale fibers or tubes for dental regeneration: Review”, *BioMed Research International*, 2014, <http://dx.doi.org/10.1155/2014/542958>.
55. Sheng Guo, R.I. Todd, “Quantitative optical fluorescence microprobe measurements of stresses around indentations in Al<sub>2</sub>O<sub>3</sub> and Al<sub>2</sub>O<sub>3</sub>/SiC nanocomposites: The influence of depth resolution and specimen translucency”, *Acta Materialia*, 59 (2011): 2637–2647.
56. Brian D. Bertram and Rosario A. Gerhardt, “Properties and Applications of Ceramic Composites Containing Silicon Carbide Whiskers”, [www.intechopen.com](http://www.intechopen.com) Accessed 3, 20, 2014.
57. A. Yu. Bugaeva and B. N. Dudkin, “Modification of the Surface of Alumina Oxide Nanofibers by Zirconia Nanoparticles”, *Glass physics and chemistry*, 40(2014):37-40.
58. J. M. Bonard, T. Stora, J. P. Salvetat, F. Maier, T. Stockli, C. Duschi, L. Forró, W. A. de Heer and A. Châtelain, “Purification and Size Selection of Carbon Nanotubes”, *Adv. Mater.*, 9(1997), 827–831.
59. Hyungsuk Oh, Hansung. Kim, “Distribution of Pt Catalysts on Hydrophobic Carbon Supports to Prevent Carbon Corrosion for the Application of PEM Fuel Cells”, *218<sup>th</sup> ECS Meeting*, 2010.
60. Shi-Chen Tjong, “Nanocrystalline Materials: Their Synthesis-Structure-Property-Relationships and Applications”, 2<sup>nd</sup> Edition, Elsevier, 2006, ISBN 0-080-44697-3.
61. A. Yazdanbakhsh, Z. Grasley, B. Tyson, and R. K. Abu Al-Rub, “Distribution of Carbon Nanofibers and Nanotubes in Cementitious Composites,” *Transportation Research Record*, 2142( 2010):89–95.
62. Georgatikas V, Kordatos K, Prato M, Guldi DM, Holzinger M, Hirsch A, “Organic functionalization of carbon nanotubes”, *J Am chem Soc*, 124(5) 2002:760–761.
63. Zoi S. Metaxa, Maria S. Konsta-Gdoutos, Surendra P. Shah, “Carbon nanofiber-cementitious composites: Effect of debulking procedure on dispersion and reinforcing efficiency”, *Cement and Concrete Composites*, 36(2013): 25-32.
64. Byung-Koog Jang and Yoshio Sakka, “Dispersion and Shortening of Multi-Walled Carbon Nanotubes by Size Modification”, *Mater Transac*, 51(2010), 192-195.

65. R. Samsur, V. K. Rangari, S. Jeelani, L. Zhang, and Z. Y.Cheng, “Fabrication of carbon nanotubes grown woven carbon fiber/epoxy composites and their electrical and mechanical properties”, *J. Appl. Phys.*, 2013, 113, 214903; doi: 10.1063/1.4808105.
66. ShamaParveen, SohelRana and Raul Fanguero, “A Review on Nanomaterial Dispersion, Microstructure, and Mechanical Properties of Carbon Nanotube and Nanofiber Reinforced Cementitious Composites”, *Journal of Nanomaterials*, 2013, doi: 10.1155/2013/710175.
67. S.Q. Wang , H.Q. Ye, “Theoretical studies of solid–solid interfaces”, *Current Opinion in Solid State and Materials Science* ,10 (2006) 26–32.
68. Y. Mishin, P. Sofronis , J.L. Bassani, “Thermodynamic and kinetic aspects of interfacial decohesion”, *Acta Materialia*, 50 (2002) 3609–3622
69. Valeria F.F.Barbosa, Kenneth J.D. Mackenzie, “Thermal behavior of inorganic geopolyemrs and composites derived from sodium polysialate”, *Material research bulletin* 38(2003)319-331.
70. William D. A. Rickard, Arie van Riessen and Philip Walls, “Thermal Character of Geopolymers Synthesized from Class F Fly Ash Containing High Concentrations of Iron and a-Quartz”, *Int. J. Appl. Ceram. Technol.*, 7(1) (2010), 81-88, DOI:10.1111/j.1744-7402.2008.02328.
71. R. Morrell, “Fractography and Fracture Toughness Measurement”, Report, Key Engineering Materials 409, 2009, 17-27.
72. David Roylance, “Introduction to fracture mechanics”, Department of Materials Science and Engineering, Massachusetts Institute of Technology Cambridge, MA 02139.
73. G.R. Anstis, P. Chintakul, B.R. Lawn and D.B. Marshall, “A critical Evaluation of Indentation Fracture Toughness: I , Direct Crack Measurements”, *J am. Ceram. Soc*, 64(1981), 533.
74. Kruzic J.J. and Ritchie R.O. Comments on “Measurement of the microstructural fracture toughness of cortical bone using indentation fracture”, Letter to the editor. *J Biomech*, 2008(41), 1379-1380.
75. B.R. Lawn, A.G Evans and D.B. Marshall, “Elastic/Plastic Indentation Damage in Ceramics: The Mean/Radial crack System” , *J Am. Ceram. Soc.*, 1980, 63, 574.
76. M.T. Laugier, “The elastic plastic indentation of ceramics”, *J Mater. Sci. Lett.*, 1985,4,1539-1541
77. Quinn, J.B., Quinn, G.D., 1997, “Indentation brittleness of ceramics: A fresh approach”, *J Mater.Sci*, 32(1997), 4331-4346.
78. Wang, X., Padture, N. P. & Tanaka, H, “Contact-damage-resistant ceramic/single-wall carbon nanotubes and ceramic/graphite composites”, *Nature Materials*. 3(2004), 539–544.

79. Sheldon, B. W. and Curtin, W. A., "Nanoceramic composites: Tough to test", *Nature Materials*, 3(8), (2004), 505-506.
80. G. A. Gogotsi, "Mechanical Behaviour of Yttria- and Ferric Oxide-Doped Zirconia at Different Temperatures", *Ceramics International* 24 (1998) 589-595.
81. R. Damani, R. Gstrein and R Danzer, "Critical notch root radius effect in SENB-S fracture toughness testing", *J Eur. Ceram. Soc.*, 16(1996), 695-702.
82. Technical Data: Meyeb™ Resin for Composite Materials, Saint-Quentin, France, InstitutGeopolymere < [http://www.geopolymer.org/fichiers\\_pdf/meyeb.pdf](http://www.geopolymer.org/fichiers_pdf/meyeb.pdf) >
83. Davidovits, J., "Geopolymer Inorganic Polymeric New Materials." *Journal of Thermal Analysis*, 37 (1991): 1633-1656.
84. W M Kriven, J L Bell, M Gordon, "Microstructure & microchemistry of fully reacted geopolymers and Geopolymer matrix composites." *Advances in Ceramic Matrix Composites IX*.
85. Michael Vargas, Dr. Nick Kioussis, "Alumina  $\alpha$ -Al<sub>2</sub>O<sub>3</sub> (110):An *ab-initio* Examination of the Surface Electronic Structure".
86. R. G. Munro, "Evaluated Material Properties for a Sintered alpha-Al<sub>2</sub>O<sub>3</sub>", *Journal of the American Ceramic Society*, 80(1997),1919-1928.
87. J.J. Petrovic, J.V. Milewski, D.L. Rohr, "Tensile Mechanical Properties of SiC Whiskers". *J Mater Sci*, 1985,20,1167-1177.
88. Demczyk, B.G.; Wang, Y.M; Cumings, J; Hetman, M; Han, W; Zettl, A; Ritchie, R.O, "Direct mechanical measurement of the tensile strength and elastic modulus of multiwalled carbon nanotubes". *Materials Science and Engineering A*, 2002,334 (1-2): 173-178. doi:10.1016/S0921-5093(01)01807.
89. <http://www.nafen.eu/products/nafen-tm-technical-properties-presentation>, URL, Last accessed 11/26/2013.
90. A.H. Rashed, "Properties and characteristics of Silicon Carbide", Poco Graphite Inc.,2002.URL: [www.poco.com](http://www.poco.com).
91. Zhen Fan,Chao WuJinhua Chen, "Growth of carbon nanotubes on the surface of carbon fibers", *Carbon*, 2008,46, 365 -389.
92. <http://pyrografproducts.com/nanofiber.html>, "PR-19-XT-PS\_Data\_Sheet", URL, Last accessed 7/5/2015.
93. *Nextel™ Ceramic Textiles Technical Notebook*. November 2004. 3M Company. Accessed 3<sup>rd</sup> April, 2015 .[http://www.3m.com/market/industrial/ceramics/misc/tech\\_notebook.html](http://www.3m.com/market/industrial/ceramics/misc/tech_notebook.html)

94. ASTM C1421-10, “Standard Test Methods for Determination of Fracture Toughness of Advanced Ceramics at Ambient Temperature”, ASTM International, West Conshohocken, PA, 2010, [www.astm.org](http://www.astm.org)
95. ASTM C20-00(2010) “Standard Test Methods for Apparent Porosity, Water Absorption, Apparent Specific Gravity, and Bulk Density of Burned Refractory Brick and Shapes by Boiling Water”, ASTM International, West Conshohocken, PA, 2010, [www.astm.org](http://www.astm.org).
96. <http://www.britannica.com/EBchecked/topic/32827/Archimedes-principle>”, URL, Last accessed 11/26/2013.
97. Felipe Montes, Srinivas Valavala, and Liv M. Haselbach, “A New Test Method for Porosity Measurements of Portland Cement Pervious Concrete”, *Journal of ASTM International*, January 2005, (2), 1.
98. ASTM C1421-10, “Standard Test Methods for Determination of Fracture Toughness of Advanced Ceramics at Ambient Temperature”, ASTM International, 100 Barr Harbor Dr. PO Box C-700 West Conshohocken, Pennsylvania 19428-2959, United States.
99. ASTM D790-10, “Standard Test Methods for Flexural Properties of Unreinforced and Reinforced Plastics and Electrical Insulating Materials”, ASTM International, West Conshohocken, PA, 2010, [www.astm.org](http://www.astm.org).
100. Jakob Kubler, “Fracture Toughness of ceramics using the SEVNB Method; Round Robin”, VAMAS Report No.37, ISSN 1016-2186, September 1999.
101. E. Huerta, J. E. Corona, A. I. Oliva, F. Avilés, and J. González- Hernández, “Universal testing machine for mechanical properties of thin materials,” *Revista Mexicana de Física*, 56(4), (2010), 317–322.
102. Donald R Askeland, Pradeep P Fulay, Wendelin J Wright, “The science and engineering of Materials”, Sixth Edition, Published by Global Engineering, 2006, pp168-175.
103. William D. A. Rickard, Arie van Riessen and Philip Walls, “Thermal Character of Geopolymers Synthesized from Class F Fly Ash Containing High Concentrations of Iron and a-Quartz”, *Int. J. Appl. Ceram. Technol.*, 2010(7), 1,81–88, DOI:10.1111/j.1744-7402.2008.02328.
104. Ceramic Textiles Technical Notebook. 3M Nextel™. <[http://www.zeningenieria.com/pdf-productos/Nextel\\_Tech\\_Notebook\\_11.04.pdf](http://www.zeningenieria.com/pdf-productos/Nextel_Tech_Notebook_11.04.pdf)>
105. Kingery W.D, Bowen H.K, Uhlmann, “Introduction to Ceramics”, 2<sup>nd</sup> edition, Wiley-Interscience, New York; Chichester, 1976, p.595.
106. Provis J.L, Deventer J.S., “Geopolymers structure, processing, properties and industrial applications”, Woodhead Publishing & CRC Press Limited, 2009.

107. ASTM E112-13, "Standard Test Methods for Determining Average Grain Size", ASTM International, West Conshohocken, PA, 2013, [www.astm.org](http://www.astm.org).
108. <http://caur.uga.edu/EDS.pdf>, "Energy Dispersive X-ray Microanalysis Hardware-Explained", Oxford Instruments Analytical-Technical Briefing. URL, Last accessed 11/26/2013.
109. Bob Hafner, "Energy dispersive spectroscopy on the SEM: A Primer"
110. AMTEK Materials Analysis Division, "Octane Silicon Drift Detectors". Product Bulletin-EDS.
111. [http://acm-usa.com/site/user/files/1/Datasheet\\_SC\\_9M.pdf](http://acm-usa.com/site/user/files/1/Datasheet_SC_9M.pdf), URL, Last accessed 06/06/2014.
112. Li Hong Zhang, Hao Gong, Jian Ping Wang, "Thermal decomposition kinetics of amorphous carbon nitride and carbon films", *J Phys: condens mater* 14(2002) 1697-1708.
113. A.H. Rashed, "Properties and characteristics of Silicon Carbide", Technical Article, Poco Graphite, [www.poco.com](http://www.poco.com).
114. Johann Cho, Aldo R Boccaccini, Milo SP Shaffer, "Ceramic matrix composites containing carbon nanotubes", Review, *J Mater Sci*, DOI 10.1007/s10853-009-3262-9.
115. J.K. Wells, P.W.R. Beaumont, "De-bonding and pull-out processes in fibrous composites", *J Mater Sci*, 20(1985).
116. Terry Tiegs, "SiC whisker Reinforced Alumina", In *Handbook of ceramics*, 2005.
117. Deborah D. L. Chung, "Composite Materials: Science and Applications (Engineering Materials and Processes)", Second Edition, 2010, P 315 ISBN 1-84882-830-6.
118. L. Salvo, G.L'Espérance, M.Suery and J.G. Legoux, "Interfacial reaction and age hardening in Al-Mg-Si metal matrix composites reinforced with SiC particles", *Materials Science and Engineering*, A 177 (1994) 173-183.
119. M. Sørliie and H. A. Øye, "Deterioration of Carbon Linings in Aluminum Reduction Cells. Part II - Chemical and Physical Characterization of Cathode Carbons," *Metall*, 38 (1984), 109-115.
120. Paolo J Faraboli, Keith T Kedward, "In search of the true inter-laminar shear strength"
121. ASTM D2344 / D2344M-13, "Standard Test Method for Short-Beam Strength of Polymer Matrix Composite Materials and Their Laminates", ASTM International, West Conshohocken, PA, 2013, [www.astm.org](http://www.astm.org).
122. ASTM C1341-13, "Standard Test Method for Flexural Properties of Continuous Fiber Reinforced Advanced Ceramic Composites", ASTM International, West Conshohocken, PA, 2013, [www.astm.org](http://www.astm.org).



## APPENDIX

### APPENDIX A: PROPERTIES OF THE MATERIALS

#### A1. Properties of PR-XT19 CNFs

Table A. 1. Properties of PR-XT19 CNFs

Properties	Unit	Value
Diameter	Nm	150
CVD carbon overcoat presence		Yes
Surface area	m <sup>2</sup> /gm	20-30
Dispersive surface energy	mJ/m <sup>2</sup>	120-140
Moisture	wt%	<5
Iron	ppm	<14,000

## A2. Properties of Silar SC 9M Silicon carbide whisker

Table A. 2. Properties of Silar SC 9M Silicon carbide whisker.

Properties	Unit	Value
Crystal Type		Beta (Poly type)
Geometry		Long, rigid rod nanotube
Diameter	$\mu\text{m}$	0.65
Length	$\mu\text{m}$	10-12
Modulus	GPa	450
Tensile Strength	GPa	8.4
Density	$\text{g}/\text{cm}^3$	3.2
Free carbon	wt%	0.5-3
Silica	wt%	35-75

## A3. Properties of HSC Silicon Carbide Nanoparticles

Table A. 3. Properties of HSC Silicon Carbide Nanoparticles.

Properties	Unit	Values
Grade		HSC059NSF
Surface area, BET	$\text{M}^2/\text{g}$	20
diameter	$\mu\text{m}$	$0.45 \pm 0.2$
Density	$\text{g}/\text{cm}^3$	3.2

#### A4. Size distribution of Silicon Carbide particles

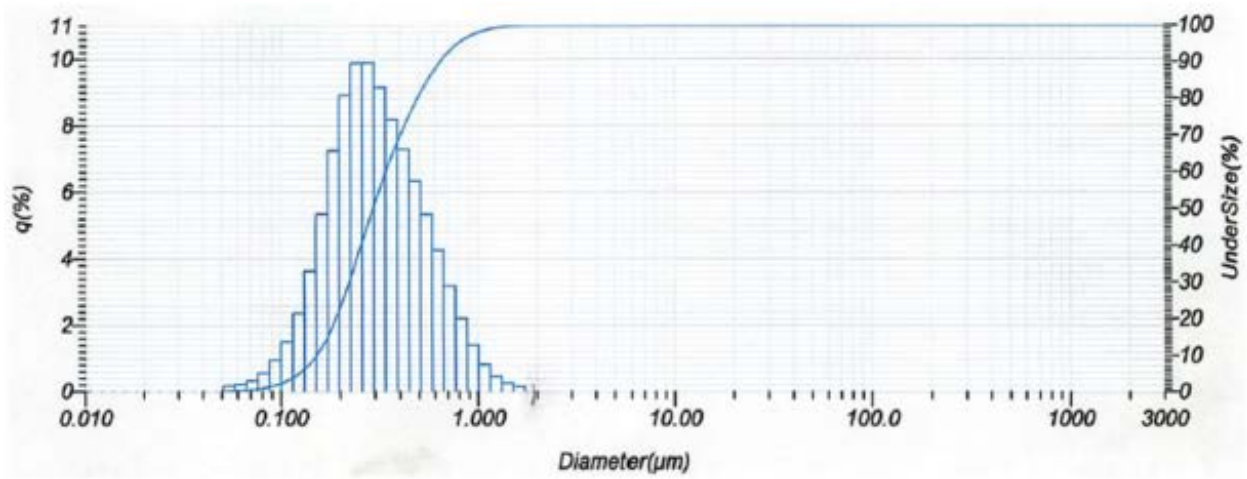


Figure A. 1. Size distribution of Silicon Carbide Particle d50 (Instrument: HORIBA Laser scattering particle size distribution analyzer LA-950).

## A5. Properties of Acetal Co-Polymer<sup>1</sup>

Table A. 4. Properties of Acetal Co-Polymer.

Property	Units	Values
Density	g/cm <sup>3</sup>	1.41
Water Absorption	24 hrs, %	0.2
Co-efficient of Thermal Expansion (CTE)	×10 <sup>-6</sup> m/m/°C	5.4
Melting Point Temp	°C	168
Maximum operating Temp	°C	90
Minimum operating Temp	°C	- 40
Chemical resistance	Sodium hydroxide	Excellent
	Potassium Hydroxide	Excellent
	Alcohols	Excellent
	Acetones	Excellent
	Sodium Silicate	Fair

Note: Fair is defined by Moderate effect and not recommended for continuous use. Continuous use may result in softening, loss of strength and swelling.

<sup>1</sup> [http://www.plasticsintl.com/plastics\\_chemical\\_resistance\\_chart.html](http://www.plasticsintl.com/plastics_chemical_resistance_chart.html)

## A6. Typical properties of 3M™ Nextel™ 610 Ceramic Fiber<sup>2</sup>

Table A. 5 Typical properties of 3M™ Nextel™ 610 Ceramic Fiber

Property	Units	Value
Use Temperature	°C	1200
Filament Diameter		
Density	g/cc	3.88
Cryustal Type		Alpha Al <sub>2</sub> O <sub>3</sub>
Filament tensile strength	MPa	2930
Filament Tensile Modulus	GPa	373
Surface area	M <sup>2</sup> /g	<0.2
Composition	Wt.%	>99 Al <sub>2</sub> O <sub>3</sub> 0.2-0.3-SiO <sub>2</sub> 0.4-0.7 Fe <sub>2</sub> O <sub>3</sub>
Thermal Expansion (100-1100 °C)	(μm/m)/°C	7.9

<sup>2</sup> <http://www.3m.com/market/industrial/ceramics/materials/nextel.html>

## A7. Specifications of AMTEK EDAX Octane Series Silicon Drift Detectors

Table A. 6. Specifications of AMTEK EDAX Octane Series Silicon Drift Detectors.

Model Name	Octane super
Detector Type	Silicon drift detector
Standard Resolution	130 eV
Energy Resolution	MnK $\alpha$ down to 129 eV
Resolution Stability	>90%
Mapping speed	200000 cps
Microscope Port	JEOL JSM 6500F/WDS
Country Manufactured	USA

## APPENDIX B: CALCULATIONS

### B1. Calculation of the Failure strength of ANF <sup>3</sup>

Failure strength of single ANF was calculated using the load deflection results from the measurement with AFM, which is shown in Figure below.

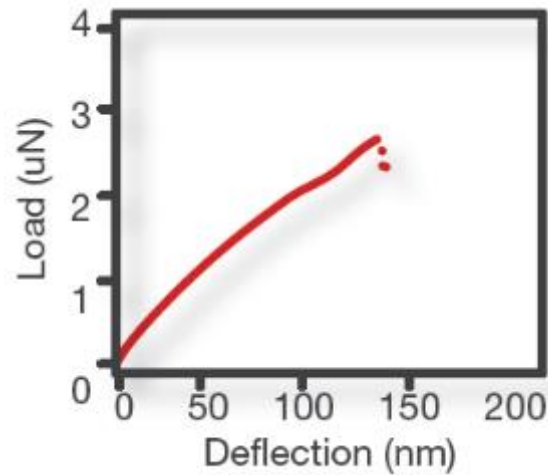


Figure B. 1. ANF strength measurement with AFM.

Table B. 1. Failure strength measurement of ANF using the load deflection curve.

Diameter (m)	Area(m <sup>2</sup> )	Force (N)	Tensile Strength( GPa)
4.00E-08	1.26E-15	3.00E-06	2.39

<sup>3</sup> <http://anftechnology.com/fibers-and-powders/>

## B2. Failure strain calculation of the nanofibers

Failure strains of the nanofillers were calculated using the following formula

$$\text{Failure Strain, \%} = \frac{\text{Tensile Strength}}{\text{Tensile Modulus}} \times 100 \quad (32)$$

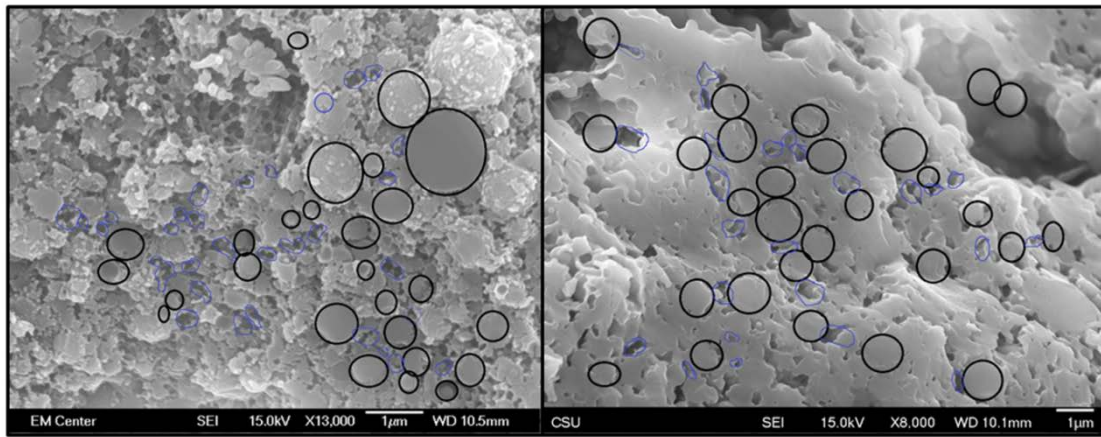
Table below presents the failure strains of the nanofibers used in the current investigation.

Table B. 2. Failure strain of the nanofibers of the investigation .

Nanofibers	Tensile strength (GPa)	Tensile modulus (GPa)	Failure strain (%)
ANF	2.38	220	1.08
SCW	8.4	580	1.45
CNF	8.7	600	1.45



### B3. Estimation of Particle Diameter and Inter-particle Porosities



(a)

(b)

Figure B. 2. Presentation of the particles and inter-particle porosities of neat MEYEB at (a) 80 °C and (b) 650 °C. Particles and porosities are presented in black and blue circles, respectively.

Table B. 3. Diameters of particles and inter-particle porosities at various treatment temperatures.

Temp Particle No	80 °C		250 °C		650 °C	
	Particle Diameter ( $\mu\text{m}$ )	Inter-particle Pore ( $\mu\text{m}$ )	Particle Diameter ( $\mu\text{m}$ )	Inter-particle Pore ( $\mu\text{m}$ )	Particle diameter ( $\mu\text{m}$ )	Inter-particle Pore ( $\mu\text{m}$ )
	0.968	0.561	0.507	0.169	2.053	0.442
1	1.358	0.181	0.432	0.285	2.411	0.413
2	0.608	0.236	0.648	0.148	1.924	0.325
3	0.717	0.194	0.456	0.307	1.506	0.246
4	0.567	0.166	0.672	0.299	1.851	0.146
5	0.415	0.196	0.672	0.260	2.205	0.229
6	0.435	0.198	0.683	0.342	1.800	0.219
7	0.310	0.319	0.540	0.235	1.142	0.275
8	0.548	0.195	0.546	0.374	1.594	0.297
9	0.903	0.199	0.678	0.279	1.212	0.268
10	0.919	0.263	0.585	0.326	2.086	0.230
11	0.587	0.224	0.542	0.290	1.194	0.302
12	0.459	0.175	0.493	0.441	1.672	0.333
13	1.079	0.189	0.570	0.352	1.158	0.230
14	1.054	0.189	0.481	0.556	1.354	0.205
15	1.031	0.298	0.406	0.365	2.029	0.310
16	0.405	0.150	0.399	0.230	1.743	0.302
17	0.331	0.180	0.420	0.259	1.497	0.214
18	1.04	0.193	0.463	0.293	1.149	0.317
19	0.361	0.129	0.370	0.280	1.344	0.427
20	0.221		0.403	0.320	1.032	0.448

Temp Particle No	80 °C		250 °C		650 °C	
	Particle Diameter ( $\mu\text{m}$ )	Inter- particle Pore ( $\mu\text{m}$ )	Particle Diameter ( $\mu\text{m}$ )	Inter-particle Pore ( $\mu\text{m}$ )	Particle diameter ( $\mu\text{m}$ )	Inter-particle Pore ( $\mu\text{m}$ )
21	0.331		0.323	0.257	1.160	0.345
22	0.432		0.365		0.957	0.221
23	0.305		0.292		0.981	0.297
24	0.312		0.365		0.862	0.450
25	0.222		0.234		1.039	0.318
26	0.334		0.299		0.619	0.349
27	0.313		0.337		0.613	0.341
28	0.332		0.310		0.920	0.293
29	0.312		0.603		0.634	0.488
30	0.209		0.603		0.786	0.306
31	0.33		0.296		0.757	0.263
32	0.213		0.548		0.860	0.195
33	0.433		0.349		0.950	0.363
34			0.296		0.839	0.164
35			0.342		0.845	0.397
36			0.414		0.940	
37			0.371		1.170	
38			0.387			
39			0.392			
<b>Average</b>	0.514	0.222	0.452	0.303	1.287	0.305
<b>Standard deviation</b>	0.304	0.092	0.126	0.086	0.489	0.085

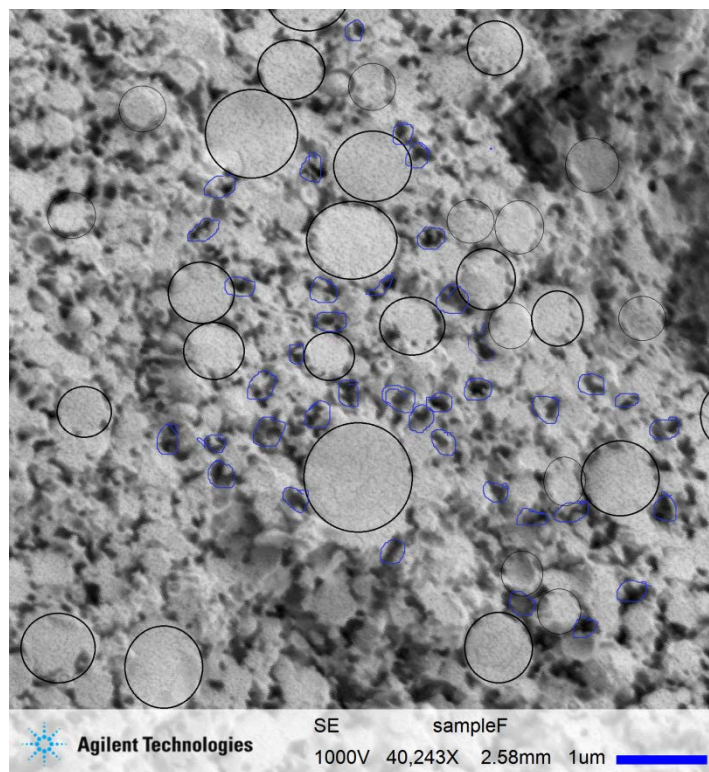


Figure B. 3. Neat MEYEB treated at 650 °C using process schedule B2.

Table B. 4. Particle diameter and inter-particle porosities of neat MEYEB sample shown in .

Figure above .

Treatment Temperature 650 °C					
Particle diameter		Inter-particle pore diameter			
Particle No.	Diameter (µm)	Particle Number	Pore Diameter (µm)	Particle Number	Pore Diameter (µm)
1	2.102	1	0.284	20	0.195
2	2.544	2	0.227	21	0.171
3	1.906	3	0.231	22	0.187
4	2.259	4	0.162	23	0.167
5	1.563	5	0.236	24	0.210
6	1.050	6	0.137	25	0.201
7	1.781	7	0.194	26	0.182
8	1.730	8	0.158	27	0.166
9	1.880	9	0.250	28	0.163
10	1.395	10	0.242	29	0.175
11	1.216	11	0.235	30	0.193
12	1.008	12	0.195	31	0.175
13	1.272	13	0.152	32	0.218
14	1.635	14	0.189	33	0.162
15	1.399	15	0.146	34	0.279
16	1.388	16	0.193	35	0.118
17	1.283	17	0.243	36	0.208
18	1.388	18	0.231	37	0.167
19	1.295	19	0.167	38	0.180
				39	0.189
				40	0.141
Average (µm)	1.584	0.193			
Standard Deviation (µm)	0.413	0.038			

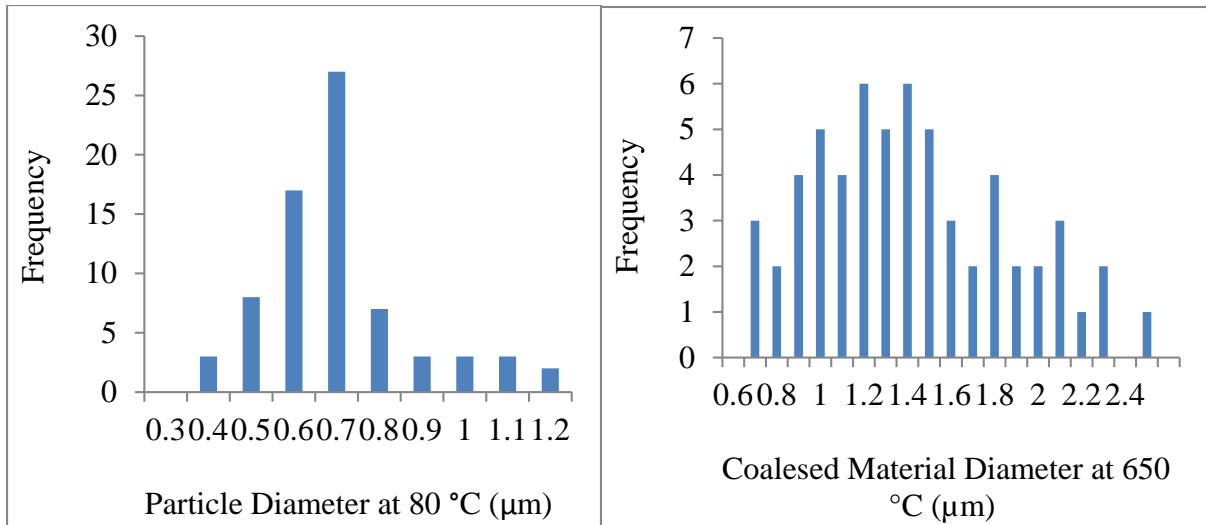


Figure B. 4. Distribution of neat MEYEB (a) Precipitated particle diameter at 80 °C and (b) coalesced materials diameter at 650 °C.

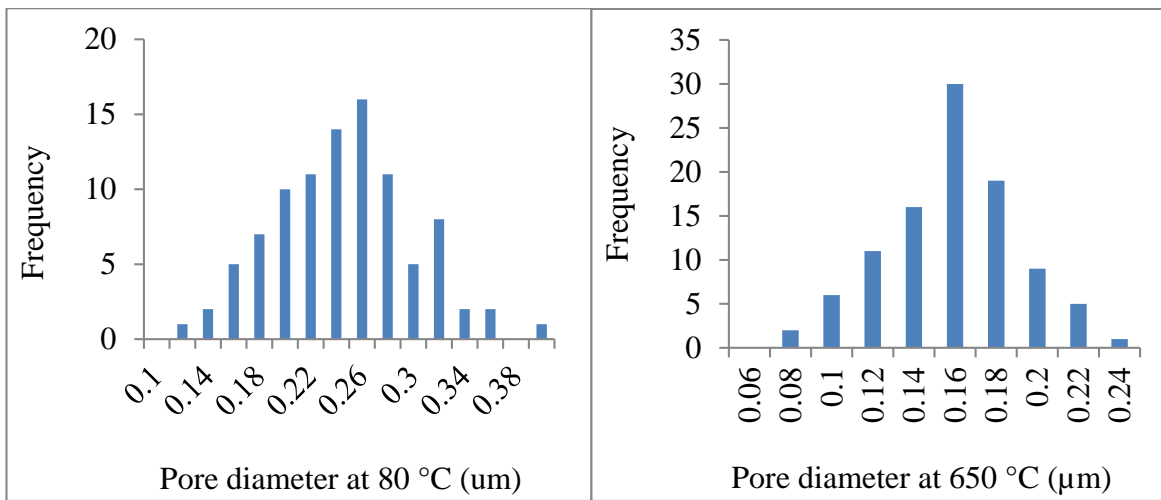


Figure B. 5. Distribution of neat MEYEB (a) Pore diameter at 80 °C (b) 650 °C.

#### B4. Calculation of Minimum length of Nano-fillers

Minimum length requirement of nanofillers for effective reinforcement is associated with particle diameter and inter-particle porosities of neat MEYEB. Nanofiller minimum length was

calculated using equation (27). Average diameters of the particles and inter-particle porosities are found from . .

Table B. 5. Average diameters of particles, porosities and required lengths of nanofillers .

	80 °C	250 °C	650 °C
Particle diameter,( μm)	0.68	0.45	1.25
S.D., (μm)	0.29	0.13	0.53
Inter-particle porosity diameter, (μm)	0.22	0.30	0.16
S.D., (μm)	0.09	0.09	0.11
Minimum length of nanofillers, (μm)	2.56	1.94	4.10

### B5. Calculation of the Theoretical Fiber Mass in the Composite

The mass of fiber was calculated based on the total number of tows of Nextel 610 fibers used to make a composite stick at a constant length of 203.2 mm.

$$\text{Theoretical, } m_f = \left( \frac{10000}{9000 \cdot 100} \right) * L_s * N_t \quad (33)$$

Where,  $\frac{10000}{9000 \cdot 100}$  = Denier reduction in gm/cm

$L_s$  = Length of the sample in cm

$N_t$  = Nominal number of fiber tows of the stick length used

In this investigation one composite stick with approximately 50 vol% of continuous fiber required total of 33 tows of fiber equal to the length of the stick.

## APPENDIX C: IMAGES & MICROSTRUCTURES

### C1: Images of Samples

This appendix includes images of neat MEYEB samples and MEYEB with various nanofillers which were treated at various temperature and environment.

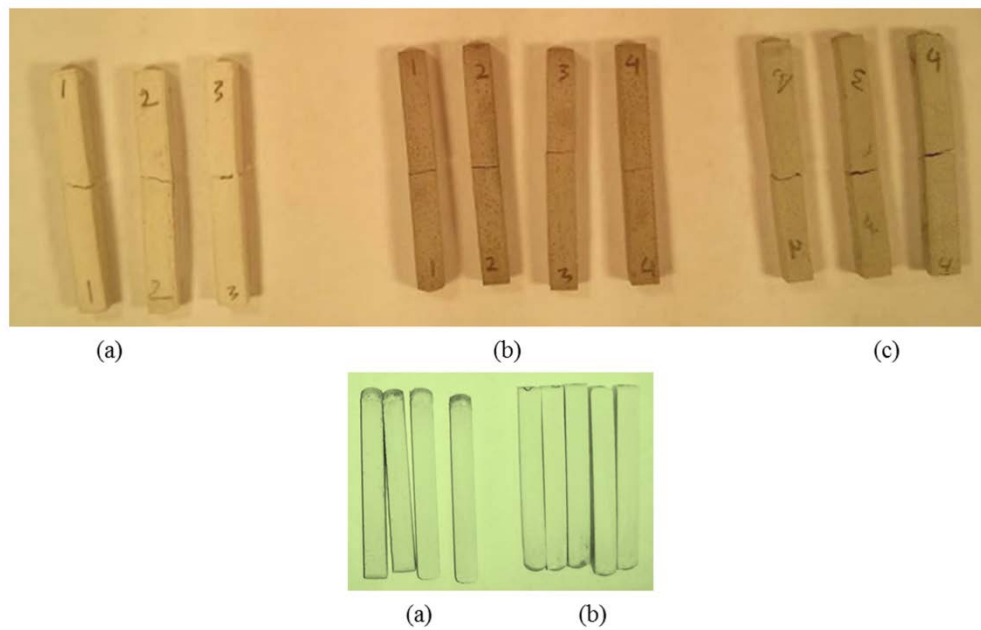


Figure C. 1.(a) Neat, (b) 2 vol% SCP and (c) 2vol% SCW (d) Neat & (e) 2% ANF reinforced MEYEB post heat treated at 250 °C.



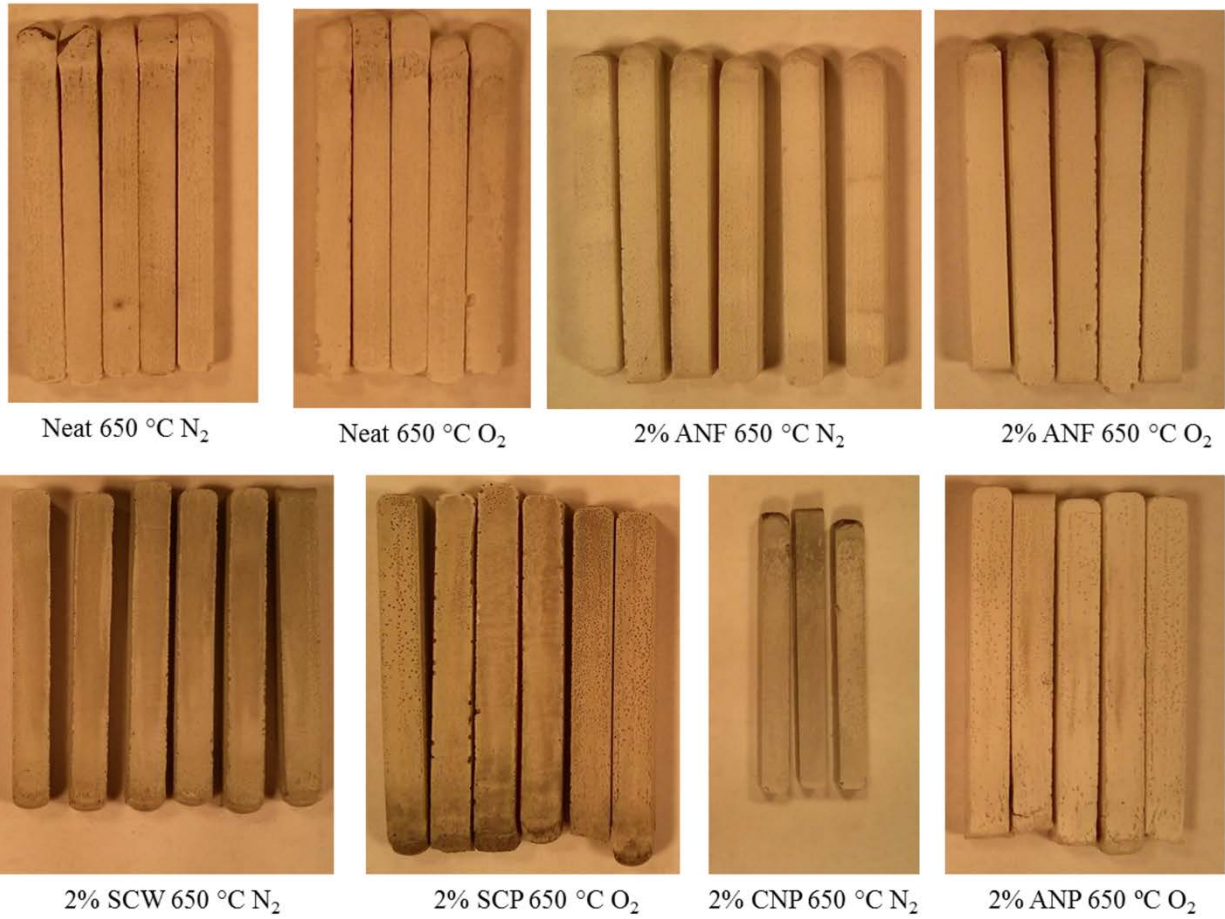


Figure C. 2. Samples treated at 650 °C in oxygen and nitrogen.

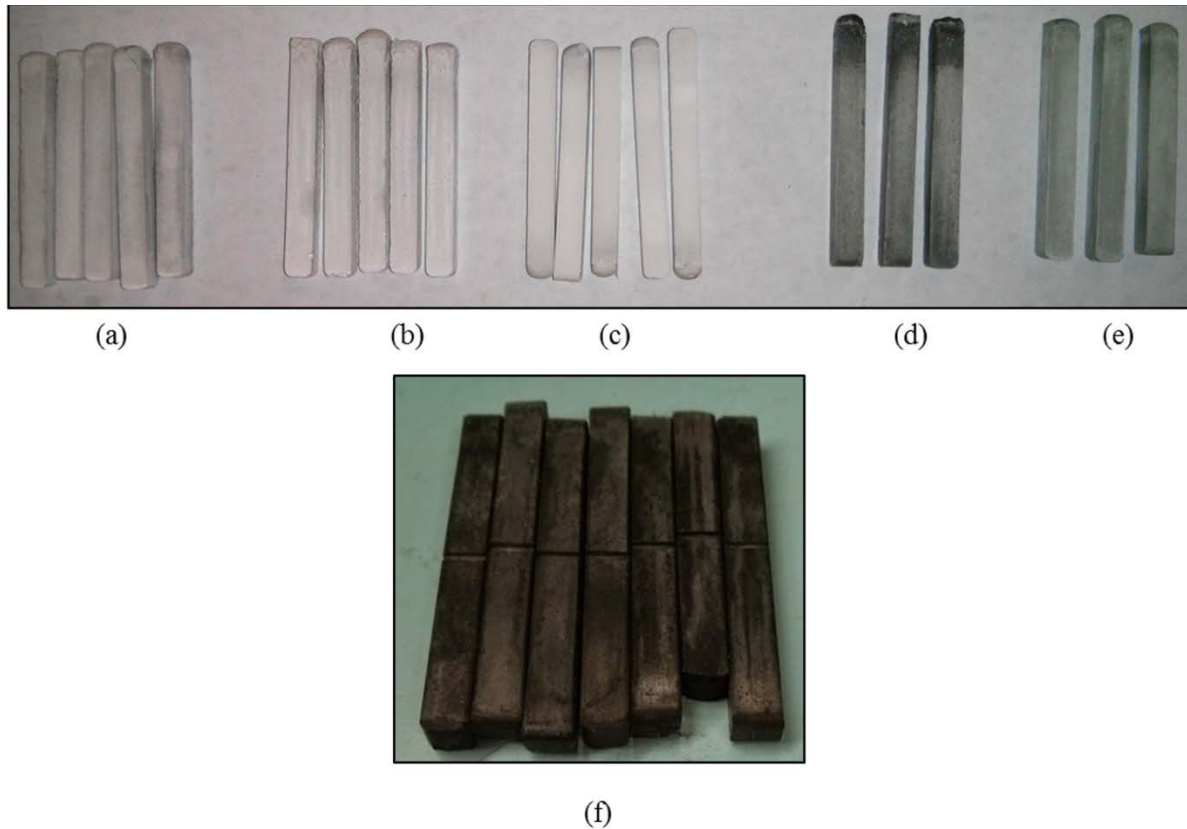


Figure C. 3. From top left (a) Neat (b) 2% ANP (c) 2% ANF (d) 2% SCP and (e) 2% SCW (f) 2% CNF reinforced MEYEB treated at 760 °C in (N<sub>2</sub>).

### C2: Poly-condensed and Coalesced Materials Area with Temperature

In order to find polycondensed area fractions, first total area of the micrograph ( $A_t$ ) is measured, then the total area of polycondensed structures were measured by counting individual area of the polycondensed structure ( $A'_{pc}$ ) over the micrograph. Then polycondensed area fraction was calculated using the following equation-

$$\%A_{pc} = \frac{\sum A'_{pc}}{A_t} \times 100\% \quad (34)$$

In order to find the polycondensed area for the sample treated at 870 °C, the area of non-polycondensed structure was measured and then subtracted from the total area of the micrograph. Then area fraction was calculated using equation (34).

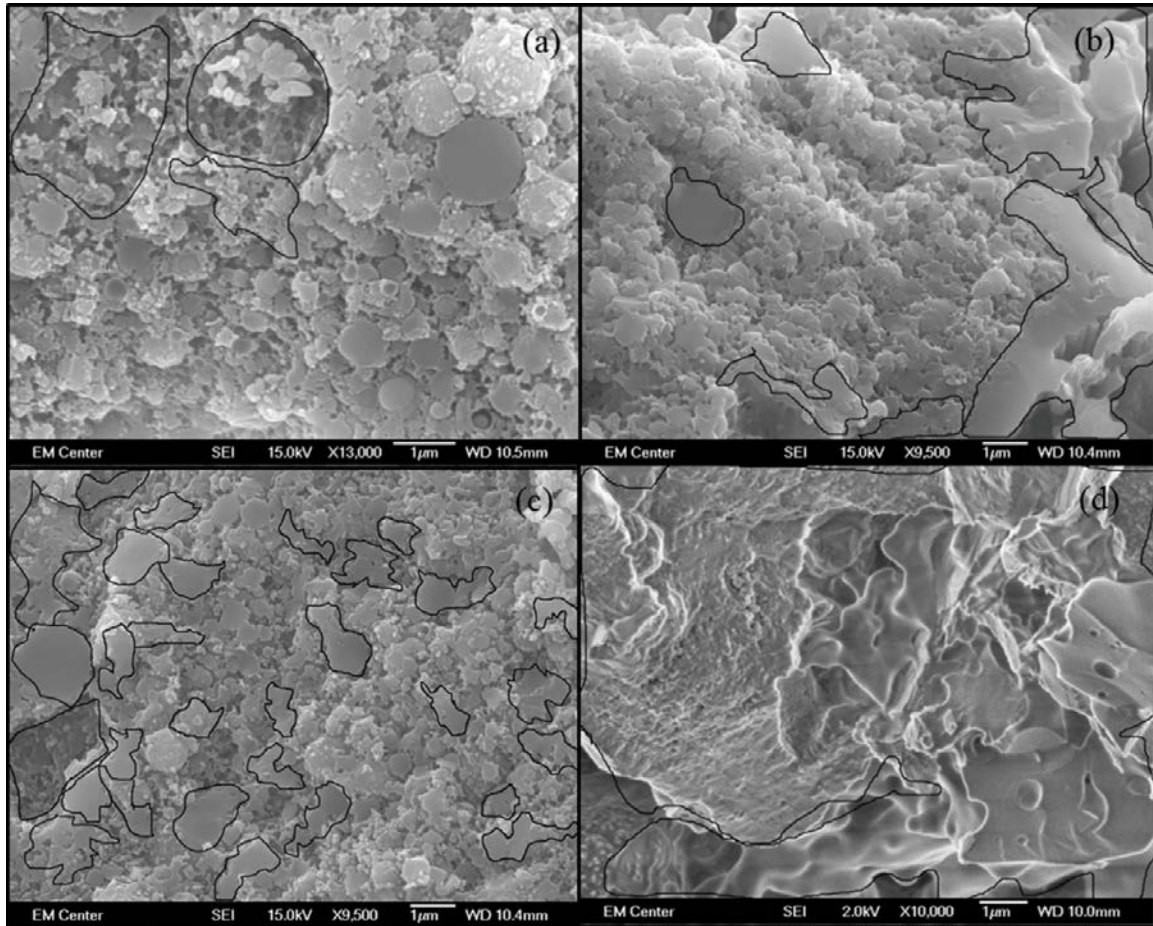


Figure C. 4. Microstructures of neat MEYEB treated at (a) 80° C (b) 250 °C (c) 650 °C and (d) 870 °C. Poly-condensed and coalesced areas are shown in the closed region.

Table C. 1. Estimation of Poly-condensed (PC) area fractions of neat MEYEB with temperature

Total Area, ( $\mu\text{m}^2$ )	PC Area, ( $\mu\text{m}^2$ )			Total PC Area , ( $\mu\text{m}^2$ )	PC Area (%)
65.82	3.60			8.20	12.46
	2.00				
	2.60				
120.55	1.66	4.87	5.83	30.67	25.44
	1.77	7.53	9.02		
113.74	1.303	0.605	0.91	36.59	32.17
	5.54	0.505	1.053		
	0.739	0.628	1.055		
	2.752	1.484	0.382		
	0.846	1.529	3.821		
	0.381	1.652	1.601		
	0.909	1.411	1.264		
	1.253	1.339	0.622		
	0.557		2.452		
	Non-PC Area				
384.66	0.41	5.84	13.39	357.49	92.94
	1.47	1.06	0.73		
			4.26		

**C3: Estimation of Pull out Length of Nanofillers**

Two Figures below present pull out lengths of SCW at 250 °C and 650 °C, respectively. For the statistical analysis of the pull out length, this presentation a number of images, which are basically, tread at the respective temperature.

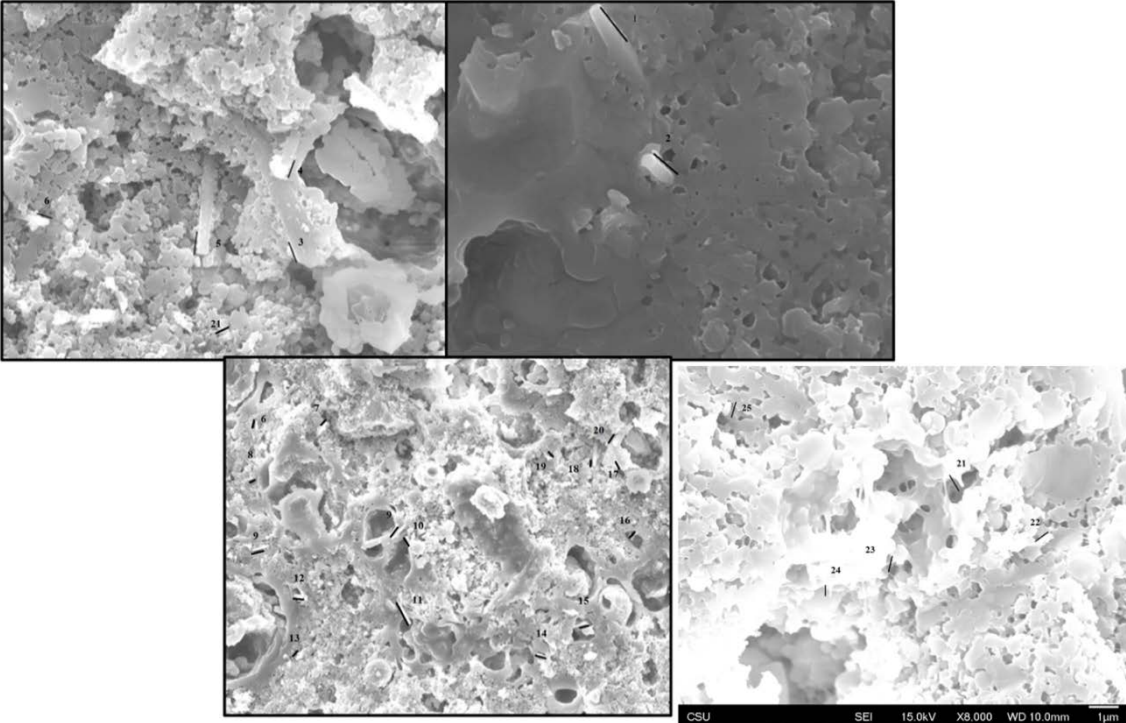


Figure C. 5. 2% SCW reinforced geopolymer samples treated at 250 °C.

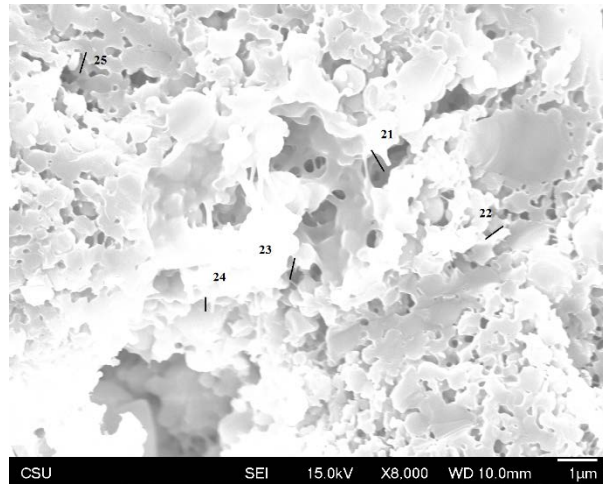


Figure C. 6. 2% SCW reinforced geopolymer samples treated at 250 °C (fourth sample from figure above).

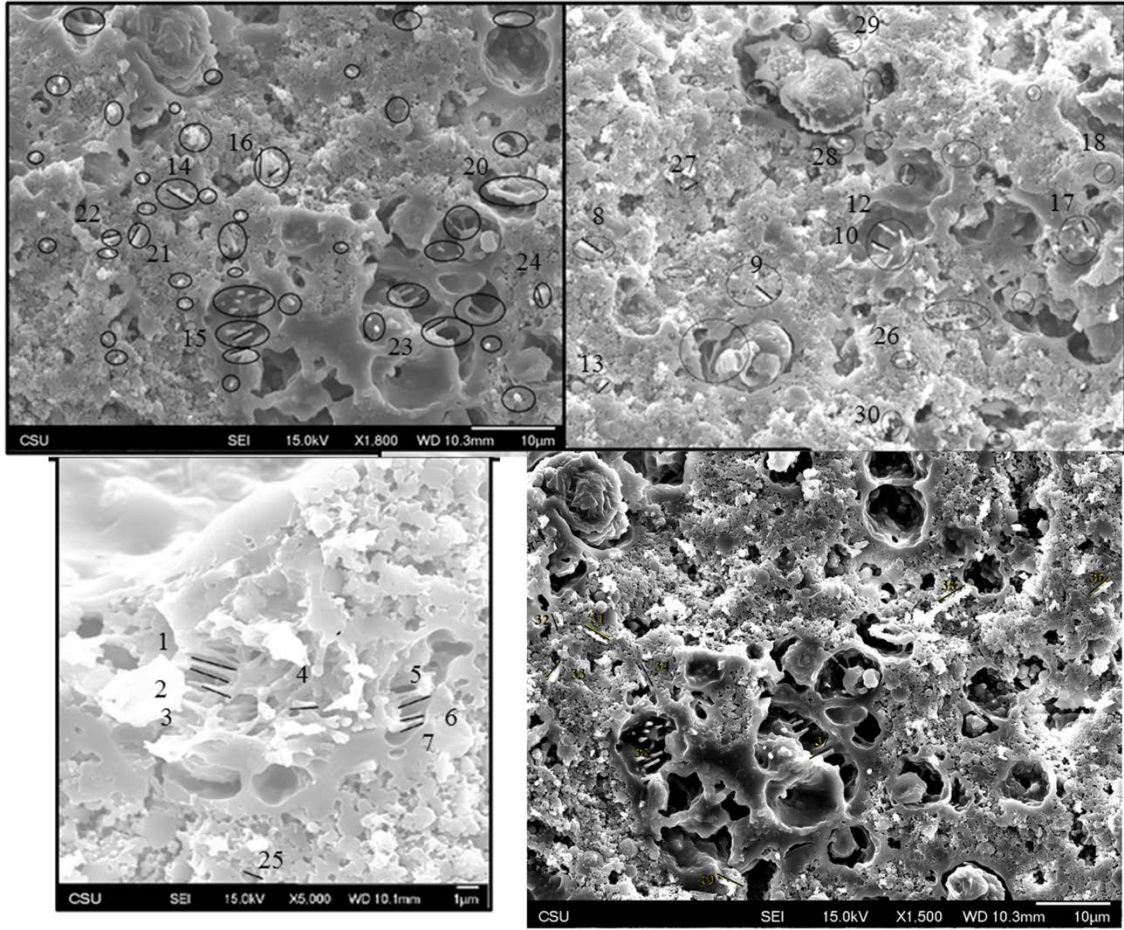


Figure C. 7. 2% SCW reinforced geopolymer samples treated at 650 °C.

Table C. 2. Pull out lengths of SCWs at 250 °C and 650 °C.

Treatment Temperatures, (°C )					
250 °C		650 °C			
SCW number	Length (µm)	SCW number	length (µm)	SCW number	Length (µm)
1	0.977	1	3.83	21	1.585
2	0.782	2	3.899	22	2.347
3	1.029	3	3.782	23	3.644
4	0.789	4	2.658	24	2.553
5	1.072	5	2.69	25	2.082
6	1.519	6	2.875	26	2.485
7	1.4	7	2.439	27	1.97
8	1.416	8	2.359	28	1.898
9	1.305	9	2.887	29	1.672
10	1.076	10	2.126	30	2.675
11	0.904	11	2.804	31	3.964
12	0.887	12	2.257	32	2.476
13,14	0.919, 1.086	13	1.744	33	3.831
15,16	0.711, 0.915	14	2.955	34	3.535
17,18	0.933, 0.875	15	2.886	35	4.5
19,20	0.757, 0.746	16	3.177	36	3.525
21,22	0.715, 0.854	17	2.201	37	3.29
23,24	0.934, 0.875	18	2.4	38	3.077
25,	1.001	19	1.986	39	3.502
20		20	2.163	40	3.5
Average length, (µm)	0.9768				2.81
Standard Deviation, (µm)	0.223				0.73



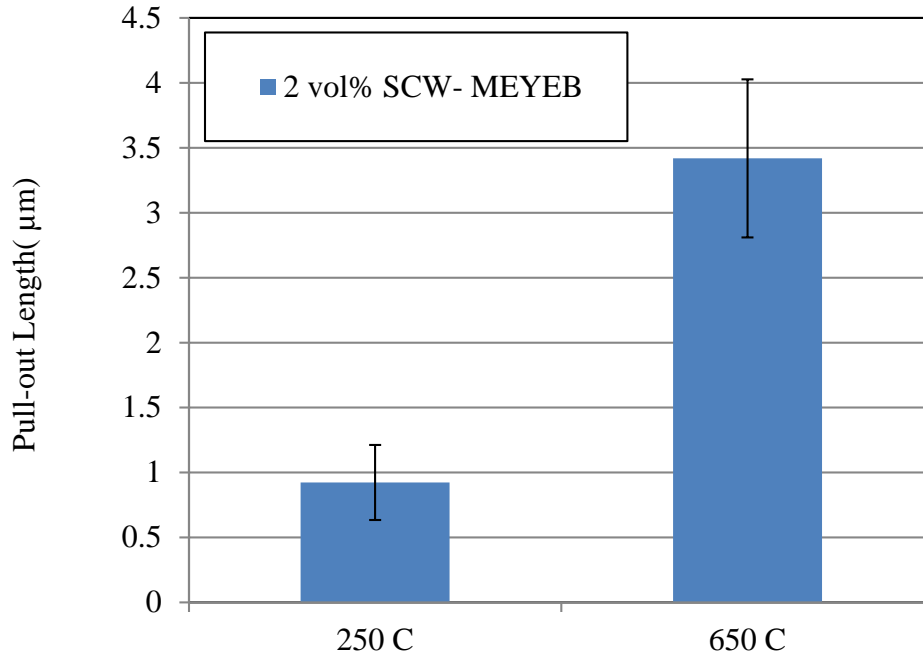


Figure C. 8. Comparisons to the pull out lengths of SCW in 2vol% SCW reinforced MEYEB heat treated at 250C and 650 °C (O<sub>2</sub>) (The statistical significance was estimated using the pull out lengths with statistics of 30-40 nanofibers in each system as shown in Table C.2 . )

Figure C. 9 shows the evidence of pull out lengths of CNFs in 2% CNF. Two pictures presenting a number of nanofibers that pulled out of the matrix. Table below presents the length of pull out with standard deviation.

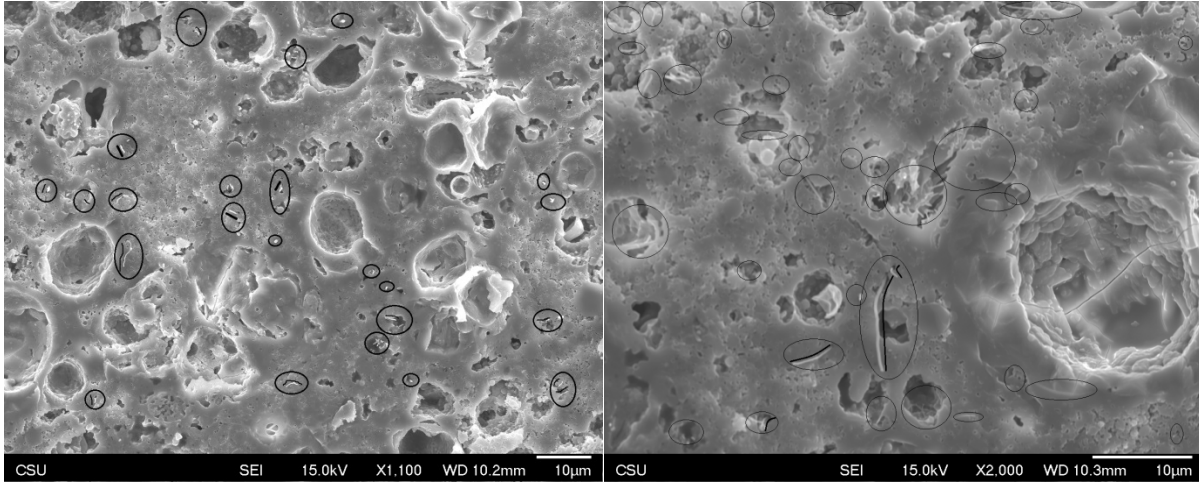


Figure C. 9. Estimation of the pull out lengths of CNFs treated at 650 °C in nitrogen

Table C. 3. Pull out lengths of CNFs at 650 °C in nitrogen.

Nanofiber No.	Length, $\mu\text{m}$	Nanofiber No.	Length, $\mu\text{m}$
1	4.586	10	5.182
2	6.71	11	2.211
3	2.194	12	2.359
4	2.419	13	4.353
5	2.201	14	3.216
6	2.454	15	3.361
7	2.391	16	3.657
8	1.801	17	1.981
9	2.648	18	2.536
Average, $\mu\text{m}$			3.094
Standard deviation, $\mu\text{m}$			1.28

#### C4: Data of EDS Analysis

Figure C.10 and Table C.4 present EDS spectrum of 2% SCW reinforced MEYEB treated at 650 °C in oxygen. Figure C.11 and Table C.5 EDS on the surface and the interface of SCW and MEYEB at SCW reinforced MEYEBE treated in the similar condition.

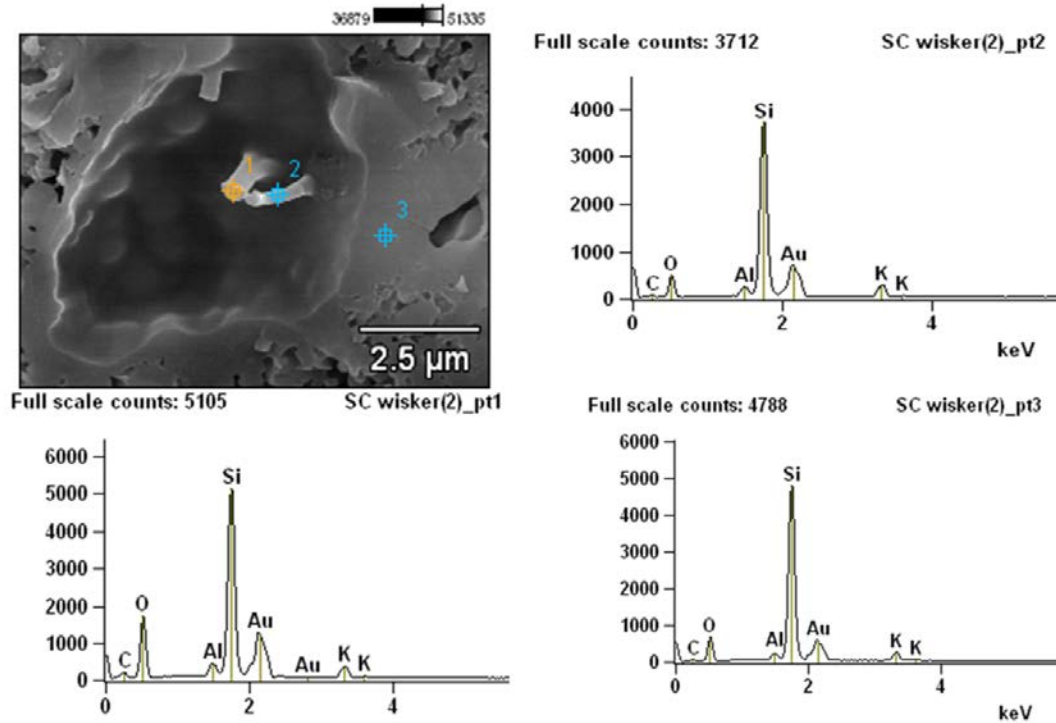


Figure C. 10. EDS spectrum of various locations of SCW reinforced MEYEB treated at 650 °C in oxygen.

Table C. 4. Atomic wt % of the EDS spectrum on various locations of Figure above.

	C-K	O-K	Al-K	Si-K	K-K	Au-M
SCW_pt1	6.98	39.54	1.39	25.86	3.32	22.90
SCW_pt2	7.16	24.50	1.48	35.24	5.33	26.28
SCW_pt3	3.58	30.51	0.87	40.99	4.35	19.71

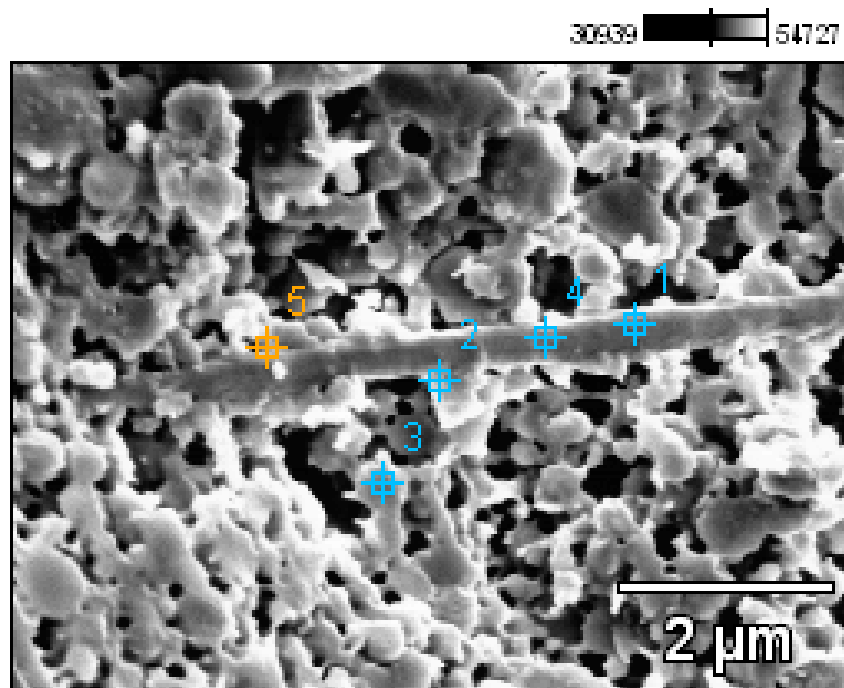


Figure C. 11. EDS spectrum of the interface locations of SCW in SCW reinforced MEYEB treated at 650 °C in oxygen.

Table C. 5. Atomic wt % of the EDS spectrum on various locations of Figure above.

	C-K	O-K	Si-K	Au-M
SCW)_pt1	0.87	2.46	24.52	72.15
SCW)_pt2	0.87	4.36	27.05	67.71
SCW)_pt3	0.39	2.43	30.20	66.98
SCW)_pt4	0.38	2.46	26.94	70.22
SCW)_pt5	0.56	3.36	51.00	45.08

The following data is for EDS spectrum of ANF rich and ANF lean microstructures of 2% ANF reinforced MEYEB.

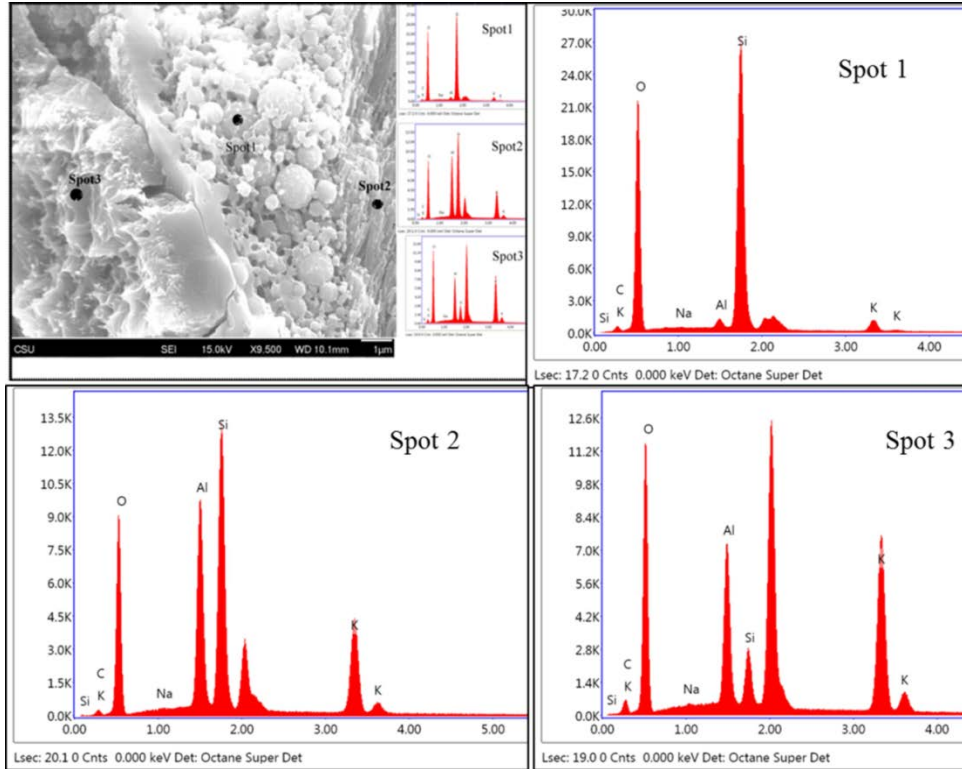


Figure C. 12. EDS spectrum of ANF rich and ANF lean microstructures of 2% ANF reinforced MEYEB.

Table C. 6. Element wt% from the EDS spectrum of the Figure above

Element	Spot1 (Weight %)	Spot 2 (Weight %)	Spot 3 (Weight %)
C K	6.09	2.21	2.53
O K	53.56	40.92	53.38
NaK	1.21	0.00	0.92
AlK	1.52	15.89	12.04
SiK	34.38	24.28	4.46
K K	3.24	16.70	26.67

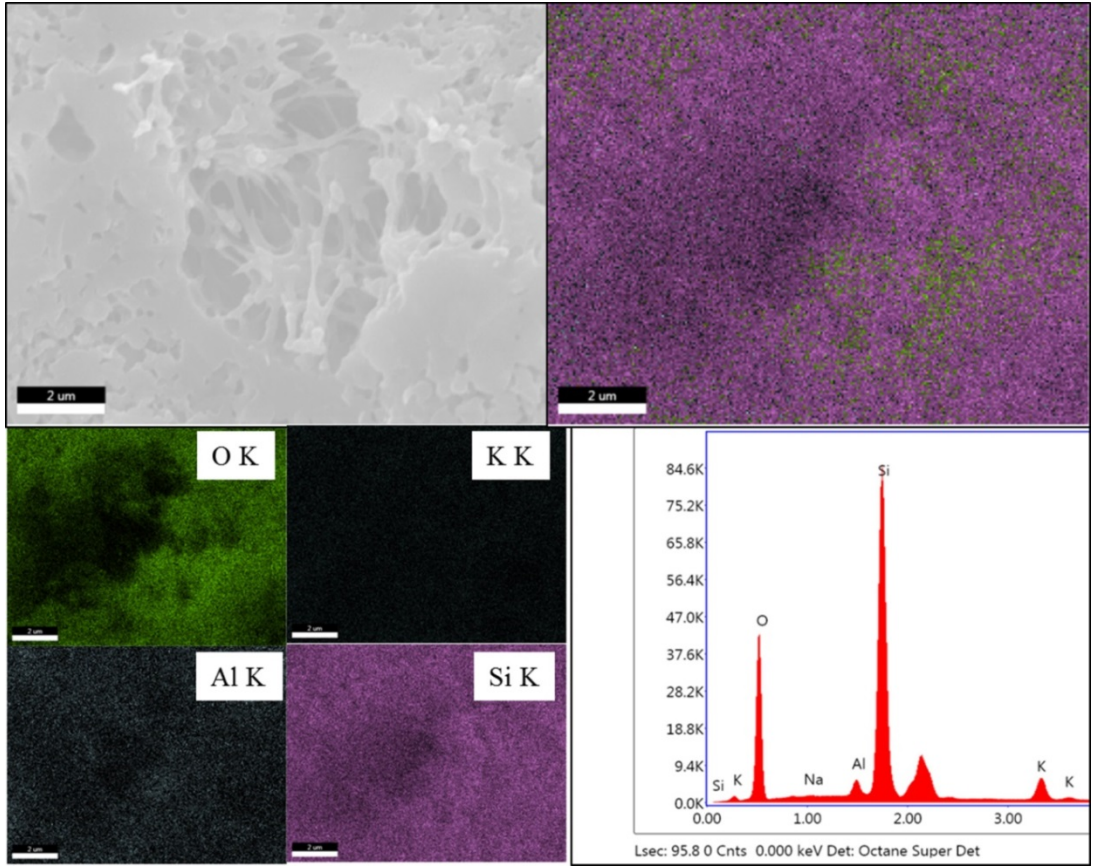


Figure C. 13. EDS spectrum of overall microstructures of 2% ANF reinforced MEYEB treated at 650 °C from area analysis.

Table C. 7. Elements wt% from the EDS spectrum of the Figure above

Element	Weight, %	Atomic, %
O K	46.70	61.43
Na K	0.08	0.07
Al K	2.04	1.59
Si K	44.34	33.22
K K	6.84	3.68

The following data is for EDS spectrum of similar sample (2% ANF reinforced MEYEB treated at 650 °C) from point analysis. Area and point analysis gave same results.

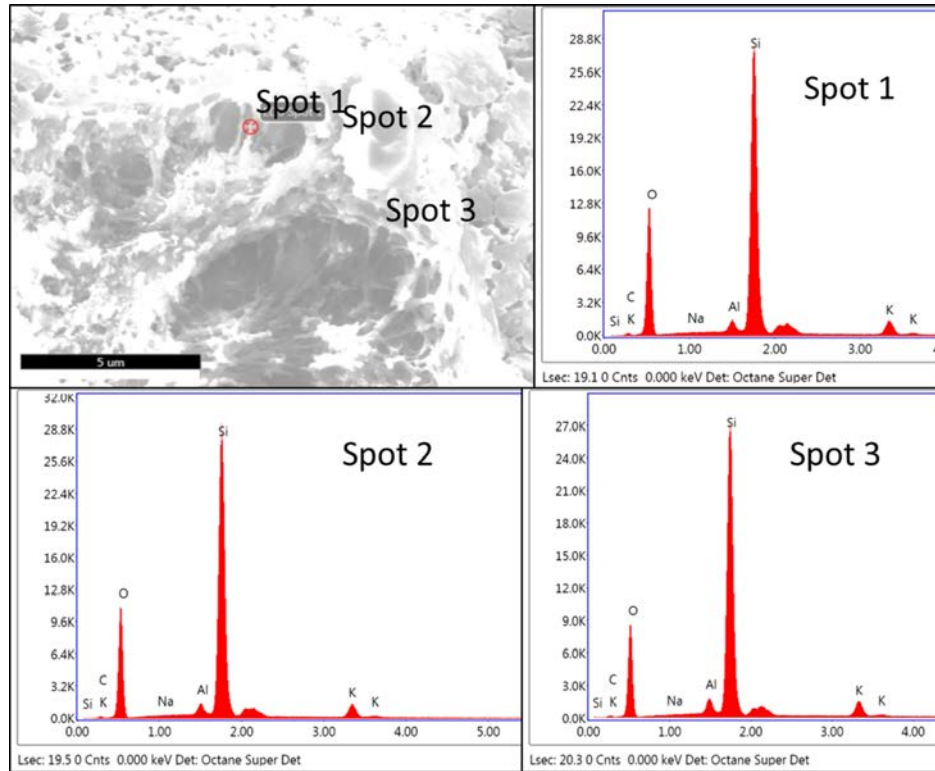


Figure C. 14. EDS specturm of overall microstructures of 2% ANF reinforced MEYEB treated at 650 °C from point analysis.

Table C. 8. Elemnets wt% from the EDS spectrum of the Figure above.

Element	Spot1 (Weight %)	Spot 2 (Weight %)	Spot 3 (Weight %)
C K	2.40	2.08	1.74
O K	44.44	42.03	38.22
Na K	0.05	0.00	0.00
Al K	2.03	1.96	2.52
Si K	45.68	48.63	51.26
K K	5.41	5.30	6.26



## LIST OF ABBREVIATIONS

IS- Interfacial Strength

AR-Aspect Ratio

VF- Volume Fraction

T- Temperature

E-Environment

SCW-Silicon Carbide Whisker

SCP-Silicon Carbide Particles

SEM- Scanning Electron Microscopy

ANF-Alumina Nanofiber

ANP-Alumina Nanoparticles

ANNOVA-Analysis of Variations

AFM- Atomic Force Microscopy

CNF-Carbon Nanofiber

CNP-Carbon Nanoparticles

CVD- Chemical Vapor Deposition

CVI-Chemical Vapor Infiltration

GMC-Geopolymer Matrix Composites

O<sub>2</sub>- Diatomic Oxygen

MEYEB- Research Grade Sodium Based Inorganic Polymer

MTA- Material Transfer Agreement

N-The SI unit of force, Newton

N<sub>2</sub>- Diatomic Nitrogen

PTFE- Poly Tetra Fluoro Ethylene

T<sub>g</sub>- Glass Transition Temperature

DTA- Differential Thermal Analysis

TMA- Thermo Mechanical Analysis

TGA- Thermo Gravimetry Analysis

DSC- Differential Scanning Calorimetry

DOE- Design of Experiments

SEVNB- Single Edge V-notch Beam

EDS- Energy Dispersive Spectroscopy

EDAX- Energy Dispersive X-ray Spectroscopy

MnK $\alpha$ - X-ray Energy Line of pure Manganese

XRD- X Ray Diffraction